

**UCLA**

**UCLA Electronic Theses and Dissertations**

**Title**

Mechanisms of detection sensitivity and adaptation in the rod visual pathway

**Permalink**

<https://escholarship.org/uc/item/4tt400wt>

**Author**

Griffis, Christopher Gilbert

**Publication Date**

2022

Peer reviewed|Thesis/dissertation

UNIVERSITY OF CALIFORNIA

Los Angeles

Mechanisms Of Detection Sensitivity And Adaptation In The Rod Visual Pathway

A dissertation submitted in partial satisfaction

of the requirements for the degree

Doctor of Philosophy in Molecular, Cellular, and Integrative Physiology

by

Christopher Gilbert Griffis

2022



© Copyright by  
Christopher Gilbert Griffis  
2022

## ABSTRACT OF THE DISSERTATION

Mechanisms Of Detection Sensitivity And Adaptation In The Rod Visual Pathway

by

Christopher Gilbert Griffis

Doctor of Philosophy in Molecular, Cellular, and Integrative Physiology

University of California, Los Angeles, 2022

Professor Alapakkam P. Sampath, Chair

Vision begins in the retina, where photoreceptors have the task of discriminating incoming photons from intrinsic cellular noise. Vertebrates have evolved a duplex retina, in which rod and cone photoreceptors respond over a broad range of light intensities from single photons to bright light. Rods evolved from less sensitive cone-like photoreceptors and are responsible for mediating the lowest 8 orders of magnitude of light intensity. At the lowest threshold of vision, rods detect single photons and transmit signals to downstream neurons in a specialized circuit. In the rod visual pathway, tens of rods converge onto a single rod bipolar cell, where noise from the rods is filtered, and rod signals are processed for further downstream transmission. It is unclear which evolutionary changes imparted such sensitivity to rods, and how these advantages allow for rods to discriminate single photons from intrinsic noise. In downstream bipolar cells, the mechanism for setting the filtering threshold is unknown. Further, it is unclear what implications of the thresholding of rod bipolar cells have on vision in scotopic light levels.

In this thesis, I investigated the mechanisms that work together to define the threshold of vision. To gain understanding of the nature of vision at the absolute threshold, I worked with three main goals in mind:

- *Goal 1:* Determine the set of changes that make feasible the incredible sensitivity of rods.

- *Goal 2:* Assess contributions of transduction proteins to the detection of single photons versus intrinsic noise.
- *Goal 3:* Measure the ability of rod bipolar cells to shape and parse rod signals over several orders of magnitude of ambient light levels.

To achieve these goals, I collected single-cell electrophysiological from mouse rods and rod bipolar cells. I analyzed the data with statistical models to determine parameters that described the mechanisms of visual threshold and adaptation. I also used statistical modeling to help validate results of mathematical modeling from our collaborators in the Reingruber Lab (Paris, France), which show that the important differences between rods and cones are reflected in the cone as a reduced outer segment volume, a decreased amplification through the transduction cascade, a faster turnover rate of the cyclic guanosine monophosphate second messenger, and an accelerated rate of decay of the phosphodiesterase (PDE) enzyme (goal 1). Through analysis of intrinsic noise in rods, I showed that PDE is the critical transduction element both setting the noise level and limiting the detection threshold and variability for single-photon absorptions (goal 2). Further, measurements in rod bipolar cells revealed that rod bipolar cells have a calcium-dependent feedback mechanism that allows rod bipolar cells to respond robustly to single-photon absorptions in the minority of the rods, while continuing to signal in brighter backgrounds that also cause rod adaptation (goal 3). Taken together, my work has helped delineate the fundamental mechanisms of signal detection and processing at the threshold of vision and over the dynamic range of rod vision.

The dissertation of Christopher Gilbert Griffis is approved.

Gordon L. Fain

Mark A. Frye

Thomas J. O'Dell

Alapakkam P. Sampath, Committee Chair

University of California, Los Angeles

2022

*For Gil, who never made “BIG mistakes”. For Grancy, who lived and loved to the fullest.  
To Oliver and Declan, who, in your everlasting patience, never forgot about a ‘Happy’ story.*

## TABLE OF CONTENTS

<b>List of Figures</b> . . . . .	<b>x</b>
<b>List of Tables</b> . . . . .	<b>xiii</b>
<b>List of Abbreviations</b> . . . . .	<b>xiv</b>
<b>Acknowledgments</b> . . . . .	<b>xv</b>
<b>Curriculum Vitae</b> . . . . .	<b>xvii</b>
<b>1 Introduction</b> . . . . .	<b>1</b>
1.1 Vision! . . . . .	1
1.2 Architecture of the vertebrate retina . . . . .	3
1.2.1 Cell types of the mammalian retina . . . . .	3
1.2.2 Photoreceptors . . . . .	5
1.3 Rod vision . . . . .	7
1.4 Adaptation . . . . .	14
1.5 Goals of the thesis . . . . .	16
References . . . . .	18
<b>2 A kinetic analysis of mouse rod and cone photoreceptor responses</b> . . . . .	<b>21</b>
2.1 Preface to Chapter 2 . . . . .	21
2.2 Abstract . . . . .	22
2.3 Introduction . . . . .	23
2.4 Materials and methods . . . . .	25

2.5	Results . . . . .	35
2.5.1	Normalized log-transform of the rod and cone light response . . . . .	36
2.5.2	Model for the rod and cone response . . . . .	37
2.5.3	Adjusting the rod model . . . . .	37
2.5.4	Transforming rod dynamics into cone dynamics . . . . .	42
2.5.5	Adjusting the cone model . . . . .	43
2.5.6	Response to a single photon . . . . .	48
2.6	Discussion . . . . .	49
2.7	Additional information . . . . .	53
2.7.1	Competing interests . . . . .	53
2.7.2	Author Contributions . . . . .	53
2.7.3	Funding . . . . .	53
2.7.4	Acknowledgements . . . . .	54
2.8	Supplemental materials . . . . .	54
	References . . . . .	56

<b>3</b>	<b>The molecular basis for continuous noise and its implications on the threshold of photon detection . . . . .</b>	<b>63</b>
3.1	Abstract . . . . .	63
3.2	Introduction . . . . .	64
3.3	Materials and Methods . . . . .	65
3.4	Results . . . . .	76
3.4.1	Biophysical properties of the flash response . . . . .	76
3.4.2	Transducin activity increases flash sensitivity . . . . .	78
3.4.3	Reduced PDE6 activity increases flash sensitivity . . . . .	79

3.4.4	Severe reduction of PDE6 activity alters response kinetics . . . . .	85
3.4.5	Continuous noise in rod photoreceptors . . . . .	88
3.4.6	Isolation of the single-photon response . . . . .	93
3.4.7	Transduction proteins shape the single-photon response . . . . .	94
3.5	Discussion . . . . .	101
	References . . . . .	107
<b>4</b>	<b>Rod bipolar cell contributions to adaptation in the mammalian rod path-</b>	
	<b>way . . . . .</b>	<b>113</b>
4.1	Abstract . . . . .	113
4.2	Introduction . . . . .	114
4.3	Methods . . . . .	115
4.4	Results . . . . .	121
4.4.1	Determination of the rod collecting area . . . . .	121
4.4.2	Photoreceptor gain is dependent on background light levels . . . . .	122
4.4.3	Background light asynchronously affects rod-bipolar response dynamics	125
4.4.4	Background light suppresses the RBC maximal response . . . . .	130
4.4.5	Calcium entry during light exposure modulates the RBC maximal re-	
	sponse . . . . .	136
4.5	Discussion . . . . .	139
4.5.1	Feed-forward adaptation . . . . .	141
4.5.2	A role for calcium . . . . .	143
4.5.3	Mechanisms of adaptation . . . . .	144
	References . . . . .	146
<b>A</b>	<b>Iris: data visualization and analysis . . . . .</b>	<b>152</b>



A.1	Introduction . . . . .	152
A.2	Software Interface . . . . .	152
A.2.1	Data Navigation . . . . .	154
A.2.2	Metadata Viewers . . . . .	156
A.3	Preferences . . . . .	157
A.3.1	Navigation . . . . .	159
A.3.2	Workspace . . . . .	159
A.3.3	Data . . . . .	162
A.4	Data Analysis . . . . .	166
A.4.1	Importing Data . . . . .	167
A.4.2	Exporting Data . . . . .	171
A.4.3	Custom Analysis . . . . .	171
A.4.4	Custom Modules . . . . .	176
A.5	Quick Start . . . . .	178
A.5.1	Requirements . . . . .	178
A.5.2	Installation . . . . .	178
A.5.3	Known Issues . . . . .	179
A.5.4	Application Development . . . . .	180
	References . . . . .	183

## LIST OF FIGURES

1.1	Vertebrate retina . . . . .	4
1.2	Retinal cell types . . . . .	6
1.3	Rod and cone photoreceptors . . . . .	8
1.4	Rod phototransduction . . . . .	10
1.5	Rod bipolar cells repond through mGluR6 . . . . .	13
1.6	Statistical nature of photon detection . . . . .	14
1.7	The retina is the site of light adaptation . . . . .	15
1.8	Rod pathway adaptation progresses outward . . . . .	16
2.1	Experimental current recordings from mouse rod and cones . . . . .	29
2.2	Normalized log-transforms of response waveforms . . . . .	31
2.3	Schema of transduction cascade showing rates of activation and decay used in the model . . . . .	38
2.4	Adjusting the rod model . . . . .	41
2.5	Transition from rod to cone kinetics . . . . .	44
2.6	Adjusting the cone model . . . . .	46
2.7	Single-photon response (SPR) for rod and cone model . . . . .	47
3.1	Biophysical properties of the flash response . . . . .	77
3.2	Transducin concentration and active lifetime modulate flash sensitivity . . . . .	80
3.3	PDE6A <sup>D167A/D167A</sup> mutants show reduced basal activity in the retina . . . . .	82
3.4	Effects of PDE concentration on response properties . . . . .	83
3.5	Flash response kinetics . . . . .	87
3.6	Isolation of the continuous noise spectrum . . . . .	89

3.7	Reduced transducin expression has no effect on continuous noise . . . . .	91
3.8	Reduced PDE expression shifts frequency composition of continuous noise . . .	92
3.9	Isolation of the single-photon response . . . . .	95
3.10	The single-photon response is shaped by transduction proteins . . . . .	96
3.11	Transduction components alter kinetics of the single-photon response . . . . .	99
4.1	Determination of effective collecting area . . . . .	122
4.2	Rod dim flash responses are accelerated and reduced in amplitude by background light . . . . .	123
4.3	Gain at rod photoreceptors is reduced in background light . . . . .	124
4.4	Rod bipolar cell flash response is reduced in background light . . . . .	126
4.5	Effects of background light on rod bipolar cell stimulus-response relationships .	127
4.6	Rod bipolar cell response properties are differentially altered by background light	129
4.7	Rod bipolar cell maximal flash response is reduced in background light . . . . .	132
4.8	Rod bipolar cell flash response is reduced in background light . . . . .	134
4.9	Buffering internal calcium increases nonlinearity . . . . .	135
4.10	Large positive holding voltage and BAPTA decrease the effects of background illuminance on maximal response amplitudes . . . . .	137
4.11	Calcium entry reduces maximal response amplitude . . . . .	140
A.1	Iris main view . . . . .	153
A.2	Data overview interface . . . . .	155
A.3	Notes viewer . . . . .	156
A.4	File information viewer . . . . .	157
A.5	Data properties viewer . . . . .	158
A.6	Preferences interface . . . . .	159

A.7	Navigation control . . . . .	161
A.8	Workspace variables . . . . .	162
A.9	Display preferences . . . . .	163
A.10	Digital filtering preferences . . . . .	163
A.11	Statistics processing preferences . . . . .	164
A.12	Scaling preferences . . . . .	166
A.13	Reader I/O . . . . .	168
A.14	Iris application structure . . . . .	169
A.15	Datum response structure . . . . .	170
A.16	Analysis export user interface . . . . .	172
A.17	New analysis creation . . . . .	173
A.18	Custom analysis header . . . . .	173
A.19	Custom Analysis Example . . . . .	177
A.20	Iris application structure . . . . .	181

## LIST OF TABLES

2.1	Parameter descriptions for rod and cone model . . . . .	33
2.2	Parameter values for rod and cone models . . . . .	39
3.1	Biophysical properties of the flash response family . . . . .	85
3.2	Single-photon response properties . . . . .	97
4.1	Stimulus-response properties . . . . .	131
A.1	Iris keyboard shortcuts . . . . .	160
A.2	Iris utilities . . . . .	174
A.3	IrisData Properties . . . . .	177
A.4	Iris command line interface . . . . .	179

LIST OF ABBREVIATIONS

## ACKNOWLEDGMENTS

Albert Einstein wrote: ‘Many times a day I realize how much my own outer and inner life is built upon the labors of my fellow men, both living and dead, and how earnestly I must exert myself in order to give in return as much as I have received. My peace of mind is often troubled by the depressing sense that I have borrowed too heavily from the work of other men.’. It is with this sentiment that find myself unable to list all of the people whose dedication to my achievements have sustained me on my endeavors. So, I begin with an apology to those who deserve acknowledgment, and without whom, I would have never recovered from my failures or celebrated my successes.

I’d like to thank my dissertation committee for so much. A particularly special thank you to my committee chair, Dr. Alapakkam “Sam” Sampath, for giving me the opportunity to work in his laboratory. I am grateful for his continuous support, our discussions, his unending patience, and his great wealth of knowledge, both in and out of science. To Dr. Gordon Fain, who I could never think of as the ‘Lab Grandpa’, because his vigor and enthusiasm for life, the arts, and science preclude any notion of age. I am incapable of expressing the thanks I have to give to Gordon; his unquenchable thirst for the next ‘thing’ is matched only by his infinite patience and understanding. Thank you to Dr. Mark Frye, to Dr. Tom O’Dell. There’s nothing like having a committee who knows when to push and when to let you coast. It is with incredible fortuity that I have come to work with such giants.

I’d like to thank my current and former colleagues in the Sampath Lab. It really is a treat to be in a place with people who not only share your curiosity in a particular scientific field, but with people who can also cheer the loudest at an Ace Frehley show, master a c-stand on a photography set, run through mud at full speed while laughing maniacally, spill beer all over celebrating a Kings goal, peruse the weekly farmer’s market, and hit a hiking trail to catch the magical sunrise; to name just a few of our follies together. Our times together had a huge impact on my mental health and kept me going even when experiments failed or projects fizzled. I can’t thank that crew enough.

Over the years, the one constant was the support of my family. I want to thank my two boys, Oliver and Declan, for being a light that guides me, and my wife, Dana, for the support, the sacrifice, and for always believing in me. To my mom and Brian, to my in-loves, and to the Yosemite family and beyond, their support and constant uplifting conversations have always meant so much to me. A thank you to my family and friends who are now relieved of the troubles of this world. Their lives, and the way they lived them, are a source of inspiration and joy.



## CURRICULUM VITAE

- 2015 – 2021 *Ph.D Candidate.* Molecular, Cellular, and Integrative Physiology, UCLA; Los Angeles CA.  
Department of Ophthalmology, Stein Eye Institute  
Laboratory of Alapakkam P. Sampath, Ph. D.
- 2013 – 2015 *Graduate Student Researcher.* Department of Integrative Biology and Physiology, UCLA; Los Angeles CA  
Laboratories of Patricia E. Phelps, Ph. D. and V. Reggie Edger-ton, Ph. D.
- 2011 – 2013 *Laboratory Technician.* Department of Integrative Biology and Physiology, UCLA; Los Angeles CA  
Laboratories of Patricia E. Phelps

## SELECT PUBLICATIONS

1. Reingruber, J., Ingram, N.T., Griffis, K.G. and Fain, G.L. (2020), A kinetic analysis of mouse rod and cone photoreceptor responses. *J Physiol*, 598: 3747-3763. doi.org/10.1113/JP279524.

## SELECT PRESENTATIONS

1. “Rod bipolar cell contributions to changes in response sensitivity during light adaptation” at ARVO 2021.

# CHAPTER 1

## Introduction

We begin with an overview of my general fascination of vision to the specific questions I endeavored to illuminate during my doctorate. I open the thesis with a brief look into the retina. Then, I outline the importance of studying mechanisms of sight at the visual threshold and implications for adaptation. I end this chapter with an introduction of the goals and questions I am addressing.

### 1.1 Vision!

“The most beautiful thing we can experience is the mysterious. It is the source of all true art and science. He to whom this emotion is a stranger, who can no longer pause to wonder and stand rapt in awe, is as good as dead: his eyes are closed.” (Einstein, 1930).

The living experience is encoded in the information extracted from the environment through our senses. Sensory stimuli, such as light, chemicals, pressure, and temperature are detected through specialized receptors that transduce stimuli into signals through the modulation of neurotransmitter release. These signals are transmitted through the neural circuitry, which, like any other electrical system, is host to many noisy processes. The task of discriminating the signal from the noise is nontrivial, yet sensory systems have evolved strategies that allow detection approaching the physical limits of the stimulus. For vision, this limit is at the detection of a single photon, which elicits a signal that reaches neural processing centers of the brain with minimal lag, in perceptual ‘real-time’.

Not only must the sensory modality detect signals near the absolute threshold of the stimulus, the system must also avoid saturation and continue to operate over a broad range of stimuli. This is accomplished by modulating the gain of the system in order to maximize sensitivity to newly arriving stimuli, even when the stimulus is weak in comparison to the background. A common strategy to amplify the weak signal is to place sensory neurons in a pool, from which second-order neurons sample in large groups. However, this amplification comes at the cost of, potentially, amplifying any noise from the pool of sensory receptors. Modalities employing the pooling strategy often have multiple levels of pooling, potentially increasing intrinsic cellular noise exponentially. Thus, the intrinsic noise of the system's constituents is critical to setting the detection limit of any sensory system. This leads one to ask the question: how does a sensory system minimize noise, manage noise generated by stimulation, and maximize salient features of the signal?

The mammalian visual system provides an opportunity to study how light is detected near the absolute threshold, how noise is managed, and how signals are processed and optimized for transmission through the neural circuitry. What makes the visual system optimal for studying these phenomena? Mostly, our current level of technology, which makes possible the accurate and reliable measurement of both signals and noise within well-defined sensory pathways. This measurement is made easier by the accessibility of the neural tissue, which, for most vertebrates, requires minimal dissection and processing. Importantly, rod photoreceptors and the rod sensory pathway have a very specific modality which can be easily manipulated, i.e., rods are sensitive to a narrow band of the visible electromagnetic spectrum and the light stimulus can be finely controlled. Further, we are able to evaluate, in single cells, the relationship between signals and noise, and how this relationship changes through several orders of magnitude of ambient light levels. Additionally, one advantage of studying the outer retina in particular is that stimuli evoke proportionally graded responses that lend themselves well to direct measurement and straight-forward analysis.

In this chapter, I focus primarily on background research which introduces the cellular and biochemical mechanisms of light detection, noise processing, and adaptation at the first

visual synapse. I place emphasis on the murine rod pathway; however, some insight into the evolution of the rod photoreceptor will also be provided. To understand the nature of the mechanisms that work together to define the threshold of sight, I first consult a model of the photoresponse to investigate the origin of photodetection (*goal 1*); I then measure the contributions of transduction proteins to the visual threshold and intrinsic photoreceptor noise (*goal 2*); and, finally, I measure the ability of rod bipolar cells to further process rod signals over several orders of ambient light levels (*goal 3*).

## 1.2 Architecture of the vertebrate retina

The visual experience begins as photons of light enter the eye. The anatomical features of the eye provide a means of attenuating, focusing, and overcoming aberrations from the incoming light. The vertebrate eye has many conserved features across species, with some anatomical specializations depending on those features of the visual scene that are most salient. Nevertheless, we can make comparisons across vertebrates using the human eye as an example (Fig. 1.1A). Generally, vertebrates have a large, camera-type eye with a single lens. Light enters the eye through the pupillary aperture, after passing through the transparent cornea, and is refracted by the lens onto the sensory tissue, called the retina. In humans, the cornea and lens focus the light onto a cone-dense region of the retina, called the fovea. The light must then traverse the 200 to 300  $\mu\text{m}$  thickness of the retina, passing through the retinal circuitry before being absorbed by the photoreceptors or the retinal pigmented epithelium (RPE) (Fig. 1.1B).

### 1.2.1 Cell types of the mammalian retina

Some of the earliest anatomical studies into the structure of the retina came from Santiago Ramón y Cajal, and have been expanded upon vastly in the 21<sup>st</sup> century. The mammalian retina is comprised of three somata-containing layers. Within these layers are the cell bodies for five classes of neurons with varying numbers of subtypes (Fig. 1.2). The outermost layer

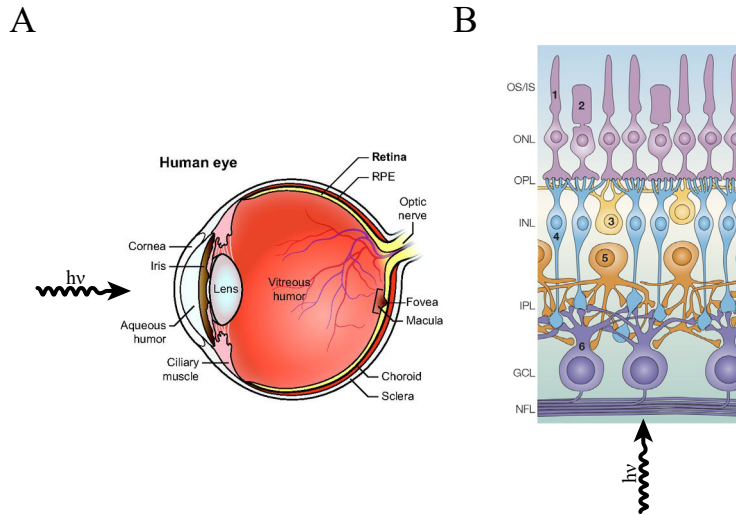


Figure 1.1: *Overview of the camera-type eye.* **A.** Cross-sectional diagram of the human eye. Light ( $h\nu$ ) passes through the transparent cornea and lens where it is focused onto the retina. The iris attenuates incoming light like the aperture of a camera lens. Light absorbed by the sensory receptors first passes through all the layers of the retina. Light not absorbed by photoreceptors is either absorbed or reflected back by the RPE. *Image adapted from (Veleri et al., 2015).* **B.** Schematic of the neural retina. The outer nuclear layer (ONL) contains the somata from two types of photoreceptors: rods (1, long outer segments) and cones (2, short outer segments). The sensory cilia, inner segments (IS), and outer segments (OS) from photoreceptors extend up into the RPE. Axons from photoreceptors extend into the outer plexiform layer (OPL) and synapse with dendrites and axons of second-order neurons, which have somata located in the inner nuclear layer (INL). The INL is comprised of horizontal (3), bipolar (4) and amacrine (5) cells. The ganglion cell layer (GCL), contains the cell bodies from the ganglion cells (6). *Image adapted from (Wässle, 2004).*

of the retina, contains the light-sensitive pigments, which are packed into the outer segments (OS) of the photoreceptors whose somata are located in the ONL. Photoreceptors project their axons toward the dendrites of the bipolar and horizontal cells, and the interconnected meshwork of synapses forms the OPL. Parallel pathways of transmission are formed by three or more types of horizontal cell, 9 to 11 different types of cone-driven bipolar cell, and the rod bipolar cells (Masland, 2001, Masland, 2012). Bipolar cells with somata in the INL project neural processes into a highly organized, synapse-rich region called the inner plexiform layer (IPL). Signals coming from photoreceptor outer segments are separated by bipolar cells into two distinct ON and OFF pathways. From the IPL, the signals are fed to nearly 30 types of amacrine cells and to at least as many types of ganglion cells. The ganglion cells then project axons through the optic disc to form the optic nerve, whose axons extend to higher neural processing areas of the central nervous system.

### 1.2.2 Photoreceptors

The thesis will focus primarily on a specialized circuit in which only one type of photoreceptor transmits information to one type of second-order neuron. Shown in green in Figs. 1.4 and 1.5, the rod-to-rod bipolar pathway is responsible for vision in the lowest orders of magnitude of light, from starlight to dim indoor lighting (Field et al., 2005, *for review*). Vertebrates have evolved a retina with two types of photoreceptors, referred to as a duplex retina, with each type responsible for vision in different ambient light levels (Schultze, 1866). The rods mediating scotopic dim light vision and the cones mediating photopic bright light vision carry fundamental information about their respective dynamic ranges through their dedicated circuits. While rods make functional synapses primarily with rod bipolar cells, cones make diverse connections with a vast array of cone bipolar-cell types (Fig. 1.2). Rods and cones derive from a single, cone-like, precursor (Fain et al., 2010, Lamb, 2020), and appeared very early in vertebrate evolution (Asteriti et al., 2015, Morshedean and Fain, 2015). They both use a similar transduction cascade (Fig. 1.3A). The differences in sensitivity and response kinetics between rods and cones, shown in Fig. 1.3B, were long thought to be explained by

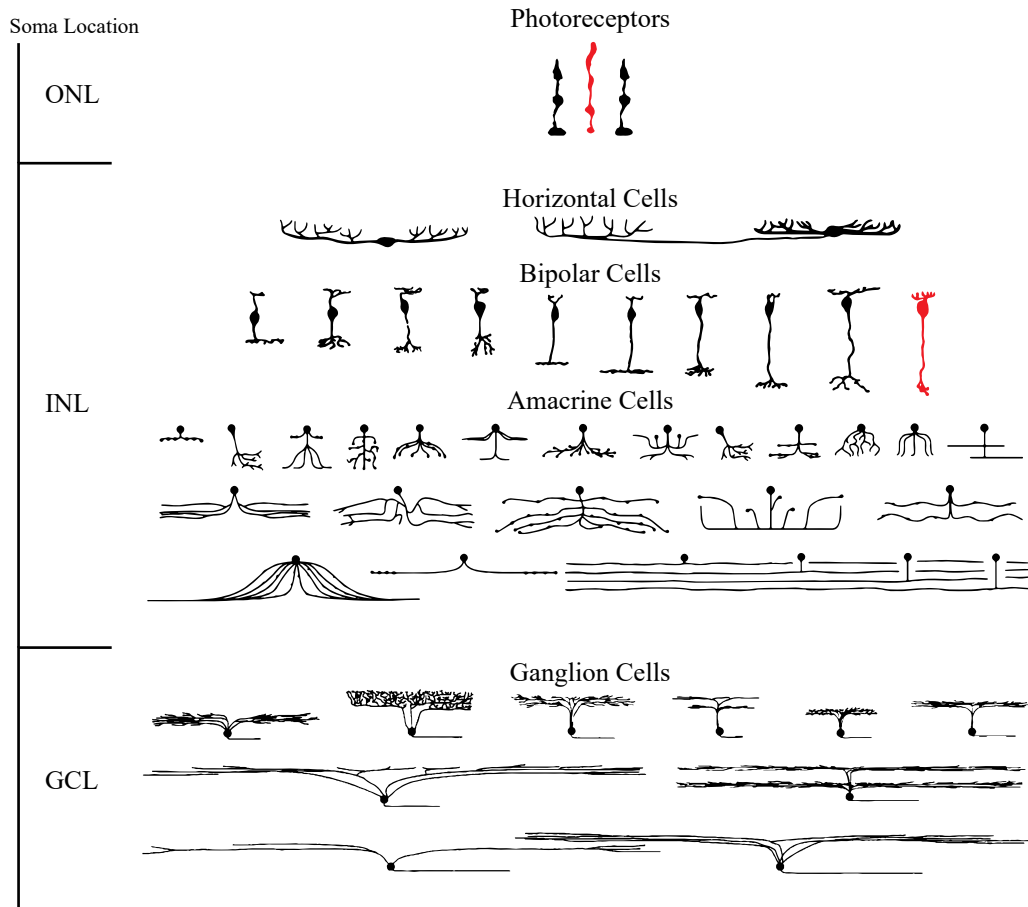


Figure 1.2: *The five major classes of retinal neurons.* Five major classes of retinal neurons have their cell bodies located in three nuclear layers. This thesis will focus on the rod-to-rod bipolar pathway, shown highlighted in red. *Image modified from (Masland, 2001).*

the differences in morphology. Cones have outer segments with lamellae that are continuous with the outer-segment membrane, while rods have encapsulated, stacked discs. However, we now know that these morphological differences contribute very little, if at all, to the physiological differences (Morshedean and Fain, 2015). Yet it remains unclear why rods are so much more sensitive than cones (Fain and Dowling, 1973).

The transduction machinery is embedded in the outer segments of the photoreceptors. Many attempts to express cone isoforms in rods, and rod isoforms in cones, have failed to elucidate one single mechanism responsible for the physiological discrepancies, though through molecular biological studies it is clear that the isoforms found in rods likely appeared gradually (Ingram et al., 2016, *for review*). Others have made perturbations of expression levels of shared proteins, such as over-expression of GTPase accelerating proteins (GAPs) (Krispel et al., 2006, Chen et al., 2010). Albeit insightful of the transduction mechanisms of rods, these experiments failed to transform the rod response into that of a cone. One issue with the aforementioned approaches is the difficulty with which a genetic model can be made in a timely manner, and the uncertainty that the perturbation is enough to produce a facsimile of one or the other photoreceptor phenotype. In Ch. 2, I describe our approach to the problem of determining what changes were accumulated to produce the highly sensitive rod from a cone. We utilized existing mathematical models (described in detail in Ch. 2) with electrophysiological data to gain insight into how rods became so sensitive in the mammalian retina.

### **1.3 Rod vision**

The outer segments of photoreceptors contain tightly packed, light-sensitive proteins that are selectively sensitive to narrow bands of the visible electromagnetic spectrum (Wald, 1968). These photopigments undergo structural changes when they absorb light, a process called photoisomerization (Fain, 2019, *for example*). Upon absorption of a photon, the activated photopigment initiates a G protein cascade resulting in a changes to the membrane potential and an alteration in the rate of glutamate release. The major proteins and mechanisms are



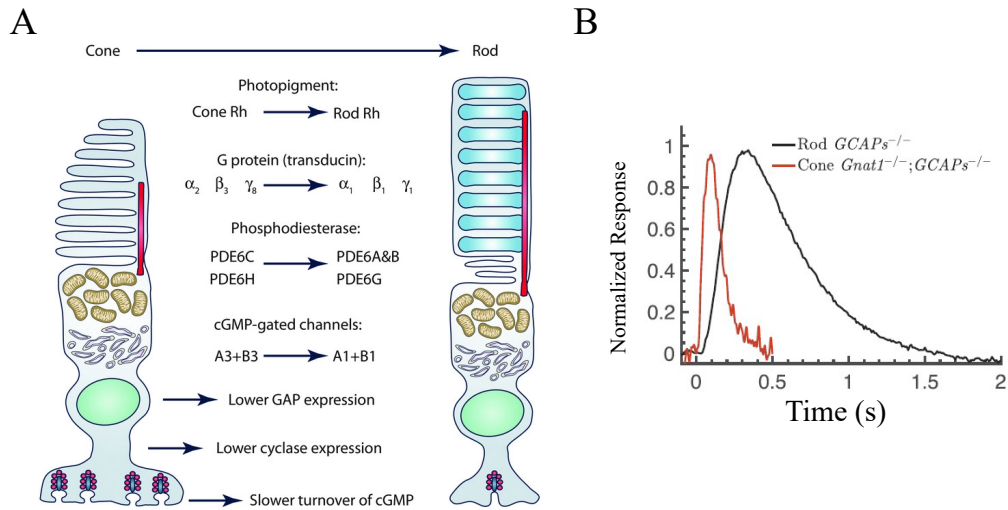


Figure 1.3: *Rod and cone photoreceptor differences*. **A**. Rods and cones contain much of the same molecular machinery, differing only in isoforms and expression levels. Morphological differences are manifest in the shape of the outer segments; the cone lamellae are continuous with the outer-segment membrane while rod lamellae are free-floating discs. Rods and cones also differ in the number of synapses they form with downstream neurons. *Image originally published in (Ingram et al., 2016)*. **B**. Normalized average mouse rod (black) and cone (red) photoresponses to brief flashes delivered at time 0. Rod responses are slower and longer lasting but orders of magnitude more sensitive than those of cones. *Image from Ch. 2 and (Reingruber et al., 2020)*.

shown in Fig. 1.4B. In darkness, photoreceptors have a moderately depolarized membrane potential<sup>1</sup> ( $\sim -40$  mV), due to the constant influx of sodium ( $\text{Na}^+$ ) and calcium ( $\text{Ca}^{2+}$ ) through open cyclic-nucleotide gated channels (CNG channels), called the ‘dark current’. Upon the absorption of a photon, the photopigment becomes activated ( $\text{Rh}^*$ ). With a gain of about 10 to 20 (Arshavsky and Burns, 2014),  $\text{Rh}^*$  catalyzes the replacement of guanosine 5'-diphosphate (GDP) with guanosine 5'-triphosphate (GTP) on the  $\alpha$  subunit of the heterotrimeric GTP-binding protein, transducin ( $\text{G}_T$ ). The light activated  $\alpha$ -transducin ( $\text{G}\alpha_T^*$ ) dissociates from the  $\beta$  and  $\gamma$  subunits and interacts with the  $\gamma$  subunits of the phosphodiesterase (PDE) to disinhibit PDE, allowing for the rapid hydrolysis of cyclic guanosine monophosphate (cGMP). The rapid decline in cGMP triggers the gating mechanism on CNG channels and the open probability of the channels decreases, causing a reduction of the dark current and a hyperpolarization of the membrane potential. The voltage-sensitive L-type  $\text{Ca}^{2+}$  channel at the rod spherule active zone (AZ) is modulated by the hyperpolarized membrane potential and interaction with  $\text{Ca}^{2+}$ -binding protein 4 (CaBP4). This modulation reduces vesicle dynamics and decreases glutamate release (Dowling and Ripps, 1973) (Fig. 1.5B-*top*).

A major feature of excitable cells is the ability to return to a stable point after an initial stimulus-induced response. For photoreceptors, the light response is recovered in multiple steps. Just as the visual pigment is activated, it must also be inactivated. Inactivation is achieved by multiple phosphorylation of rhodopsin by a G protein receptor kinase (GRK), in a manner that likely causes stepwise reductions in  $\text{Rh}^*$  activity (Field and Rieke, 2002a). Phosphorylated rhodopsin is then bound with arrestin and can no longer activate  $\text{G}_T$ .  $\text{G}\alpha_T^*$  and activated PDE are also deactivated through binding with GAPs in a complex, which accelerates the hydrolysis of GTP to GDP, releasing PDE $\gamma$  subunits to inhibit light-activated PDE activity. To restore cGMP levels, guanylyl cyclase (GC) activity is accelerated through  $\text{Ca}^{2+}$ -dependent interaction with guanylyl cyclase activating proteins (GCAPs), and the CNG channels reopen, restoring the dark current.

---

<sup>1</sup>Relative to typical excitable cells ( $\sim -70$  to  $-90$  mV).

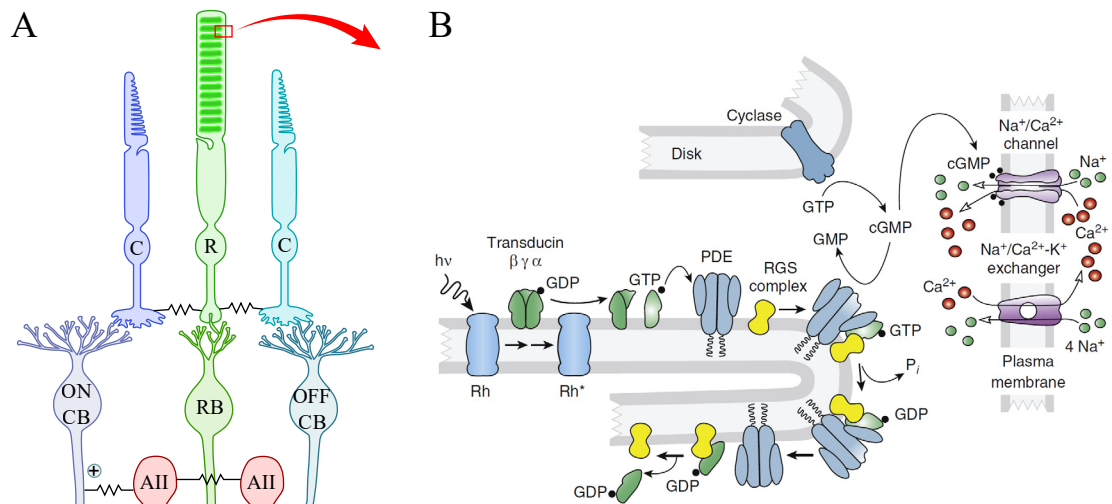


Figure 1.4: *Rod phototransduction cascade*. **A.** Schematic of the functional connections of the outer retina. Rod photoreceptors make a single synapse with the dendrites of two different rod bipolar cells (RBCs) (only one shown) and two horizontal cells (not shown). Cones make synapses with ON and OFF pathways through associated cone bipolar cells (CBCs). Rods and cones are electrically coupled by gap junctions. Red rectangle indicates the level of the rod outer segment depicted in B. Abbreviations: C, cone; R, rod; CB, cone bipolar cells; RB, rod bipolar cell; AII, AII amacrine cells. **B.** Schematic of the major proteins and mechanisms in vertebrate phototransduction. Abbreviations:  $h\nu$ , light;  $Rh^*$ , activated form of the photopigment rhodopsin; GTP, guanosine triphosphate; GDP, guanosine diphosphate; cGMP, guanosine 3',5'-cyclic monophosphate; GMP, guanosine monophosphate; PDE, guanosine nucleotide phosphodiesterase; RK, rhodopsin kinase; RGS complex, group of three proteins including RGS9 which accelerate the hydrolysis of GTP by the alpha subunit of transducin; and  $P_i$ , inorganic phosphate. *Image adapted from (Fain et al., 2010).*

Closely apposed to the CNG channels are  $\text{Na}^+/\text{Ca}^{2+}$ ,  $\text{K}^+$  exchanger proteins (NCKXs) (Bauer, 2006), which extrude  $\text{Ca}^{2+}$  by utilizing the inward  $\text{Na}^+$  and outward potassium ( $\text{K}^+$ ) gradients (Cervetto et al., 1989). During a prolonged light response, this exchanger continually extrudes  $\text{Ca}^{2+}$  and, through  $\text{Ca}^{2+}$ -feedback, the light response is accelerated with decreased sensitivity (Fain et al., 2001). This change in the response profile is referred to as adaptation. In Ch. 4, we characterize how adaptation in rods is manifest in gain changes for the response to single photons, and what contributions these changes make to rod-bipolar adaptation.

Although the above overview of phototransduction was focused on rod photoreceptors, the process is similar in cones, albeit with less sensitivity and faster response kinetics, as shown in Fig. 1.3B.

In the above passages, I described the biochemical processes by which phototransduction, at the absorption of a photon, initiates a cascade of amplifying events to elicit a reduction in glutamate output, propagating the signal through the retina. These biochemical processes are inherently noisy. In darkness, discrimination of the signal from a small number of photon absorptions is obscured by photoreceptor current fluctuations. However, the detection and transmission of single-photon events at near-threshold levels is feasible (Baylor et al., 1979) and is apparently dependent on the level of intrinsic noise generated by the phototransduction mechanism (Barlow, 1956, Baylor et al., 1980, Rieke and Baylor, 1998). Rod photoreceptors generate two major forms of noise which have to be mitigated in some fashion, in order for single-photon responses to propagate downstream. The first form of noise arises from the rare occurrence of rhodopsin spontaneously activating through thermal events (Baylor et al., 1980). This discrete noise is indistinguishable from actual photon absorptions. The second form of noise is a constant fluctuation in the membrane current (Yau et al., 1979). The molecular origin of continuous noise has long been thought to arise from the spontaneous rate of cGMP hydrolysis by PDE (Rieke and Baylor, 1996), but despite decades of investigation the form of noise that ultimately sets the limits for detection near visual threshold remains unclear. In Ch. 3, I utilize a novel genetic murine model to investigate the origin of these

noise sources and their implications for detection threshold.

The discovery of rhodopsin in the 19th century enabled scientists to pose the question of how the retina accomplishes adjusting visual sensitivity to accommodate changes in the ambient light. Early work focused on the outer retina, on how photopigment content or duplex vision with both rods and cones could account for adaptation. The primary rod signaling pathway transmits light information over a range that covers more than 7 orders of magnitude of light intensity. This phenomenon requires the pathway to adapt to changes in available light by adjusting its sensitivity, a process that reflects presynaptic changes in the rods and postsynaptic changes in the bipolar cell of the G protein-coupled receptor (GPCR) signaling cascade (Fig. 1.5B-*bottom*).

The mechanisms of the GPCR cascade in RBC dendrites remains somewhat of a mystery. Rod bipolar cells have a resting membrane potential in darkness that is hyperpolarized ( $\sim -60$  mV) compared to that of the photoreceptors ( $\sim -40$  mV) and closer to the equilibrium potential of  $K^+$ . In darkness, the invaginating synapse within the rod spherule is flooded with constant glutamate release from the rods. Glutamate activates the GPCR cascade through the metabotropic glutamate receptor 6 (mGluR6) (Fig. 1.5B). At the binding of glutamate to the receptor, two splice variants of the GPCR  $\alpha$  subunit,  $G\alpha_{o1}$  and  $G\alpha_{o2}$ , are activated and GDP is replaced with GTP (Tsukamoto et al., 1991). The activated  $G\alpha_o$  dissociates from the heterotrimeric G protein and, through an unknown mechanism, triggers a putative effector enzyme that may control the closed state of the nonselective cation channel responsible for light-activated RBC currents. This channel is the transient receptor potential melastatin channel 1 (TRPM1) (Morgans et al., 2009). In response to light, glutamate is reduced at the synapse, the mGluR6 cascade is turned off, and TRPM1 channels open, initiating a strong depolarizing response within the RBC.

This synapse is remarkable because RBCs pool from 20 to 100 rods in a manner so optimized as to eliminate noise from the photoreceptor pool, in order to detect individual photons absorbed in only a few of the rods (Van Rossum and Smith, 1998, Field and Rieke, 2002b). To describe how this quantal detection works at the threshold of vision, an experi-

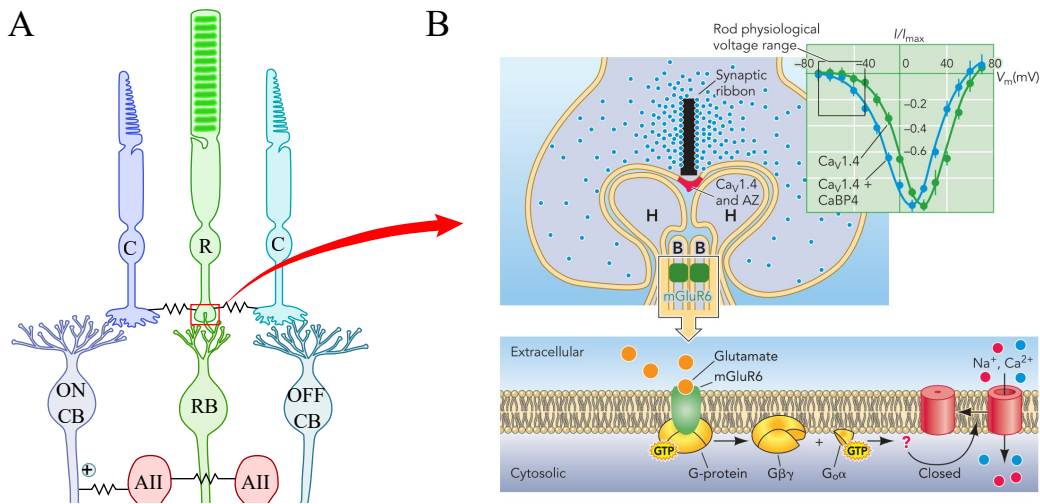


Figure 1.5: *Rod bipolar G protein-coupled receptor cascade*. **A.** Schematic of the functional connections of the outer retina. Rod photoreceptors make a single synapse with the dendrites of two different RBCs (only one shown) and two horizontal cells (not shown). Cones make synapses with ON and OFF pathways through associated CBCs. Rods and cones are electrically coupled by gap junctions. Red rectangle indicates the level of the rod spherule and RBC dendrite depicted in B. Abbreviations: C, cone; R, rod; CB, cone bipolar cells; RB, rod bipolar cell; AII, AII amacrine cells. **B.** Schematic of the major proteins involved in the rod glutamate release and the rod bipolar transduction cascade. Abbreviations: H, horizontal cell; B, rod bipolar cell; Ca<sub>v</sub>1.4, Ca<sup>2+</sup> channels; AZ, active zone; CaBP4, Ca<sup>2+</sup> binding protein 4; *Image adapted from (Okawa and Sampath, 2007).*

ment was conducted in which a subject was shown a series of flashes of different intensities the subject was and asked whether the flash was observed (Hecht et al., 1942). The percentages of correctly observed flashes were related to the logarithm of the flash intensity with a cumulative Poisson function whose single parameter,  $n$ , reflects the probability of observing at least as many photons per flash (Fig. 1.6). From these ‘frequency of seeing’ experiments, it was determined the threshold for vision was between 5 and 7 photons absorbed among thousands of rods (Fig. 1.6B). It appears that the statistical nature of vision is related to the statistical nature of light itself.

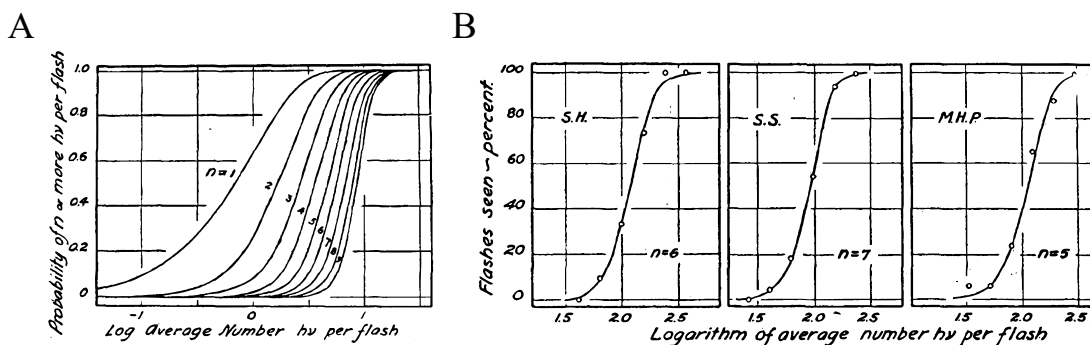


Figure 1.6: *Characterization of the absolute visual threshold.* **A.** A cumulative Poisson probability distribution has the useful feature of have a single parameter,  $n$ , which relates the probability of absorbing  $n$  photons to the flash intensity. Theoretical curves for  $n$  values of 1, 2, 3, 4, 5, 6, 7, 8 and 9 are shown. **B.** Experimental data from ‘frequency of seeing’ experiments shows that the absolute threshold of human vision is at a level where  $5 < n < 7$  photons are absorbed among thousands of rods. *Images adapted from (Hecht et al., 1942).*

## 1.4 Adaptation

In the 1960s, John Dowling observed that there was both a fast and a slow component of adaptation to darkness from a previous exposure to a background light. He found that for dim background levels, which did not measurably bleach photopigment, there was rapid dark adaptation, and slow adaptation at bleaching background levels. Work at the time had established that the electroretinogram (ERG) could be dissected reasonably well to

distinguish between inner and outer retinal activity by simply analyzing the peak responses to graded light stimuli of the b- and a-waves. Dowling showed in rat retinas that the b-wave exhibited remarkable adaptation, such that responses could be elicited over a larger range of background intensities and the operating range adjusted accordingly (Fig. 1.7). He concluded that adaptation may be a result of synaptic arrangement within the retina (Dowling, 1967).

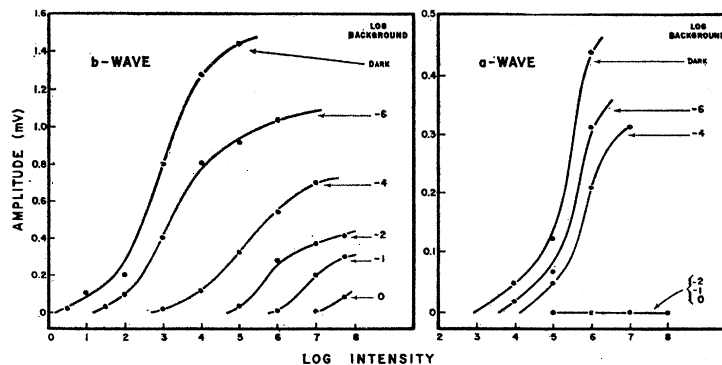


Figure 1.7: *Adaptation to light begins in the retina.* Electroretinograms recorded from rat retinas which show how changes in ambient light levels influence the amplitude of the b-wave (*left*) and the a-wave (*right*) as a function of the logarithm of the flash intensity. The b-wave is now thought to describe the response behavior of bipolar cells and the a-wave of photoreceptors. Increasing background levels (log background from  $-6$  to  $-4$ ) had a pronounced effect on the operating range of the b-wave but not on the a-wave, indicating that the inner retina (bipolar cells) may be a site of adaptation in the retina. *Images from (Dowling, 1967).*

Studies nearly 4 decades later, found that adaptation to background light begins in the circuitry and progresses to photoreceptors such that the range over which each cell type in the circuit operates is distinct from the others (Dunn, 2006). These findings suggest that convergence functions to increase the sensitivity of the downstream neurons. That is, RBCs are made more sensitive because of the large pool of rods from which they may sample. Likewise, AII amacrine cells are tuned even more sensitive from the sampling of several RBCs. Thus, through this convergence of thousands of rods, sensitivity is maximized for centrally targeted ganglion cells (Fig. 1.8). This leaves one to ask, which changes in sensitivity are inherited from rods, if any, and which are intrinsic to the interneurons of the



retina? In Ch. 4, I investigate mechanisms of light adaptation in rods and in rod bipolar cells in an attempt to answer this question.

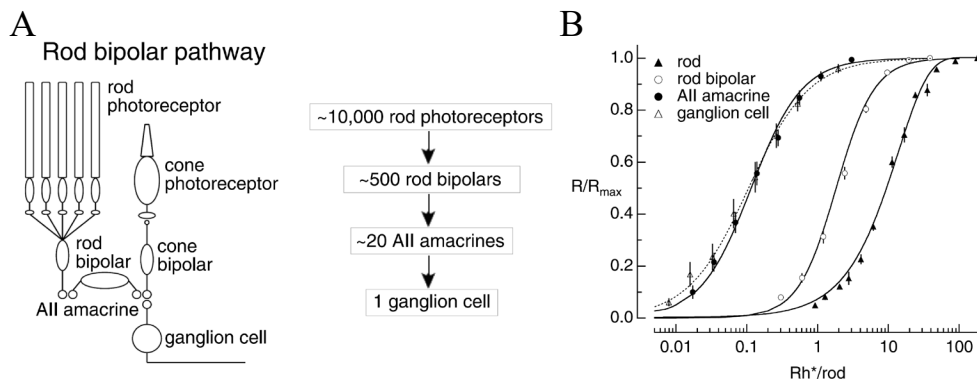


Figure 1.8: *Operating ranges of cells in the rod signaling pathway.* **A.** Schematic of the rod pathway and estimates of the pooling convergence through the circuitry. **B.** Stimulus-response relationships for cell across the rod pathway showing the normalized maximal response amplitude ( $R_{\max}$ ) as a function of flash intensity presented as the number of photoisomerizations per rod photoreceptor ( $Rh^*/rod$ ). Operating ranges of AII amacrine cells and ganglion cells overlap, followed by RBCs, with an order of magnitude less sensitivity, and rod photoreceptors, with another order magnitude less sensitivity. *Images adapted from (Dunn, 2006).*

## 1.5 Goals of the thesis

Three main goals were pursued in this dissertation. In each chapter I consider the question of how the rod visual pathway parses incoming light information near the absolute visual threshold, and how changes in the ambient light levels are transmitted through the first visual synapse. I approached these questions by combining mathematical and statistical modeling and single-cell electrophysiological recording techniques.

*Goal 1: A kinetic analysis of mouse rod and cone photoreceptor responses.*

In the first goal, we set out to understand how rod photoreceptors came to be sensitive enough to detect and transmit as little light as a single photon. We modified existing mathematical models of phototransduction to determine the functional changes required

in rods to convert their responses into the more primitive cone responses. My primary contribution to this research was in the use of statistical methods to test the adequacy of the modeling.

*Goal 2: The molecular basis for continuous noise and its implications on the threshold of photon detection.*

In the second goal, we dissected contributions of transduction-cascade proteins to the continuous noise that obscures the single-photon response in rod photoreceptors. To do so, we used a novel murine model of reduced PDE levels, along with several other genetic models with perturbations to other cascade proteins expression, and made whole-cell patch recordings in individual rods. Through our experiments, we characterized rod continuous noise and investigated its molecular origin to ask if any one component both sets the continuous noise level and limits the detection of single photons.

*Goal 3: Rod bipolar cell contributions to rod adaptation.*

In the third goal, we investigated the mechanisms underlying the nonlinearity that exists at the rod-to-rod bipolar synapse. To understand how noise intrinsic to the rod photoreceptor is mitigated from the pool of tens of rods, we systematically characterized light responses in rod bipolar cells over the range of light adaptation in the rod photoreceptors. To do this, we used calibrated light stimuli and recorded light-evoked currents in single cells. We devised a technique to study the calcium dependence of the nonlinearity and investigated the origin of the nonlinear threshold by which the rod bipolar cell discerns rod signals from rod noise. Additionally, we characterized adaptational mechanisms in rod bipolar cells that are distinct from rods through statistical modeling and data analysis.

After the introductory chapter, we present our results in three chapters. Each chapter is written as a stand-alone manuscript addressing each goal of the thesis individually, and the first of these chapters has already been published (Reingruber et al., 2020). In the appendix (Appendix A), I provide a description of software that I developed during the pursuit of aforementioned goals. The software described in Appendix A was critical for the completion of the data management, analytics, and analyses of the data presented in each goal.

## REFERENCES

- Arshavsky, Vadim Y and Burns, Marie E (2014). Current understanding of signal amplification in phototransduction. *Cellular Logistics*, 4(2):e29390. 10.4161/cl.29390.
- Asteriti, Sabrina, Grillner, Sten, and Cangiano, Lorenzo (2015). A Cambrian origin for vertebrate rods. *eLife*, 4:1–16. 10.7554/eLife.07166.
- Barlow, H. B. (1956). Retinal Noise and Absolute Threshold. *Journal of the Optical Society of America*, 46(8):634. 10.1364/JOSA.46.000634.
- Bauer, Paul J. (2006). Binding of the Retinal Rod  $\text{Na}^+/\text{Ca}^{2+}\text{-K}^+$  Exchanger to the cGMP-Gated Channel Indicates Local  $\text{Ca}^{2+}$ -Signaling in Vertebrate Photoreceptors. *Annals of the New York Academy of Sciences*, 976(1):325–334. 10.1111/j.1749-6632.2002.tb04755.x.
- Baylor, D. A., Lamb, T. D., and Yau, K. W. (1979). Responses of retinal rods to single photons. *The Journal of physiology*, 288(1):613–34. 10.1113/jphysiol.1979.sp012716.
- Baylor, D A, Matthews, G, and Yau, K W (1980). Two components of electrical dark noise in toad retinal rod outer segments. *The Journal of Physiology*, 309(1):591–621. 10.1113/jphysiol.1980.sp013529.
- Cervetto, L., Lagnado, L., Perry, R. J., Robinson, D. W., and McNaughton, P. A. (1989). Extrusion of calcium from rod outer segments is driven by both sodium and potassium gradients. *Nature*, 337(6209):740–743. 10.1038/337740a0.
- Chen, C.-K., Woodruff, M. L., Chen, F. S., Shim, H., Cilluffo, M. C., and Fain, G. L. (2010). Replacing the rod with the cone transducin  $\alpha$  subunit decreases sensitivity and accelerates response decay. *The Journal of Physiology*, 588(17):3231–3241. 10.1113/jphysiol.2010.191221.
- Dowling, J E and Ripps, H (1973). Effect of magnesium on horizontal cell activity in the skate retina. *Nature*, 242(5393):101–3. 10.1038/242101a0.
- Dowling, John E. (1967). The Site of Visual Adaptation. *Science*, 155(3760):273–279. 10.1126/science.155.3760.273.
- Dunn, Felice A. (2006). Controlling the Gain of Rod-Mediated Signals in the Mammalian Retina. *Journal of Neuroscience*, 26(15):3959–3970. 10.1523/JNEUROSCI.5148-05.2006.
- Einstein, Albert (1930). What I Believe: Living Philosophies XIII. *Forum and Century*, LXXXIV(4):192.
- Fain, G. L., Matthews, H. R., Cornwall, M. C., and Koutalos, Y. (2001). Adaptation in vertebrate photoreceptors. *Physiological Reviews*, 81(1):117–151. 10.1152/physrev.2001.81.1.117.

- Fain, Gordon L. (2019). *Sensory Transduction*. Oxford University Press. ISBN 9780198835028.
- Fain, Gordon L and Dowling, John E (1973). Intracellular Recordings from Single Rods and Cones in the Mudpuppy Retina. *Science*, 180(4091):1178–1181. 10.1126/science.180.4091.1178.
- Fain, Gordon L., Hardie, Roger, and Laughlin, Simon B. (2010). Phototransduction and the Evolution of Photoreceptors. *Current Biology*, 20(3):R114–R124. 10.1016/j.cub.2009.12.006.
- Field, Greg D. and Rieke, Fred (2002a). Mechanisms Regulating Variability of the Single Photon Responses of Mammalian Rod Photoreceptors. *Neuron*, 35(4):733–747. 10.1016/S0896-6273(02)00822-X.
- Field, Greg D. and Rieke, Fred (2002b). Nonlinear signal transfer from mouse rods to bipolar cells and implications for visual sensitivity. *Neuron*, 34(5):773–785. 10.1016/S0896-6273(02)00700-6.
- Field, Greg D., Sampath, Alapakkam P., and Rieke, Fred (2005). Retinal processing near absolute threshold: from behavior to mechanism. *Annual review of physiology*, 67(1):491–514. 10.1146/annurev.physiol.67.031103.151256.
- Hecht, Selig, Shlaer, Simon, and Pirenne, Maurice Henri (1942). Energy, Quanta, And Vision. *Journal of General Physiology*, 25(6):819–840. 10.1085/jgp.25.6.819.
- Ingram, Norianne T., Sampath, Alapakkam P., and Fain, Gordon L. (2016). Why are rods more sensitive than cones? *The Journal of Physiology*, 594(19):5415–5426. 10.1113/JP272556.
- Krispel, Claudia M., Chen, Desheng, Melling, Nathan, Chen, Yu Jiun, Martemyanov, Kirill A., Quillinan, Nidia, Arshavsky, Vadim Y., Wensel, Theodore G., Chen, Ching Kang, and Burns, Marie E. (2006). RGS Expression Rate-Limits Recovery of Rod Photoresponses. *Neuron*, 51(4):409–416. 10.1016/j.neuron.2006.07.010.
- Lamb, Trevor D. (2020). Evolution of the genes mediating phototransduction in rod and cone photoreceptors. *Progress in Retinal and Eye Research*, 76(August 2019):100823. 10.1016/j.preteyeres.2019.100823.
- Masland, Richard H. (2001). The fundamental plan of the retina Richard. *Nature Publishing Group*, 4(9):877–886.
- Masland, Richard H. (2012). The Neuronal Organization of the Retina. *Neuron*, 76(2):266–280. 10.1016/j.neuron.2012.10.002.
- Morgans, Catherine W., Zhang, Jianmei, Jeffrey, Brett G., Nelson, Steve M., Burke, Neal S., Duvoisin, Robert M., and Brown, R. Lane (2009). TRPM1 is required for the depolarizing light response in retinal ON-bipolar cells. *Proceedings of the National*

- Academy of Sciences of the United States of America*, 106(45):19174–19178. 10.1073/pnas.0908711106.
- Morshedian, Ala and Fain, Gordon L. (2015). Single-photon sensitivity of lamprey rods with cone-like outer segments. *Current Biology*, 25(4):484–487. 10.1016/j.cub.2014.12.031.
- Okawa, Haruhisa and Sampath, Alapakkam P. (2007). Optimization of Single-Photon Response Transmission at the Rod-to-Rod Bipolar Synapse. *Physiology*, 22(4):279–286. 10.1152/physiol.00007.2007.
- Reingruber, Jürgen, Ingram, Norianne T., Griffis, Khris G., and Fain, Gordon L. (2020). A kinetic analysis of mouse rod and cone photoreceptor responses. *Journal of Physiology*, 598(17):3747–3763. 10.1113/JP279524.
- Rieke, F. and Baylor, D. A. (1996). Molecular origin of continuous dark noise in rod photoreceptors. *Biophysical Journal*, 71(5):2553–2572. 10.1016/S0006-3495(96)79448-1.
- Rieke, F. and Baylor, D. A. (1998). Single-photon detection by rod cells of the retina. *Reviews of Modern Physics*, 70(3):1027–1036. 10.1103/RevModPhys.70.1027.
- Schultze, Max (1866). Zur Anatomie und Physiologie der Retina. *Archiv für Mikroskopische Anatomie*, 2(1):175–286. 10.1007/BF02962033.
- Tsukamoto, Toshihiko, Toyama, R, Itoh, H, Kozasa, Tohru, Matsuoka, Masaaki, and Kaziro, Y (1991). Structure of the human gene and two rat cDNAs encoding the alpha chain of GTP-binding regulatory protein Go: two different mRNAs are generated by alternative splicing. *Proceedings of the National Academy of Sciences*, 88(8):2974–2978. 10.1073/pnas.88.8.2974.
- Van Rossum, M. C.W. and Smith, R. G. (1998). Noise removal at the rod synapse of mammalian retina. *Visual Neuroscience*, 15(5):809–821. 10.1017/S0952523898155037.
- Veleri, Shobi, Lazar, Csilla H., Chang, Bo, Sieving, Paul A., Banin, Eyal, and Swaroop, Anand (2015). Biology and therapy of inherited retinal degenerative disease: Insights from mouse models. *DMM Disease Models and Mechanisms*, 8(2):109–129. 10.1242/dmm.017913.
- Wald, George (1968). Molecular Basis of Visual Excitation. *Science*, 162(3850):230–239. 10.1126/science.162.3850.230.
- Wässle, Heinz (2004). Parallel processing in the mammalian retina. *Nature Reviews Neuroscience*, 5(10):747–757. 10.1038/nrn1497.
- Yau, K.-W., Lamb, T.D., Matthews, G, and Baylor, D.A. (1979). Current fluctuations across single rod outer segments. *Vision Research*, 19(4):387–390. 10.1016/0042-6989(79)90100-7.

## CHAPTER 2

# A kinetic analysis of mouse rod and cone photoreceptor responses

### 2.1 Preface to Chapter 2

Rod and cone photoreceptors are homologous in many aspects of their ability to parse incoming photon-streams into meaningful information about the visual world. Where these first-order sensory neurons are distinct from each other is in their sensitivity to the absolute quantity of photons, their responsiveness to temporal changes in the arrival of photons, and in their outer-segment morphology. These differences are realized by variations in transduction protein species and their relative concentrations, and the presence of lamellae, of which rods have very few located only at the interface between the inner and outer segment. While cones in vertebrates today closely resemble early photoreceptors, rods have apparently accumulated several evolutionary changes that have afforded them the ability to detect as few as a single photon. It remains unclear which of these differences are the most important for imparting the specificity with which rods detect and propagate incoming light signals. To understand how light-responses are generated in vertebrate photoreceptors, we constructed a model of phototransduction and analyzed rod and cone light-responses. We show that, in addition to outer-segment volume, the most important differences between rods and cones are: (1) decreased transduction gain, reflecting smaller amplification in the G-protein cascade; (2) a faster rate of turnover of the second messenger cGMP in darkness; and (3) an accelerated rate of decay of the effector enzyme phosphodiesterase and perhaps also of activated visual pigment.

In this chapter, I present the work from our manuscript entitled, *A kinetic analysis of mouse rod and cone photoreceptors* by Jürgen Reingruber<sup>1</sup>, Norianne T. Ingram<sup>2,3</sup>, Khristian G. Griffis<sup>2,3</sup>, and Gordon L. Fain<sup>2,3</sup>. The manuscript was first published in *The Journal of Physiology (online)*, 17 June 2020.

## 2.2 Abstract

Most vertebrates have rod and cone photoreceptors, which differ in their sensitivity and response kinetics. We know that rods evolved from cone-like precursors through the expression of different transduction genes or the same genes at different levels, but we do not know which molecular differences were most important. We have approached this problem in mouse retina by analyzing the kinetic differences between rod flash responses and recent voltage-clamp recordings of cone flash responses, using a model incorporating the principal features of photoreceptor transduction. We apply a novel method of analysis using the log-transform of the current, and we ask which of the model's dynamic parameters need be changed to transform the flash response of a rod into that of a cone. The most important changes are a decrease in the gain of the response, reflecting a reduction in amplification of the transduction cascade; an increase in the rate of turnover of cGMP in darkness; and an increase in the rate of decay of activated phosphodiesterase, with perhaps also an increase in the rate of decay of light-activated visual pigment. Although we cannot exclude other differences, and in particular alterations in the calcium ( $\text{Ca}^{2+}$ ) economy of the photoreceptors, we believe that we have identified the kinetic parameters principally responsible for the differences in the flash responses of the two kinds of photoreceptors, which were likely during evolution to have resulted in the duplex retina.

---

<sup>1</sup>*Institut de Biologie de l'École Normale Supérieure, 46 rue d'Ulm, Paris 75005, France*

<sup>2</sup>*Department of Integrative Biology and Physiology, University of California, Los Angeles, CA 90095, USA*

<sup>3</sup>*Department of Ophthalmology and Stein Eye Institute, University of California, Los Angeles, CA 90095, USA*

## 2.3 Introduction

In most vertebrate retinas there are rod photoreceptors, which are more sensitive and mediate vision in dim light; and cone photoreceptors, which are less sensitive but respond at higher temporal frequencies and are used for most bright-light vision. As Schultze first proposed over 150 years ago (Schultze, 1866), these two photoreceptor types form a duplex retina, which we now know must have appeared very early during the evolution of vertebrates (Asteriti et al. 2015; Morshedien & Fain, 2015). Rods appear to have evolved from more primitive cone-like photoreceptors through gene duplication, modification of transduction enzymes, and changes in protein expression levels to accommodate vision in dimmer light (see Fain et al. 2010; Morshedien & Fain, 2017; Lamb, 2019).

Although rods and cones both use a similar transduction cascade, there are many molecular differences in the proteins they utilize, which are thought to be responsible for their different response properties. For several of the components of transduction, the two kinds of photoreceptors use different protein isoforms (see Ingram et al. 2016). That is true of their photopigments, transducin Gproteins, phosphodiesterase (PDE6) effector enzymes, and cyclic nucleotide-gated channels. In other cases, the rods and cones are thought to use the same protein isoform but with different levels of expression. The GTPase-activating proteins (GAPs) and guanylyl cyclase are both more highly expressed in cones than in rods (Cowan et al. 1998; Zhang et al. 2003; Takemoto et al. 2009). These molecular differences must in some way have been responsible for the evolution of the differences in the physiology of the two photoreceptor types. Rods and cones also differ in the morphology of their outer segments, with rods having cytoplasmic discs and cones membrane lamellae. This difference is, however, now known not to contribute to the different sensitivities and kinetics of the rod and cone photocurrent responses (Asteriti et al. 2015; Morshedien & Fain, 2015).

Many attempts have been made to determine which of the different isoforms or different expression levels are responsible for the differences in sensitivity and response kinetics of rods and cones. The cone isoforms of visual pigment (Sakurai et al. 2007; Shi et al. 2007; Fu et al. 2008), transducin (Deng et al. 2009; Chen et al. 2010b; Mao et al. 2013), and the



phosphodiesterase-6 effector enzyme (PDE, Deng et al. 2013; Majumder et al. 2015) have been expressed in rods with variable results, sometimes producing alterations in response properties and sometimes producing no change at all. In other experiments, the expression of the GAP proteins in rods was increased (Krispel et al. 2006; Chen et al. 2010b), which may mimic the greater expression of these proteins in cones. In none of these experiments did a single molecular change in a rod produce responses similar to those of a cone.

These studies indicate that many different alterations in isoforms and expression levels must have been required during evolution to produce the duplex retina. It is, however, still unclear which alterations were most important. Because it may be difficult to make further progress with purely experimental methods, we approached this problem by combining experiment and theory. We began with a model of the mouse rod photoreceptor response that incorporates the principal features of the transduction cascade (Pugh & Lamb, 1993; Rieke & Baylor, 1996; Andreucci et al. 2003; Hamer et al. 2003; Hamer et al. 2005; Reingruber & Holcman, 2008; Chen et al. 2010c; Gross et al. 2012a; Reingruber et al. 2013). Although similar models have been proposed for cones (see, for example, Klaus et al. 2019), these attempts have suffered from a paucity of cone recordings. Suction-electrode recordings from mouse cones have been obtained by several investigators (Nikonov et al. 2005, 2006; Sakurai et al. 2011, 2015; Cao et al. 2014), including our own laboratory (Ingram et al. 2016; Kaylor et al. 2017), but these recordings are unlikely to provide an accurate reflection of the kinetics of the light-dependent change in outer-segment conductance because of the rapid kinetics of the cone response and the high capacitance of the cone membrane (Perry & McNaughton, 1991). Whole-retina measurements of massed cone responses (as in Sakurai et al. 2011, 2015; Morshedian et al. 2019) reflect the change in the cone membrane potential rather than the change in outer-segment conductance.

A more accurate assessment of changes in cone conductance could be obtained from voltage clamp (Perry & McNaughton, 1991). We have recently described voltage-clamp recordings from dark-adapted mouse cones in retinal slices (Ingram et al. 2019), not only from wild-type (WT) cones but also from cones with mutations in key transduction proteins. We

now use these responses together with responses from mouse rods to define the minimal changes required to transform the dynamics of a rod response into those of a cone. We focus our study on dark-adapted responses to dim and non-saturating flash intensities, from which dynamical parameters can already be inferred.

In agreement with the molecular biology, we show that no one change is sufficient but that several changes need to be made, particularly in the amplification of the G-protein cascade, the dark rate of cGMP turnover, the rate of decay of activated PDE, and perhaps also the rate of decay of activated visual pigment. Our analysis also predicts that a much lower number of PDEs are activated per photon in cones than in rods. These studies help clarify the physiological differences between the two photoreceptor types and may indicate which molecular changes were most important in forming the duplex retina over 500 million years ago.

## 2.4 Materials and methods

*Animals and ethical approval.* The data we used to determine model parameters came from experiments performed in accordance with the rules and regulations of the NIH guidelines for research animals, as approved by the Institutional Animal Care and Use Committee of the University of California, Los Angeles, USA, and were in conformity with regulations as described by Grundy (2015). Mice were kept under cyclic light (12-on/12-off) with ad libitum food and water in approved cages. Retinas lacking the genes for the two guanylyl-cyclase-activating proteins (GCAPs) (GCAPs<sup>-/-</sup>) were obtained from Jeannie Chen of the University of Southern California, Los Angeles, CA (Mendez et al. 2001). Mice in which the rod-specific alpha subunit of the G-protein transducin had been deleted (Gnat1<sup>-/-</sup>) were originally made in the laboratory of Janice Lem at Tufts University, Boston, MA (Calvert et al. 2000), and were obtained locally from the laboratory of Dr Gabriel Travis at UCLA in Los Angeles, CA. Mice with deletions of both Gnat1 and the genes for the GCAPs (Gnat1<sup>-/-</sup>;GCAPs<sup>-/-</sup>) were made by mating animals from the two lines. At least three generations of double-deletion animals were produced before data collection commenced. All animals were on a C57BL/6J

background; approximately equal numbers of male and female mice were used to obtain the recordings. Mice were killed by cervical dislocation.

*Recordings.* Wild-type (WT, C57BL/6J) rod responses and all cone responses were recorded with patch electrodes and voltage clamp from retinal slices (Ingram et al. 2019). Rod GCAPs<sup>-/-</sup>-responses were recorded with suction electrodes and have been previously published (Chen et al. 2010c). These earlier studies should be consulted for details of the experimental procedure. In both sets of experiments, temperature was measured with a thermocouple inside the chamber and was adjusted to 37°C for the suction recordings and 35°C for the voltage-clamp recordings; the value of the temperature was regulated to within 1°C with feedback controllers (TC-324B; Warner Instruments). Cone recordings were made from mice that lacked the rod transducin alpha subunit (Gnat1<sup>-/-</sup>), in order to prevent rod signals contributing to cone responses (Ingram et al. 2019). Cell membrane potential was clamped near the dark resting membrane potential (-40 mV for rods and -50 mV for cones).

Rod WT responses and all cone responses were recorded in Ames' medium bubbled with 95% O<sub>2</sub>/5% CO<sub>2</sub> and buffered with 1.9 g L<sup>-1</sup> sodium bicarbonate, pH 7.3 to 7.4. Rod GCAPs<sup>-/-</sup>-responses were recorded in Dulbecco's Modified Eagle's medium supplemented with 15mM NaHCO<sub>3</sub>, 2mM Na succinate, 0.5mM Na glutamate, 2mM Na gluconate, and 5 mM NaCl, bubbled with 5% CO<sub>2</sub>, pH 7.4. Although rods in these two media have been reported to have somewhat different kinetic properties (Azevedo & Rieke, 2011), these differences are small in comparison with the differences in kinetics between rods and cones and are likely to result from a difference in Ca<sup>2+</sup>-dependent cyclase feedback, which would not affect responses from GCAPs<sup>-/-</sup>-rods. We attempted to record from mouse GCAPs<sup>-/-</sup>-rods with patch clamp in retinal slices under the same conditions we used for WT rods and cones. Despite considerable effort (four animals, over 30 successful seals), we were unable to obtain stable voltage-clamp recordings from these cells, which seemed fragile and were unusually noisy in comparison with WT rods. The GCAPs<sup>-/-</sup>-rod responses even to dim flashes decayed with an extremely slow time course, and responses to bright flashes often 'hung up' and failed to return to baseline during the duration of the recording. From that point onward, the rod no longer

responded even to the brightest flash. We will show, however, that WT rods with patch clamp in Ames' medium (Fig. 1A) can be fitted with the same parameters as GCAPs<sup>-/-</sup> rods recorded with suction electrodes, with the addition to the WT model of GCAP-dependent Ca<sup>2+</sup> feedback (see Fig. 4). Though the fits are not as good for WT as for GCAPs<sup>-/-</sup> rods, we think this difference is more likely the result of over- simplification in our model for Ca<sup>2+</sup> and feedback than methods of recording and perfusion solutions. Data were analysed either with pCLAMP and Origin (for suction recordings) or in MATLAB with custom scripts (for patch clamp recordings).

*Derivation of the phototransduction model.* We have used a simplified, spatially homogeneous model for photoreceptors (see, for example, Hamer et al. 2005; Reingruber & Holcman, 2008; Chen et al. 2010c; Korenbrot, 2012; Reingruber et al. 2013; Wang et al. 2018). The photoreceptor current,  $I$ , is taken to be a function of the cyclic guanosine nucleotide (cGMP) concentration  $c_{cg}$  according to:

$$I = I_d \left( \frac{c_{cg}}{c_{cg,d}} \right)^{n_{ch}}, \quad (2.1)$$

where  $I_d$  and  $c_{cg,d}$  are the current and cGMP concentration in darkness, and  $n_{ch}$  is the cooperativity constant of the channel, which we will take to be 2.5 (see, for example, Haynes & Yau, 1985; Zimmerman & Baylor, 1986; Yau & Baylor, 1989). We will make the simplifying assumption that changes in Ca<sup>2+</sup> during the flash response are sufficiently rapid for mouse cones that they can be assumed to occur in proportion to the change in current, that is:

$$\frac{c_{ca}}{c_{ca,d}} = \frac{I}{I_d}, \quad (2.2)$$

where  $c_{ca}$  is the calcium concentration, and  $c_{ca,d}$  is the calcium concentration in darkness. We make this assumption because light-dependent changes in Ca<sup>2+</sup> are much faster in cones than in rods in salamanders (Sampath et al. 1999), and because this simplifying assumption gave a reasonable fit of the model to our cone responses. We further assume that  $\alpha$ , the Ca<sup>2+</sup>-dependent rate of synthesis of cGMP, quickly adapts to the changing Ca<sup>2+</sup> concentration. We then compute the rate from the Ca<sup>2+</sup> concentration according to:

$$\alpha(c_{ca}) = \alpha_{\min} \frac{c_{ca}^2 + r_{\alpha} K_{\alpha}^2}{c_{ca}^2 + K_{\alpha}^2}, \quad (2.3)$$

where  $K_\alpha$  determines the sensitivity of the rate to  $\text{Ca}^{2+}$ ,  $\alpha_{min}$  is the minimum value of the cyclase rate at high  $\text{Ca}^{2+}$ , and  $r_\alpha$  is the ratio of maximum to minimum rates, i.e.  $\alpha_{max}/\alpha_{min}$ .

To simplify the solution of the equations, we introduce dimensionless quantities by normalizing with steady-state values in darkness. That is, we set:

$$\begin{aligned}\hat{I} &= \frac{I}{I_d}, \hat{c}_{cg} = \frac{c_{cg}}{c_{cg,d}}, \hat{c}_{ca} = \frac{c_{ca}}{c_{ca,d}} \\ \hat{\alpha} &= \frac{\alpha}{\alpha_d}, \text{ and } \hat{K}_\alpha = \frac{K_\alpha}{c_{ca,d}}.\end{aligned}\tag{2.4}$$

The rate of synthesis of cGMP in darkness is  $\alpha_d = \beta_d c_{cg,d}$  where  $\beta_d$  is the rate constant of cGMP hydrolysis in darkness (turnover rate). With our assumption that the  $\text{Ca}^{2+}$  concentration is directly proportional to the current,  $\hat{c}_{ca} = \hat{I}$ , we can express the normalized  $\text{Ca}^{2+}$ -dependent rate of synthesis of cGMP as a function of the current as:

$$\hat{\alpha}(\hat{I}) = \frac{\hat{I}^2 + r_\alpha \hat{K}_\alpha^2}{\hat{I}^2 + \hat{K}_\alpha^2} \frac{1 + \hat{K}_\alpha^2}{1 + r_\alpha \hat{K}_\alpha^2} \approx \frac{1 + \hat{K}_\alpha^2}{\hat{I}^2 + \hat{K}_\alpha^2}.\tag{2.5}$$

The approximation to the right in eqn (5) is valid for  $r_\alpha \hat{K}_\alpha^2 \gg 1$  and was used in most of our calculations. Using the full expression, we verified  $r_\alpha$  largely satisfied this condition. The light-dependent rate constant of cGMP hydrolysis by PDE depends on the number of activated PDE molecules,  $P^*$ , according to  $\beta_{sub} P^*$ , where  $\beta_{sub}$  is the rate constant of cGMP hydrolysis by a single light-activated PDE. The equation for the change in normalized cGMP concentration is:

$$\frac{d}{dt} \hat{c}_{cg} = \beta_d \hat{\alpha} - (\beta_d + \beta_{sub} P^*) \hat{c}_{cg}.\tag{2.6}$$

*Log-transform of current.* To facilitate the analysis of the rod and cone flash responses, we introduce the log-transform of the normalized current  $y = -\ln \hat{I}$  so that  $\hat{I} = e^{-y}$ . We reasoned as follows. The initial phase of the light response was shown by Pugh & Lamb (1993) to follow to a first approximation an equation of the form:

$$\hat{I} = e^{-\frac{1}{2} \kappa \phi \Delta t A (t - t_{eff})^2},\tag{2.7}$$

with  $\kappa$  the collecting area,  $\phi$  the light intensity,  $\Delta t$  the flash duration,  $t_{eff}$  an effective delay at the beginning of the response, and  $A$  the amplification constant. If we let  $\hat{I}(t) = e^{-y(t)}$ ,

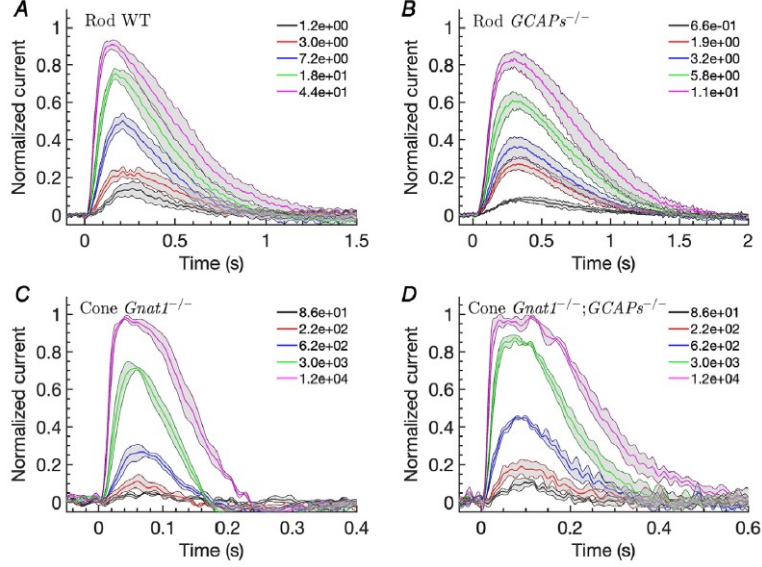


Figure 2.1: *Experimental current recordings from mouse rods and cones.* Currents from individual rods and cones have been normalized to their corresponding steady-state current in darkness  $I_d$ , with  $\hat{I} = I/I_d$  (such that  $\hat{I} = 1$  in darkness) and then averaged point by point among cells to compute mean responses. Ordinates give the mean current  $\hat{i} = 1 - \hat{I}$  (such that  $\hat{i} = 0$  in darkness), which is equivalent to the change in current normalized to the change produced by a bright light closing all of the outer-segment channels. The shaded regions indicate standard error of the mean computed point by point. Saturating responses to the brightest stimuli were not used in our model calculations (see Methods) and are not shown. **A.**, mean responses of seven wild-type (WT) rods. **B.**, rod  $GCAPs^{-/-}$ . Mean responses of five rods from Chen et al. (2010c). **C.**, cone  $Gnat1^{-/-}$  (equivalent to WT or control, see text). Mean responses from three cones. **D.**, cone  $Gnat1^{-/-};GCAPs^{-/-}$  (equivalent to cone  $GCAPs^{-/-}$ , see text). Mean responses from three cones. Flash durations are 10 ms in (**A.**), 20 ms in (**B.**) and 5 ms in (**C.**, **D.**). The figure inserts give the expected number of pigment isomerizations,  $R^*$ , computed with collecting areas = 0.2 (**A.**) or 0.5 (**B.**) for rod responses, and = 0.013 for cone responses.

then the initial waveform of  $y(t)$  becomes linear with the flash intensity  $\phi$ . We shall show that for responses to dim flashes, and over much of the intensity range when the GCAPs have been knocked out and there is no  $\text{Ca}^{2+}$ -dependent cyclase feedback (Mendez et al. 2001), not only the initial phase but the entire waveform of  $y(t)$  is, to a good approximation, linear with the flash intensity  $\phi$ . If, therefore, the waveforms  $y(t)$  of responses at different flash intensities are normalized by their corresponding peak amplitudes, the waveform of the normalized log-transform of a flash response is to a good approximation invariant with light intensity (see Fig. 2). In this way, the kinetics of flash responses can be pooled and analysed together. From eqn (1) after normalization from eqn (4), we get  $\hat{I} = \hat{c}_{cg}^{n_{ch}} = e^{n_{ch} \ln \hat{c}_{cg}}$ . From this expression we get  $y = -n_{ch} \ln \hat{c}_{cg}$ , and with eqn (6) we obtain:

$$\frac{d}{dt}y = n_{ch}\beta_{sub}P^* - \beta_d H(y), \quad (2.8)$$

with

$$H(y) = n_{ch} \left[ e^{\frac{y}{n_{ch}}} \hat{\alpha} (e^{-y}) - 1 \right] = n_{ch} \left[ e^{\frac{y}{n_{ch}}} \frac{1 + \hat{K}_\alpha^2}{e^{-2y} + \hat{K}_\alpha^2} - 1 \right]. \quad (2.9)$$

*Transduction equations.* To obtain a closed system of equations for the rod or cone light response, we additionally need equations for the production and decay of the components of the transduction cascade. We assume that light-activated visual pigment activates the G-protein transducin, which activates PDE6. We let  $R^*$  be the number of pigment molecules activated in the rod or cone by the flash,  $T^*$  be the number of activated transducins, and  $P^*$  be the number of activated PDEs. We have:

$$\begin{aligned} \frac{d}{dt}R^* &= \phi(t)\kappa - \mu_{rh}R^* \\ \frac{d}{dt}T^* &= k_{act}R^* - \mu_{tr}T^* \\ \frac{d}{dt}P^* &= \mu_{tr}T^* - \mu_{pde}P^* \\ \frac{d}{dt}y &= n_{ch}\beta_{sub}P^* - \beta_d H(y). \end{aligned} \quad (2.10)$$

For flashes with duration  $\Delta t$  and flash intensity  $\phi$  we have  $\phi(t) = \phi(\theta(t) - \theta(t - \Delta t))$ , where  $\theta$  is the unit step or Heaviside function (i.e.  $\theta(t) = 0$  for  $t < 0$  and  $\theta(t) = 1$  for  $t \geq 0$ ). All of the parameters in eqn (10) are defined in Table 1. For the collecting areas  $\kappa$

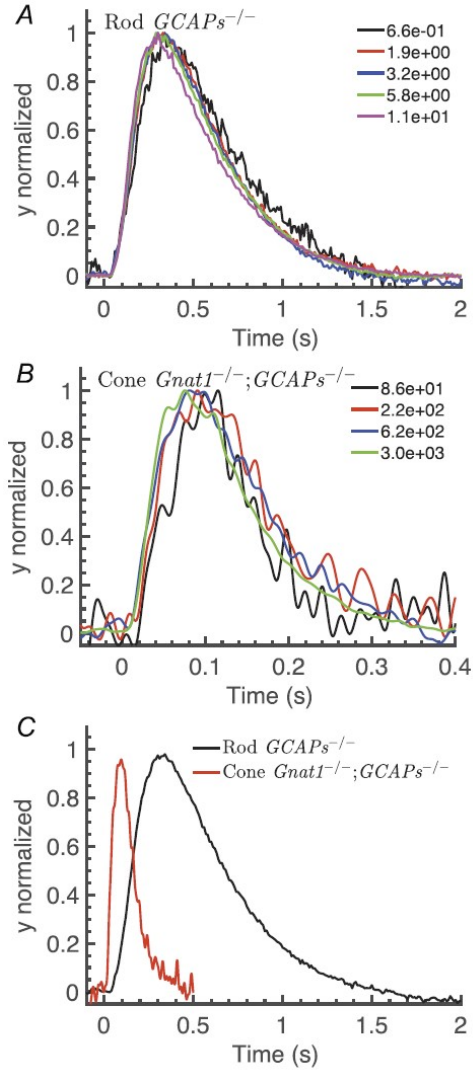


Figure 2.2: *Normalized log-transforms of response waveforms.* The  $GCAPs^{-/-}$  responses from Fig. 1B and D were transformed, first by taking the negative log of the current,  $y(t) = -\ln \hat{I}(t)$ , and then by normalizing the value of  $y(t)$  to give  $\hat{y}(t) = y(t)/y_{peak}$ . **A.**, plots of  $\hat{y}(t)$  for rod  $GCAPs^{-/-}$  responses of Fig. 1B. **B.**, plots of  $\hat{y}(t)$  for cone  $Gnat1^{-/-};GCAPs^{-/-}$  responses of Fig. 1D. **C.**, comparison of mean values of  $\hat{y}(t)$  from (A.) and (B.).



we used  $0.5\mu m^2$  for GCAPs<sup>-/-</sup>rods recorded with suction electrodes (Field & Rieke, 2002), and  $0.2\mu m^2$  for WT rods and  $0.013\mu m^2$  for Gnat1<sup>-/-</sup> and Gnat1<sup>-/-</sup>;GCAPs<sup>-/-</sup>cones recorded in retinal slices with voltage clamp (Ingram et al. 2019). The parameter  $k_{act}$  is the rate of activation of transducin by a single activated visual pigment,  $\mu_{rh}$  is the deactivation rate of a light-activated visual pigment,  $\mu_{pde}$  is the deactivation rate of a light-activated PDE, and  $\mu_{tr}$  is the rate by which a T<sup>\*</sup> is converted into P<sup>\*</sup> but can be more generally viewed as an effective parameter that accounts for intermediate processes that contribute to PDE activation and delay the response without amplifying it. To simplify the analysis of eqn (10), we transform the variables according to  $\tilde{P}^* = n_{ch}\beta_{sub}P^*$ ,  $\tilde{T}^* = n_{ch}\beta_{sub}\mu_{tr}/\mu_{pde}T^*$  and  $\tilde{R}^* = n_{ch}\beta_{sub}k_{act}/\mu_{pde}R^*$ . With the transformed variables, eqn (10) becomes:

$$\begin{aligned}
\frac{d}{dt}\tilde{R}^* &= \mu_{rh} \left( \phi(t)\kappa\xi - \tilde{R}^* \right) \\
\frac{d}{dt}\tilde{T}^* &= \mu_{tr} \left( \tilde{R}^* - \tilde{T}^* \right) \\
\frac{d}{dt}\tilde{P}^* &= \mu_{pde} \left( \tilde{T}^* - \tilde{P}^* \right) \\
\frac{d}{dt}y &= \tilde{P}^* - \beta_d H(y),
\end{aligned} \tag{2.11}$$

where we introduced the transduction gain:

$$\xi = \frac{n_{ch}\beta_{sub}k_{act}}{\mu_{pde}\mu_{rh}}. \tag{2.12}$$

Equation (11) reveals that  $y(t)$  and the current do not depend upon the individual values of  $\kappa$ ,  $n_{ch}$ ,  $\beta_{sub}$  and  $k_{act}$  but only on their product. We call  $\xi$  the gain because it determines the amplitude of  $\tilde{P}^*(t)$  and that of the dim flash responses (see next paragraph).

*Result for PDE activation.* The solution of eqn (11) for PDE is  $\tilde{P}^*(t) = \kappa\xi \int_0^t \phi(s)g_p(t-s) ds$  with Green's function:

$$\begin{aligned}
g_p(t) &= \mu_{rh}\mu_{tr}\mu_{pde} \left( \frac{e^{-\mu_{rh}t}}{(\mu_{rh} - \mu_{tr})(\mu_{rh} - \mu_{pde})} \right. \\
&\quad + \frac{e^{-\mu_{tr}t}}{(\mu_{tr} - \mu_{rh})(\mu_{tr} - \mu_{pde})} \\
&\quad \left. + \frac{e^{-\mu_{pde}t}}{(\mu_{pde} - \mu_{rh})(\mu_{pde} - \mu_{tr})} \right)
\end{aligned} \tag{2.13}$$

Parameter	Description
$\kappa(\mu m^2)$	Photoreceptor collecting area
$n_{ch}$	Cyclic-nucleotide-gated channel cooperativity (Hill coefficient)
$\beta_d(s^{-1})$	Rate constant of cGMP hydrolysis in darkness (cGMP turnover rate in darkness)
$\mu_{rh}(s^{-1})$	Rate of deactivation of an activated visual pigment Rate
$\mu_{pde}(s^{-1})$	Rate of deactivation of a light-activated phosphodiesterase (PDE) Rate
$\mu_{tr}(s^{-1})$	Rate for the transformation of light-activated transducin into light-activated PDE
$\hat{K}_\alpha$	Sensitivity of the cyclase activity on the $Ca^{2+}$ concentration scaled by the dark $Ca^{2+}$ concentration
$\xi$	Gain $\xi = \frac{n_{ch}\beta_{sub}k_{act}}{\mu_{pde}\mu_{rh}}$
$k_{act}(s^{-1})$	Rate of transducin activation by an activated visual pigment
$\beta_{sub}(s^{-1})$	Rate constant of cGMP hydrolysis by a light-activated PDE

Table 2.1: Parameter descriptions for rod and cone model

Note that  $g_p(t)$  is symmetrical in  $\mu_{rh}$ ,  $\mu_{tr}$  and  $\mu_{pde}$ . For a short flash of duration  $\Delta t$  we have  $\tilde{P}^*(t) = R_0^* \xi g_p(t)$ , where  $R_0^* = \phi \kappa \Delta t$  is the number of isomerizations generated by the flash. The number of activated PDEs is  $P^*(t) = \tilde{P}^*(t) / n_{ch} \beta_{sub} = R_0^* g_p(t) \xi / n_{ch} \beta_{sub}$ . The number of PDEs activated during a single-photon response is obtained with  $R_0^* = 1$ .

*Asymptotic result for dim flashes.* The equation for  $y(t)$  is non-linear due to  $H(y)$  (see eqn (9)) and cannot be solved analytically. However, for GCAPs<sup>-/-</sup> photoreceptors where non-linear  $Ca^{2+}$  feedback is absent, and for dim flashes where  $y(t)$  remains small, we can use the first order approximation  $\beta_d H(y) \approx \beta y$  with:

$$\beta = \beta_d (1 - n_{ch} \hat{\alpha}') \quad (2.14)$$

and  $\hat{\alpha}' = \frac{d}{dx} \hat{\alpha}(x) \Big|_{x=1} = -\frac{2}{1 + \hat{K}_\alpha^2}$  to derive an asymptotic expression for the current. The solution of eqn (11) with the linear approximation  $\beta_d H(y) = \beta y$  is  $y(t) = \kappa \xi \int_0^t \phi(s) g_y(t - s) ds$ , where:

$$\begin{aligned}
g_y(t) = & \mu_{rh}\mu_{tr}\mu_{pde} \left( \frac{e^{-\mu_{rh}t}}{(\mu_{tr} - \mu_{rh})(\mu_{rh} - \mu_{pde})(\mu_{rh} - \beta)} \right. \\
& + \frac{e^{-\mu_{tr}t}}{(\mu_{rh} - \mu_{tr})(\mu_{tr} - \mu_{pde})(\mu_{tr} - \beta)} \\
& + \frac{e^{-\mu_{pde}t}}{(\mu_{rh} - \mu_{pde})(\mu_{pde} - \mu_{tr})(\mu_{pde} - \beta)} \\
& \left. + \frac{e^{-\beta t}}{(\mu_{rh} - \beta)(\beta - \mu_{tr})(\beta - \mu_{pde})} \right)
\end{aligned} \tag{2.15}$$

For short flashes we get  $y(t) = \phi\kappa\Delta t\xi g_y(t) = R_0^*\xi g_y(t)$ . For photoreceptors in which the genes for the GCAPs have been deleted and which therefore lack  $\text{Ca}^{2+}$ -dependent feedback of cyclase activity,  $\hat{\alpha}' = 0$  and  $\beta = \beta_d$ . Because the dim flash analysis is valid for WT and GCAPs<sup>-/-</sup>photoreceptors, we conclude that, to first approximation, a WT cell behaves like a GCAPs<sup>-/-</sup>cell with an increased cGMP turnover rate of  $\beta_d(1 - n_{ch}\hat{\alpha}')$ .

By dividing  $y(t)$  by its peak value  $y_{peak}$  we define the normalized log-transform:

$$\hat{y}(t) = \frac{y(t)}{y_{peak}} \approx \frac{g_y(t)}{g_{y, peak}}. \tag{2.16}$$

For dim flashes the normalized log-transform is independent of the light intensity  $\phi$  and the gain  $\xi$  and depends only on the dynamic parameters, and the waveform of  $\hat{y}(t)$  characterizes the shape of a flash response.

*Fitting procedure.* Fitting was done with the Data to Dynamics framework (Raue et al. 2013, 2015). The optimization algorithm that we used for fitting and parameter estimation is the nonlinear least-squares solver LSQNONLIN from MATLAB. Because the model is non-linear in parameters, we give goodness of fit values as root-mean-squarederror (RMSEs; see, for example, Dekking et al. 2005). Lower values of RMSE indicate a better fit of the model to the data.

## 2.5 Results

Figure 1 illustrates dark-adapted photoresponses of rods and cones, normalized to the maximum response to light bright enough to close all of the outer-segment channels. Saturating responses to the brightest stimuli were not used in our model calculations (see Methods) and are not shown. For our analysis we consider two different expressions for the normalized currents: first  $\hat{I}$ , which is unity in darkness and decreases with light; and the complementary current  $\hat{i} = 1 - \hat{I}$ , which is zero in darkness and increases to unity in bright light. The latter expression is more common in the literature and is depicted in Fig. 1.

The responses of WT mouse rods in Fig. 1A are averaged responses from seven rods recorded with voltage clamp from retinal slices (see Methods). As we explain in the Methods, we were unable to obtain similar voltage-clamp recordings from GCAPs<sup>-/-</sup>-mouse rods which were sufficiently stable to be used for model calculations. The responses of GCAPs<sup>-/-</sup>-mouse rods in Fig. 1B are therefore averaged suction-electrode recordings from five rods taken from previously published experiments (Chen *et al.* 2010c). The GCAPs<sup>-/-</sup>-rods lack the GCAPs, which are closely associated with guanylyl cyclase in both rods and cones and mediate Ca<sup>2+</sup>-dependent modulation of the rate of the cyclase. The use of this mutant to disable Ca-dependent feedback simplifies the fitting of the model. Cone responses are recent voltage-clamp recordings from mouse retinal slices recorded under the same conditions as the WT rod responses in Fig. 1A (Ingram *et al.* 2019). Recordings from cones were made from Gnat1<sup>-/-</sup>-retinas lacking Gnat1, the alpha subunit of the rod G-protein transducin. Cones in the mouse retina receive input from rods through connexin-36 gap junctions (Asteriti *et al.* 2017; see Fain & Sampath, 2018), and this input is deleted in Gnat1<sup>-/-</sup>-cones (Ingram *et al.* 2019). In Fig. 1C, we show averaged responses from three Gnat1<sup>-/-</sup>-cones, which are effectively WT cone responses lacking rod input. Responses of a very similar waveform were recorded from Cx36<sup>-/-</sup>-retinas lacking connexin 36 (Ingram *et al.* 2019). In Fig. 1D we show averaged responses from three Gnat1<sup>-/-</sup>;GCAPs<sup>-/-</sup>-cones lacking both Gnat1 and the GCAP proteins, which are effectively GCAPs<sup>-/-</sup>-responses lacking any rod input.

From the recordings in Fig. 1, we will proceed in the following way: we first use the

normalized log-transform of GCAPs<sup>-/-</sup> current responses from Fig. 1B and D, which lack Ca<sup>2+</sup> feedback, to compare the striking difference in kinetics between mouse rods and mouse cones (Fig. 2). We then analyse both WT and GCAPs<sup>-/-</sup> rod responses together to define a set of rod parameters (Fig. 4), which we use as reference and starting values for our cone analysis. In the model calculations of Fig. 5 we identify those dynamic parameters that have to be considerably different between rods and cones. We then concurrently fit the cone WT and GCAPs<sup>-/-</sup> responses to estimate values for the unknown cone parameters, including the gain and Ca<sup>2+</sup> sensitivity of the cyclase rate; and we probe our cone model by fixing certain parameters and varying others (Fig. 6). Finally, we use our simulations to compare the single-photon response and the number of PDE molecules activated per photon between a rod and a cone (Fig. 7).

### 2.5.1 Normalized log-transform of the rod and cone light response

We begin by considering the log-transform of  $\hat{I}$  of rod and cone GCAPs<sup>-/-</sup> responses, since we have shown (see eqn (15) in the Methods) that the entire waveform of the log-transform of the photoreceptor response in the absence of cyclase feedback should be proportional to the strength of the stimulus overmuch of the range of stimulus intensities. To demonstrate this phenomenon, we have taken the logarithms of the GCAPs<sup>-/-</sup> responses  $\hat{I} = 1 - \hat{i}$  of Fig. 1B (for rods) and Fig. 1D (for cones) and have normalized each curve to its peak value. That is, we have calculated the negative log of the current,  $y = -\ln \hat{I}$ , and then normalized it to the peak value to give  $\hat{y} = y/y_{peak}$  (see also eqn (16) in the Methods). For both rods (Fig. 2A) and cones (Fig. 2B),  $\hat{y}$  follows a very similar time course at each light intensity which is, however, quite different for the two kinds of photoreceptors. In Fig. 2C, we compare on the same time base the mean waveforms of  $\hat{y}$  for rods and cones from Fig. 2A and B. This figure illustrates the considerable difference in the kinetics of the rod and cone responses.

### 2.5.2 Model for the rod and cone response

As we describe in the Methods section, we used a parsimonious, spatially homogeneous model of vertebrate phototransduction. Our model was derived from earlier models (see, for example, Hamer *et al.* 2005; Reingruber & Holcman, 2008; Chen *et al.* 2010c; Korenbrot, 2012; Reingruber *et al.* 2013; Wang *et al.* 2018), which were based on the known transduction reactions (see eqn (10) in the Methods). In brief (see Fig. 3), we assume that light-activated visual pigment ( $R^*$ ) activates the G-protein transducin ( $T^*$ ), which activates PDE6 ( $P^*$ ). The  $P^*$  hydrolyses the second messenger cGMP, which controls the opening of the cyclic-nucleotide-gated (CNG) channels in the outer-segment plasma membrane. In a WT rod or cone, the synthesis of cGMP by guanylyl cyclase is modulated by  $Ca^{2+}$  feedback via the GCAPs (not shown in Fig. 3). This feedback is eliminated in GCAPs<sup>-/-</sup> photoreceptors. We use the same equations to model both the WT and GCAPs<sup>-/-</sup> responses of both kinds of photoreceptors, because the biological transduction pathway is very similar between rods and cones (see Ingram *et al.* 2016). This molecular similarity suggests that, to a first approximation, the same model structure can be used to describe both rods and cones with differences faithfully captured by adjustment of model parameters, which we have circled in Fig. 3. Equations (15) and (16) in the Methods show that the difference in the kinetics of the rod and cone responses in Fig. 2 are generated by differences in the deactivation rate of a light-activated pigment  $\mu_{rh}$ , the rate  $\mu_{tr}$  by which an activated transducin is converted into an activated PDE, the deactivation rate of a light-activated PDE  $\mu_{pde}$ , and the cGMP turnover rate in darkness  $\beta_d$ . The question then becomes: how many of these parameters are different, and which ones are most important?

### 2.5.3 Adjusting the rod model

To answer this question, we begin with the model for rods, where we have used kinetic parameters for the most part derived from the literature (see Table 2). We assumed a value for  $\mu_{rh}$  of  $28\text{ s}^{-1}$  (for a time constant of 36 ms, see Krispel *et al.* 2006; Chen *et al.* 2010a), a value for  $\mu_{pde}$  of  $5\text{ s}^{-1}$  (for a time constant of 200 ms, see for example Krispel *et al.* 2006;

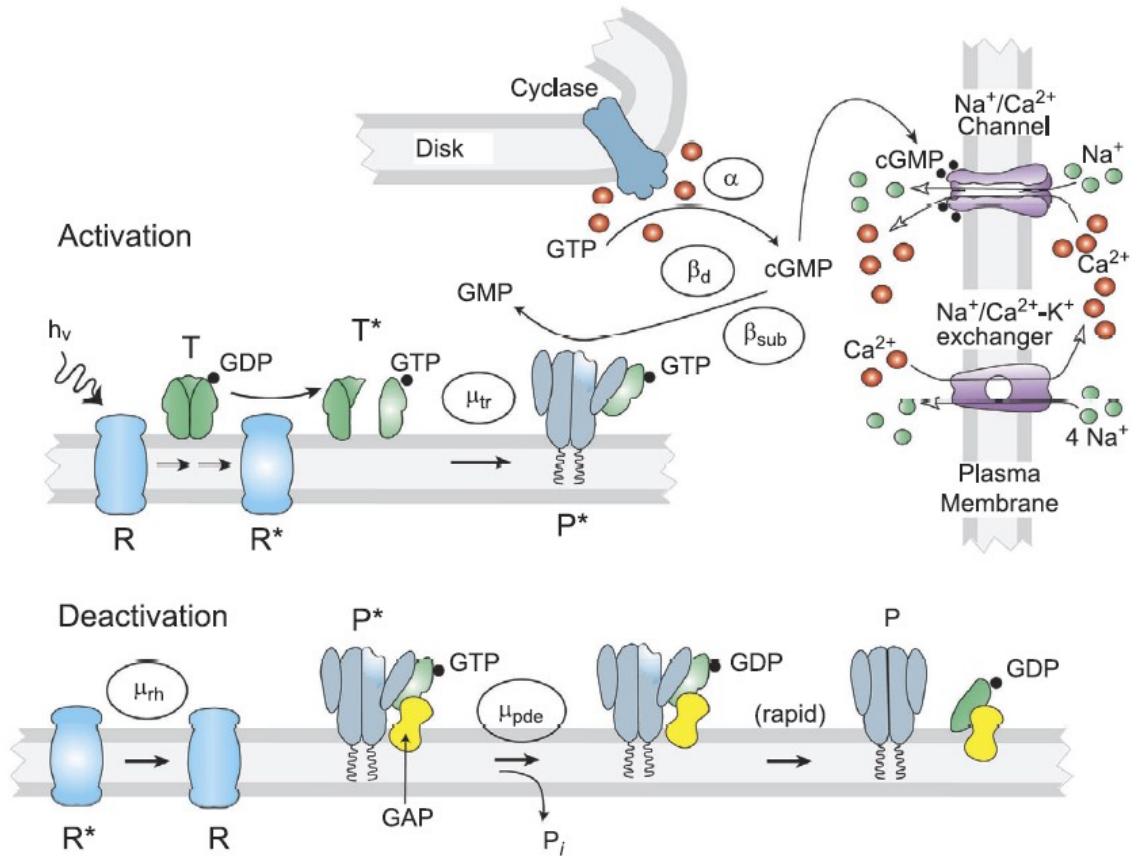


Figure 2.3: *Schema of transduction cascade showing rates of activation and decay used in the model.* Model parameters are given in bold and are circled; they are defined in Table 1. Abbreviations:  $h\nu$ , light; R, visual pigment;  $R^*$ , activated visual pigment; T, transducin;  $T^*$ , activated transducin; P, phosphodiesterase;  $P^*$ , activated phosphodiesterase; GAP, GTPase-activating proteins; GTP, guanosine triphosphate; GDP, guanosine diphosphate; GMP, guanosine monophosphate; cGMP, 3',5'-cyclic guanosine monophosphate.

Tsang *et al.* 2006), and a value for  $\beta_d$  of  $4.1 \text{ s}^{-1}$  (Gross *et al.* 2012b; Reingruber *et al.* 2013). In contrast to  $\mu_{rh}$ ,  $\mu_{pde}$ , and  $\beta_d$ , no clear estimate for  $\mu_{tr}$  can be found in the literature. The value of  $\mu_{tr}$  is often assumed to be very large, in which case the model in eqn (11) can be further simplified by removing the intermediate state  $T^*$  such that  $R^*$  directly activates PDE (Pugh & Lamb, 2000; Gross & Burns, 2010; Gross *et al.* 2012b). More generally,  $\mu_{tr}$  can be viewed as an effective parameter that delays the initial rising of the response but does not contribute to amplification, provided each activated transducin (or each pair of transducins, see Qureshi *et al.* 2018) activates only a single PDE. To obtain a better fit to the initial rising phase of the responses, we decided to keep  $\mu_{tr}$  as a model parameter.

Parameter	Cone				
	Rod	Scenario 1	Scenario 2	Scenario 3	Scenario 4
$\kappa(\mu m^2)$	0.2 (wild-type) 0.5 (GCAPs <sup>-/-</sup> )	0.013	0.013	0.013	0.013
$n_{ch}$	2.5	2.5	2.5	2.5	2.5
$\xi$	0.45	0.0018	0.0019	0.0020	0.0024
$\beta_d(s^{-1})$	4.1	11.0	12.4	12.4	16.6
$\mu_{pde}(s^{-1})$	5	37.8	85.9	40 (ul)	20 (ul)
$\mu_{rh}(s^{-1})$	28	70.7	28	40 (ul)	101.5
$\mu_{tr}(s^{-1})$	23.8	70.7	85.9	100 (ul)	101.5
$\hat{K}_\alpha$	0.87	0.84	0.82	0.78	0.80
RMSE		0.031	0.034	0.033	0.044

Table 2.2: Parameter values for rod and cone models. Fixed input values are in black and fitted parameter values are in blue. For each cone scenario the same and ; data have been used for the fitting. The root-mean-squared error (RMSE) makes possible the comparison of the goodness of fit between the different cone scenario (ul = the fitted parameter value reached the upper limit of the parameter range that we imposed)



In addition to the kinetic parameters  $\mu_{rh}$ ,  $\mu_{tr}$ ,  $\mu_{pde}$ , and  $\beta_d$ , the flash response further depends on the dimensionless gain parameter  $\xi = \frac{n_{ch}\beta_{sub}k_{act}}{\mu_{pde}\mu_{rh}}$  (see eqn (12) in the Methods) and the cyclase  $\text{Ca}^{2+}$ -sensitivity parameter  $\hat{K}_\alpha$ . In the expression for  $\xi$ ,  $n_{ch}$  is the cooperativity constant (Hill coefficient) of the channel,  $\beta_{sub}$  is the rate constant by which a single light-activated PDE molecule hydrolyses cGMP, and  $k_{act}$  is the rate constant of activation of  $\text{T}^*$  by a single  $\text{R}^*$ . To estimate the parameters  $\xi$ ,  $\mu_{tr}$  and  $\hat{K}_\alpha$  we concurrently fit the WT and GCAPs<sup>-/-</sup>rod responses from Fig. 1A and B to the non-linear eqn (11) in the Methods using known kinetic parameters from Table 2 (indicated in black) as input and  $\xi$ ,  $\mu_{tr}$  and  $\hat{K}_\alpha$  as fitting parameters. In Fig. 4A and B we show the agreement between the best-fitting simulation and the data for the current  $\hat{i} = 1 - e^{-y(t)}$ . We emphasize that the fitting and simulations for WT and GCAPs<sup>-/-</sup>rod were performed with exactly the same parameter values but with the cyclase feedback switched off for the GCAPs<sup>-/-</sup>simulations. The best-fitting parameter values were  $\xi = 0.45$ ,  $\mu_{tr} = 23.8\text{s}^{-1}$  and  $\hat{K}_\alpha = 0.87$ . The agreement between simulation and data is reasonably good for both WT and GCAPs<sup>-/-</sup>rods, even though recordings were made with different techniques and in different perfusion solutions (see Methods). Discrepancies are greater for WT rods, probably because our assumptions about  $\text{Ca}^{2+}$  feedback were over-simplified.

Because rod fittings were performed with the averaged data from Fig. 1, we checked these values by additionally performing a single-cell analysis. We chose the five GCAPs<sup>-/-</sup>cells whose mean currents are given in Fig. 1B together with five WT cells, randomly chosen from among the seven WT cells used for the averaging in Fig. 1A. We then performed concurrent fittings with 25 different combinations of single-cell data. We fitted the single-cell data in exactly the same way as we performed the fittings with the averaged data. The results for the fitted parameters were (mean  $\pm$  SD)  $\xi = 0.49 \pm 0.12$ ,  $\mu_{tr} = 27.9 \pm 37\text{s}^{-1}$ ,  $\hat{K}_\alpha = 0.85 \pm 0.47$ . Although there was considerable variability, the mean values were very close to the values we obtained from the fit to the mean responses. Confidence intervals calculated by Monte Carlo simulations of individual cell fit parameters showed that, for all rod parameters, values obtained by fitting to mean responses were within calculated 95%

confidence intervals of values obtained by fitting to individual responses. Thus we conclude that, within an alpha rate of 5%, fitting to the mean response does not yield a value that is significantly different from the mean of fitting to individual responses.

In Fig. 4C, we plot data and simulations of the log-transforms of the GCAPs<sup>-/-</sup> responses, and in Fig. 4D we show the agreement between simulation and data for the normalized log-transforms corresponding to Fig. 2B. Table 2 provides a summary of all the rod parameters, with black parameter values giving fixed input values, and blue parameter values giving results from fittings.

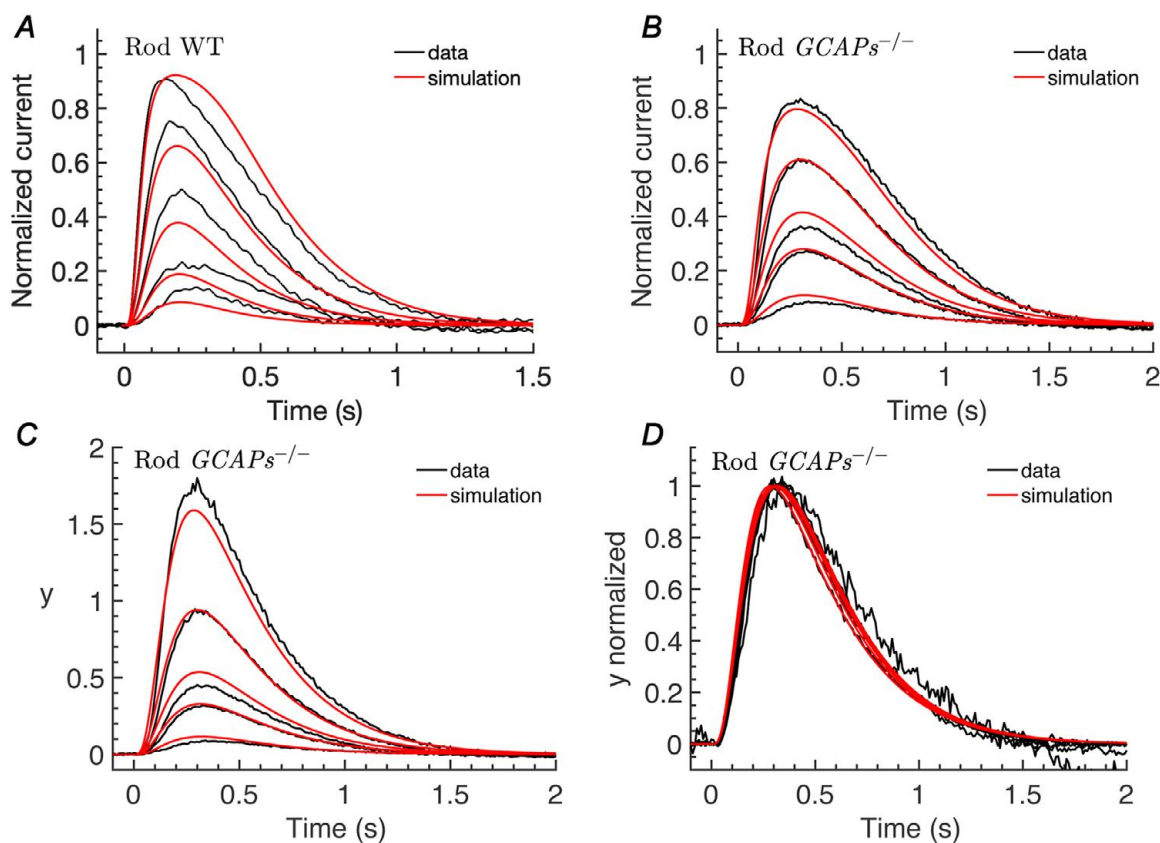


Figure 2.4: *Adjusting the rod model.* **A-B.**, to estimate the rod parameters  $\xi$ ,  $\mu_{tr}$  and  $\hat{K}_\alpha$  we concurrently fit the wild-type (WT) and GCAPs<sup>-/-</sup> traces from Fig. 1A and B to the non-linear eqn (11) in the Methods using the kinetic parameters from Table 2 (in black) as input and  $\xi$ ,  $\mu_{tr}$  and  $\hat{K}_\alpha$  as fitting parameters. The best fit was obtained with  $\xi = 0.45$ ,  $\mu_{tr} = 23.8s^{-1}$  and  $\hat{K}_\alpha = 0.87$ . Black traces show the data, red traces show simulations. **C.**, comparison of the log-transforms from (B.). **D.**, comparison of the normalized log-transforms from (C.).

#### 2.5.4 Transforming rod dynamics into cone dynamics

We next used the GCAPs<sup>-/-</sup> responses to examine which of the parameters  $\mu_{rh}$ ,  $\mu_{pde}$ ,  $\mu_{tr}$ , and  $\beta_d$  have to be modified in order to turn the dynamics of rod responses into those of cones, as shown in Fig. 2C. In Fig. 5A-D we show the effect of changing only a single one of  $\mu_{rh}$ ,  $\mu_{pde}$ ,  $\mu_{tr}$ , and  $\beta_d$  (indicated in the panels). That is, we kept three of the four parameters the same as in the rod model and determined the best fit to the cone responses for the fourth using eqn (11). For all four possibilities, fits were poor. RMSE values were 0.14 for  $\beta_d$  alone (Fig. 5A), 0.21 for  $\mu_{rh}$  alone (Fig. 5B), 0.15 for  $\mu_{pde}$  alone (Fig. 5C) and 0.20 for  $\mu_{tr}$  alone (Fig. 5D). For each of parameters, the fitting program always returned the value we set for the upper limit of the fitting range of  $200s^{-1}$  (corresponding to a time constant of 5 ms). Higher values did not seem reasonable to us and, in addition, did not alter the results. Even with this very high value, a change in only a single parameter was insufficient to capture the kinetics of decay of the cone response.

We then tested whether we could turn a GCAPs<sup>-/-</sup> rod into a GCAPs<sup>-/-</sup> cone by altering only the dynamic parameters  $\mu_{rh}$ ,  $\mu_{pde}$  and  $\mu_{tr}$ . We therefore fitted the GCAPs<sup>-/-</sup> responses using  $\mu_{rh}$ ,  $\mu_{pde}$ ,  $\mu_{tr}$  as fitting parameters while keeping  $\beta_d$  equal to the rod value. Again, no reasonable fit could be obtained (Fig. 5E, RMSE of 0.1). Similarly, when we used  $\beta_d$  as a fitting parameter and kept rod values for  $\mu_{rh}$ ,  $\mu_{pde}$ ,  $\mu_{tr}$  we could not obtain good fits (not shown, RMSE of 0.11). This shows that both  $\beta_d$  and PDE kinetics have to be altered. When we let both  $\mu_{pde}$  and  $\beta_d$  vary, we could obtain a reasonable fit to the normalized log-transform (RMSE of 0.02, Fig. 5F). In contrast, when we varied only  $\mu_{rh}$  and  $\beta_d$ , or only  $\mu_{tr}$  and  $\beta_d$ , we obtained poor fits; the fitting program returned rates for both parameters at the value of  $200s^{-1}$  we had set for the upper limit of the fitting range, and RMSE was 0.11 and 0.12 (not shown). In summary, we found that, at a minimum, the rate of turnover of cGMP ( $\beta_d$ ) and the PDE deactivation rate ( $\mu_{pde}$ ) need to be increased to fit the kinetics of the cone waveform.

### 2.5.5 Adjusting the cone model

To examine in more detail the alterations we need to make in the parameters of the model to fit cone responses, we first fitted concurrently both the Gnat1<sup>-/-</sup> and Gnat1<sup>-/-</sup>;GCAPs<sup>-/-</sup> cone data from Fig. 1C and D with eqn (11) from the Methods. We did not make any assumptions about the cone parameter values and used all the parameters  $\xi$ ,  $\mu_{rh}$ ,  $\mu_{tr}$ ,  $\mu_{pde}$ ,  $\beta_d$  and  $\hat{K}_\alpha$  as unconstrained fitting parameters. Although the gain  $\xi = \frac{n_{ch}\beta_{sub}k_{act}}{\mu_{pde}\mu_{rh}}$  depends on  $\mu_{rh}$  and  $\mu_{pde}$ , the product  $\beta_{sub}k_{act}$  is unknown. We therefore used  $\xi$  as an independent fitting parameter. The best-fitting values for  $\xi$ ,  $\mu_{rh}$ ,  $\mu_{tr}$ ,  $\mu_{pde}$ ,  $\beta_d$  and  $\hat{K}_\alpha$  are given in Table 2 as scenario 1 (RMSE was 0.031). The reason the RMSE is now higher than in Fig. 5F (RMSE was 0.02) is that in Fig. 5F we fitted only Gnat1<sup>-/-</sup>;GCAPs<sup>-/-</sup> responses, and in addition these responses were normalized, which reduced the variability due to the response amplitude. We verified that the model and the fitting parameters are identifiable (Raue *et al.* 2009). We show the results of these fits in Fig. 6A and B. We compare the current  $\hat{i} = 1 - e^{-y(t)}$  for the Gnat1<sup>-/-</sup> and Gnat1<sup>-/-</sup>;GCAPs<sup>-/-</sup> data (black traces) to simulations (red traces) obtained with eqn (11) from the Methods and the fitted parameter values. These simulations show that the model, together with the fitted parameter values, faithfully reproduces the Gnat1<sup>-/-</sup>;GCAPs<sup>-/-</sup> and the Gnat1<sup>-/-</sup> cone responses.

As for the rod fittings, we performed a single-cell analysis with the three Gnat<sup>-/-</sup> and three Gnat<sup>-/-</sup>;GCAPs<sup>-/-</sup> cells that were used for the averaged data in Fig. 1. We concurrently fitted nine different combinations of single-cell data for scenario 1. We found parameter values of (mean  $\pm$  SD)  $\xi = 0.0019 \pm 0.005$ ,  $\beta_d = 11.8 \pm 2.6 s^{-1}$ ,  $\mu_{rh} = 65.1 \pm 20.2 s^{-1}$ ,  $\mu_{tr} = 69.9 \pm 19.9 s^{-1}$ ,  $\mu_{pde} = 43.4 \pm 8.1 s^{-1}$ ,  $\hat{K}_\alpha = 0.81 \pm 0.11$ . These values were again very close to the values we obtained from fitting the mean responses (Table 2). Confidence intervals calculated by Monte Carlo simulations showed that, for all cone parameters, parameters fit to mean responses were within the calculated 95% confidence intervals of parameters fit to individual responses. Thus we again conclude, with an alpha rate of 5%, that fitting to the mean response does not yield a value that is significantly different from fitting to the mean of the individual responses.

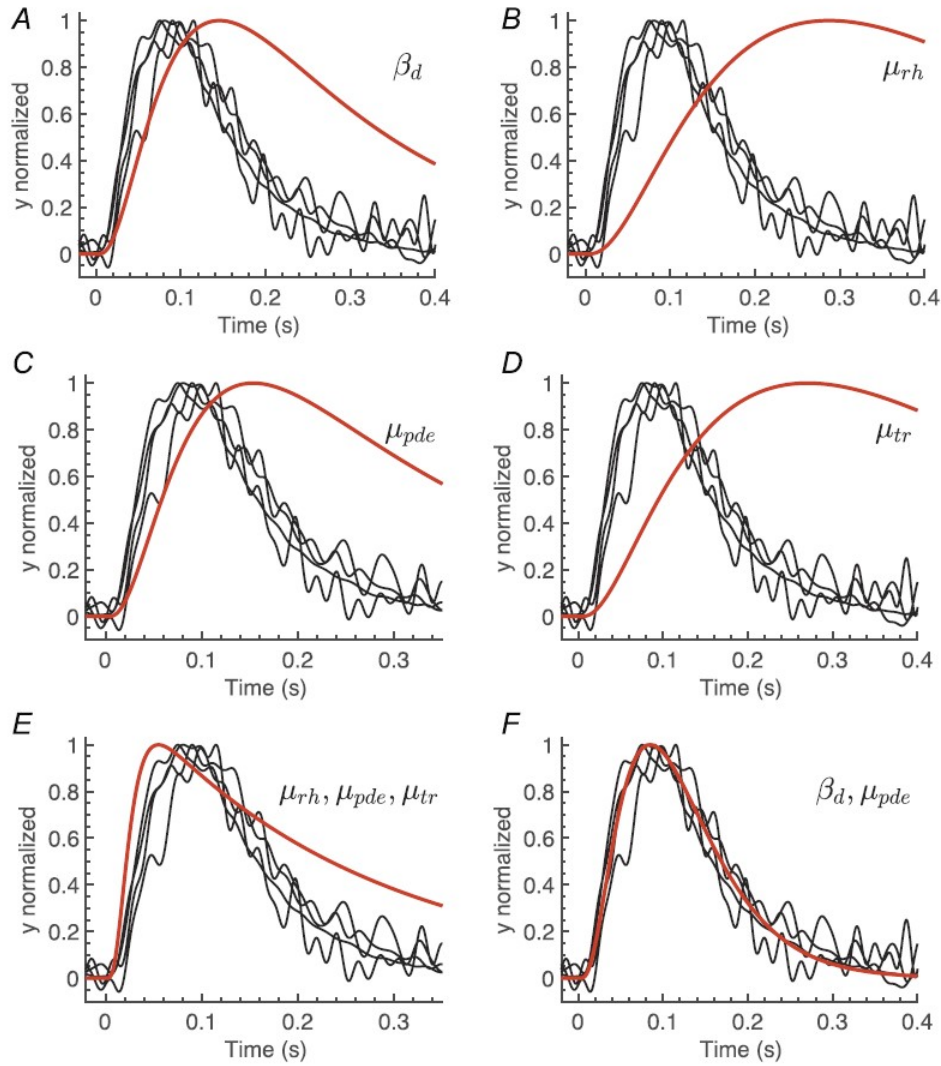


Figure 2.5: *Transition from rod to cone kinetics.* The black traces are normalized log-transforms  $\hat{y}(t)$  from cone Gnat1<sup>-/-</sup>;GCAPs<sup>-/-</sup> responses from Fig. 2B. The red traces show a simulation of a normalized log-transform computed with rod parameter values for  $\mu_{rh}$ ,  $\mu_{tr}$ ,  $\mu_{pde}$ , and  $\beta_d$  as given in Table 2, except for the parameter indicated in each of the panels, which has been estimated by fitting the normalized cone Gnat1<sup>-/-</sup>;GCAPs<sup>-/-</sup> responses with eqn (11). **A-D.**, the best-fitting parameter values were  $\beta_d = 200s^{-1}$ ,  $\mu_{rh} = 200s^{-1}$ ,  $\mu_{tr} = 200s^{-1}$ , and  $\mu_{pde} = 200s^{-1}$ , corresponding to the upper limit of  $200s^{-1}$  that we imposed for the parameter range. Root-mean-squared errors (RMSEs) were as follows: 0.14 (**A.**), 0.21 (**B.**), 0.15 (**C.**), and 0.20 (**D.**). **E.**, the best-fitting parameter values were  $\mu_{rh} = \mu_{tr} = \mu_{pde} = 130s^{-1}$ . RMSE was 0.1. **F.**, the best-fitting parameter values were  $\beta_d = 31s^{-1}$  and  $\mu_{pde} = 183s^{-1}$ . RMSE was 0.02.

We next varied possible values of the parameters  $\mu_{rh}$ ,  $\mu_{tr}$  and  $\mu_{pde}$ . As we showed in the Methods section (see eqn (13)), we cannot decide which of the fitted parameter values corresponds to which parameter because of the symmetry among  $\mu_{rh}$ ,  $\mu_{tr}$  and  $\mu_{pde}$ ; that is, interchanging the values of  $\mu_{rh}$ ,  $\mu_{tr}$  and  $\mu_{pde}$  with fixed  $\xi$  results in identical responses. We also note that because  $\beta_{sub}k_{act} = \xi \frac{\mu_{rh}\mu_{pde}}{n_{ch}}$ , the predicted value of  $\beta_{sub}k_{act}$  might depend upon the way the fitted parameter values are attributed to  $\mu_{rh}$ ,  $\mu_{tr}$  and  $\mu_{pde}$ . For the parameters in Table 2 for cone scenario 1 we chose  $\mu_{pde} \leq \mu_{rh} \leq \mu_{tr}$ .

In order to better explore the parameter space, we adopted three additional fitting scenarios. In scenario 2 we performed exactly the same fitting procedure as in scenario 1, except that  $\mu_{rh}$  was fixed to the rod value. The fitting waveforms were very similar to the ones from scenario 1 (not shown), and the RMSE was only slightly increased from 0.031 to 0.034. This result indicates that a satisfactory fit can be obtained by accelerating  $\mu_{pde}$  alone without any change in  $\mu_{rh}$ .

In scenarios 1 and 2, either the rate of decay of activated visual pigment ( $\mu_{rh}$ ) or of activated phosphodiesterase ( $\mu_{pde}$ ) was rapid. In scenario 3 we tested the possibility that both rates are slow and below  $40s^{-1}$  (for time constants of decay greater than 25 ms). We also constrained the range for  $\mu_{tr}$  to  $100s^{-1}$ . The best-fitting parameter values for this scenario were the upper limits  $\mu_{rh} = \mu_{pde} = 40s^{-1}$ . The fitting results were again very similar to scenarios 1 and 2, and the RMSE was 0.033. This result, together with scenarios 1 and 2, shows that  $\mu_{rh}$  can be the same as the rod value or faster, but it is unlikely to be slower.

In our final scenario, 4, we tested the possibility that the PDE lifetime in cones is longer than 50 ms, corresponding to the upper limit of  $20s^{-1}$  for the fitting range of  $\mu_{pde}$ . The best-fitting values were the upper limit  $\mu_{pde} = 20s^{-1}$ , and the fitted values for  $\mu_{rh}$  and  $\mu_{tr}$  were very large ( $101s^{-1}$ ), indicating extremely rapid activation of transducin and pigment decay. Because in mice the extinction of visual pigment is catalyzed by the same enzyme (GRK1) in both rods and cones, we think it unlikely that the rate of decay of visual pigment is several-fold larger in cones than in rods. Combined with the around 30% larger RMSE for

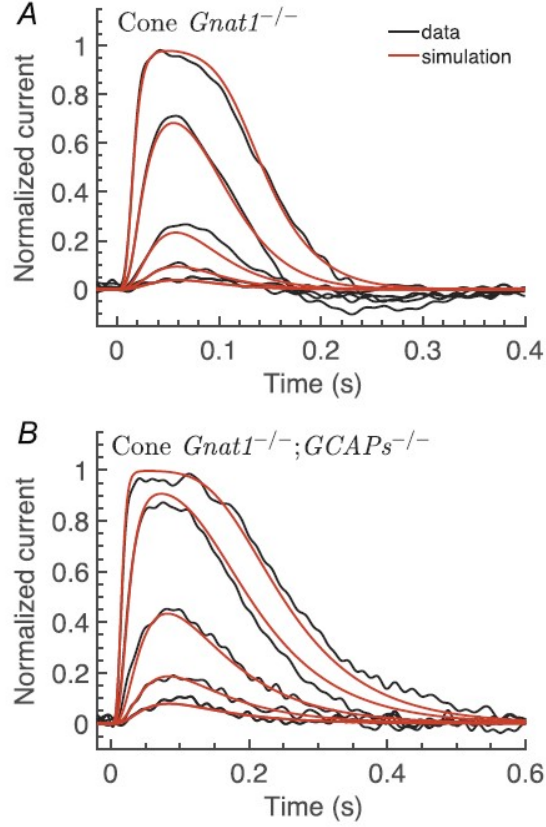


Figure 2.6: *Adjusting the cone model.* To estimate cone parameter values, the currents  $\hat{i} = 1 - e^{-y(t)}$  of  $Gnat1^{-/-};GCAPs^{-/-}$ -cones and  $Gnat1^{-/-}$ -cones (effectively wild type) from Fig. 1C and D have been fitted concurrently with the non-linear model in eqn (11) from the Methods with fitting parameters  $\xi$ ,  $\mu_{rh}$ ,  $\mu_{tr}$ ,  $\mu_{pde}$ ,  $\beta_d$ , and  $\hat{K}_\alpha$ . We explored four different fitting scenarios as explained in the text. The best-fitting parameter values for each scenario are summarized in Table 2 (fixed parameter values are in black, fitted values are in blue). **A.**, and **B.**, current data (black traces) and the corresponding simulation results obtained with the parameters for cone scenario 1 (red traces) for  $Gnat1^{-/-}$ (**A.**) and  $Gnat1^{-/-};GCAPs^{-/-}$ -cones (**B.**).

scenario 4 (0.044) compared with the three other scenarios (0.031-0.034), we conclude that  $\mu_{pde}$  in a cone is very likely to be larger than  $20s^{-1}$  (with a time constant of PDE decay less than 50 ms) and several-fold larger than the value in rods. When we retained  $\mu_{pde}$  at its rod value and attempted to fit the cone responses, the fit was again poor (RMSE 0.18).

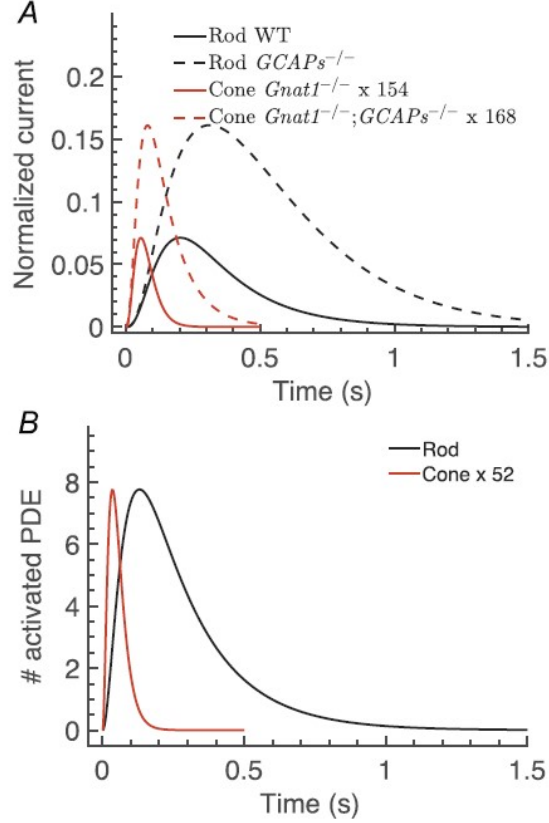


Figure 2.7: *Single-photon response (SPR) for rod and cone model.* **A.**, comparison of the SPR current for wild-type (WT) and  $GCAPs^{-/-}$ -rod with  $Gnat1^{-/-}$  (effectively wild type) and  $Gnat1^{-/-};GCAPs^{-/-}$ -cones. The currents are computed with the analytic formula  $\hat{i}_{spr}(t) = 1 - e^{-\xi g_y(t)}$  with  $g_y(t)$  from eqn (15) in the Methods and parameter values from Table 2 (scenario 1 for cone). **B.**, comparison of the time-dependent number of activated PDEs corresponding to the response in (A). The number of activated PDEs is computed as  $P^*(t) = \frac{\xi}{n_{ch}\beta_{sub}}g_p(t)$ , with  $g_p(t)$  from eqn (13) in the Methods with parameter values from Table 2 and  $\beta_{sub} = 0.07$ .

The best-fitting parameter values corresponding to each scenario are summarized in Table 2 (fixed input values are in black, fitted parameter values are in blue). From these values we draw the following conclusions. First, the gain parameter  $\xi$  varies little among the



various scenarios and is at least 200 times smaller for cones than for rods. The value of  $\beta_d$  is consistently 3-4 times larger in cones than in rods, indicating a higher rate of cGMP turnover in darkness. The rate  $\mu_{pde}$  is consistently higher in cones, indicating a much shorter time constant of decay of activated PDE probably reflecting the higher concentration of GAPs in cones. Because of the similarity of the RMSE for the first three scenarios nothing definite can be said about the relative rates of pigment decay ( $\mu_{rh}$ ), which may or may not be higher in cones than in rods.

### 2.5.6 Response to a single photon

The difference in sensitivity and dynamics between rods and cones can be well exemplified by comparing responses to a single-photon excitation. To compute the single-photon response current, we used the analytic formula  $\hat{i}_{spr}(t) = 1 - e^{-\xi g_y(t)}$  with  $g_y(t)$  from eqn (15) and with parameter values from Table 2. Because  $y(t)$  is small during the single-photon response, this analytic result is in excellent agreement with a single-photon response simulation obtained with eqn (11). In Fig. 7A we compare the single-photon response for WT and GCAPs<sup>-/-</sup>rods with those for Gnat1<sup>-/-</sup> and Gnat1<sup>-/-</sup>;GCAPs<sup>-/-</sup>cones, using for cones the parameters of scenario 1. Results with parameters from the other three scenarios were similar both in magnitude and waveform.

The calculated rod single-photon current in Fig. 7A is similar in amplitude and waveform to those of recorded mouse single-photon responses (for example, Mendez *et al.* 2001; Sampath *et al.* 2005; Chen *et al.* 2010c; Azevedo & Rieke, 2011), with normalized peak amplitudes ( $r/r_{max}$ ) and integration times ( $t_i$ ) of 0.07 and 390 ms (WT), and 0.165 and 640 ms (GCAPs<sup>-/-</sup>). The rod responses are larger by about a factor of 150 (WT) and 165 (GCAPs<sup>-/-</sup>) than in cones (Fig. 6A), similar to previous estimates (Nikonov *et al.* 2006). The amplitude of the single-photon current is about 2.3 times larger in a GCAPs<sup>-/-</sup>rod than in a WT rod and a 2.1 times larger in a GCAPs<sup>-/-</sup>cone than in a WT cone, somewhat smaller than found by Sakurai *et al.* (2011).

Next, we investigated how the number of activated PDEs varies between rods and cones

during a single-photon response. The number of activated PDEs does not depend on  $\text{Ca}^{2+}$  feedback and is therefore the same for WT and GCAPs<sup>-/-</sup> photoreceptors. To compute the number of activated PDEs we used the analytic expression  $P^*(t) = \frac{\xi}{n_{ch}\beta_{sub}}g_p(t) = \frac{k_{act}}{\mu_{rh}\mu_{pde}}g_p(t)$ , where  $g_p(t)$  is given by eqn (13) in the Methods. For a rod we have assumed  $k_{act} = 350s^{-1}$  (Reingruber *et al.* 2013), which leads to a maximum of around eight PDEs activated at any one time during the response. With  $k_{act} = 350s^{-1}$  and the rod parameters from Table 2, we compute  $\beta_{sub} = \frac{\xi\mu_{rh}\mu_{pde}}{n_{ch}k_{act}} \approx 0.07s^{-1}$ , which is similar to the value used by Reingruber *et al.* (2013). The parameter  $\beta_{sub}$  is the rate of hydrolysis of cGMP by a single P\* and is proportional to the catalytic activity of an activated PDE ( $k_{cat}$ ) and inversely proportional to the outer-segment volume ( $V_{os}$ ); that is,  $\beta_{sub} \propto k_{cat}/V_{os}$  (Pugh & Lamb, 2000; Reingruber & Holcman, 2008, 2009). Experiments expressing cone PDE in a rod indicate that  $k_{cat}$  is smaller by about a factor of 2 for cone PDE than for rod PDE (Majumder *et al.* 2015). Since the ratio of the cone-to-rod volumes of the outer segments is about 0.4 (Nikonov *et al.* 2006), the value of  $\beta_{sub}$  for a cone may be similar to the rod value. We therefore assumed  $\beta_{sub} = 0.07s^{-1}$  for both rods and cones, and we computed the number of activated PDEs from  $P^*(t) = \frac{\xi}{n_{ch}\beta_{sub}}g_p(t)$ . In Fig. 7B we compare the number of activated PDEs corresponding to the single-photon simulations shown in Fig. 7A. The peak number of PDEs activated at any one time during the single-photon response is reduced by a factor of around 52 in a cone compared with a rod.

## 2.6 Discussion

During the evolution of the vertebrate eye, more ancient cone-like precursors gave rise to photoreceptors with greater sensitivity, in part from a greater gain of the transduction cascade, and in part from a slower decay of the light response and longer time of integration of incoming photons (see Fain *et al.* 2010; Morshedien & Fain, 2017; Lamb, 2019). This process resulted in the duplex retina of the vertebrates with highly specialized rod and cone photoreceptors, which greatly differ in their sensitivity and response kinetics. Results from molecular biology (summarized in Ingram *et al.* 2016) indicate that evolutionary changes

were produced gradually by small effects on several transduction parameters rather than a single effect on only one, but it is still unclear which adaptations were most important in determining the different response properties of the two kinds of photoreceptors.

We have approached this problem by comparing rod responses and recent voltage-clamp recordings of mouse cone responses. To quantify the differences between rods and cones, we used a spatially homogeneous model that focuses on the main features of the transduction cascade (Fig. 3). Because of similarities in the molecular transduction pathway (see Ingram *et al.* 2016), we used the same model for rods and cones but with different parameter values. In this way we could classify the differences between the two kinds of photoreceptors. Our analysis shows that the most important changes between rods and cones are likely to be the rate of turnover of cGMP in darkness ( $\beta_d$ ), the rate of decay of the activated phosphodiesterase P\* ( $\mu_{pde}$ ) and the gain  $\xi = \frac{n_{ch}\beta_{sub}k_{act}}{\mu_{pde}\mu_{rh}}$ , where  $n_{ch}$  is the cooperativity constant of the CNG channels,  $\beta_{sub}$  is the rate constant of cGMP hydrolysis by an activated PDE and  $k_{act}$  is the rate of activation of transducin by activated visual pigment. The difference in  $\xi$  reflects the accelerated decay of P\* and perhaps R\*, but we will argue below that the product  $\beta_{sub}k_{act}$  must also be significantly altered, indicating that the amplification of transduction at the level of the rates of activation of transducin by visual pigment and/or cGMP hydrolysis by PDE must be lower in a cone. These changes alone, provided they were large enough, would have been sufficient during evolution to alter the response of a cone to produce a rod capable of responding to single photons and mediating dim light vision. There may be other differences, which we made no attempt to include in this work. In particular, there may be differences in the Ca<sup>2+</sup> economy of the two photoreceptors including buffering, mechanisms of Ca<sup>2+</sup> extrusion, and differences in the Ca<sup>2+</sup> permeability of the cyclic-nucleotide-gated channels (Perry & McNaughton, 1991; Sampath *et al.* 1999). These differences may be especially important during adaptation.

From our current model we cannot distinguish whether the changes in parameter values are generated by differences in the properties of transduction enzymes or differences in expression levels, but earlier studies have given some indication of the molecular basis for the

changes we postulate. Our analysis indicates that the rate of cGMP turnover in darkness may be around four times faster in cones than in rods (see Table 2). A six-fold difference was inferred from the rate of decline of the salamander cone photocurrent in zero- $\text{Na}^+$  solution (Perry & McNaughton, 1991; see also Cornwall *et al.* 1995), and an even higher rate of turnover was estimated for carp cones (Takemoto *et al.* 2009). One possible explanation for the increased turnover is an increase in the expression level of both the cyclase (Takemoto *et al.* 2009) and PDE (Reingruber *et al.* 2013). Direct biochemical measurement of the expression level of a cone protein is difficult in mouse because there are so few cone photoreceptors.

Our calculations indicate that the rate of PDE decay ( $\mu_{pde}$ ) is also higher in cones such that the decay time constant may be reduced from about 200 ms in rods (Krispel *et al.* 2006; Tsang *et al.* 2006) to as little as 25 ms in cones (see Table 2). Such a short time constant may result from a higher level of expression of GAP proteins in cones (Cowan *et al.* 1998; Zhang *et al.* 2003; Takemoto *et al.* 2009) and is close to the value for  $\text{Gnat1}^{-/-}$  cones of the single-exponential time constant of decay ( $\tau_{rec}$ ), which is about 30 ms for small-amplitude responses (Ingram *et al.* 2019). It is possible that the rate of decay of light-activated visual pigment ( $\mu_{rh}$ ) is also different and more rapid in cones. On the one hand, mouse rods and cones use the same GRK1 kinase and similar arrestins (see Ingram *et al.* 2016), and we might expect that the rates of decay of  $\text{R}^*$  would also be similar. On the other hand, it is possible that the expression levels of these proteins or the accessibility of pigment phosphorylation sites may be different for rods and cones. We hope to resolve this question by recording from cones with increased expression of cone visual-pigment kinase.

Our fittings in Table 2 indicate that the gain  $\xi = \frac{n_{ch}\beta_{sub}k_{act}}{\mu_{pde}\mu_{rh}}$  is smaller in cones by a factor of 200 to 250. Of the five gain parameters, the Hill coefficient of the channels  $n_{ch}$  seems not to be significantly different between rods and cones (see, for example, Haynes & Yau, 1990). We can think of the other four parameters as given by the ratios  $k_{act}/\mu_{rh}$  and  $\beta_{sub}/\mu_{pde}$ . Since  $k_{act}$  is the rate of transducin activation by visual pigment, and since the inverse of  $\mu_{rh}$  is the lifetime of  $\text{R}^*$ , this first ratio gives the response amplification due to activation of

transducin. For the second ratio,  $\beta_{sub}$  gives the rate of hydrolysis of cGMP by a single  $P^*$ , and the inverse of  $\mu_{pde}$  is the time constant of  $P^*$  decay. This second ratio therefore gives the response amplification due to hydrolysis of the second messenger cGMP by PDE. Our simulations in Table 2 indicate that the product of these two ratios is of the order of 200 to 250 times smaller in cones. That is to say, amplification in cones is around 200 to 250 times less effective than in rods. This large difference in  $\xi$  is also the primary reason for the discrepancies in the single-photon response (SPR) amplitudes between rods and cones in Fig. 7A. The ratios of the SPR amplitudes in Fig. 7A are not exactly equal to the ratios of  $\xi$  because the amplitude of the function  $g_y(t)$  from eqn (15) is slightly different between rods and cones.

With the values for  $\xi$ ,  $\mu_{pde}$  and  $\mu_{rh}$  from Table 2, we can compute that the product  $\beta_{sub}k_{act}$  must be around 13 times smaller in cones. In the Results section (Response to a single photon), we argued that the value of  $\beta_{sub}$  may not greatly differ between rods and cones despite the difference in outer-segment volume and the molecular species of the PDE. These considerations would then imply that  $k_{act}$ , which is the rate of transducin activation by visual pigment, is likely to be much smaller in cones. A smaller rate of transducin activation may explain the reduced amplification constant of mouse cones (Nikonov *et al.* 2006; Ingram *et al.* 2019).

In this work we have focused on brief flashes to estimate the minimal changes that have to be made in a dark-adapted retina to transform rod dynamics into those of cones. We made a number of assumptions and constructed a parsimonious model which focused on the principal mechanisms of transduction to facilitate the analysis of the responses. For example, we assumed that the  $Ca^{2+}$  concentration changes instantaneously in proportion to the level of the current, we neglected effects of  $Ca^{2+}$  buffering, and we assumed that the cGMP synthesis rate by guanylyl cyclase changes instantaneously with the  $Ca^{2+}$  concentration. We also modelled cyclase modulation as the only form of transduction modulation occurring in a rod or cone so that, in a GCAPs<sup>-/-</sup> photoreceptor, there is no modulation of the response of any kind within the time course of the flash response. These assumptions are unlikely all to be

true, and these over-simplifications may explain why our model is better able to fit responses of GCAPs<sup>-/-</sup> photoreceptors in the absence of Ca<sup>2+</sup> feedback than WT photoreceptors in its presence.

All of these assumptions will have to be modified for longer-duration stimuli where adaptation becomes important. A more extended model will be necessary to incorporate time-dependent changes in Ca<sup>2+</sup> concentration and cyclase activity, perhaps including additional mechanisms of transduction modulation, to explain why rods saturate in dim light but cones do not. As models become more sophisticated, our estimated parameter values are likely to alter, providing a more accurate reflection of the dynamics of the transduction cascade. We believe, however, that our calculations have already revealed some of the principal differences between the two kinds of photoreceptors, which we will use as input for the more detailed future models required to explain rod and cone differences in their totality.

## **2.7 Additional information**

### **2.7.1 Competing interests**

None.

### **2.7.2 Author Contributions**

Reingruber contributed to the conception and design of the work, designed the model, did all of the model calculations, and worked on the drafting and revision of the manuscript; Ingram and Griffis obtained the original data; and Fain contributed to the conception and design of the work and the drafting and revision of the manuscript.

### **2.7.3 Funding**

This work was funded by a grant from the Agence Nationale de Recherche (ANR) to JR, a thesis-year fellowship from the Graduate Division of UCLA to NTI, NIH EY001844 to GLF,

an unrestricted grant from Research to Prevent Blindness USA to the UCLA Department of Ophthalmology, and NEI Core Grant EY003311 to the Stein Eye Institute.

#### 2.7.4 Acknowledgements

We are grateful to Simon Laughlin and Alapakkam Sampath for reading an earlier draft of the manuscript, and to Margery Fain for composing Fig. 3.

## 2.8 Supplemental materials

Normalized currents  $\hat{i}$  from  $n$  cones have been used to compute the mean current  $\bar{\hat{i}}(t) = \frac{1}{n} \sum_{i=1}^n \hat{i}_i(t)$ . The standard error (deviation) of the mean current is computed as  $\sigma_{mean}(t) = \sigma(t)/\sqrt{n}$ , where  $\sigma(t)$  is the normal standard deviation of the sample.

Model fitting was done with the publicly available Data to Dynamics framework (<https://github.com/Data2Dynamics/d2d/wiki>) based on maximum likelihood optimization. The optimization algorithm we chose is the nonlinear least-squares solver LSQNONLIN from MATLAB. As goodness of fit criteria, we used the root-mean-squared error (RMSE),  $RMSE^2 = \frac{1}{N} \sum_{i=1}^N (f_i - d_i)^2$ , where  $N$  is the number of data points,  $f_i$  are the fitting values, and  $d_i$  are the data. Lower values of RMSE indicate smaller deviations of the model from the data and a better fit. We checked that the parameters are identifiable with the profile likelihood routine implemented in D2D, and we searched for local and global minima by performing fittings with randomized initial conditions.

To compare fitted parameters obtained from mean responses to parameters obtained with single-cell data, we constructed 95% confidence intervals for each parameter on a response-by-response basis with non-parametric resampling techniques (Efron, B., & Tibshirani, R., 1991 ; Carpenter, J., & Bithell, J., 2000). Parameter estimates from individual single-cell fits were simulated 10,000 times with a non-parametric "bootstrap" approximation to compute 95% confidence intervals. The parameters obtained from fitting averaged data were all within their respective confidence intervals. Thus, we conclude that fitting to the averaged responses

does not yield a value that is significantly different from fitting to individual responses.



## REFERENCES

- Andreucci, D., Bisegna, P., Caruso, G., Hamm, H. E., and DiBenedetto, E. (2003). Mathematical model of the spatio-temporal dynamics of second messengers in visual transduction. *Biophysical Journal*, 85(3):1358–1376. 10.1016/S0006-3495(03)74570-6.
- Asteriti, Sabrina, Gargini, Claudia, and Cangiano, Lorenzo (2017). Connexin 36 expression is required for electrical coupling between mouse rods and cones. *Visual Neuroscience*, 34. 10.1017/S0952523817000037.
- Asteriti, Sabrina, Grillner, Sten, and Cangiano, Lorenzo (2015). A Cambrian origin for vertebrate rods. *eLife*, 4:1–16. 10.7554/eLife.07166.
- Azevedo, Anthony W. and Rieke, Fred (2011). Experimental protocols alter phototransduction: The implications for retinal processing at visual threshold. *Journal of Neuroscience*, 31(10):3670–3682. 10.1523/JNEUROSCI.4750-10.2011.
- Calvert, P. D., Krasnoperova, N. V., Lyubarsky, A. L., Isayama, T., Nicoló, M., Kosaras, B., Wong, G., Gannon, K. S., Margolskee, R. F., Sidman, R. L., Pugh, E. N., Makino, C. L., and Lem, J. (2000). Phototransduction in transgenic mice after targeted deletion of the rod transducin  $\alpha$ -subunit. *Proceedings of the National Academy of Sciences of the United States of America*, 97(25):13913–13918. 10.1073/pnas.250478897.
- Cao, Li Hui, Luo, Dong Gen, and Yau, King Wai (2014). Light responses of primate and other mammalian cones. *Proceedings of the National Academy of Sciences of the United States of America*, 111(7):2752–2757. 10.1073/pnas.1400268111.
- Carpenter, James and Bithell, John (2000). Bootstrap confidence intervals: When, which, what? A practical guide for medical statisticians. *Statistics in Medicine*, 19(9):1141–1164. 10.1002/(SICI)1097-0258(20000515)19:9<1141::AID-SIM479>3.0.CO;2-F.
- Carter Cornwall, M., Matthews, H. R., Crouch, Rosalie K., and Fain, Gordon L. (1995). Bleached pigment activates transduction in salamander cones. *Journal of General Physiology*, 106(3):543–557. 10.1085/jgp.106.3.543.
- Chen, C.-K., Woodruff, M. L., Chen, F. S., Shim, H., Cilluffo, M. C., and Fain, G. L. (2010a). Replacing the rod with the cone transducin  $\alpha$  subunit decreases sensitivity and accelerates response decay. *The Journal of Physiology*, 588(17):3231–3241. 10.1113/jphysiol.2010.191221.
- Chen, C.-K., Woodruff, Michael L., Chen, F. S., Chen, Desheng, and Fain, Gordon L. (2010b). Background Light Produces a Recoverin-Dependent Modulation of Activated-Rhodopsin Lifetime in Mouse Rods. *Journal of Neuroscience*, 30(4):1213–1220. 10.1523/JNEUROSCI.4353-09.2010.

- Chen, Jeannie, Woodruff, Michael L., Wang, Tian, Concepcion, Francis A., Tranchina, Daniel, and Fain, Gordon L. (2010c). Channel Modulation and the Mechanism of Light Adaptation in Mouse Rods. *Journal of Neuroscience*, 30(48):16232–16240. 10.1523/JNEUROSCI.2868-10.2010.
- Cowan, Christopher W., Fariss, Robert N., Sokal, Izabela, Palczewski, Krzysztof, and Wensel, Theodore G. (1998). High expression levels in cones of RGS9, the predominant GTPase accelerating protein of rods. *Proceedings of the National Academy of Sciences of the United States of America*, 95(9):5351–5356. 10.1073/pnas.95.9.5351.
- Dekking, Frederik Michel, Kraaikamp, Cornelis, Lopuhaä, Hendrik Paul, and Meester, Ludolf Erwin (2005). A Modern Introduction to Probability and Statistics. 10.1007/1-84628-168-7.
- Deng, Wen Tao, Sakurai, Keisuke, Kolandaivelu, Saravanan, Kolesnikov, Alexander V., Dinculescu, Astra, Li, Jie, Zhu, Ping, Liu, Xuan, Pang, Jijing, Chiodo, Vince A., Boye, Sanford L., Chang, Bo, Ramamurthy, Visvanathan, Kefalov, Vladimir J., and Hauswirth, William W. (2013). Cone phosphodiesterase-6 $\alpha$  restores rod function and confers distinct physiological properties in the rod phosphodiesterase-6 $\beta$ -deficient rd10 mouse. *Journal of Neuroscience*, 33(29):11745–11753. 10.1523/JNEUROSCI.1536-13.2013.
- Deng, Wen Tao, Sakurai, Keisuke, Liu, Jianwen, Dinculescu, Astra, Li, Jie, Pang, Jijing, Min, Seok Hong, Chiodo, Vince A., Boye, Sanford L., Chang, Bo, Kefalov, Vladimir J., and Hauswirth, William W. (2009). Functional interchangeability of rod and cone transducin  $\alpha$ -subunits. *Proceedings of the National Academy of Sciences of the United States of America*, 106(42):17681–17686. 10.1073/pnas.0901382106.
- Efron, Bradley and Tibshirani, Robert (1991). Statistical data analysis in the computer age. *Science*, 253(5018):390–395. 10.1126/science.253.5018.390.
- Fain, Gordon and Sampath, Alapakkam P. (2018). Rod and cone interactions in the retina [version 1; referees: 4 approved]. *F1000Research*, 7:1–10. 10.12688/f1000research.14412.1.
- Fain, Gordon L., Hardie, Roger, and Laughlin, Simon B. (2010). Phototransduction and the Evolution of Photoreceptors. *Current Biology*, 20(3):R114–R124. 10.1016/j.cub.2009.12.006.
- Field, Greg D. and Rieke, Fred (2002). Nonlinear signal transfer from mouse rods to bipolar cells and implications for visual sensitivity. *Neuron*, 34(5):773–785. 10.1016/S0896-6273(02)00700-6.
- Fu, Yingbin, Kefalov, Vladimir, Luo, Dong Gen, Xue, Tian, and Yau, King Wai (2008). Quantal noise from human red cone pigment. *Nature Neuroscience*, 11(5):565–571. 10.1038/nn.2110.

- Gross, Owen P. and Burns, Marie E. (2010). Control of rhodopsin's active lifetime by arrestin-1 expression in mammalian rods. *Journal of Neuroscience*, 30(9):3450–3457. 10.1523/JNEUROSCI.5391-09.2010.
- Gross, Owen P., Pugh, Edward N., and Burns, Marie E. (2012a). Calcium Feed-back to cGMP Synthesis Strongly Attenuates Single-Photon Responses Driven by Long Rhodopsin Lifetimes. *Neuron*, 76(2):370–382. 10.1016/j.neuron.2012.07.029.
- Gross, Owen P., Pugh, Edward N., and Burns, Marie E. (2012b). Spatiotemporal cGMP dynamics in living mouse rods. *Biophysical Journal*, 102(8):1775–1784. 10.1016/j.bpj.2012.03.035.
- Grundy, David (2015). Principles and standards for reporting animal experiments in The Journal of Physiology and Experimental Physiology. *Experimental Physiology*, 100(7):755–758. 10.1113/EP085299.
- Hamer, R. D., Nicholas, S. C., Tranchina, D., Lamb, T. D., and Jarvinen, J. L.P. (2005). Toward a unified model of vertebrate rod phototransduction. *Visual Neuroscience*, 22(4):417–436. 10.1017/S0952523805224045.
- Hamer, R. D., Nicholas, S. C., Tranchina, D., Liebman, P. A., and Lamb, T. D. (2003). Multiple steps of phosphorylation of activated rhodopsin can account for the reproducibility of vertebrate rod single-photon responses. *Journal of General Physiology*, 122(4):419–444. 10.1085/jgp.200308832.
- Haynes, Lawrence and Yau, King Wai (1985). Cyclic GMP-sensitive conductance in outer segment membrane of catfish cones. *Nature*, 317(6032):61–64. 10.1038/317061a0.
- Ingram, Norianne T., Sampath, Alapakkam P., and Fain, Gordon L. (2016). Why are rods more sensitive than cones? *Journal of Physiology*, 594(19):5415–5426. 10.1113/JP272556.
- Ingram, Norianne T., Sampath, Alapakkam P., and Fain, Gordon L. (2019). Voltage-clamp recordings of light responses from wild-type and mutant mouse cone photoreceptors. *Journal of General Physiology*, 151(11):1287–1299. 10.1085/JGP.201912419.
- Kaylor, Joanna J., Xu, Tongzhou, Ingram, Norianne T., Tsan, Avian, Hakobyan, Hayk, Fain, Gordon L., and Travis, Gabriel H. (2017). Blue light regenerates functional visual pigments in mammals through a retinyl-phospholipid intermediate. *Nature Communications*, 8(1):1–9. 10.1038/s41467-017-00018-4.
- Klaus, Colin, Caruso, Giovanni, Gurevich, Vsevolod V., and DiBenedetto, Emmanuele (2019). Multi-scale, numerical modeling of spatio-temporal signaling in cone phototransduction. *PLoS ONE*, 14(7):1–23. 10.1371/journal.pone.0219848.
- Korenbrod, Juan I. (2012). Speed, adaptation, and stability of the response to light in cone photoreceptors: The functional role of Ca-dependent modulation of ligand sensitivity in cGMP-gated ion channels. *Journal of General Physiology*, 139(1):31–56. 10.1085/jgp.201110654.

- Krispel, Claudia M., Chen, Desheng, Melling, Nathan, Chen, Yu Jiun, Martemyanov, Kirill A., Quillinan, Nidia, Arshavsky, Vadim Y., Wensel, Theodore G., Chen, Ching Kang, and Burns, Marie E. (2006). RGS Expression Rate-Limits Recovery of Rod Photoresponses. *Neuron*, 51(4):409–416. 10.1016/j.neuron.2006.07.010.
- Lamb, Trevor D. (2020). Evolution of the genes mediating phototransduction in rod and cone photoreceptors. *Progress in Retinal and Eye Research*, 76(August 2019):100823. 10.1016/j.preteyeres.2019.100823.
- Majumder, Anurima, Pahlberg, Johan, Muradov, Hakim, Boyd, Kimberly K., Sampath, Alapakkam P., and Artemyev, Nikolai O. (2015). Exchange of cone for rod phosphodiesterase 6 catalytic subunits in rod photoreceptors mimics in part features of light adaptation. *Journal of Neuroscience*, 35(24):9225–9235. 10.1523/JNEUROSCI.3563-14.2015.
- Mao, Wen, Miyagishima, K. J., Yao, Yun, Soreghan, Brian, Sampath, Alapakkam P., and Chen, Jeannie (2013). Functional comparison of rod and cone Gat on the regulation of light sensitivity. *Journal of Biological Chemistry*, 288(8):5257–5267. 10.1074/jbc.M112.430058.
- Mendez, Ana, Burns, Marie E., Sokal, Izabela, Dizhoor, Alexander M., Baehr, Wolfgang, Palczewski, Krzysztof, Baylor, Denis A., and Chen, Jeannie (2001). Role of guanylate cyclase-activating proteins (GCAPs) in setting the flash sensitivity of rod photoreceptors. *Proceedings of the National Academy of Sciences of the United States of America*, 98(17):9948–9953. 10.1073/pnas.171308998.
- Morshedean, Ala and Fain, Gordon L. (2015). Single-photon sensitivity of lamprey rods with cone-like outer segments. *Current Biology*, 25(4):484–487. 10.1016/j.cub.2014.12.031.
- Morshedean, Ala and Fain, Gordon L. (2017). The evolution of rod photoreceptors. *Philosophical Transactions of the Royal Society B: Biological Sciences*, 372(1717). 10.1098/rstb.2016.0074.
- Morshedean, Ala, Kaylor, Joanna J., Ng, Sze Yin, Tsan, Avian, Frederiksen, Rikard, Xu, Tongzhou, Yuan, Lily, Sampath, Alapakkam P., Radu, Roxana A., Fain, Gordon L., and Travis, Gabriel H. (2019). Light-Driven Regeneration of Cone Visual Pigments through a Mechanism Involving RGR Opsin in Müller Glial Cells. *Neuron*, 102(6):1172–1183.e5. 10.1016/j.neuron.2019.04.004.
- Nikonov, Sergei S., Daniele, Lauren L., Zhu, Xuemei, Craft, Cheryl M., Swaroop, Anand, and Pugh, Edward N. (2005). Photoreceptors of *Nrl*<sup>-/-</sup> mice coexpress functional S- and M-cone opsins having distinct inactivation mechanisms. *Journal of General Physiology*, 125(3):287–304. 10.1085/jgp.200409208.
- Nikonov, Sergei S., Kholodenko, Roman, Lem, Janis, and Pugh, Edward N. (2006). Physiological features of the S- and M-cone photoreceptors of wild-type mice from single-cell recordings. *Journal of General Physiology*, 127(4):359–374. 10.1085/jgp.200609490.

- Perry, R. J. and McNaughton, P. A. (1991). Response properties of cones from the retina of the tiger salamander. *The Journal of Physiology*, 433(1):561–587. 10.1113/jphysiol.1991.sp018444.
- Pugh, E. N. and Lamb, T. D. (1993). Amplification and kinetics of the activation steps in phototransduction. *BBA - Bioenergetics*, 1141(2-3):111–149. 10.1016/0005-2728(93)90038-H.
- Pugh, E. N. and Lamb, T. D. (2000). Chapter 5 Phototransduction in vertebrate rods and cones: Molecular mechanisms of amplification, recovery and light adaptation. *Handbook of Biological Physics*, 3(C):183–255. 10.1016/S1383-8121(00)80008-1.
- Qureshi, Bilal M., Behrmann, Elmar, Schöneberg, Johannes, Loerke, Justus, Bürger, Jörg, Mielke, Thorsten, Giesebrecht, Jan, Noé, Frank, Lamb, Trevor D., Hofmann, Klaus Peter, Spahn, Christian M.T., and Heck, Martin (2018). It takes two transducins to activate the cGMP-phosphodiesterase 6 in retinal rods. *Open Biology*, 8(8). 10.1098/rsob.180075.
- Raue, A., Steiert, B., Schelker, M., Kreutz, C., Maiwald, T., Hass, H., Vanlier, J., Tönsing, C., Adlung, L., Engesser, R., Mader, W., Heinemann, T., Hasenauer, J., Schilling, M., Höfer, T., Klipp, E., Theis, F., Klingmüller, U., Schöberl, B., and Timmer, J. (2015). Data2Dynamics: A modeling environment tailored to parameter estimation in dynamical systems. *Bioinformatics*, 31(21):3558–3560. 10.1093/bioinformatics/btv405.
- Raue, Andreas, Kreutz, C., Maiwald, T., Bachmann, J., Schilling, M., Klingmüller, U., and Timmer, J. (2009). Structural and practical identifiability analysis of partially observed dynamical models by exploiting the profile likelihood. *Bioinformatics*, 25(15):1923–1929. 10.1093/bioinformatics/btp358.
- Raue, Andreas, Schilling, Marcel, Bachmann, Julie, Matteson, Andrew, Schelke, Max, Kaschek, Daniel, Hug, Sabine, Kreutz, Clemens, Harms, Brian D., Theis, Fabian J., Klingmüller, Ursula, and Timmer, Jens (2013). Lessons Learned from Quantitative Dynamical Modeling in Systems Biology. *PLoS ONE*, 8(9). 10.1371/journal.pone.0074335.
- Reingruber, Jürgen and Holcman, David (2008). The dynamics of phosphodiesterase activation in rods and cones. *Biophysical Journal*, 94(6):1954–1970. 10.1529/biophysj.107.116202.
- Reingruber, Jürgen and Holcman, David (2009). Diffusion in narrow domains and application to phototransduction. *Physical Review E - Statistical, Nonlinear, and Soft Matter Physics*, 79(3):1–4. 10.1103/PhysRevE.79.030904.
- Reingruber, Jürgen, Pahlberg, Johan, Woodruff, Michael L., Sampath, Alapakkam P., Fain, Gordon L., and Holcman, David (2013). Detection of single photons by toad and mouse rods. *Proceedings of the National Academy of Sciences of the United States of America*, 110(48):19378–19383. 10.1073/pnas.1314030110.

- Rieke, F. and Baylor, D. A. (1996). Molecular origin of continuous dark noise in rod photoreceptors. *Biophysical Journal*, 71(5):2553–2572. 10.1016/S0006-3495(96)79448-1.
- Sakurai, Keisuke, Chen, Jeannie, and Kefalov, Vladimir J. (2011). Role of guanylyl cyclase modulation in mouse cone phototransduction. *Journal of Neuroscience*, 31(22):7991–8000. 10.1523/JNEUROSCI.6650-10.2011.
- Sakurai, Keisuke, Chen, Jeannie, Khani, Shahrokh C., and Kefalov, Vladimir J. (2015). Regulation of mammalian cone phototransduction by recoverin and rhodopsin kinase. *Journal of Biological Chemistry*, 290(14):9239–9250. 10.1074/jbc.M115.639591.
- Sakurai, Keisuke, Onishi, Akishi, Imai, Hiroo, Chisaka, Osamu, Ueda, Yoshiki, Usukura, Jiro, Nakatani, Kei, and Shichida, Yoshinori (2007). Physiological properties of rod photoreceptor cells in green-sensitive cone pigment knock-in mice. *Journal of General Physiology*, 130(1):21–40. 10.1085/jgp.200609729.
- Sampath, A P, Matthews, H R, Cornwall, M C, Bandarchi, J, and Fain, G L (1999a). Light-dependent changes in outer segment free-Ca<sup>2+</sup> concentration in salamander cone photoreceptors. *Journal of General Physiology*, 113(2):267–277. 10.1085/jgp.113.2.267.
- Sampath, A. P., Matthews, H. R., Cornwall, M. C., Bandarchi, J., and Fain, G. L. (1999b). Light-dependent changes in outer segment free-Ca<sup>2+</sup> concentration in salamander cone photoreceptors. *Journal of General Physiology*, 113(2):267–277. 10.1085/jgp.113.2.267.
- Sampath, Alapakkam P., Strissel, Katherine J., Elias, Rajesh, Arshavsky, Vadim Y., McGinnis, James F., Chen, Jeannie, Kawamura, Satoru, Rieke, Fred, and Hurley, James B. (2005). Recoverin improves rod-mediated vision by enhancing signal transmission in the mouse retina. *Neuron*, 46(3):413–420. 10.1016/j.neuron.2005.04.006.
- Schultze, Max (1866). Zur Anatomie und Physiologie der Retina. *Archiv für mikroskopische Anatomie*, 2(1):175–286. 10.1007/BF02962033.
- Shi, Guang, Yau, King Wai, Chen, Jeannie, and Kefalov, Vladimir J. (2007). Signaling properties of a short-wave cone visual pigment and its role in phototransduction. *Journal of Neuroscience*, 27(38):10084–10093. 10.1523/JNEUROSCI.2211-07.2007.
- Takemoto, Norihiko, Tachibanaki, Shuji, and Kawamura, Satoru (2009). High cGMP synthetic activity in carp cones. *Proceedings of the National Academy of Sciences of the United States of America*, 106(28):11788–11793. 10.1073/pnas.0812781106.
- Tsang, Steven H., Woodruff, Michael L., Chen, Ching Kang, Yamashita, Clyde Y., Cilluffo, Marianne C., Rao, Anjali L., Farber, Debora B., and Fain, Gordon L. (2006). GAP-independent termination of photoreceptor light response by excess  $\gamma$  subunit of the cGMP-phosphodiesterase. *Journal of Neuroscience*, 26(17):4472–4480. 10.1523/JNEUROSCI.4775-05.2006.

Wang, Tian, Reingruber, Jürgen, Woodruff, Michael L., Majumder, Anurima, Camarena, Andres, Artemyev, Nikolai O., Fain, Gordon L., and Chen, Jeannie (2018). The PDE6 mutation in the rd10 retinal degeneration mouse model causes protein mislocalization and instability and promotes cell death through increased ion influx. *Journal of Biological Chemistry*, 293(40):15332–15346. 10.1074/jbc.RA118.004459.

Yau, K. W. and Baylor, D. A. (1989). Cyclic GMP-activated conductance of retinal photoreceptor cells. *Annual Review of Neuroscience*, 12:289–327. 10.1146/annurev.ne.12.030189.001445.

Zhang, Xue, Wensel, Theodore G., and Kraft, Timothy W. (2003). GTPase regulators and photoresponses in cones of the eastern chipmunk. *Journal of Neuroscience*, 23(4):1287–1297. 10.1523/jneurosci.23-04-01287.2003.

Zimmerman, A. L. and Baylor, D. A. (1986). Cyclic GMP-sensitive conductance of retinal rods consists of aqueous pores. *Nature*, 321(6065):70–72. 10.1038/321070a0.

## CHAPTER 3

# The molecular basis for continuous noise and its implications on the threshold of photon detection

### 3.1 Abstract

Perception of the visual landscape begins at the absorption of photons by light-sensitive pigment molecules in the retinal rod and cone photoreceptors. Rods can respond to as little as a single photon absorption, and the threshold of detection is set by the intrinsic “dark” noise within the photoreceptor. Here we dissect the contributions of transduction proteins to continuous noise and single-photon detection in mouse rods with genetic perturbations in transduction protein concentrations. We show that transducin ( $G_T$ ) and phosphodiesterase (PDE) have concentration-dependent effects on flash sensitivity and the shape of single-photon response. We also found that reducing PDE concentration by half or more, but not rod  $G_T$ , significantly changed the power of the continuous noise and increased the variability and amplitude of the single-photon response. Interestingly, overexpression of the GTPase accelerating protein (GAP) regulator of G-protein signaling 9-1 (RGS9-1) had no impact on continuous noise but significantly reduced flash sensitivity and single-photon response kinetics. Our work demonstrates that PDE is the critical transduction element in setting the continuous noise level and limits both the variability and detection threshold for single-photon events.



## 3.2 Introduction

Perception of the visual landscape begins at the absorption of photons by light-sensitive pigment molecules in the retinal rod and cone photoreceptors. The incoming photon stream is processed by the phototransduction machinery and leads to closure of cyclic guanosine monophosphate (cGMP)-gated channels and, ultimately, hyperpolarization of the photoreceptor membrane. In darkness, a large number of cyclic-nucleotide gated channels (CNG channels) are in the open state, allowing for cations to enter the outer segment and depolarize the resting membrane potential. The detection of photons arriving at the retina is predicated on the ability for the absorbed photon to exceed a threshold set by fluctuating membrane currents (Barlow, 1957). Decades of observations suggest that detection limits arise from the statistical nature of ion flux through the outer segment.

The first evaluations of the statistical nature of photon absorption at the retina were performed 80 years ago in psychophysical experiments that compared the frequency of observed flashes with expectations from Poisson statistics (Hecht et al., 1942, van der Velden, 1946). From these “frequency of seeing” experiments (see Ch. 1) it was concluded that, from a dark-adapted state, the likelihood of detecting a flash was related to the strength of the flash in a cumulative probability space, and that the threshold for seeing could be as low as a single photon absorbed by a single rod photoreceptor. Discrimination of the signal from a small number of photon absorptions is obscured by photoreceptor current fluctuations; noise events like a ‘dark light’, even in complete darkness (Barlow, 1957). However, the detection and transmission of single-photon events at near-threshold levels is feasible (Baylor et al., 1979) and is apparently dependent on the level of intrinsic noise generated by the phototransduction mechanism (Barlow, 1956, Baylor et al., 1980, Rieke and Baylor, 1998).

Two major types of intrinsic noise exist, termed *discrete* and *continuous*, and may impose limitations on the single-photon response. Due to the rare occurrence and distinctive shape and kinetics which make them indistinguishable from single-photon responses, discrete noise events arise spontaneously from thermally activated rhodopsin (Baylor et al., 1980),

indicated by a 2-fold reduction in discrete events for rods lacking calcium feedback with half the concentration of rhodopsin (*unpublished data*). In contrast, continuous noise is a persistent, low-amplitude fluctuation in membrane current (Yau et al., 1979). Continuous noise is present in all rods and is maximal in darkness and thus may impart limitations to transmission of a single-photon response in an individual rod (Field and Rieke, 2002b). The molecular origin of continuous noise has long been understood to arise from the spontaneous rate of cGMP hydrolysis by PDE (Rieke and Baylor, 1996, Nikonov et al., 2000, Reingruber et al., 2013). Despite decades of investigation, the form of noise that ultimately sets the limit for detection near visual threshold remains unclear. With new genetic murine models, we are able to investigate the origin of these noise sources and their implications for detection threshold.

To investigate the molecular nature of photoreceptor noise we generated mouse models with alterations in the level of intrinsic noise. We used voltage-clamp recordings from single rods in murine models with genetically altered concentrations of either rod  $\alpha$ -transducin ( $T_{\alpha\text{-ROD}}$ ) or PDE, or increased expression of the GAP, RGS9-1. We then analyzed 1) the stimulus-intensity relationship, 2) the flash response kinetics, 3) the continuous noise in darkness (continuous noise), and 4) the biophysics of the single-photon response. We show that  $G_T$  and PDE have concentration-dependent effects on flash sensitivity and the shape of the single-photon response. We also found that reducing PDE concentration by half or more, but not rod the expression level  $G_T$ , significantly changed the power of the continuous noise and increased variability and amplitude of the single-photon response. Interestingly, overexpression of the GAP, RGS9-1, had no impact on continuous noise but significantly reduced flash sensitivity and single-photon response kinetics. Our work demonstrates that PDE is the critical transduction element in setting the continuous noise level and limits both the variability and detection threshold for single-photon events.

### 3.3 Materials and Methods

*Animals.* This study was conducted in accordance with the recommendations of the *Guide*

for the care and use of laboratory animals of the National Institutes of Health, and the Association for Research in Vision and Ophthalmology Statement for the Use of Animals in Ophthalmic and Vision Research. The animal-use protocol was approved by the University of California, Los Angeles, Animal Research Committee (Protocol nos. 14-005 and 96-051). Euthanasia was performed by cervical dislocation.

All animals used in this study were between 2 to 6 months of age, except *PDE6B<sup>rd1/+</sup>* which mice were 6 to 8 weeks of age. Animals used in experiments were from approximately equal numbers of both sexes, and were reared under a 12 h dark-light cycle. Wildtype (C57BL/6J) and *PDE6B<sup>rd1/rd1</sup>* mice were purchased from The Jackson Laboratory (Bar Harbor, ME). C57BL/6J mice were not screened for the absence of the Rd8 mutation (Chang et al., 2002). *PDE6B<sup>rd1/rd1</sup>* mice were bred with C57BL/6J mice to produce mice heterozygous for the Rd1 mutation, i.e., *PDE6B<sup>rd1/+</sup>* mice. Rod transducin knockout (*GNAT1<sup>-/-</sup>*) mice were originally made in the laboratory of Janice Lem at Tufts University in Boston, MA (Calvert et al., 2000), and were obtained locally from the laboratory of Gabriel Travis at the University of California, Los Angeles (Los Angeles, CA). Cone transducin knockout (*GNAT2<sup>-/-</sup>*) mice were generously provided by Marie Burns of the University of California, Davis. Details of this strain were previously described (Ronning et al., 2018). *GNAT2<sup>-/-</sup>* mice were crossed with *GNAT1<sup>-/-</sup>* mice for successive generations to produce mice heterozygous for rod  $\alpha$ -transducin ( $T_{\alpha\text{-ROD}}$ ) on the *GNAT2<sup>-/-</sup>* background, i.e., *Gnat1<sup>+/-</sup>;Gnat2<sup>-/-</sup>*. These mice had were expected to contain between 50 to 80 % of wildtype expression levels of  $T_{\alpha\text{-ROD}}$ . The R9AP95 mouse line was generated and described previously and levels of regulator of G-protein signaling 9-1 (RGS9-1) in retinal extracts were 6-fold higher in the R9AP95 background than in control animals (Chen et al., 2010a). Tux mice, which express a transgenic  $T_{\alpha\text{-ROD}}$  at 6 % of wildtype, were described previously (Yue et al., 2019) and obtained through the laboratory of Jeannie Chen at the University of Southern California (Los Angeles, CA).

*PDE6A<sup>D167A/D167A</sup>* mice were generated previously and were transferred to our laboratory (Morshedien et al., 2022). Briefly, C57BL/6J mouse single-cell embryos, from mice

purchased through Shanghai Laboratory Animal Center (Shanghai, China), were microinjected with sgRNA and Cas9 protein to produce a mutation in the non-catalytic binding site for cyclic guanosine monophosphate (cGMP) in the GAF A domain. The mutation results in a substitution of alanine for aspartate in the residue at position 167 of the  $\alpha$ -subunit of PDE6. Injected embryos were transferred into pseudo-pregnant mice. Animals were transferred to the laboratory of Alapakkam Sampath at the University of California, Los Angeles (Los Angeles, CA) and kept under standard 12 hour dark-light cycle. To distinguish between wildtype and *PDE6A<sup>D167A/D167A</sup>* animals, we used the following primers: 5'-TGGATGCTGGAGGTGTACGTGGTCGCCTCA and 5'-ATAGCAAGGTTGGAGAATTCCGTGAACTGG. We subjected 10  $\mu$ L of the PCR product to 0.5  $\mu$ L of the Tsp45I endonuclease (New England Biolabs, Ipswich, MA) at 65 °C for 1 hour. The wildtype allele yielded bands at 12 and 200 bp (base-pairs), but the disrupted allele generated a 380 bp product.

*Solutions.* Retinal slices were made in HEPES-buffered Ames' medium (Sigma), which contained 2.38 g L<sup>-1</sup> HEPES, and was balanced with 0.875 g L<sup>-1</sup> NaCl to give an osmolarity of 284  $\pm$  1 mOsm at pH 7.35  $\pm$  0.05. Ames-HEPES was kept on ice and continuously bubbled with 100 % O<sub>2</sub>. Bicarbonate buffered Ames' medium (referred to as buffered Ames' medium henceforth) was made from Ames' medium supplemented with 1.9 g L<sup>-1</sup> NaHCO<sub>3</sub> and equilibrated with 95 % O<sub>2</sub>/5 % CO<sub>2</sub> at pH 7.4. Internal solution for recording electrodes contained (in mM): 125 K-aspartate, 10 KCl, 10 HEPES, 5 NMG-HEDTA, 0.5 CaCl<sub>2</sub>, 0.5 MgCl<sub>2</sub>, 1 ATP-Mg, 0.2 GTP-Tris, 2.5 NADPH; pH was adjusted to  $\sim$ 7.3 with NMG-OH and osmolarity was adjusted to  $\sim$ 280 mOsm.

*Dissection and slice preparation.* Mice were dark-adapted for 12 to 20 h prior to the start of the experiment. All experiments began in the morning. Dissections were performed under infrared illumination ( $\lambda \geq 900$  nm) with infrared image converters, which were head mounted (ITT Industries) or scope mounted (B.E. Meyers, Redmond, WA). Following euthanasia, eyes from mice were enucleated, the anterior portion of the eye was cut, and the lens and cornea were removed. Eyecups were stored at 32 °C in buffered Ames' medium in a light-tight container machined from Delrin<sup>®</sup> (DuPont, Wilmington, DE). Under an

infrared-equipped dissection microscope (Carl Zeiss), eyecups were bisected through the optic nerve head with a #10 scalpel, and the retina was carefully removed from the retinal pigmented epithelium (RPE) with fine forceps. The isolated retinal piece was embedded in a low-temperature gelling Agarose (3%; Sigma-Aldrich) in HEPES-buffered Ames' medium. Cross-sectional retinal slices (200  $\mu\text{m}$  in thickness) were cut in chilled, oxygenated Ames-HEPES with a vibratome (VT-1000S; Leica) and transferred either to a recording chamber, or to the storage container, for use later in the experiment. During recordings, the retinal slice was stabilized with a custom-made, laser-cut, stainless steel (420 grade; polished) anchor, which was adhered to the recording chamber with a small amount of petroleum jelly (Vaseline<sup>®</sup>). The slice was superfused with buffered Ames' medium at  $\sim 4 \text{ mL min}^{-1}$ . The bath temperature was held at  $36 \pm 1^\circ \text{C}$  by a temperature controller with feedback (TC-324B; Warner Instruments, Holliston, MA).

*Immunoblotting.* Retinas from C57BL/6J and *PDE6A*<sup>D167A/D167A</sup> mice were homogenized in 1x phosphate-buffered solution (PBS) with Halt protease inhibitor mixture (Life Technologies, Carlsbad, CA). Protein samples were treated with benzonase nuclease (Sigma-Aldrich) at room temperature for 1 h and then rehomogenized with 1% sodium dodecyl sulfate (SDS) in PBS. Cellular debris was removed by centrifugation (20,000 g, 2 min, 4°C), and the protein concentration was determined with the Micro BCA Protein Assay Kit (Thermo Fisher Scientific). We then ran 5–20  $\mu\text{g}$  of total protein from C57BL/6J or *PDE6A*<sup>D167A/D167A</sup> retinas on 4–12% or 12% SDS/PAGE gels (Novex, Thermo Fisher; Invitrogen, Thermo Fisher). Membranes were blocked with Odyssey Blocking Buffer (LI-COR Biosciences, Lincoln, NE) followed by incubation at room temperature, and they were then probed with primary antibodies at a final dilution of  $1 \mu\text{g mL}^{-1}$ . Antibodies were as follows: PDE6A (PA1-770, Thermo Fisher), PDE6B (PA1-772, Thermo Fisher), PDE6G (PA1-773, Thermo Fisher), Ros-GC1 (sc-376217, Santa Cruz Biotechnology, Dallas, TX),  $\alpha$ -transducin ( $\alpha_T$ ) (sc-136143, Santa Cruz Biotechnology), guanylate cyclase E (sc-136313, Santa Cruz Biotechnology), GCAP2 (sc-166056, Santa Cruz Biotechnology), transducin beta subunit (NB120-3433, Novus Biologicals, Centennial, CO), Recoverin (ab31928, Abcam, Cambridge, UK),

and  $\alpha$ -tubulin (T9026, Sigma-Aldrich). Western blot analysis was performed with cognate IR dye-labeled secondary antibodies at a dilution of 1:15,000 and detected with an Odyssey CLx Infrared Imaging System (LI-COR).

*Biochemical assays of PDE activity.* For each C57BL/6J and  $PDE6A^{D167A/D167A}$  mice, four mouse retinas were homogenized by sonication (two 5 s pulses) in 220  $\mu$ L of 20 mM Tris-HCl buffer (pH 7.5) containing 120 mM NaCl, 1 mM MgSO<sub>4</sub>, and 1 mM mercaptoethanol. After brief centrifugation (20,000 g, 2 min, 4 °C) to remove cell debris, retinal homogenates (typically, 5–6 mg mL<sup>-1</sup>) were used to measure basal PDE6 activities with final dilutions of 1:140 for WT retinas, and 1:24 for  $PDE6A^{D167A/D167A}$  retinas. Maximal (trypsin-activated) PDE6 activities were measured from retinal homogenates treated with trypsin (100 mg mL<sup>-1</sup>) for 10 min at 25 °C. Trypsin treatment was terminated by the addition of 10X soybean trypsin inhibitor (SBTI, Sigma) and incubation for 5 min at 25 °C, followed by centrifugation at 20,000 g for 3 min at 4 °C. The final dilutions of trypsin-treated retinal homogenates in the assays of maximal PDE6 activity were 1:4000 for WT retinas and 1:400 for  $PDE6A^{D167A/D167A}$  retinas. PDE6 assays were carried out in 40  $\mu$ L of 20 mM Tris-HCl, pH 7.5 buffer containing 120 mM NaCl, 2 mM MgSO<sub>4</sub>, 1 mM 2-mercaptoethanol, 0.1 units of bacterial alkaline phosphatase, and 10  $\mu$ M [<sup>3</sup>H] cGMP (100,000 counts/min) for 10-15 min at 25 °C. The reaction was terminated by the addition of AG1-X2 cation exchange resin (0.5 mL of 20 % bed volume suspension, Bio-Rad, Hercules, CA). Samples were incubated for 6 min at 25 °C with occasional mixing and spun at 10,000 g for 3 min. Then 0.25 mL of the supernatant was removed for counting in a scintillation counter.

*Physiological recordings from rod photoreceptors.* Recordings from individual cells were made by whole-cell patch-clamp from dark adapted retinal slices as described previously (Arman and Sampath, 2010). Rods were visualized at 60x magnification with an infrared light-emitting diode (LED) source ( $\lambda = 940$  nm; Cairn Research) attached to the transmitted light path of the physiology microscope (Eclipse FN1; Nikon). Rod somata were identified by morphology and location in the outer nuclear layer (ONL).

Filamented borosilicate-glass capillaries (BF120-69-10; Sutter Instruments, Novato, CA)

were pulled on the day of the experiment with a P-97 Flaming/Brown micropipette puller (Sutter Instruments) to a tip resistance in the bath medium of 15 to 19 M $\Omega$  for rods and 13 to 16 M $\Omega$  for rod bipolar cells (RBCs). Rod photoreceptors were voltage-clamped at  $-40$  mV with an Axopatch 200B patch-clamp amplifier (Molecular Devices). Series resistance of the recording pipette was compensated at 75 to 80 % to prevent error in clamping potentials, and pipette capacitance was neutralized prior to “break-in” (Sherman et al., 1999, Sigworth, 1995). The patch seal was assessed after “break-in”, and recordings were terminated if the seal resistance was below  $\sim 1$  G $\Omega$  or the access resistance exceeded  $\sim 200$  M $\Omega$ . All reported potentials have been corrected for liquid junction potentials (Neher, 1992), which were estimated previously to be  $\sim 10$  mV for our recording solutions (Ingram et al., 2019).

Recordings were low-pass filtered at 5 kHz by the patch-clamp amplifier and digitized at 10 kHz with a 16-bit A/D converter (ITC18/USB18; HEKA Elektronik). The sampling rate was high enough to ensure negligible variability between stimulus and acquisition clock-synchronization from experiment to experiment. Further zero-phase shift digital filtering was performed offline with a 7th order Butterworth filter and the FilterM C-Mex package (Simon, 2011). Typical filtering bandwidths were 0 to 30 Hz, and any deviations from this value for specific experiments are listed in the corresponding text of the figure legends and results section. Data were collected in MATLAB (R2018b; The Math Works, Natick Massachusetts, USA) with the open-source software package, Symphony Data Acquisition System (<https://symphony-das.github.io>). All offline data visualization and analysis was performed with custom scripts and the Iris DVA framework (open-source; <https://github.com/sampath-lab-ucla/IrisDVA>; see also Appendix A) for MATLAB (R2021a-2022a).

*Light stimulation.* Stimuli were delivered with a dual OptoLED light stimulation system (Cairn Research, Faversham, UK) through a custom-built optical pathway that feeds into the transmitted light path of the physiology microscope. The stimulus LED had a peak wavelength of  $505 \pm 5$  nm. Light sources were attenuated by absorptive neutral-density filters (Thorlabs). At the beginning of each experiment, the microscope field-stop aperture was focused at the level of the slice to provide uniform illumination and was reduced to limit

the stimulation region to a spot  $\sim 200 \mu\text{m}$  in diameter.

The intensities of the LEDs were measured with a calibrated photodiode (Graseby Optonics) through a photodiode amplifier (PDA200C; Thorlabs). Light intensities were calibrated as effective photons ( $\lambda\text{s}$ ) per squared micrometer ( $\gamma \mu\text{m}^{-2}$ ) and adjusted for the absorption spectrum of rhodopsin (Govardovskii et al., 2000, Nymark et al., 2012). Stimulus intensities were then converted to light-activated rhodopsin ( $R^*$ ) by accounting for the effective collecting area of a rod outer segment.

We estimated the effective collecting area of individual rods from the trial-to-trial variability in the responses to a fixed-stimulus. Under the assumption that photon absorption obeys Poisson statistics, the mean number of photoisomerizations produced by the flash can be estimated by dividing the squared mean response by its variance:  $\bar{\eta} = \bar{I}^2 / \sigma_I^2$ , where  $\bar{I}$  is the average response and  $\sigma_I^2$  is the variance produced by the flash (Field and Rieke, 2002b). We calculated  $\bar{\eta}$  from 4 to 6 flash intensities for 15 rods, and the collecting area was determined as the slope of the line relating  $\bar{\eta}$  to the flash intensity. The average and 95% bias-corrected and *accelerated* ( $BC_a$ ) confidence interval (see *Statistics*) of the collecting area was estimated to be  $0.26$  ( $0.14, 0.35$ )  $\mu\text{m}^2$  (*data not shown here, see Ch. 4*). Method #2 is described below under *single-photon response properties*, and results may be found in Table 3.2.

*Stimulus intensity - response relationships.* To calculate the normalized amplitude for the photoresponse to a given stimulus intensity, we correlated each response with a template generated from the average response across all flash intensities. We then took the amplitude relative to a baseline measured in the 200 ms prior to flash delivery (Sampath and Rieke, 2004). The amplitudes were scaled by the maximal response to the brightest flashes. This template-scaling procedure produced more consistent estimates of the more variable dim flash responses compared to measuring peak current deflections. Response amplitudes were then related to flash intensities,  $\Phi$ , with a Hill equation,

$$\frac{R}{R_{Max}} = \frac{1}{1 + \left(\frac{I_{1/2}}{\Phi}\right)^n} \quad (3.1)$$

where  $I_{1/2}$  is the value of the stimulus intensity producing a half-maximal response, and  $n$



is the Hill coefficient.

*Continuous noise.* Continuous noise was isolated from the current fluctuations of rod photoreceptors in darkness in a manner similar to previous descriptions (Baylor et al., 1980, Rieke and Baylor, 1996, Reingruber et al., 2013). The methods described here differ slightly because of the observed variability of dark currents (see Table 3.1). To isolate the continuous noise, we acquired whole-cell voltage-clamp recordings ( $V_m = -40$  mV) of 11 to 21 s in darkness and in the presence of a saturating light. Linear trends were removed from the current traces. To allow for single-sideband power spectral density (PSD) estimation, the analytic signal was computed by Hilbert transformation (Kak, 1970). Because instrumental and continuous noise sources are independent, we computed PSD spectra for each current traces in light and in darkness, and subtracted the spectrum in light from the dark-spectrum to obtain an estimate for the continuous noise (see Fig. 3.6).

To account for the variations in total dark current ( $R_{\max}$ ) between cells and across genotypes (see  $R_{\max}$  of Table 3.2), we performed a variance stabilizing transform. Because current traces in the dark and in the light represent signals comprised of independent noise sources with variances that are apparently unequal (see **A** of Figs. 3.6, 3.7, and 3.8) and scale proportionally to the total outer-segment conductance (Baylor et al., 1980), we scaled the total variance by the sum of the weighted variances of the current fluctuations as calculated by the Welch-Satterthwaite approximation (Welch, 1938, Satterthwaite, 1946, Satterthwaite, 1941). The variances,  $s_i^2$ ,  $i = \{\text{dark, light}\}$ , for the current traces of lengths,  $n_i$ , were weighted and linearly combined such that  $s_{cont.}^2 = \sum_i k_i s_i^2$ , where  $k_i = 1/n_i \sum_i 1/n_i$ . This variance stabilizing transform of the total variance resulted in robust PSD estimates across cells that exhibited broad ranges of  $R_{\max}$ .

PSD estimates were calculated for traces in both the light and dark by Welch’s method (Welch, 1967). Current traces were segmented into  $K$  blocks of length  $L$  with overlap allowed and modulated by a windowing function  $W(j)$ , for  $j = [1, \dots, L]$ , to form the sequences  $[X_1(j)W(j), \dots, X_K(j)W(j)]$ . The finite Fourier transforms were taken as  $A_k(n) = 1/L \sum_j^L X_K(j)W(j) \exp(-2kijn/L)$ , and the  $K$  modified periodograms were ob-

tained from  $I_k(f_n) = L/U|A - k(n)|^2$  for  $n = [0, \dots, L/2]$ , i.e., the Nyquist limit, and  $f_n = n/L$ .  $U$  is the scaling factor to account for the energy of the windowing function and is defined as,  $U = 1/L \sum_j W^2(j)$ . Welch's estimate of the spectral density is the average of the modified periodograms across the  $K$  segments:

$$\hat{P}(f_n) = \frac{L}{UK} \sum_{k=1}^K |A - k(n)|^2. \quad (3.2)$$

Here we used a segment length corresponding to 4.2 s with 99.9% overlap. We implemented a Blackman periodic windowing function, defined as  $W(j) = (1 - \alpha)/2 - \cos(2\pi j/L)/2 + \alpha \cos(4\pi j/L)/2$  with  $\alpha = 0.16$  over the interval,  $0 \leq j \leq M$ , and  $W(j) = 0$  otherwise (Oppenheim, 1999). Segments were symmetrically padded with zeros to the next-power-of-two from twice the segment length.

To estimate the bandwidth average power, i.e., total variance per bandwidth, integrals of the continuous noise traces were approximated for each cell by taking Riemann sums of trapezoids with respect to the frequency bandwidth. Integration estimates from each genotype were averaged, and statistics were performed as described below in *Statistics*.

*Single-photon response properties.* To estimate the amplitude of unitary responses, we collected voltage-clamped responses of rods to 15 to 60 flashes of a fixed intensity, and we derived the single-photon response from the trial-to-trial variability in the responses as has been described previously (Baylor et al., 1979). Briefly, the mean number of unitary events produced by the flash ( $m$ ) with amplitude  $a$  can be estimated from the ensemble mean ( $\mu$ ) such that,  $\mu = am$ . Under the assumption that photon absorption obeys Poisson statistics, the mean number of unitary events is related to the variance of the unitary responses and the squared amplitude, i.e.,  $m = \sigma^2/a^2$ . Thus, we squared and scaled the ensemble mean of the dim-flash responses so that the rising phase coincided with the ensemble variance, i.e.,  $\sigma^2 = \mu^2/m$ . From this, we derived an estimate of  $m$  that we used to calculate individual response contributions to  $a$ . From the calibrated light intensity and the mean number of unitary events, we estimated each rod's effective collecting area with the relation,  $A_c = m/\Phi$ , where  $\Phi$  is the stimulus intensity in photons per square micron ( $\gamma \mu\text{m}^{-2}$ ). Although from an indirect metric, the values we generated for effective collecting areas of C57BL/6J rods

using this method were in agreement with our more elaborate method described in the *Light stimulation* of Ch. 4.

Single-photon response traces are shown as the averaged response with  $BC_a$  95% confidence regions across as many cells as indicated for the genotype (see Table 3.2). Confidence regions for single-photon response traces were calculated by resampling the time-locked single-photon responses across all cells of a given genotype. Individual traces were synchronized by the start of the stimulus presentation. Given the high sampling frequency (10,000 Hz) this clock-synchronization is unlikely to introduce any artifacts and should produce the best estimates for kinetic analysis.

We further separated single-photon responses from failures and multi-photon responses by fitting amplitude histograms with a Gaussian mixture model with an Expectation-Maximization (EM) algorithm. First we identified suspect “misses” and “hits” from the correlation between individual responses and the normalized average response over a window which included the rising phase and peak of the response but not the recovery phase (Field and Rieke, 2002a, Okawa et al., 2010). We fit a single Gaussian to the amplitudes of the suspect “misses” and naively fit a Gaussian mixture model to the “hits” amplitudes with initial parameter estimates of 2 to 3 Gaussian models. From these estimates, we seeded the EM algorithm with the best 3 to 4 Gaussian parameter estimates, and iteratively fit the mixture model to the data. Posterior probabilities were calculated from the amplitudes as probability of their membership to each Gaussian component in the mixture model. Estimates of the single-photon response amplitude with this method corresponded well with averaged unitary amplitude estimates outlined above (see also Figs. 3.9 and 3.10).

The signal-to-noise ratio (SNR) for rods was defined as the distance between the two Gaussian probability distributions that describe the noise,  $D \sim \mathcal{N}(\bar{D}, \sigma_D^2)$ , and single-photon responses,  $A \sim \mathcal{N}(\bar{A}, \sigma_A^2)$ . Under the assumption that the noise and single-photon response variances are independent and additive, the SNR is defined as the difference between the means, scaled by their total variance, i.e.  $SNR = (\bar{A} - \bar{D})(2\sigma_D^2 + \sigma_A^2)^{-1/2}$  (Dunn, 2006, Okawa et al., 2010).

*Response kinetics.* Kinetic parameters were obtained identically for averaged response families and single-photon responses as follows. The time to response peak ( $T_{peak}$ ) was measured as the duration from the start of the flash to the peak response. The single-exponential time constant of recovery ( $\tau_{REC}$ ) was estimated by nonlinear least squares fit to a single-exponential decay function of the form,

$$f(t) = R_{offset} + (R_{0.5} - R_{offset}) \exp\left(-\frac{t}{\tau_{REC}}\right) + \epsilon, \quad (3.3)$$

where  $R_{0.5}$  is the response at 50% recovery,  $R_{offset}$  represents the plateau region of the response, and  $\epsilon$  represents residual error. This form was used to accommodate undershoot regions in the responses, particularly for R9AP95 mice, which otherwise exhibited poor fits. The time to flash onset ( $T_{onset}$ ) was measured as the duration from the start of the flash to the response onset threshold, which was set to 5% of the flash response peak transient.

*Statistics.* All uncertainties were calculated by Monte Carlo simulations (bootstrap) with 10,000, replicates except for time-series data which instead used 2000 simulations in the interest of reducing computation time. Uncertainty is generally expressed as 95% confidence intervals, with two exceptions: the results of phosphodiesterase (PDE) biochemical assays are presented as mean and standard error, and the maximal response amplitude ( $R_{max}$ ) values in Table 3.1 are given as the median and range of recorded maximal response amplitudes. To increase accuracy and mitigate errors that arise from the nonparametric situation, confidence intervals were estimated by the BC<sub>a</sub> method (Efron, 1987, DiCiccio and Efron, 1996).

In cases where fitting procedures were used, e.g., stimulus-response relations, fits were performed with a logistic-weighted robust, iterative, nonlinear least squares approach (Statistics and Machine Learning Toolbox; The Math Works, Natick Massachusetts, USA). Confidence regions are presented as percentile 95% confidence intervals from 10,000 bootstrapped fitting procedures and displayed as a shaded region surrounding the fitted traces.

Statistical comparisons across genotypes for fit parameter estimates, kinetics, and average bandwidth power estimates were made by first calculating a one-way ANOVA with a custom bootstrap approach for unbalanced design. This custom algorithm is equivalent to the standard linear mixed-effects model, except that bootstrap replicates are calculated

from the residuals as the fixed-effects estimator. *Post hoc* analysis proceeded if ANOVA results indicated a significant genotype effect, i.e.,  $p < 0.05$ . Pairwise testing was performed on all pairs with a custom bootstrap algorithm of Welch’s T-test for unequal variances. To account for multiple testing errors, all p-values, except those in PDE activity assays, were adjusted for false discovery rate (Benjamini and Hochberg, 1995). Confidence regions for reported effects sizes are presented as mean difference (95 %  $BC_a$  confidence interval), unless otherwise noted. Statistical analysis for PDE activity assays were performed with Student’s T-test for significant difference of the means.

### 3.4 Results

Photoactivation of rhodopsin in rod photoreceptors results in the closure of outer segment cyclic-nucleotide gated channels (CNG channels) through stimulation of cGMP hydrolysis over multiple amplification steps in the phototransduction cascade. Light activation of rhodopsin leads to many light activated  $\alpha$ -transducins ( $G\alpha_T^*$ s), which dissociate from the heterotrimeric G-protein complex and activate PDE ( $P^*$ ) by disabling the inhibitory  $\gamma$ -subunits. Light activated PDE6 ( $P^*$ ) is then able to hydrolyze cGMP, a key substrate used to increase the probability of opening of CNG channels in darkness. To determine the contributions of the transduction proteins transducin ( $G_T$ ) and PDE on the threshold of detection, we analyzed light response properties, continuous noise, and derived single-photon responses from rods of mice with moderate and extreme reductions of  $G_T$  or PDE, or with overexpression of GTPase accelerating proteins (GAPs).

#### 3.4.1 Biophysical properties of the flash response

We characterized flash response properties and kinetics in C57BL/6J mice by whole-cell voltage-clamp from individual rod photoreceptors in retinal slices (Fig. 3.1). We recorded current responses to increasing intensity flashes, 5 to 10 ms in duration, which produced 0.59 to 290  $R^*$ . Responses increased proportionally with the stimulus intensity and reached a

maximum amplitude (a median and range of 23.5 (16.4, 32.5) pA), which we used to normalize the responses shown in Fig. 3.1 A. For comparison, data from Fig. 3.1 are also shown in Figs. 3.2, 3.4, and 3.5.

To characterize the intensity dependency of the rod response, we fit averaged, normalized response amplitudes from 10 cells to a Hill equation with 2 free parameters using Eqn. 3.1 (Fig. 3.1 B). The Hill equation owes its usefulness to the Hill coefficient, a representation of available active sites per unit stimulation. In the case of rod photoreceptors, specifically rhodopsin, this allows the assumption that a single photon activates a single rhodopsin, and the deviation from  $n = 1$  indicates the variability, from cell to cell, of the efficiency with which this absorption is converted into a recorded response. We chose the Hill form of the equation for rod photoresponses, rather than the Michaelis-Menten form, to test the effects of genotype on the relationship between photon absorption and cGMP activated currents. From these fits, the stimulus intensity producing a half-maximal response ( $I_{1/2}$ ) was determined to be 15.0 (11.2, 17.9)  $R^*$ , closely matching previous reports (Ingram et al., 2019); and we calculated an  $n$  of 1.12 (0.926, 1.43).

Rod CNG channels respond to changes in cGMP concentration rapidly, within a few milliseconds (Cobbs and Pugh, 1987); thus the resulting waveform from a brief flash is a reflection of rhodopsin lifetime, the coincidence between activated  $\alpha_T$  and PDE, and the turnover rate of cGMP (Pugh and Lamb, 1993, Rieke and Baylor, 1996, Lyubarsky et al., 1996, Gross et al., 2012). To understand how transduction proteins contribute to the kinetics of the photoresponse, we calculated the time to response peak (Fig. 3.1 C), single-exponential time constant of recovery (Fig. 3.1 D), and time to flash onset (Fig. 3.1 E). In C57BL/6J rods, there was a clear dependence on flash intensity for each of the kinetic parameters we characterized, which generally followed a monotonic trend. Over the flash intensity range from 0.60 to 290  $R^*$ , the time to peak latency shortened from 208 (179, 238) ms to 58.3 (50.2, 66.3) ms, and the response onset latency decreased from 30.3 (9.8, 61.3) ms to 8.05 (6.22, 10.2) ms.  $\tau_{\text{REC}}$ , as a function of logarithmically increasing stimulus intensity, increased in a qualitatively linear fashion from 83.6 (61.5, 106) ms to 289 (280, 293) ms, which is in line with

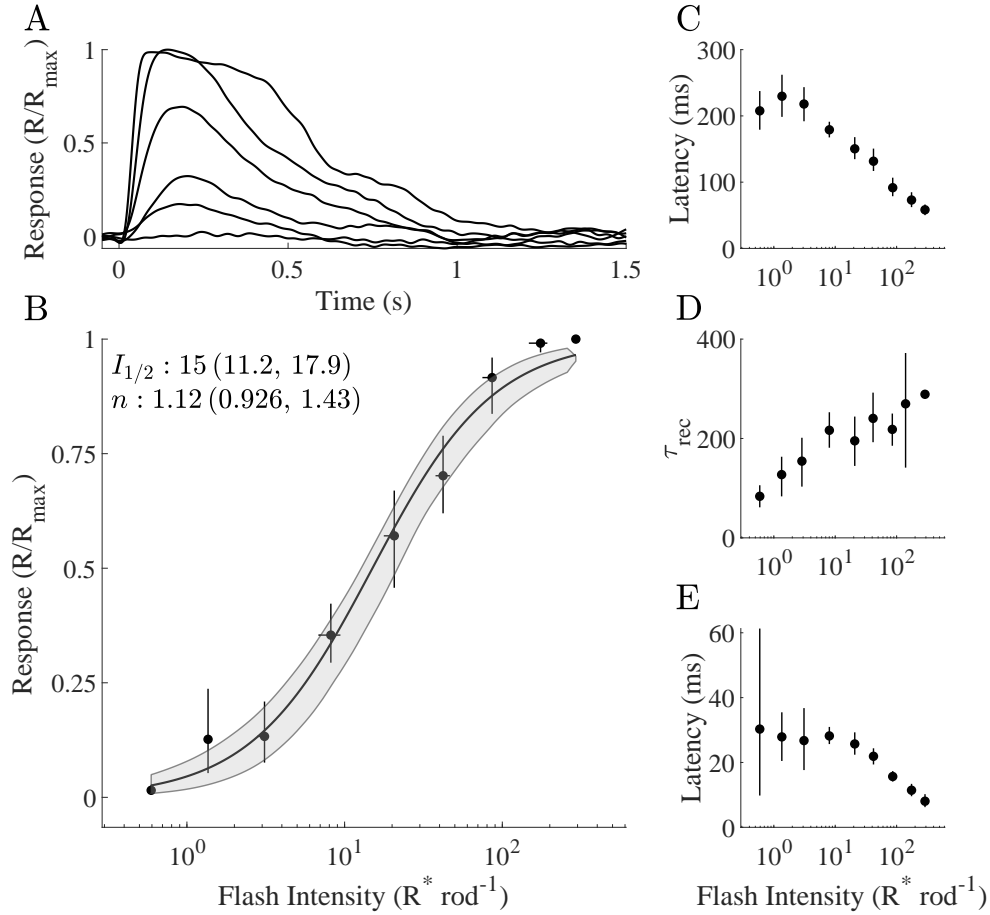


Figure 3.1: *Physiological responses of C57BL/6J rods.* **A.** Light-evoked responses scaled by  $R_{\max}$  in dark-adapted rods. Responses were produced from brief flashes delivered at 0s, which yielded 1.9 to 170  $R^*$ . **B.** Averaged Response-Intensity relationship ( $n = 10$ ) fit (dark trace, 95% CI shaded region) with a modified Hill equation (see § 3.3) to determine the stimulus intensity producing a half-maximal response ( $I_{1/2}$ ) and Hill coefficient ( $n$ ) (also see Table 3.1). **C-E.** Response kinetics. **C.** Averaged time-to-peak latency as a function of flash intensity measured from the stimulus start to the peak of the response. **D.** The single-exponential time constant of recovery from the fit to a single exponential decay function (Eqn. 3.3) along the tail region following 50% recovery from the peak of the mean response. **E.** Latency to response onset measured from the start of the stimulus to 5% of the peak. *Data are presented as means with vertical lines indicating  $BC_a$  95%  $BC_a$  confidence intervals.*

previous reports (Chen et al., 2010a, Ingram et al., 2019). We used the values determined here as a reference for observations in our other murine models; see Table 3.1 for a summary.

### 3.4.2 Transducin activity increases flash sensitivity

To investigate the role of  $G_T$  concentration and deactivation rate in setting the sensitivity of the flash response, we recorded flash response families in rods of *Gnat1<sup>+/-</sup>;Gnat2<sup>-/-</sup>*, Tux and R9AP95 mice (Fig. 3.2A). Flash responses from rods in the mice with  $G_T$  expression at  $\sim 50\%$  (*Gnat1<sup>+/-</sup>;Gnat2<sup>-/-</sup>*) and  $\sim 10\%$  (Tux) were characteristically similar to those of C57BL/6J responses with a sharp activation phase and bimodal recovery phase (Fig. 3.2A) consisting of a rapid and a slow feature prominent at brighter flash intensities. However, in rods with both moderate and severe reduction of  $G_T$ , the time course of the response was shorter in a manner apparently dependent on the concentration of  $G_T$ . R9AP95 mice, which have a six-fold increase in GAPs, exhibited a distinctly truncated recovery phase, which presented as a rapid recovery followed by a slight undershoot at moderate and bright flash intensities, which parallels previously reported suction-electrode recordings (Chen et al., 2010a). Flash intensities below 25 to 50% of  $R_{\max}$  were similar across these genotypes, but at brighter intensities even the severe reduction of  $G_T$  in Tux rods maintained a bimodal recovery waveform. Only when the deactivation of  $G\alpha_T^*$  is accelerated by overexpression of RGS9-1 does the slower component of the recovery phase disappear.

Flash families recorded from rods were normalized by scaling with the maximal response peak ( $R_{\max}$ ), aggregated, and the response peaks were related to flash intensity with Eqn. 3.1. From the fit procedures, we calculated  $I_{1/2}$  for *Gnat1<sup>+/-</sup>;Gnat2<sup>-/-</sup>* (22.0 (15.8, 25.5)  $R^*$ ), Tux (32.3 (24.7, 35.7)  $R^*$ ) and R9AP95 (32.5 (24.7, 35.7)  $R^*$ ) rods. While flash sensitivity decreased for *Gnat1<sup>+/-</sup>;Gnat2<sup>-/-</sup>* ( $\Delta I_{1/2} = 7.02$  (-1.28, 15.6)  $R^*$ ), the difference was not statistically significant ( $p = 0.151$ ). An increased sample size may have brought the observed difference into statistical significance. However, the *Gnat1<sup>+/-</sup>;Gnat2<sup>-/-</sup>* flash sensitivity fell in between that for C57BL/6J and Tux mice, which demonstrates the dependence of flash sensitivity on the amount of available  $G_T$ . In Tux mice, the large reduction of  $G_T$  led to



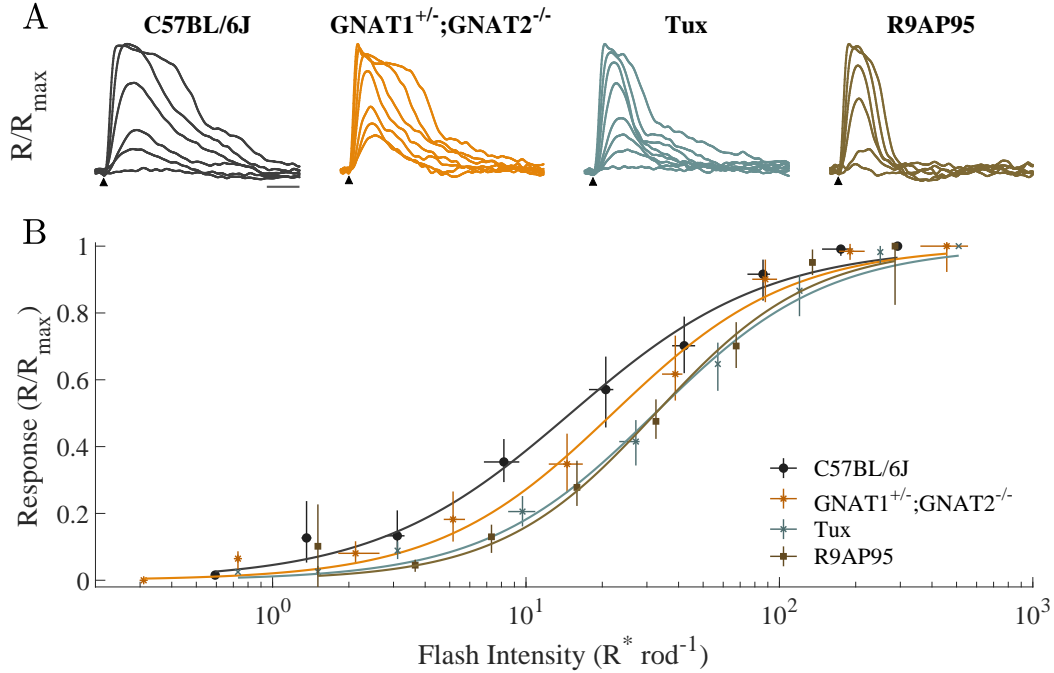


Figure 3.2: *Transducin modulates flash sensitivity.* **A.** Representative voltage-clamp response families for C57BL/6J, *Gnat1*<sup>+/-</sup>;*Gnat2*<sup>-/-</sup>, Tux, and GAP overexpression (R9AP95) mice. Arrowheads indicate time of flash presentation. Intensities for shown responses are as follows: C57BL/6J, (1.9, 9.2, 20, 41, 85 and 170) R<sup>\*</sup>; *Gnat1*<sup>+/-</sup>;*Gnat2*<sup>-/-</sup>, (4.6, 9.2, 20, 41, 85, 170 and 360) R<sup>\*</sup>; Tux, (1.5, 3.1, 6.6, 13, 28, 57, 120 and 250) R<sup>\*</sup>; R9AP95, (9.2, 20, 41, 85, 170 and 360) R<sup>\*</sup>. *Scale bar is 200 ms.* **B.** Response-intensity relations. Sensitivity was assessed by the  $I_{1/2}$  parameter from fits to a modified Hill equation (smooth traces). Heavily reduced expression of T $\alpha$ -ROD in Tux mice ( $\sim 10\%$  of wildtype) and overexpression of RGS9-1 in R9AP95 mice corresponded with a significant desensitization (increased  $I_{1/2}$ ) of the flash response ( $p = 0.0008$  ANOVA; Tux 32.3 (25.5, 35.5) R<sup>\*</sup>,  $\Delta I_{1/2} = 17.3$  (7.52, 28.3) R<sup>\*</sup>,  $p = 0.0321$ ; R9AP95 32.5 (24.7, 35.7) R<sup>\*</sup>,  $\Delta I_{1/2} = 17.5$  (11.0, 23.8) R<sup>\*</sup>,  $p = 0.003$ ). No appreciable difference between  $n$  parameters was detected by ANOVA ( $p = 0.1158$ ).

a significant reduction in the flash sensitivity ( $\Delta I_{1/2} = 17.3 (7.52, 28.3) R^*$ ,  $p = 0.0321$ ). Interestingly, this reduction matched that due to high RGS9-1 levels in R9AP95 rods ( $\Delta I_{1/2} = 17.5 (11, 23.8) R^*$ ,  $p = 0.003$ ), which are expected to have a normal expression of  $G_T$  (Chen et al., 2010a). These results show that decreases in  $G_T$  concentration are proportionally related to the flash sensitivity of rod photoreceptors, and that flash sensitivity is dependent upon the lifetime of  $G\alpha_T^*$ .

### 3.4.3 Reduced PDE6 activity increases flash sensitivity

Mice with heterozygous mutations in *Pde6b* (*PDE6B<sup>rd1/+</sup>* mice) undergo slow degeneration compared to homozygotes (Bowes et al., 1990) and produce half the protein levels of PDE6B, normal levels of PDE6A, and a specific activity for cGMP at half of wildtype levels (Cunnick and Takemoto, 1992). Our laboratory previously created a mouse line without a key aspartate in the GAF A domain of PDE6A, *PDE6A<sup>D167A/D167A</sup>*, which led to slow degeneration ( $\sim 50\%$  of rods were present at 6 months) and the elimination of nearly all PDE6A (Morshedien et al., 2022). To better estimate the levels of PDE subunits and their effects on enzymatic activity, western blots and PDE activity assays were done on retinal homogenates of *PDE6A<sup>D167A/D167A</sup>* mice. In Fig. 3.3, I show average optical densities over multiple protein concentrations (averaged into each data point), normalized by the optical density of the band for tubulin (Fig. 3.3 A). While PDE6A (*left*) and PDE6B (*middle*) levels were significantly reduced, PDE6G (*right*) levels were no different than that of wildtype.

In Fig. 3.3 I compare basal PDE activity (Fig. 3.3 B *left*) and trypsin-activated activity (Fig. 3.3 B *right*) measured from C57BL/6J and *PDE6A<sup>D167A/D167A</sup>* retinas (Morshedien et al., 2022). To estimate the maximal value of the enzymatic activity of PDE on cGMP, PDE6G subunits were cleaved by treatment with trypsin, which exposed catalytic sites for cGMP constitutively (Baehr et al., 1979). These measurements show that basal and total PDE activity are reduced by factors of 9 and 14, respectively, in *PDE6A<sup>D167A/D167A</sup>* photoreceptors. The reduction in rod activity is likely to be somewhat greater, because cone activity is expected to contribute 1 to 2% of total activity in both C57BL/6J and

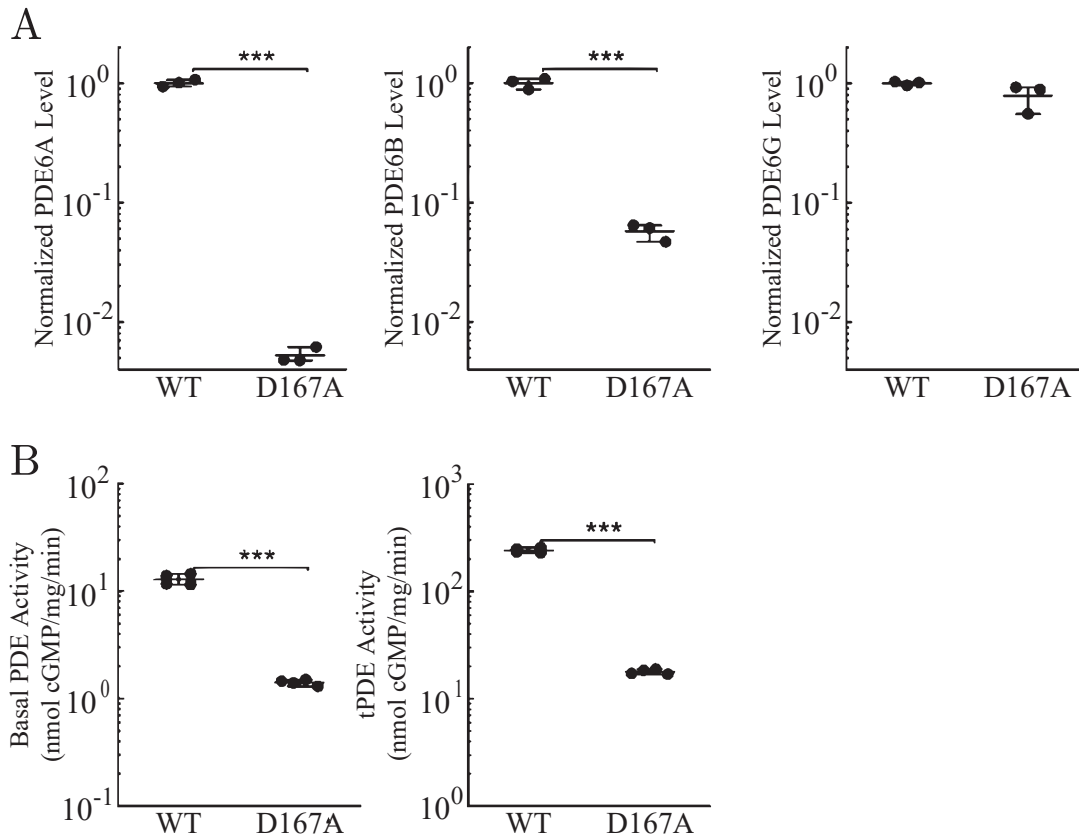


Figure 3.3: *PDE6* concentration and activity is reduced in the *PDE6A<sup>D167A/D167A</sup>* mouse. **A.** PDE6A, PDE6B and PDE6G concentration in the wildtype is compared to the mutant in retinal homogenates. Both PDE6A ( $0.0052 \pm 0.0001$ ) and PDE6B ( $0.057 \pm 0.007$ ) had a significant reduction in activity ( $p = 0.0006$  and  $p = 0.02$  respectively). Although PDE6G ( $0.78 \pm 0.1$ ) had a slight reduction compared to wildtype it was not statistically different from wildtype. Levels are shown as optical density of the PDE band normalized to that of the band for tubulin. **B.** Basal PDE activity was significantly reduced from wildtype, from  $12.9 \pm 1.5$  nmol cGMP/mg/min to  $1.4 \pm 0.08$  nmol cGMP/mg/min, a factor of  $\sim 10$  ( $n = 4, p = 0.0003$ ). Total (trypsin-activated) PDE activity also showed a significant reduction in *PDE6A<sup>D167A/D167A</sup>* animals, from  $241 \pm 13$  nmol cGMP/mg/min to  $17 \pm 0.9$  nmol cGMP/mg/min ( $n = 4, p = 0.00002$ ). Data are presented as mean  $\pm$  standard deviation (s.d.). Horizontal lines and capped vertical lines through individual data points (filled circles) indicate mean and 1 s.d., respectively. Stars above graphs indicate significance level for null hypothesis testing. *Data kindly provided from (Morshedian et al., 2022).*

*PDE6A*<sup>D167A/D167A</sup> mice. Because the decrease in enzyme activity in Fig. 3.3 **B** is similar to the decrease in protein expression in Fig. 3.3 **A**, these measurements suggest that the specific activity of PDE is similar between C57BL/6J and *PDE6A*<sup>D167A/D167A</sup> mice. Because PDE function is dependent on the formation of dimers between PDE6A and PDE6B subunits (Cote, 2021, Gao et al., 2020), these data suggest the remaining PDE activity in *PDE6A*<sup>D167A/D167A</sup> rods is likely due to PDE6B homodimers. However, we were unable to make any physical measurements of enzyme properties from the small amount of PDE6B available from the *PDE6A*<sup>D167A/D167A</sup> mice.

Sensitivity and kinetics of the photoresponse are influenced by the basal rate of PDE activity (Rieke and Baylor, 1996, Nikonov et al., 2000). In *PDE6B*<sup>rd1/+</sup> rods, basal PDE activity as a fraction of maximal trypsin-activated PDE activity is similar to that of C57BL/6J rods, however the maximal trypsin-activated PDE activity is nearly half of C57BL/6J levels (Majumder et al., 2015). In darkness, cGMP is likely bound in the noncatalytic GAF domains of the PDE holoenzyme, which may limit the turnover rate of cGMP. That is, this occupancy of cGMP may increase the affinity for the PDE6G subunit, which in turn enhances the binding affinity for cGMP in the two GAF domains (Arshavsky et al., 1992, Yamazaki et al., 1996). During light-induced activation,  $G\alpha_T^*$  suppresses the PDE6G subunit increasing cGMP turnover rapidly, and the GAF-bound cGMP dissociates. In moderately dim lights, RGS9-1 forms a complex with R9AP and G $\beta$ 5L, which targets the  $G\alpha_T^*P^*$  complex, accelerating GTPase activity. Ultimately, this process deactivates  $P^*$  and allows the outer segment to return to dark rates of cGMP turnover by spontaneous activation of PDE and guanylyl cyclase (GC). We sought to investigate how this process is effected by moderate and severe reductions in PDE concentration.

To determine the effects of PDE activity on the flash response, we compare response families of increasing strength flashes between C57BL/6J, *PDE6B*<sup>rd1/+</sup>, and *PDE6A*<sup>D167A/D167A</sup> mice in Fig. 3.4. Flash responses from rods in mice with a reduction in PDE activity at  $\sim 50\%$  (*PDE6B*<sup>rd1/+</sup>) were similar to C57BL/6J responses; however,  $I_{1/2}$  was lower on average (Fig. 3.4B). Flash response waveforms in *PDE6A*<sup>D167A/D167A</sup> rods ( $\sim 10\%$  of

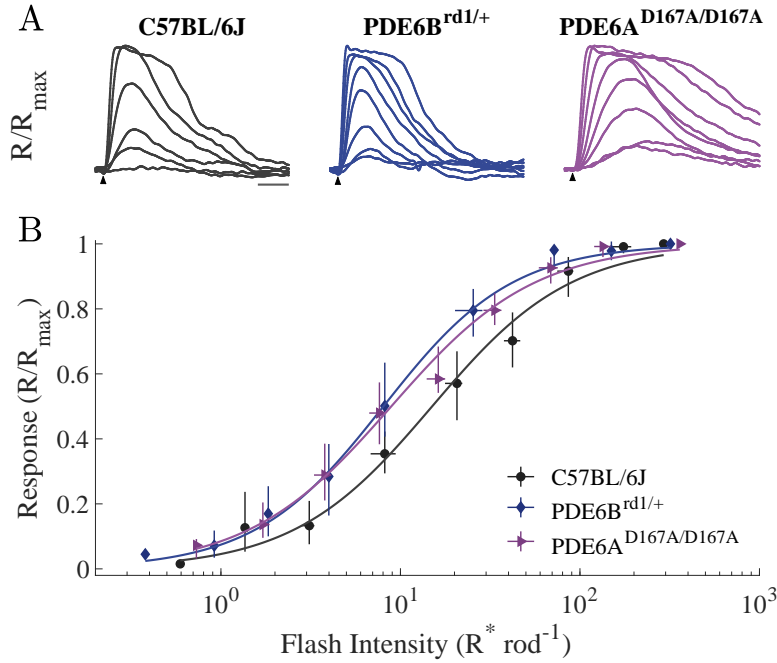


Figure 3.4: *Reduced phosphodiesterase activity increases sensitivity of the flash response.* **A.** Representative flash response families for wildtype (C57BL/6J) and PDE under-expression mice ( $PDE6B^{rd1/+}$ :  $\sim 50\%$  reduction;  $PDE6A^{D167A/D167A}$ :  $\sim 10\%$ ). Reduced PDE activity in the  $PDE6A^{D167A/D167A}$  mouse yielded a marked change in the response waveform compared to  $PDE6B^{rd1/+}$  and C57BL/6J mice. Arrowheads indicate time of flash presentation. Intensities for shown responses area as follows: C57BL/6J, (1.9, 9.2, 20, 41, 85 and 170)  $R^*$ ;  $PDE6B^{rd1/+}$ , (1.9, 4.6, 9.2, 20, 41, 85, 170 and 360)  $R^*$ ;  $PDE6A^{D167A/D167A}$ , (0.73, 1.6, 3.3, 6.7, 14, 29, 59 and 120)  $R^*$ . Scale bar is 200 ms. All plots are on the same time scale. **B.** Response-intensity relations. Overall reduction in PDE activity corresponded with small but statistically significant increases in flash sensitivity ( $p = 0.0008$  ANOVA;  $PDE6B^{rd1/+}$   $I_{1/2} = 8.04$  (6.1, 9.49)  $R^*$ ,  $\Delta I_{1/2} = -6.98$  (-11.8, -2.23)  $R^*$ ,  $p = 0.034$ ;  $PDE6A^{D167A/D167A}$   $I_{1/2} = 8.89$  (7.2, 10.7)  $R^*$ ,  $\Delta I_{1/2} = -6.13$  (-10.6, -1.7)  $R^*$ ,  $p = 0.040$ ). Data and fits are presented as means and  $BC_a$  95% confidence intervals.

C57BL/6J PDE activity, see Fig. 3.3) were markedly slower and longer lasting compared to C57BL/6J and  $PDE6B^{rd1/+}$  rods (Fig. 3.4A). Hill fits to the normalized responses produced  $I_{1/2}$  values of 8.04 (6.1, 9.49)  $R^*$  for  $PDE6B^{rd1/+}$  rods and 8.89 (7.2, 10.7)  $R^*$  for  $PDE6A^{D167A/D167A}$  rods. In both PDE reduced rods, we saw a sensitization of the flash response of  $-6.98$  ( $-11.8$ ,  $-2.23$ )  $R^*$  for  $PDE6B^{rd1/+}$  mice ( $p = 0.0335$ ) and  $-6.13$  ( $-10.6$ ,  $-1.7$ )  $R^*$  for  $PDE6A^{D167A/D167A}$  mice ( $p = 0.0401$ ), an increase in sensitivity by a factor of  $\sim 1.75$ . Given the large reduction in basal PDE activity in  $PDE6B^{rd1/+}$  and  $PDE6A^{D167A/D167A}$  rods, these increases in flash sensitivity were not surprising (Rieke and Baylor, 1996, Majumder et al., 2015); however, the waveforms of  $PDE6A^{D167A/D167A}$  responses were unexpectedly longer and slower. We saw no appreciable difference in the  $n$  parameter for any genotype tested ( $p = 0.1158$  ANOVA), suggesting that flash sensitivity in darkness is set by a linear dependency on the relative concentrations of transduction intermediates, and by the first-order interaction between their activation and deactivation rates.

#### 3.4.4 Severe reduction of PDE6 activity alters response kinetics

Flash sensitivity is differentially altered by reductions in  $G_T$  and PDE, where the relationship between flash strength and response amplitude differs in the  $I_{1/2}$  parameter, but not in the  $n$  parameter, with  $G_T$  being responsible for sensitization and PDE responsible for desensitization (Table 3.1). This difference suggests that flash sensitivity is achieved as a tradeoff between  $G_T$  and PDE activity. We summarize the flash response family properties in Table 3.1. We report the median and range of  $R_{max}$  values of the cells used for analysis in Figs. 3.1, 3.2, 3.4, and 3.5. Interestingly, we found no significant differences between the means, or medians, of the  $R_{max}$  values across genotypes ( $p = 0.185$  for ANOVA of the medians). This result may be due to the large variation of  $R_{max}$  values across genotypes. We did not attempt to describe the variability of the  $R_{max}$  values statistically, because the interpretation of such a description is confounded by the stability of the patch-clamp technique, the selection criteria, and potential biochemical differences in the outer segments. Given prior characterizations of

Genotype	Marker	$\Phi$ (R*)	$I_{1/2}$ (R*)	$n$	$R_{\max}$ (pA)
C57BL/6J (10)	●	0.59→290	15.0 (11.2, 17.9)	1.12 (0.926, 1.43)	23.5 (16.4, 32.5)
GNAT1 <sup>+/-</sup> ;GNAT2 <sup>-/-</sup> (5)	*	0.31→460	22.0 (15.8, 25.5)	1.25 (1, 1.64)	15 (10.2, 26.9)
Tux (8)	×	0.73→510	32.3 (25.5, 35.5)	1.28 (1.09, 1.56)	23.4 (15.5, 32.6)
R9AP95 (9)	■	1.5→290	32.5 (24.7, 35.7)	1.41 (1.12, 1.79)	19.6 (12.9, 29.9)
PDE6B <sup>rd1/+</sup> (7)	◆	0.38→320	8.04 (6.1, 9.49)	1.21 (1.05, 1.49)	23.8 (15.1, 26.8)
PDE6A <sup>D167A/D167A</sup> (9)	▶	0.73→360	8.89 (7.2, 10.7)	1.09 (0.939, 1.31)	26.6 (18, 76.8)

Table 3.1: Properties of the stimulus intensity-response relationship.  $\Phi$  is the stimulus intensity interval. Parameter estimates from fits to a modified Hill equation with 2 free parameters (Eqn. 3.1) where  $R_{\max}$  is the maximal response amplitude,  $I_{1/2}$  is the stimulus intensity producing a half-maximal response, in  $R^*$   $\text{rod}^{-1}$ ,  $n$  is the Hill coefficient. *Parameter estimates are presented as mean (BCa 95% Confidence Interval).  $R_{\max}$  is presented as median (minimum, maximum).*

the animal models used, we did not expect any morphological differences in outer segment length and volume (see Materials and Methods (§ 3.3)). We further quantified the changes observed in the flash-response dynamics by calculating kinetic parameters for  $T_{peak}$ ,  $\tau_{REC}$ , and  $T_{onset}$  and show the results in Fig. 3.5.

The tail of the response waveform following a fall to 50% of the peak was fit to a single-exponential decay function (Eqn. 3.3) to determine the recovery time constant,  $\tau_{REC}$ . Generally, with increasing flash intensity, the recovery latency rose marginally leading to a total increase by a factor of 2 to 3. While trending in shorter durations, there was no appreciable speeding of the flash responses recovery in rods of either  $G_T$  reduction models (Fig. 3.5B-top)<sup>1</sup>. However in R9AP95 rods, recovery rates were consistently faster than those of C57BL/6J rods, from 42.1 (40.8, 43.1) ms to 123 (50.8, 207) ms for R9AP95 rods compared to 83.6 (61.5, 106) ms to 289 (280, 293) ms for C57BL/6J rods. Conversely, we show that *PDE6A<sup>D167A/D167A</sup>* rods exhibited a marked increase in the time course of recovery of about two-fold compared to C57BL/6J rods at every flash intensity, from 507 (298, 723) ms to a maximum of 743 (566, 903) ms (Fig. 3.5B-bottom). This two-fold increase in kinetics is consistent with previous recordings made by suction electrode (Morshedian et al., 2022).

The rising phase of the photoresponse has been described by a delayed ramp where the onset latency,  $T_{onset}$ , is the effective time between photon absorption and the activation of PDE (Lamb and Pugh, 1992). We calculated  $T_{onset}$  by measuring the elapsed time between the start of the flash until the rising phase of the photoresponse reached  $\sim 5\%$  of the respective peak and compared values across genotypes in Fig. 3.5C.  $T_{onset}$  latencies decreased with increasing flash intensity in a monotonic manner.  $T_{onset}$  values measured for Tux, R9AP95 and C57BL/6J rods were indistinguishable from each other. In *Gnat1<sup>+/-</sup>;Gnat2<sup>-/-</sup>* rods,  $T_{onset}$  was reduced by a factor of about 2 for flash intensities  $< 10 R^*$ . For brighter flash intensities,  $T_{onset}$  was not appreciably different between *Gnat1<sup>+/-</sup>;Gnat2<sup>-/-</sup>* rods and C57BL/6J rods (Fig. 3.5C-top). *PDE6A<sup>D167A/D167A</sup>* rods exhibited significantly longer latencies than C57BL/6J

---

<sup>1</sup>The point for *Gnat1<sup>+/-</sup>;Gnat2<sup>-/-</sup>* at the brightest intensity is an artifact of poor fitting due to the length of the recording being too short to determine a plateau region.



rods, from a maximum of 63.5 (55.2, 72.5) ms to 25.6 (23.4, 27.9) ms for  $PDE6A^{D167A/D167A}$  versus 30.3 (9.8, 61.3) ms to 8.05 (6.22, 10.2) ms for C57BL/6J rods (Fig. 3.5C-bottom). This large reduction in the kinetics of flash responses in  $PDE6A^{D167A/D167A}$  rods is remarkable and certainly warrants further investigation.

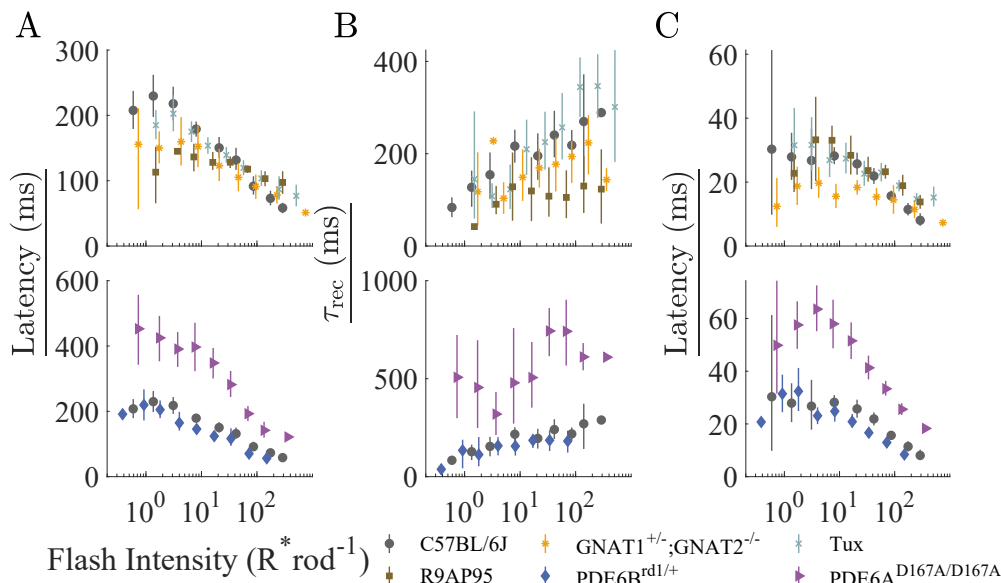


Figure 3.5: *Response family kinetics.* Two panels are shown for each measurement to clarify the differences between perturbations to  $\alpha_T$  (top panels) and those of PDE (bottom panels), note the difference in ordinate scales. **A.** Latency, in ms, to the peak of the response declined as a function of flash intensity, in  $R^*$ . **B.** Recovery time constant from fits to a single exponential decay (Eqn. 3.3) function increases with flash intensity. **C.** Latency to onset, measured from the start of the flash to 5% of the response peak, generally reduced as a function of flash intensity. *All data are presented as means and vertical lines indicate  $BC_a$  95% confidence intervals.*

In the dimmest flashes tested, we observed that both the  $Gnat1^{+/-};Gnat2^{-/-}$  and R9AP95 had  $T_{peak}$  latencies that were  $\sim 75\%$  of C57BL/6J (Fig. 3.5A-top). This suggests that the activation phase of the the photoresponse at dim flash intensities is a tradeoff between rapid activation of PDE by  $G\alpha_T^*$ , and the rapid deactivation of  $G\alpha_T^*$  or  $P^*$  by RGS9-1. Interestingly, we did not observe a speeding of the  $T_{peak}$  latency for Tux rods. In Figs. 3.10 and 3.11, we show that the derived single-photon response is significantly faster and smaller in Tux rods, and the discrepancy with these results is likely due to the greater stimulus intensity

required to generate reliable responses ( $\sim 9.0 R^*$  for flash families versus  $1.6 R^*$  for single-photon derivation). Regardless of the amount of reduction of  $G_T$  in rods, the  $T_{peak}$  values were indistinguishable from C57BL/6J at flash intensities  $> 10 R^*$ . These results indicate the activation phase of the flash response is remarkably stable across the rod dynamic range. Perhaps most interestingly,  $PDE6A^{D167A/D167A}$  rods exhibited a slower  $T_{peak}$  at all intensities tested (Fig. 3.5A-bottom), albeit following the same general trend as C57BL/6J rods by decreasing over the operating range (from 453 (335, 557) ms to 122 (119, 124) ms). Together, these results show that the flash response is differentially altered by reduced activity of  $G_T$  and PDE. Because  $PDE6A^{D167A/D167A}$  rods may have remaining PDE activity due to homodimers of PDE6B subunits, rather than PDE6A:PDE6B heterodimers, these results might be suggestive of a role for the noncatalytic binding site of the PDE6A subunit, which is non-identical to that of the PDE6B subunit (Arshavsky et al., 1992, Cote, 2021).

### 3.4.5 Continuous noise in rod photoreceptors

Rod photoreceptors must be able to distinguish the single-photon response from both *discrete* noise events and the *continuous* noise. Arising from fluctuations in spontaneous PDE activation, continuous noise is characterized by seemingly stochastic fluctuations in the outer segment current of rods (Baylor et al., 1980, Rieke and Baylor, 1996, Field and Sampath, 2017). However, outer segment current fluctuations, less the discrete events, can also arise from the phototransduction cascade, from other cellular sources, and from the instrumentation of the recording circuitry. To isolate continuous noise, we made whole-cell patch recordings over 10 to 20s in darkness (Fig. 3.6A-bottom) to collect all noise sources, and in the presence of a saturating light (Fig. 3.6A-top) to contain sources with transduction suppressed. We calculated the power spectral density (PSD) for each condition and subtracted the instrumentation spectrum from the dark spectrum to generate the continuous-noise spectrum (Fig. 3.6B). The continuous-noise spectrum contained nearly all the energy within the bandwidth of 0 to 10 Hz. The inflection point of the spectrum, the frequency at which the energy falloff begins, was around 1 Hz, and we used this point to compare

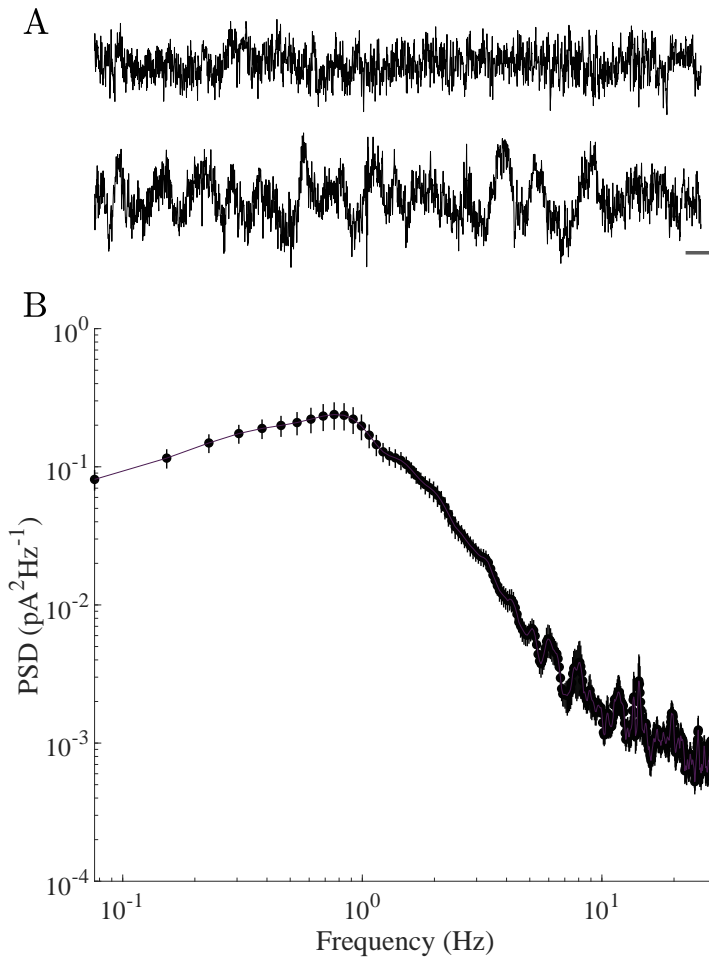


Figure 3.6: *Isolation of the continuous noise in C57BL/6J mice.* **A.** Representative experimental procedure of rod noise traces in darkness (bottom) and in a saturating light (top). *Scale bars are 1 s and 1 pA for abscissa and ordinate, respectively.* **B.** Isolated average continuous noise PSD. *Data are presented as means per frequency bin with vertical lines indicating the  $BC_a$  95% confidence intervals.*

average spectral power (in units of variance,  $\text{pA}^2$ ) across genotypes. For C57BL/6J rods, we calculated  $\sigma_{0-10\text{Hz}}^2 = 0.374$  (0.347, 0.417)  $\text{pA}^2$ ,  $\sigma_{0-1\text{Hz}}^2 = 0.182$  (0.164, 0.217)  $\text{pA}^2$ , and  $\sigma_{1-10\text{Hz}}^2 = 0.177$  (0.165, 0.192)  $\text{pA}^2$ .

To characterize the molecular basis for continuous noise, we next evaluated the continuous noise power spectra for rods with reduced  $G_T$  expression levels. We asked whether  $G_T$  concentration could impart limitations on the cGMP turnover rates through spontaneous activation. We reasoned that if continuous noise arose from spontaneous activation of PDE by rogue  $G_T$ , then reducing the concentration of  $G_T$  by 50 % and 90 % should impact continuous noise in a corresponding manner. In Fig. 3.7 we show that neither halving (*Gnat1*<sup>+/-</sup>; *Gnat2*<sup>-/-</sup>;  $\sigma_{0-10\text{Hz}}^2 = 0.399$  (0.331, 0.468)  $\text{pA}^2$ ,  $p = 0.58$ ) nor decimating (Tux  $\sigma_{0-10\text{Hz}}^2 = 0.296$  (0.255, 0.368)  $\text{pA}^2$ ,  $p = 0.07$ ) the  $G_T$  concentration had a statistically significant effect on the total continuous noise compared to C57BL/6J. Similarly, reducing the lifetime of  $G\alpha_T^*$  through overexpression of the GAP complex had little impact on the total continuous noise (R9AP95  $\sigma_{0-10\text{Hz}}^2 = 0.397$  (0.333, 0.468)  $\text{pA}^2$ ,  $p = 0.586$ ). Interestingly, the noise profiles differed consistently around 1 Hz, which corresponds with the expected period length of the single-photon response. While not statistically significant, the power at 1 Hz decreased with reduced  $G_T$  and increased GAPs. These results indicate that the continuous-noise component in rod photoreceptors is not dominated by the spontaneous activation of  $G_T$ .

Because there was no appreciable effect of reduction of  $G_T$ , we looked at the next component downstream in the phototransduction cascade, PDE (Fig. 3.8). Consistent with transduction models (Reingruber et al., 2013), we show an increase in the total noise of *PDE6B*<sup>rd1/+</sup> rods, which have a ~50 % reduction in PDE ( $\sigma_{0-10\text{Hz}}^2 = 0.797$  (0.672, 0.911)  $\text{pA}^2$ ,  $p = 0.0082$ ). This total increase is characterized by both an increase in variance below and above the 1 Hz inflection point (below:  $\sigma_{0-1\text{Hz}}^2 = 0.428$  (0.367, 0.540)  $\text{pA}^2$ ; above:  $\sigma_{1-10\text{Hz}}^2 = 0.350$  (0.286, 0.461)  $\text{pA}^2$ ). The relationship between these noise profiles is visible in the representative dark (bottom) and light (top) traces in Fig. 3.8A-*middle*, where *PDE6B*<sup>rd1/+</sup> rods show distinctly different fluctuations from C57BL/6J rods (*left*). In *PDE6A*<sup>D167A/D167A</sup> mice, where virtually all of the PDE6A subunit is removed, the cur-

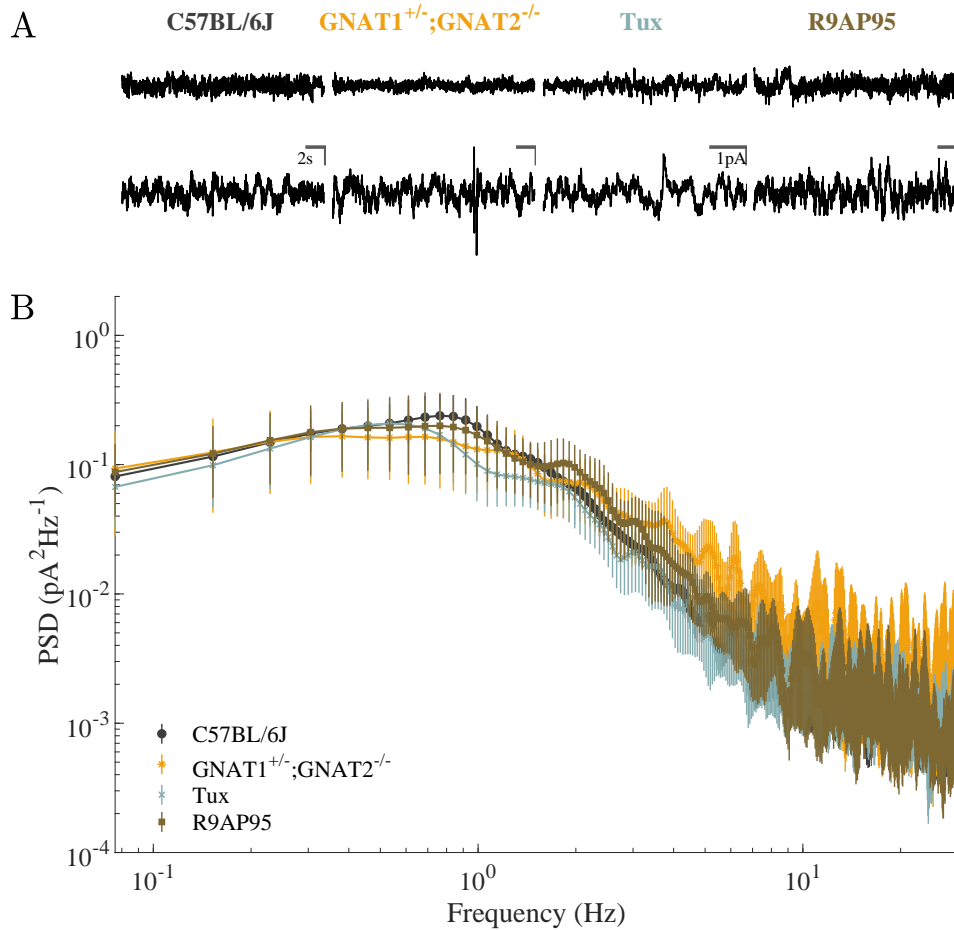


Figure 3.7: *Transducin activity has little impact on continuous noise.* **A.** Representative current recordings from C57BL/6J, *Gnat1*<sup>+/-</sup>;*Gnat2*<sup>-/-</sup>, Tux and R9AP95 rods in saturating light (top) and darkness (bottom) at a holding potential of  $-40$  mV. Scale bars indicate 2sec horizontally and 1 pA vertically for each genotype. **B.** Isolated average continuous noise PSD. Continuous noise was calculated from subtracting the PSD of the variance-corrected current recording in saturating light from that in darkness. Markers indicate means, vertical lines indicate 95 % BC<sub>a</sub> confidence intervals. Smooth lines are linear splines connecting markers.

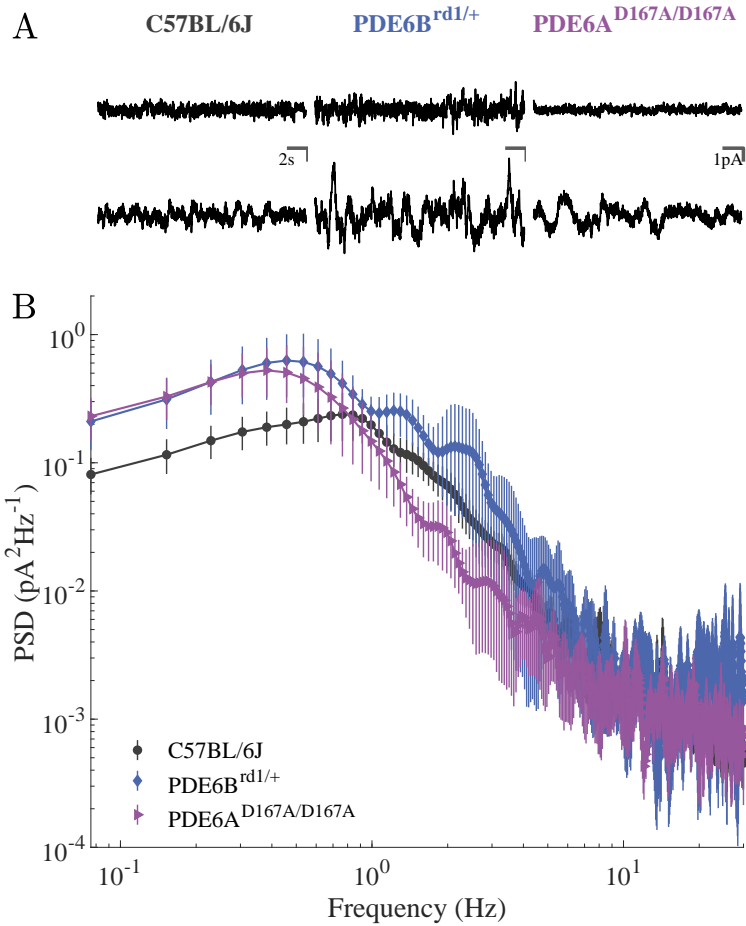


Figure 3.8: *Reductions in PDE6 slow continuous noise.* **A.** Representative current recordings from C57BL/6J, *PDE6B*<sup>rd1/+</sup> and *PDE6A*<sup>D167A/D167A</sup> rods in saturating light (top) and darkness (bottom) at a holding potential of  $-40$  mV. Scale bars indicate 2 sec horizontally and 1 pA vertically for each genotype. **B.** Isolated average continuous noise PSD. Continuous noise was calculated from subtracting the PSD of the variance-corrected current recording in saturating light from that in darkness. Markers indicate means, vertical lines indicate 95 % BC<sub>a</sub> confidence intervals. Smooth lines are linear splines connecting markers.

rent recordings showed large, slow fluctuations in darkness, but small, rapid fluctuations in light Fig. 3.8A-*right*. These fluctuations resulted in a shift of the continuous noise spectrum toward more average power in the lower frequencies ( $\sigma_{0-1Hz}^2 = 0.343$  (0.297, 0.46) pA<sup>2</sup> p = 0.0105), and less average power in the high frequencies ( $\sigma_{1-10Hz}^2 = 0.0855$  (0.0737, 0.107) pA<sup>2</sup> p = 0.0011). Together, these results indicate PDE activity is the dominant source of continuous noise.

### 3.4.6 Isolation of the single-photon response

The impact of the transduction proteins we studied on detection threshold are well exemplified by comparing the responses to single-photon absorptions. To isolate single-photon responses in rods, we collected current recordings evoked by 15 to 60 fixed-intensity flashes (Fig. 3.9A) of 1 to 3 dim intensities within the linear range of the rod dynamic range. We then identified “misses” and “hits” by correlating each trace with the normalized, averaged, response over the rising phase and peak of the response (Fig. 3.9B). We estimated the mean number of unitary events per flash by scaling the rising phase of the ensemble squared-mean to the ensemble variance (in units of pA  $\gamma^{-1}$ ; see Materials and Methods (§ 3.3)), and the average response scaled by these estimates is the derived single-photon response (Fig. 3.9E). We generated a histogram from all single-photon response amplitudes and fit a Gaussian probability distribution to the misses identified in the previous step (Fig. 3.9C). To further separate the misses from singles, doubles, and triples, we used the Gaussian estimate of the fit to the misses as seed parameters for Expectation Maximization clustering. We naively clustered a mixture of 2 to 3 additional Gaussians (Fig. 3.9C-*dashed lines*). The result from the fitting procedure to the mixture is shown as the dark enveloping line in Fig. 3.9C. The fitting procedure allows an estimation of the distributions of misses (red), singles (blue), or larger (gray). The expected membership to each category is shown in Fig. 3.9D. The distributions best-fit to the misses and singles were  $N(0.011, 0.1)$  and  $N(1.18, 0.146)$ . From these fits, we calculated the SNR to be  $\sim 2$ , consistent with previous findings (Okawa et al., 2010, Field and Rieke, 2002b). The distributions of misses and singles showed remarkable

overlap, which demonstrates the difficulty in discerning signals from the noise, despite expected contamination from multi-photon absorptions accounting for less than  $\sim 5\%$  of the singles amplitude (Field and Rieke, 2002a). The method we employed to derive the single-photon response with respect to time (Fig. 3.9E) incorporates all response categories and is thus expected to deviate from the singles response amplitudes. Because averages are sensitive to outliers in the distribution, the derived single photon response amplitude was right-shifted by responses that reached upwards of  $4 \text{ pA } \gamma^{-1}$ , i.e., potential doubles and triples, and exhibited a calculated peak response,  $I_{\text{Single}}$ , of  $1.44$  ( $1.24, 1.65$ )  $\text{pA } \gamma^{-1}$  (for a summary, see Table 3.2).

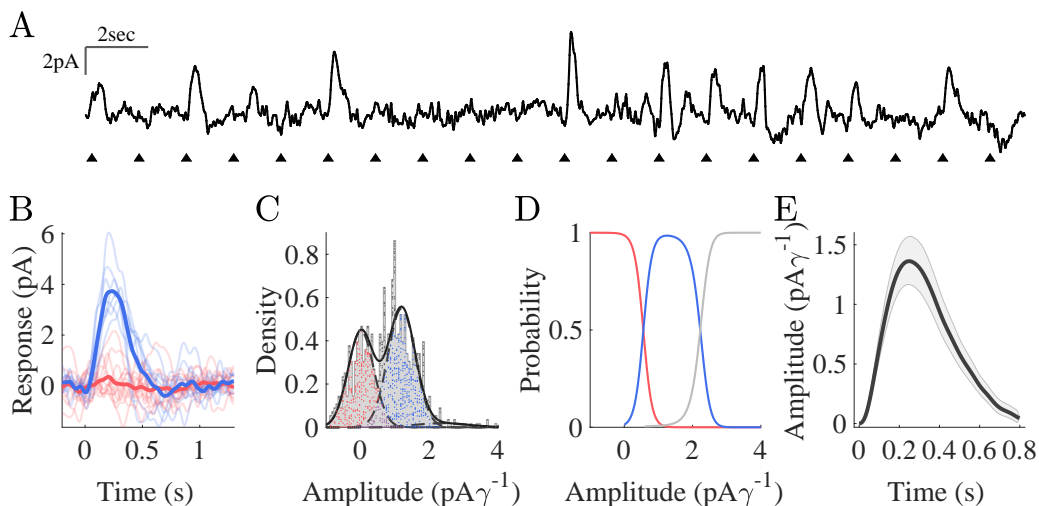


Figure 3.9: *Isolation of the single-photon response in C57BL/6J mice.* **A.** Representative responses of a C57BL/6J rod to a repeating, 10 ms flash isomerizing  $0.7R^*$ , delivered at as indicated by arrowheads. A flash strength was chosen which produced  $\sim 20\%$  of the dark current ( $32.6 \text{ pA}$  for the cell in **A-B**). **B.** Individual success (blue; faint) and failure (red; faint) responses (see Materials and Methods for detection algorithm), with means (bold lines) from the cell in (**A**). **C.** Amplitude histogram of 927 trials (28 cells) fit with a mixture of Gaussian probability functions. Responses identified as failures (red) and successes (blue) are plotted as distributions scaled by each cell’s mean single-photon response (see Materials and Methods). The overlapping region between singles and failures is indicated in purple. **D.** Probability of membership to failure (red), single (blue), or larger (gray) as a function of response amplitude. **E.** Average single-photon response with  $95\%$   $BC_a$  confidence region (light gray).



### 3.4.7 Transduction proteins shape the single-photon response

We derived single-photon responses for each of our mouse lines and compared them to that of the wildtype control (C57BL/6J) in Fig. 3.10. In Fig. 3.10A, we show a section of current traces<sup>2</sup> (*left*) and amplitude histograms (*right*) from rods stimulated with 10 ms flashes of fixed, dim intensities in retinal slices from *Gnat1*<sup>+/-</sup>;*Gnat2*<sup>-/-</sup> (top), Tux, R9AP95, *PDE6B*<sup>rd1/+</sup>, and *PDE6A*<sup>D167A/D167A</sup> (bottom) mice. We show the derived the single-photon responses in Fig. 3.10B (*left*), the normalized response (*right*) and overlaid the single-photon response from Fig. 3.9E for C57BL/6J rods (black trace). In all records, there was an obvious variability from flash to flash, some of which could be described by Poisson probabilities of photon absorption (Baylor et al., 1979) or variability inherent in the response cascade (Baylor et al., 1979, Rieke and Baylor, 1998), with the latter being the current focus. *Gnat1*<sup>+/-</sup>;*Gnat2*<sup>-/-</sup>, Tux, and R9AP95 rods exhibited smaller and faster dim flash response currents (Fig. 3.7) consistent with decreased sensitivity (Fig. 3.2B), and the slight flattening of the continuous noise spectrum. The distinction between misses and singles was apparent in the amplitude histograms. Similarly, responses from *PDE6B*<sup>rd1/+</sup> and *PDE6A*<sup>D167A/D167A</sup> rods were larger and more variable, consistent with an increase in low frequency, continuous noise.

Amplitude histograms were fit with a mixture of Gaussians (see § 3.3), from which we estimated the variance of the continuous noise (misses) and of the singles. Consistent with our continuous noise analysis, *Gnat1*<sup>+/-</sup>;*Gnat2*<sup>-/-</sup> and R9AP95 rods had dark variances which were similar to C57BL/6J values, ( $\sim 0.1 \text{ pA}^2$ ). In Tux rods, the dark variance was about half that of C57BL/6J. Discrimination between misses and singles improved, slightly, in *Gnat1*<sup>+/-</sup>;*Gnat2*<sup>-/-</sup>, Tux and R9AP95 rods, with best-fit Gaussians for singles of  $N(1.1, 0.06)$ ,  $N(0.65, 0.022)$ , and  $N(0.79, 0.012)$ . These lowered variances in the singles distributions corresponded with increases in SNR to 2.2 (*Gnat1*<sup>+/-</sup>;*Gnat2*<sup>-/-</sup>), 3 (Tux), and 2.2 (R9AP95). In *PDE6B*<sup>rd1/+</sup> rods, the dark variance increased slightly to  $0.16 \text{ pA}^2$ , which corresponded

---

<sup>2</sup>Records were down-sampled for display and truncated to a length which fit several of the *PDE6A*<sup>D167A/D167A</sup> responses on the same time scale. As a consequence, some of the faster responses of the reduced G<sub>T</sub> animals appear aliased.

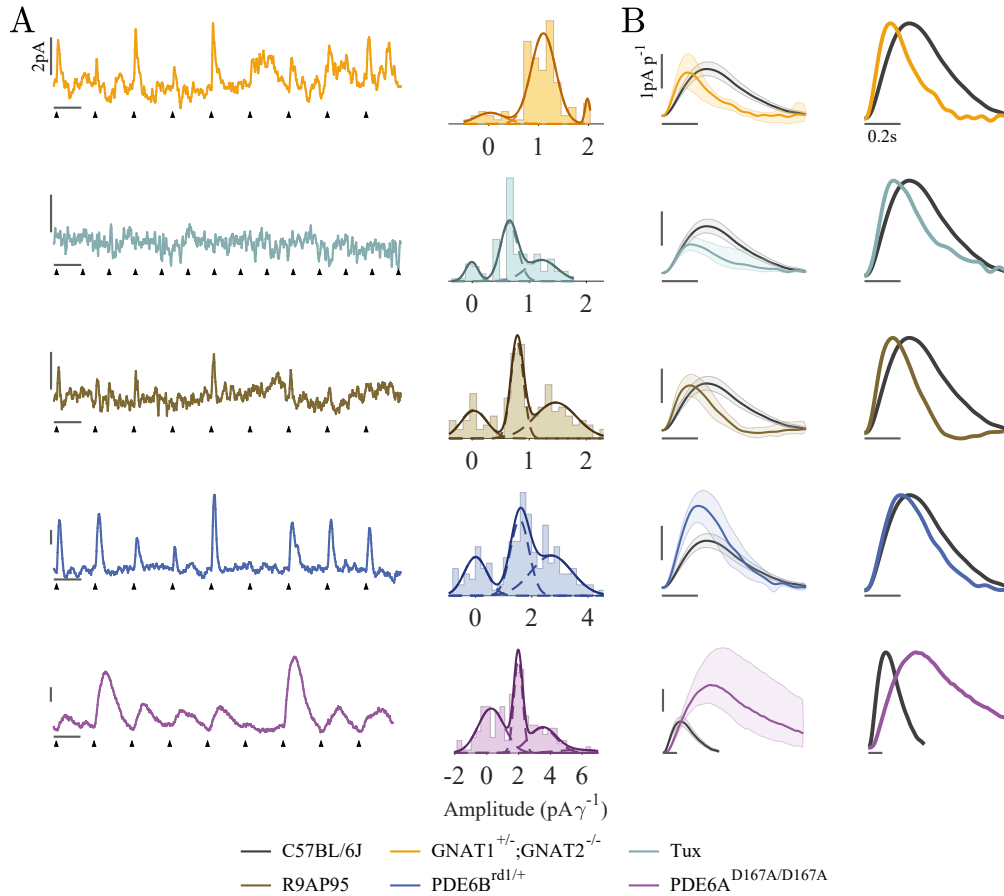


Figure 3.10: *Transduction proteins control timing and amplitude of the single-photon response.* **A.** Representative responses to fixed stimulus (left) and amplitude histograms (right) from all cells and flash intensities. Flashes (10 msec) were presented as indicated by arrowheads. Intensities used in representative responses:  $9.0 R^*$  for *Gnat1*<sup>+/+</sup>; *Gnat2*<sup>-/-</sup>,  $1.6 R^*$  for Tux,  $9.0 R^*$  for R9AP95,  $1.6 R^*$  for *PDE6B*<sup>rd1/+</sup>, and  $1.6 R^*$  for *PDE6A*<sup>D167A/D167A</sup>. Vertical scale bars indicate 2 pA, note the difference in the ordinate for *PDE6B*<sup>rd1/+</sup> and *PDE6A*<sup>D167A/D167A</sup> mice. Horizontal scale bars in A indicate 2 s. **B.** Derived single-photon responses (left) with BC<sub>a</sub> 95% confidence regions. The average single-photon response was scaled by the peak (right) to highlight differences in the time course of the responses. G<sub>T</sub> perturbation showed a marked reduction in the time course and amplitude of the single-photon response in a concentration dependent manner. PDE perturbations affected a increase in amplitude, while *PDE6A*<sup>D167A/D167A</sup> mice also showed a drastic slowing of the single-photon response. Horizontal scale bars in B indicate 200 ms.

Genotype	$I_{\text{Single}}$ (pA $\gamma^{-1}$ )	$T_{\text{peak}}$ (ms)	$\tau_{\text{rec}}$ (ms)	$T_{\text{onset}}$ (ms)	SNR	Power <sub>0-10Hz</sub> (pA <sup>2</sup> )	$A_c$ ( $\mu\text{m}^2$ )
C57BL/6J (28)	1.44 (1.23, 1.65)	260 (246, 272)	167 (147, 190)	68.5 (65.2, 72.1)	2	3.7 (2.8, 5.2)	0.24 (0.21, 0.28)
GNAT1 <sup>+/-</sup> ;GNAT2 <sup>-/-</sup> (5)	1.19 (0.802, 1.57)	147 (116, 160)	126 (91.1, 153)	48.3 (39.8, 61.3)	2.2	2.1 (0.97, 3.5)	0.17 (0.067, 0.36)
Tux (8)	0.91 (0.695, 1.15)	166 (149, 181)	52.5 (34.6, 65.7)	52.4 (45.7, 63.5)	3	2.3 (1.2, 4.6)	0.22 (0.12, 0.32)
R9AP95 (10)	1.4 (1.09, 1.72)	176 (152, 199)	47.5 (39.3, 56.2)	48.1 (42.7, 53.1)	2.2	2.4 (1.4, 4.1)	0.1 (0.078, 0.15)
PDE6B <sup>rd1/+</sup> (7)	2.41 (1.91, 2.86)	212 (190, 233)	128 (87.2, 166)	62.3 (54.5, 74)	2.4	8.1 (3.6, 19)	0.13 (0.078, 0.27)
PDE6A <sup>D167A/D167A</sup> (9)	2.75 (2.17, 3.42)	672 (559, 786)	811 (525, 1210)	176 (151, 207)	1.4	13 (6, 21)	0.14 (0.094, 0.2)

Table 3.2: Properties of the single-photon response.  $I_{\text{Single}}$ : peak amplitude of the derived single-photon response;  $T_{\text{peak}}$ : latency to peak from start of stimulus;  $\tau_{\text{rec}}$ : recovery time constant from single exponential decay fit to the 50% tail of the response;  $T_{\text{onset}}$ : latency to onset measured from the start of the stimulus; SNR: signal to noise ratio from the amplitude histograms (see § 3.3); Power<sub>0-10Hz</sub>: frequency integral of the single-photon response PSD over the 0 to 10Hz bandwidth;  $A_c$ : Estimated collecting area calculated from the mean number of unitary events per flash (see Materials and Methods). *Estimates are presented as mean (BCa 95% Confidence Interval).*

to the increase in continuous noise power, and the singles estimate showed larger responses ( $N(1.57, 0.108)$ ) with an increased SNR of 2.4. It should be noted that this increase in SNR comes with the increased continuous noise which may further complicate behavior thresholds (Okawa et al., 2010, Pahlberg and Sampath, 2011). Amplitudes from  $PDE6A^{D167A/D167A}$  rods showed remarkable increases in dark variance ( $0.67 \text{ pA}^2$ ) and amplitude ( $N(1.98, 0.074)$ ), again, consistent with our continuous-noise analysis and a decrease in SNR to 1.4. These results indicate that  $G_T$  and PDE work together to set the optimal threshold for amplitude discrimination of the single-photon response. These results, while compelling, should be taken with the following caveat: the single-photon response amplitude is expected to be independent of the flash intensity, and multi-photon absorptions should account for less than  $\sim 5\%$  of the records (Field and Rieke, 2002a). Our amplitude histograms were, however, best fit with a third Gaussian (far right peaks), which shared considerable overlap with the singles distribution. Thus, while we display the third Gaussian as separate from the singles, we expect that these amplitudes may indeed belong to the singles, less the expected 5% contamination.

The overview of the above results is visible in the time domain of the derived single-photon responses shown in Fig. 3.10B. For rods with reductions in  $G_T$ , we observed a general decrease in amplitude compared to C57BL/6J rods. The decrease in amplitude of the  $Gnat1^{+/-}; Gnat2^{-/-}$  rods (orange) was accompanied by an increase in variability, probably because the heterozygous mutation may be somewhat compensated for by the remaining allele (Calvert et al., 2000). In both  $G_T$ -reduced mice, we observed a faster time-to-peak latency, and an apparent accelerated recovery phase. Similarly, rapid hydrolysis of  $G\alpha_T^*$  and  $P^*$  in R9AP95 rods (brown) caused a faster response profile, with a slight decrease in amplitude. This observation with dim flash intensity is similar to that of bright flash intensities (Fig. 3.2), and previous reports (Krispel et al., 2006, Chen et al., 2010a). In rods with reduced PDE activity, the waveforms were more complex. In  $PDE6B^{rd1/+}$  rods (dark blue), we observed an increase in amplitude, but no discernable differences in kinetics. Interestingly, the  $PDE6A^{D167A/D167A}$  rods (purple) were both much larger in amplitude and

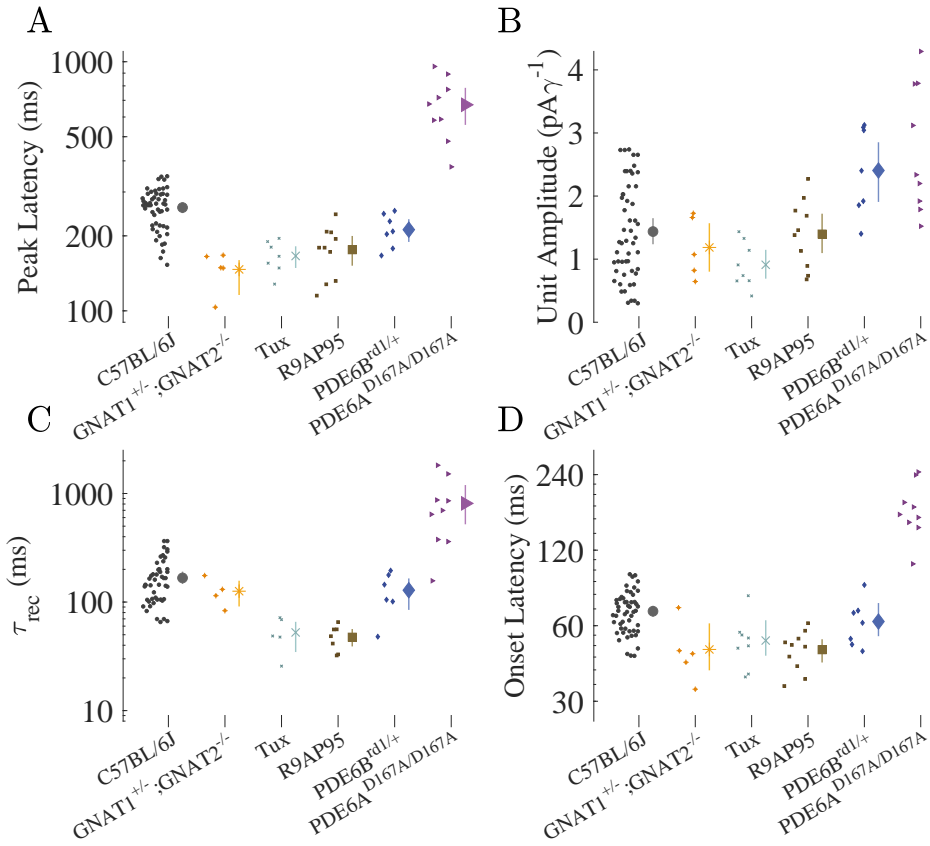


Figure 3.11: *Single-photon response kinetics*. **A.** Time-to-peak latency. **B.** Single-photon response amplitudes. **C.** Recovery time constants from fits beyond the 50% recovery point of the average single photon response. **D.** Latency from the start of the stimulus to 5% of the average single-photon response. *Individual data are plotted in the swarm plot to the left of the Average. Averages are shown as means with vertical lines indicating the BC<sub>a</sub> 95% confidence interval. Note the logarithmic scaling in panels A, C, and D.*

much slower in kinetics.

To quantify these observations, we analyzed the kinetics of the derive single-photon responses and show the results in Fig. 3.11. We plotted individual values from each stimulus intensity used and saw no obvious clustering or multiple modes within groups, confirming the independence of the single photon response on flash strength (Field and Rieke, 2002a). A summary of these results is found in Table 3.2. To begin, we analyzed latency to response peak by determining the duration between the stimulus onset and the time where the rising phase of the response reached 5% of the peak. All genetic models had single-photon responses in rods that were remarkably different from C57BL/6J (Fig. 3.11A,  $p \leq 0.0001$  ANOVA). *Gnat1<sup>+/-</sup>;Gnat2<sup>-/-</sup>* rods had the shortest latency to peak, significantly shorter than C57BL/6J ( $\Delta T_{peak} = -113$  (-139, -91.4) pA  $\gamma^{-1}$   $p = 0.0015$ ). Tux ( $\Delta T_{peak} = -93.7$  (-115, -72.7) pA  $\gamma^{-1}$   $p = 0.00075$ ), R9AP95 ( $\Delta T_{peak} = -83.9$  (-111, -56.7) pA  $\gamma^{-1}$   $p = 0.0005$ ), and *PDE6B<sup>rd1/+</sup>* ( $\Delta T_{peak} = -48.1$  (-73.7, -22.6) pA  $\gamma^{-1}$   $p = 0.013$ ) rods all had significantly shorter latencies than C57BL/6J rods. Interestingly, *PDE6A<sup>D167A/D167A</sup>* rods exhibited markedly longer latencies than C57BL/6J rods, with an effect size of  $\Delta T_{peak} = 412$  (298, 528) pA  $\gamma^{-1}$  ( $p = 0.00038$ ).

Next we analyzed the averaged, derived single-photon, response amplitudes (Fig. 3.11B), where we found a significant ( $p \leq 0.0001$  ANOVA) decrease in Tux rods ( $\Delta I_{Single} = -0.527$  (-0.832, -0.214) pA  $\gamma^{-1}$   $p = 0.028$ ). We also found increases in amplitudes for *PDE6B<sup>rd1/+</sup>* ( $\Delta I_{Single} = 0.968$  (0.452, 1.48) pA  $\gamma^{-1}$   $p = 0.029$ ) and *PDE6A<sup>D167A/D167A</sup>* ( $\Delta I_{Single} = 1.31$  (0.683, 1.97) pA  $\gamma^{-1}$   $p = 0.027$ ) rods. *PDE6A<sup>D167A/D167A</sup>* rods exhibited a larger variation in response amplitude, reflecting the increase in low-frequency and decrease in the high-frequency of the continuous-noise spectrum. These changes in amplitude reflect how activation rates of  $G_T$  and PDE work in concert to balance the trade-off between temporal resolution and sensitivity. Similar to our analysis of  $\tau_{REC}$  for flash families, the tail of the single-photon response was fit with Eqn. 3.3. We found significant acceleration of the recovery phase in Tux ( $\Delta \tau_{rec} = -114$  (-141, -88.5) pA  $\gamma^{-1}$   $p = 0.0015$ ) and R9AP95 ( $\Delta \tau_{rec} = -119$  (-143, -96.6) pA  $\gamma^{-1}$   $p = 0.00075$ ) rods. In

the opposite direction, *PDE6A<sup>D167A/D167A</sup>* rods exhibited a increase in the recovery phase ( $\Delta\tau_{rec} = 644 (337, 999) \text{ pA } \gamma^{-1}$   $p = 0.03$ ). The parameter,  $T_{onset}$ , is the sum of the delays in production of  $R^*$ ,  $G\alpha_T^*$  and  $P^*$  (Pugh and Lamb, 1993). Thus, following the trend, we expected that any changes in the activation of the single-photon response would be accompanied by changes paralleled in  $T_{onset}$ . Indeed, we observed that  $T_{onset}$  was significantly altered by transduction proteins (ANOVA  $p \leq 0.001$ ). We observed distinctly shorter onset latencies in *Gnat1<sup>+/-</sup>;Gnat2<sup>-/-</sup>* ( $\Delta T_{onset} = -20.3 (-30.4, -8.12) \text{ pA } \gamma^{-1}$   $p = 0.043$ ), Tux ( $\Delta T_{onset} = -16.1 (-24.8, -6.52) \text{ pA } \gamma^{-1}$   $p = 0.017$ ), and R9AP95 rods ( $\Delta T_{onset} = -20.4 (-26.6, -14.3) \text{ pA } \gamma^{-1}$   $p = 0.0015$ ). Further, we found longer latencies in *PDE6A<sup>D167A/D167A</sup>* rods ( $\Delta T_{onset} = 108 (81.5, 136) \text{ pA } \gamma^{-1}$   $p = 0.0005$ ). Together, these results indicate that  $G_T$  and PDE are optimally expressed to detect single-photon events, balanced between speed and sensitivity.

### 3.5 Discussion

Rods are optimized to catch single photons with a sensitivity approaching the physical limits of detection. The information parsed from the visual scene by photoreceptors is the only information we receive about the visual world, and the ability to reliably convey signals through the downstream circuitry is of utmost importance for detection. Thus, separation of signal from noise at the level of the photoreceptor is paramount to setting the absolute visual threshold. Despite decades of investigation, it remains unclear which sources of intrinsic photoreceptor noise impact visual threshold. Here, we have investigated further the molecular origin of continuous noise and the impact of transduction proteins on the threshold for detection. We found continuous noise imparts both sensitivity and temporal responsiveness to the single-photon response. Through accelerating  $G_T$  deactivation by increasing GAP concentrations, the single-photon response was accelerated, albeit at the cost of sensitivity. Decreasing the basal rate of cGMP turnover by reducing PDE concentration increases both sensitivity and variability of the single-photon response. Thus, PDE is the dominant transduction protein responsible for shaping continuous noise and consequently limiting the

detection of single-photon events and increasing reliability of the single-photon response.

Previous reports of the genotypes we used in this study suggest that we should expect no morphological differences in outer segment volumes (Calvert et al., 2000, Ronning et al., 2018, Krispel et al., 2006, Yue et al., 2019, Morshedien et al., 2022). Thus, we implemented a uniform mean collecting area of  $0.26 \mu\text{m}^2$ , as determined from dark adapted C57BL/6J rods. This uniform application of the collecting area to determine flash intensities is a conservative approach, which, if invalid, may serve to reduce actual differences in flash sensitivity. However, given the agreement of our results with previous reports, we expect that our approach is well within reason. Our own assessment of collecting areas in this chapter, albeit indirect through analysis of dim-flash responses, suggests that the effective collecting areas between genotypes may only be slightly different. *Post hoc* analysis of our collecting areas revealed that only R9AP95 rods exhibited a significant shift in the estimated collecting area ( $A_c = 0.1 (0.078, 0.15) \mu\text{m}^2$ ,  $p = 0.0015$ ). This finding certainly warrants further investigation, outside of the scope of the current study, which may shed light on still undiscovered mechanisms controlling response recovery and light adaptation.

There is some debate on whether the RGS9-1 component of the GAP complex translocates from the inner segment to the outer segment during light exposure in a manner similar to transducin (Majumder et al., 2013, Frederiksen et al., 2021), arrestin, and recoverin. In immunohistochemical analysis of dark-adapted retinas, it was shown that the GAP anchoring protein R9AP is situated at the outer segment while RGS9-1 is positioned in the inner segment (Tian et al., 2013). However, later reports using tape-peeling methods to segment the photoreceptor layers, showed that protein levels of RGS9-1 were not different from inner and outer segments (Rose et al., 2017). In the former publication, RGS9-1 was able to translocate to the outer segment under a very dim light exposure (20 lux). We observe that the recovery phase of the flash response to moderate and bright lights may be best fit by a double-exponential function, except in R9AP95 rods, which were better fit by a damped oscillation (data not shown) or a single-exponential function with a rapid time constant of recovery. Could it be that the lack of the second-order exponential decay in the flash



response of R9AP95 rods at brighter lights is due to light-dependent recruitment of RGS9-1? If this is the case, then the slower recovery in C57BL/6J rods could be explained by a change in the affinity of RGS9-1 for the  $G\alpha_T^*:P^*$  complex after the cessation of light. This change in affinity could be accomplished either through a cGMP feedback from the cyclase (as dark levels of cGMP return) or through a dissociation of the RGS9-1-G $\beta$ 5L complex, possibly by the calcium-dependant phosphorylation of RGS9-1 (Hu et al., 2001). In the R9AP95 responses, where time in saturation and  $\tau_{\text{REC}}$  are uniformly smaller at any given flash strength (Chen et al., 2010a), it is possible the large presence of RGS9-1 overcomes the rate of RGS9-1 phosphorylation. This might explain the rapid recovery and lack of the slower recovery modality; however, it is difficult to understand how modulation of the  $P^*$  active lifetime could result in a rebound greater than that of the resting current as we observed in the flash responses.

Continuous noise in darkness is carried by currents, comprised of sodium ( $\text{Na}^+$ ) and calcium ( $\text{Ca}^{2+}$ ), through CNG channels. Current fluctuations of rod photoreceptors are comprised of at least 3 well-studied sources of noise, which result from channel-gating probabilities, discrete thermal events, and continuous activity within the phototransduction cascade (Baylor et al., 1980). In the presence of a saturating light source, the first mechanism is quiesced as the CNG channel open probability approaches zero. The Poisson rate of spontaneous activation of the outstandingly stable rhodopsin molecule is estimated at 1 in every 500 to 1000 years, corresponding to a probability of activating one or more rhodopsins of 0.003 to  $0.006 \text{ s}^{-1} \text{ rod}^{-1}$ . In the context of a single rod, which contains  $\sim 10^8$  rhodopsin molecules, thermal activation of rhodopsin is rare.

It is now appreciated that continuous noise arises from the spontaneous activation of PDE, which is characteristically different from light-activated PDE (Chen et al., 2010b, Reingruber et al., 2013, Reingruber et al., 2015). cGMP turnover and CNG channel sensitivity to cGMP concentration generate continuous noise. In the wildtype condition, this noise has a broad spectrum profile over which the frequency-response curve is relatively flat, with a peak around 1 Hz (Fig. 3.6). Reduction of PDE in  $PDE6B^{\text{rd1/+}}$  or  $PDE6A^{\text{D167A/D167A}}$  rods causes a shift

toward lower frequencies. In terms of stochastic resonance, this roughening of the power spectrum would make detection of single photons more erratic due to the dominance of slower frequencies. Additionally, with the increase in power of the low-frequency bandwidth, the amplitudes of the stochastic fluctuations would also be larger and better correlated in time. These larger fluctuations may lose the stochastic buffering of smaller amplitude fluctuations, leading to the observed increase in amplitude and variability of the single-photon response. The major finding that reducing PDE increases both the response amplitude and variance of the single-photon response was predicted by a decrease in  $\beta_d$ , i.e., a reduction in cGMP turnover rate (Reingruber et al., 2013). Further analysis of the *PDE6A<sup>D167A/D167A</sup>* mouse line with this model of transduction would provide valuable insight into the role of effectors of PDE activity, such as calcium or PDE subunit isoforms.

$G_T$  reduction causes the noise curve to flatten slightly, which corresponds to a smaller and faster single-photon response. This result may indicate, while not a dominant component of the continuous noise, dark  $G_T$  activity may nevertheless function to help restrict the continuous-noise bandwidth to around 1 Hz, about the period of a wildtype single-photon response. Our method to analyze continuous noise assumes that there is no appreciable transduction noise during bright light exposure, i.e., light-activated transduction elements are saturated and either generate no noise or noise levels outside of 30 Hz, and the remaining noise is uncorrelated with the sources of noise in darkness. This works for PDE because there is a clear distinction between light-activated and spontaneous PDE activity (Chen et al., 2010b, Reingruber et al., 2013), but might underestimate the contributions by  $G_T$  in bright light, which show no apparent difference between dark-activated and light-activated forms. We show that the underexpression of  $G_T$  in Tux and *Gnat1<sup>+/-</sup>;Gnat2<sup>-/-</sup>* rods led to a slight decrease, on average, of the power in the 0.6 to 1.2 Hz bandwidth. Coincidentally, this corresponded to a decrease in amplitude of the single-photon response. Thus we cannot rule out the possibility that transducin activity may influence the relationship between continuous noise and the single-photon response.

Previous reports showed that the continuous noise scales with the square of the total dark

current (Baylor et al., 1980, Rieke and Baylor, 1996). Thus, scaling by the dark current may reduce variability in continuous noise estimates from cell to cell. We did not find a statistically significant difference in means, nor medians, of  $R_{\max}$  across genotypes (ANOVA,  $p = 0.2$ ), and thus endeavored to produce an analysis which stabilized dark currents according to total variance (see § 3.3). Using the Welch-Satterthwaite approximation, we were able to produce robust estimates of the PSD across the variable  $R_{\max}$  values for each genotype. This transform also had the effect of accounting for differences in lengths of recordings, a facet often overlooked when performing spectral analysis of time-varying signals. We also scaled the continuous noise spectrum by the dark current, and the results did not differ greatly from our report.

Variability of the single-photon response amplitude and kinetics is linked to continuous noise through basal turnover rate of PDE (Rieke and Baylor, 1996). Reductions in  $G_T$  lead to faster and smaller single-photon responses, similar to observations under light adapted conditions (Chen et al., 2010a, Fain, 2011). Since the noise generated in darkness is critically dependent on the spontaneous activity of PDE, the noise level is optimal for detecting single-photon absorptions reliably within the photoreceptor and for carrying the signal downstream in the retinal circuitry (Pahlberg and Sampath, 2011, Field and Sampath, 2017). A reduction in the amount of available PDE leads to a reshaping of the continuous noise profile, subsequently leading to larger and more variable single-photon responses. Interestingly, in *PDE6B<sup>rd1/+</sup>* rods we observed larger and more variable single-photon response amplitudes, but these effects were accompanied by faster peak and onset latencies. Only in the extreme PDE reduction model did we observe both increases in amplitude and in kinetics as a whole.

In rods, PDE naturally occurs as a functional heterodimer between PDE6A (*Pde6a*) and PDE6B (*Pde6b*) subunits, which are inhibited by two identical  $\gamma$  subunits (*Pde6g*). In the *PDE6B<sup>rd1/+</sup>* animal, the expression level of *Pde6b* is reduced by half, while the expression levels of *Pde6a* and *Pde6g* are unaffected (Cunnick and Takemoto, 1992). This expression profile produces an overall enzymatic reduction of about 50%. In *PDE6A<sup>D167A/D167A</sup>* rods, nearly all the *Pde6a* expression is gone, and there is a 10-fold reduction in *Pde6b* expression,

which yields an overall enzymatic activity of  $\sim 10\%$  of control animals. In rods with increased PDE activity from artificial overexpression of cone *Pde6c*, which occurs as a homodimer, photoresponses appeared similar to light adapted rods with a desensitization of the flash response and kinetic speeding (Majumder et al., 2015). Given those results, it is somewhat expected to see that a reduction in PDE activity in the *PDE6A<sup>D167A/D167A</sup>* animal would increase the flash sensitivity. What might explain this? The basal rate of cGMP turnover is relatively slow with cGMP in the noncatalytic binding sites of the PDE holoenzyme in the presence of low levels of  $G\alpha_T^*$ . But, while the  $G\alpha_T^*$  activated PDE heterodimer has an initially rapid activation, its deactivation is accelerated by the absence of cGMP in the noncatalytic binding site (Arshavsky et al., 1992). Taken along with the apparent difference between basal PDE activity and light-dependent PDE activity (Reingruber et al., 2013), it may be possible that there is a unique and important role for each of the PDE6A and PDE6B subunits in accelerating PDE activity. From this viewpoint, one might expect that a reduced binding affinity for cGMP in the noncatalytic binding sites of the PDE6B homodimer in *PDE6A<sup>D167A/D167A</sup>* rods would lead to either a slower turnover rate of cGMP or reduced catalytic power of the holoenzyme. Further investigation of the role of the rod subunits of PDE and their contributions to continuous noise are certainly warranted. With the novel *PDE6A<sup>D167A/D167A</sup>* mouse line, it may be possible to gain further understanding of the evolution of the highly sensitive rod photoreceptor.

The challenges for the future are to incorporate these findings into our mathematical models and identify the missing mechanisms guiding behavioral outcomes through concentration effects of transduction proteins.

## REFERENCES

- Arman, A. Cyrus and Sampath, Alapakkam P. (2010). Patch clamp recordings from mouse retinal neurons in a dark-adapted slice preparation. *Journal of visualized experiments : JoVE*, (43):5–8. 10.3791/2107.
- Arshavsky, V.Y., Dumke, C.L., and Bownds, M.D. (1992). Noncatalytic cGMP-binding sites of amphibian rod cGMP phosphodiesterase control interaction with its inhibitory gamma-subunits. A putative regulatory mechanism of the rod photoresponse. *Journal of Biological Chemistry*, 267(34):24501–24507. 10.1016/S0021-9258(18)35793-4.
- Baehr, W., Devlin, M.J., and Applebury, M.L. (1979). Isolation and characterization of cGMP phosphodiesterase from bovine rod outer segments. *Journal of Biological Chemistry*, 254(22):11669–11677. 10.1016/S0021-9258(19)86536-5.
- Barlow, H. B. (1956). Retinal Noise and Absolute Threshold. *Journal of the Optical Society of America*, 46(8):634. 10.1364/JOSA.46.000634.
- Barlow, H. B. (1957). Increment thresholds at low intensities considered as signal/noise discriminations. *The Journal of Physiology*, 136(3):469–488. 10.1113/jphysiol.1957.sp005774.
- Baylor, D. A., Lamb, T. D., and Yau, K. W. (1979). Responses of retinal rods to single photons. *The Journal of physiology*, 288(1):613–34. 10.1113/jphysiol.1979.sp012716.
- Baylor, D A, Matthews, G, and Yau, K W (1980). Two components of electrical dark noise in toad retinal rod outer segments. *The Journal of Physiology*, 309(1):591–621. 10.1113/jphysiol.1980.sp013529.
- Benjamini, Yoav and Hochberg, Yosef (1995). Controlling the False Discovery Rate: A Practical and Powerful Approach to Multiple Testing. *Journal of the Royal Statistical Society: Series B (Methodological)*, 57(1):289–300. 10.1111/j.2517-6161.1995.tb02031.x.
- Bowes, Cathy, Li, Tiansen, Danciger, Michael, Baxter, Leslie C., Applebury, Meredith L., and Farber, Debora B (1990). Retinal degeneration in the rd mouse is caused by a defect in the  $\beta$  subunit of rod cGMP-phosphodiesterase. *Nature*, 347(6294):677–680. 10.1038/347677a0.
- Calvert, P. D., Krasnoperova, N. V., Lyubarsky, A. L., Isayama, T., Nicolo, M., Kosaras, B., Wong, G., Gannon, K. S., Margolskee, R. F., Sidman, R. L., Pugh, E. N., Makino, C. L., and Lem, J. (2000). Phototransduction in transgenic mice after targeted deletion of the rod transducin alpha -subunit. *Proceedings of the National Academy of Sciences*, 97(25):13913–13918. 10.1073/pnas.250478897.
- Chang, B., Hawes, N.L., Hurd, R.E., Davisson, M.T., Nusinowitz, S., and Heckenlively, J.R. (2002). Retinal degeneration mutants in the mouse. *Vision Research*, 42(4):517–525. 10.1016/S0042-6989(01)00146-8.

- Chen, C.-K., Woodruff, Michael L., Chen, F. S., Chen, Desheng, and Fain, Gordon L. (2010a). Background Light Produces a Recoverin-Dependent Modulation of Activated-Rhodopsin Lifetime in Mouse Rods. *Journal of Neuroscience*, 30(4):1213–1220. 10.1523/JNEUROSCI.4353-09.2010.
- Chen, Jeannie, Woodruff, Michael L., Wang, Tian, Concepcion, Francis A., Tranchina, Daniel, and Fain, Gordon L. (2010b). Channel Modulation and the Mechanism of Light Adaptation in Mouse Rods. *Journal of Neuroscience*, 30(48):16232–16240. 10.1523/JNEUROSCI.2868-10.2010.
- Cobbs, W. H. and Pugh, E. N. (1987). Kinetics and components of the flash photocurrent of isolated retinal rods of the larval salamander, *Ambystoma tigrinum*. *The Journal of Physiology*, 394(1):529–572. 10.1113/jphysiol.1987.sp016884.
- Cote, Rick H. (2021). Photoreceptor phosphodiesterase (PDE6): activation and inactivation mechanisms during visual transduction in rods and cones. *Pflügers Archiv European Journal of Physiology*, 473(9):1377–1391. 10.1007/s00424-021-02562-x.
- Cunnick, Jess and Takemoto, Dolores J. (1992). Carriers of the mouse rd gene have reduced levels of the beta subunit of the retinal cyclic GMP phosphodiesterase. *Biochemical and Biophysical Research Communications*, 184(1):461–466. 10.1016/0006-291X(92)91216-D.
- DiCiccio, Thomas J and Efron, Bradley (1996). Bootstrap Confidence Intervals. *Statistical Science*, 11(3):189–212.
- Dunn, Felice A. (2006). Controlling the Gain of Rod-Mediated Signals in the Mammalian Retina. *Journal of Neuroscience*, 26(15):3959–3970. 10.1523/JNEUROSCI.5148-05.2006.
- Efron, Bradley (1987). Better Bootstrap Confidence Intervals. *Journal of the American Statistical Association*, 82(397):171–185. 10.1080/01621459.1987.10478410.
- Fain, Gordon L. (2011). Adaptation of Mammalian Photoreceptors to Background Light: Putative Role for Direct Modulation of Phosphodiesterase. *Molecular Neurobiology*, 44(3):374–382. 10.1007/s12035-011-8205-1.
- Field, Greg D. and Rieke, Fred (2002a). Mechanisms Regulating Variability of the Single Photon Responses of Mammalian Rod Photoreceptors. *Neuron*, 35(4):733–747. 10.1016/S0896-6273(02)00822-X.
- Field, Greg D. and Rieke, Fred (2002b). Nonlinear signal transfer from mouse rods to bipolar cells and implications for visual sensitivity. *Neuron*, 34(5):773–785. 10.1016/S0896-6273(02)00700-6.
- Field, Greg D. and Sampath, Alapakkam P. (2017). Behavioural and physiological limits to vision in mammals. *Philosophical Transactions of the Royal Society B: Biological Sciences*, 372(1717):20160072. 10.1098/rstb.2016.0072.

Frederiksen, Rikard, Morshedean, Ala, Tripathy, Sonia A., Xu, Tongzhou, Travis, Gabriel H., Fain, Gordon L., and Sampath, Alapakkam P. (2021). Rod Photoreceptors Avoid Saturation in Bright Light by the Movement of the G Protein Transducin. *The Journal of Neuroscience*, 41(15):3320–3330. 10.1523/JNEUROSCI.2817-20.2021.

Gao, Yang, Eskici, Gözde, Ramachandran, Sekar, Poitevin, Frédéric, Seven, Alpay Burak, Panova, Ouliana, Skiniotis, Georgios, and Cerione, Richard A. (2020). Structure of the Visual Signaling Complex between Transducin and Phosphodiesterase 6. *Molecular Cell*, 80(2):237–245.e4. 10.1016/j.molcel.2020.09.013.

Govardovskii, V I, Fyhrquist, N, Reuter, T, Kuzmin, D G, and Donner, K (2000). In search of the visual pigment template. *Visual neuroscience*, 17(4):509–28. 10.1017/s0952523800174036.

Gross, Owen P., Pugh, Edward N., and Burns, Marie E. (2012). Spatiotemporal cGMP Dynamics in Living Mouse Rods. *Biophysical Journal*, 102(8):1775–1784. 10.1016/j.bpj.2012.03.035.

Hecht, Selig, Shlaer, Simon, and Pirenne, Maurice Henri (1942). Energy, Quanta, And Vision. *Journal of General Physiology*, 25(6):819–840. 10.1085/jgp.25.6.819.

Hu, Guang, Jang, Geeng-Fu, Cowan, Christopher W., Wensel, Theodore G., and Palczewski, Krzysztof (2001). Phosphorylation of RGS9-1 by an Endogenous Protein Kinase in Rod Outer Segments. *Journal of Biological Chemistry*, 276(25):22287–22295. 10.1074/jbc.M011539200.

Ingram, Norianne T., Sampath, Alapakkam P., and Fain, Gordon L. (2019). Voltage-clamp recordings of light responses from wild-type and mutant mouse cone photoreceptors. *Journal of General Physiology*, 151(11):1287–1299. 10.1085/jgp.201912419.

Kak, S.C. (1970). The discrete Hilbert transform. *Proceedings of the IEEE*, 58(4):585–586. 10.1109/PROC.1970.7696.

Krispel, Claudia M., Chen, Desheng, Melling, Nathan, Chen, Yu Jiun, Martemyanov, Kirill A., Quillinan, Nidia, Arshavsky, Vadim Y., Wensel, Theodore G., Chen, Ching Kang, and Burns, Marie E. (2006). RGS Expression Rate-Limits Recovery of Rod Photoresponses. *Neuron*, 51(4):409–416. 10.1016/j.neuron.2006.07.010.

Lamb, T D and Pugh, E N (1992). A quantitative account of the activation steps involved in phototransduction in amphibian photoreceptors. *The Journal of Physiology*, 449(1):719–758. 10.1113/jphysiol.1992.sp019111.

Lyubarsky, A., Nikonov, S., and Pugh, E. N. (1996). The kinetics of inactivation of the rod phototransduction cascade with constant  $Ca^{2+}$ . *Journal of General Physiology*, 107(1):19–34. 10.1085/jgp.107.1.19.

- Majumder, Anurima, Pahlberg, Johan, Boyd, Kimberly K., Kerov, Vasily, Kolandaivelu, Saravanan, Ramamurthy, Visvanathan, Sampath, Alapakkam P., and Artemyev, Nikolai O. (2013). Transducin translocation contributes to rod survival and enhances synaptic transmission from rods to rod bipolar cells. *Proceedings of the National Academy of Sciences*, 110(30):12468–12473. 10.1073/pnas.1222666110.
- Majumder, Anurima, Pahlberg, Johan, Muradov, Hakim, Boyd, Kimberly K., Sampath, Alapakkam P., and Artemyev, Nikolai O. (2015). Exchange of cone for rod phosphodiesterase 6 catalytic subunits in rod photoreceptors mimics in part features of light adaptation. *Journal of Neuroscience*, 35(24):9225–9235. 10.1523/JNEUROSCI.3563-14.2015.
- Morshedean, Ala, Sendek, Gabriela, Ng, Sze Yin, Boyd, Kimberly, Radu, Roxana A., Liu, Mingyao, Artemyev, Nikolai O., Sampath, Alapakkam P., and Fain, Gordon L. (2022). Reproducibility of the Rod Photoreceptor Response Depends Critically on the Concentration of the Phosphodiesterase Effector Enzyme. *The Journal of Neuroscience*, 42(11):2180–2189. 10.1523/JNEUROSCI.2119-21.2021.
- Neher, Erwin (1992). Correction for liquid junction potentials in patch clamp experiments. In *Methods in Enzymology*, pp. 123–131. 10.1016/0076-6879(92)07008-C.
- Nikonov, S., Lamb, T.D., and Pugh, E.N. (2000). The Role of Steady Phosphodiesterase Activity in the Kinetics and Sensitivity of the Light-Adapted Salamander Rod Photoresponse. *Journal of General Physiology*, 116(6):795–824. 10.1085/jgp.116.6.795.
- Nymark, S., Frederiksen, R., Woodruff, M. L., Cornwall, M. C., and Fain, G. L. (2012). Bleaching of mouse rods: microspectrophotometry and suction-electrode recording. *The Journal of Physiology*, 590(10):2353–2364. 10.1113/jphysiol.2012.228627.
- Okawa, Haruhisa, Miyagishima, K. Joshua, Arman, A. Cyrus, Hurley, James B., Field, Greg D., and Sampath, Alapakkam P. (2010). Optimal processing of photoreceptor signals is required to maximize behavioural sensitivity. *The Journal of Physiology*, 588(11):1947–1960. 10.1113/jphysiol.2010.188573.
- Oppenheim, Alan V. (1999). *Discrete-time signal processing*. Prentice Hall,, Upper Saddle River, N.J. :, 2nd ed. edition. ISBN 0137549202.
- Pahlberg, Johan and Sampath, Alapakkam P. (2011). Visual threshold is set by linear and nonlinear mechanisms in the retina that mitigate noise. *BioEssays*, 33(6):438–447. 10.1002/bies.201100014.
- Pugh, E.N. and Lamb, T.D. (1993). Amplification and kinetics of the activation steps in phototransduction. *Biochimica et Biophysica Acta (BBA) - Bioenergetics*, 1141(2-3):111–149. 10.1016/0005-2728(93)90038-H.
- Reingruber, Jürgen, Holcman, David, and Fain, Gordon L. (2015). How rods respond to single photons: Key adaptations of a G-protein cascade that enable vision at the physical limit of perception. *BioEssays*, 37(11):1243–1252. 10.1002/bies.201500081.



- Reingruber, Jürgen, Pahlberg, Johan, Woodruff, Michael L., Sampath, Alapakkam P., Fain, Gordon L., and Holcman, David (2013). Detection of single photons by toad and mouse rods. *Proceedings of the National Academy of Sciences*, 110(48):19378–19383. 10.1073/pnas.1314030110.
- Rieke, F. and Baylor, D. A. (1996). Molecular origin of continuous dark noise in rod photoreceptors. *Biophysical Journal*, 71(5):2553–2572. 10.1016/S0006-3495(96)79448-1.
- Rieke, F. and Baylor, D. A. (1998). Single-photon detection by rod cells of the retina. *Reviews of Modern Physics*, 70(3):1027–1036. 10.1103/RevModPhys.70.1027.
- Ronning, Kaitryn E., Allina, Gabriel Peinado, Miller, Eric B., Zawadzki, Robert J., Pugh, Edward N., Hermann, Rolf, and Goswami, M. (2018). Loss of cone function without degeneration in a novel Gnat2 knock-out mouse. *Experimental Eye Research*, 171(February):111–118. 10.1016/j.exer.2018.02.024.
- Rose, Kasey, Walston, Steven T., and Chen, Jeannie (2017). Separation of photoreceptor cell compartments in mouse retina for protein analysis. *Molecular Neurodegeneration*, 12(1):28. 10.1186/s13024-017-0171-2.
- Sampath, Alapakkam P. and Rieke, Fred (2004). Selective Transmission of Single Photon Responses by Saturation at the Rod-to-Rod Bipolar Synapse. *Neuron*, 41(3):431–443. 10.1016/S0896-6273(04)00005-4.
- Satterthwaite, F E (1946). An Approximate Distribution of Estimates of Variance Components. *Biometrics Bulletin*, 2(6):110. 10.2307/3002019.
- Satterthwaite, Franklin E. (1941). Synthesis of variance. *Psychometrika*, 6(5):309–316. 10.1007/BF02288586.
- Sherman, Adam J., Shrier, Alvin, and Cooper, Ellis (1999). Series Resistance Compensation for Whole-Cell Patch-Clamp Studies Using a Membrane State Estimator. *Biophysical Journal*, 77(5):2590–2601. 10.1016/S0006-3495(99)77093-1.
- Sigworth, Fred J (1995). Electronic Design of the Patch Clamp. In Bert Sakmann and Erwin Neher, eds., *Single-Channel Recording*, chapter 4, pp. 95–127. Springer US, Boston, MA. ISBN 978-1-4419-1230-5. 10.1007/978-1-4419-1229-9\_4.
- Simon, Jan (2011). *FilterM*. MATLAB Central File Exchange. <https://www.mathworks.com/matlabcentral/fileexchange/32261-filterm>.
- Tian, Mei, Zallocchi, Marisa, Wang, Weimin, Chen, Ching-Kang, Palczewski, Krzysztof, Delimont, Duane, Cosgrove, Dominic, and Peng, You-Wei (2013). Light-Induced Translocation of RGS9-1 and G $\beta$ 5L in Mouse Rod Photoreceptors. *PLoS ONE*, 8(3):e58832. 10.1371/journal.pone.0058832.
- van der Velden, H.A. (1946). The Number of Quanta Necessary for the Perception of Light of the Human Eye. *Ophthalmologica*, 111(6):321–331. 10.1159/000300352.

Welch, B. L. (1938). The Significance of the Difference Between Two Means when the Population Variances are Unequal. *Biometrika*, 29(3/4):350. 10.2307/2332010.

Welch, P. (1967). The use of fast Fourier transform for the estimation of power spectra: A method based on time averaging over short, modified periodograms. *IEEE Transactions on Audio and Electroacoustics*, 15(2):70–73. 10.1109/TAU.1967.1161901.

Yamazaki, Akio, Bondarenko, Vladimir A., Dua, Salil, Yamazaki, Matsuyo, Usukura, Jiro, and Hayashi, Fumio (1996). Possible Stimulation of Retinal Rod Recovery to Dark State by cGMP Release from a cGMP Phosphodiesterase Noncatalytic Site. *Journal of Biological Chemistry*, 271(51):32495–32498. 10.1074/jbc.271.51.32495.

Yau, K.-W., Lamb, T.D., Matthews, G, and Baylor, D.A. (1979). Current fluctuations across single rod outer segments. *Vision Research*, 19(4):387–390. 10.1016/0042-6989(79)90100-7.

Yue, Wendy W. S., Silverman, Daniel, Ren, Xiaozhi, Frederiksen, Rikard, Sakai, Kazumi, Yamashita, Takahiro, Shichida, Yoshinori, Cornwall, M. Carter, Chen, Jeanne, and Yau, King-Wai (2019). Elementary response triggered by transducin in retinal rods. *Proceedings of the National Academy of Sciences*, 116(11):5144–5153. 10.1073/pnas.1817781116.

## CHAPTER 4

# Rod bipolar cell contributions to adaptation in the mammalian rod pathway

### 4.1 Abstract

Light adaptation at the first visual synapse is characterized by the sum of changes in presynaptic gain of rods and postsynaptic modulations of the transduction cascade in rod bipolar cells (RBCs). Here, we dissect these changes and their contributions to adaptation. We made whole-cell voltage clamp recordings in dark-adapted mouse retinal slices. Light-evoked responses were recorded in darkness and during the presentation of background light up to  $600 \text{ R}^* \text{ s}^{-1}$ . Rod photoreceptors exhibited a 2-fold reduction in normalized gain at light intensities of  $\sim 50 \text{ R}^* \text{ s}^{-1}$ . RBC stimulus-response relationships were assessed by fitting parameters of a Hill equation for stimulus intensity producing a half-maximal response ( $I_{1/2}$ ) and Hill coefficient ( $n$ ). The nonlinearity of the metabotropic glutamate receptor 6 (mGluR6) cascade was relieved in dim backgrounds, while the  $I_{1/2}$  was unchanged until brighter background intensities. The maximal response amplitude ( $R_{\text{max}}$ ) was reduced to  $\sim 90\%$  in dim background intensities. Dialysis of 10 mM BAPTA during recordings, and holding the membrane potential at 50 mV, eliminated  $R_{\text{max}}$  suppression in dim backgrounds; however,  $R_{\text{max}}$  decreased at backgrounds similar to  $I_{1/2}$ . Measurements in mouse RBCs reveal that this reduction is a combination of the gain reduction inherited from rods and calcium ( $\text{Ca}^{2+}$ )-dependent mechanisms intrinsic to the rod bipolar cells. These mechanisms allow RBCs to respond robustly to single-photon absorptions in a minority of the rods, while continuing the signal in brighter backgrounds that also cause rod adaptation.

## 4.2 Introduction

The visual system encodes information over a large range of ambient light intensities. The sensitivity of the visual circuitry needs to be appropriately set to maximize the range of outputs to the inputs. Mammalian rod photoreceptors are tuned to parse individual photon absorptions, to discriminate them from continuous noise, and to transmit the resulting membrane potential change to downstream neurons (Hecht et al., 1941, van der Velden, 1946, Barlow, 1957, Baylor et al., 1979, Rieke and Baylor, 1996). The specialized ribbon synapse at the rod spherule employs tight presynaptic calcium regulation to ensure signal transmission is robust (Morgans et al., 2001, Barnes and Kelly, 2002, Haeseleer et al., 2004). RBCs are the principal output of the rod photoreceptors, enabling the transmission of rod signals in over 7 orders of magnitude in light intensity. As adaptation in the rod circuitry progresses outward from the inner retina (Dunn, 2006), RBCs are optimally placed to study their contributions to rod adaptation. Here, we dissect RBC contributions to rod adaptation and study their underlying mechanisms by measuring light-evoked signals in both rods and rod bipolar cells.

Thousands of rod signals converge onto single AII amacrine cells in the rod circuitry. RBCs are the first point of pooling of rod outputs, allowing convergence of tens of rods (Tsukamoto et al., 2001). If the RBCs simply summed the outputs of the rod pool, any signal from a relatively small number of rods would be obscured by the noise. Yet, single-photon responses are propagated in RBCs (Field and Rieke, 2002b, Berntson et al., 2004b). Thus, some form of thresholding at the rod-to-rod bipolar synapse was suggested as a means of eliminating rod noise (Van Rossum and Smith, 1998). Indeed, in several vertebrate systems, a threshold-like filtering of the rod noise was observed (Trexler et al., 2011, Field and Rieke, 2002b, Berntson et al., 2004b, Robson et al., 2004). However, the mechanism responsible for setting the threshold is still unknown. adaptation to background light begins centrally and progresses outward, such that the range over which each cell type in the circuit operates is distinct from the others (Dunn, 2006). Evidence suggests the mechanism for setting the first threshold is located in RBC dendrites (Field and Rieke, 2002b, Sampath and Rieke, 2004).

The main channel responsible for the depolarizing current during light stimulation, transient receptor potential melastatin channel 1 (TRPM1), and the main G protein-coupled receptor (GPCR), mGluR6, are positioned closely together in the RBC dendrites (Morgans et al., 2009). In darkness, the GPCR cascade operates near saturation (Sampath and Rieke, 2004), which drives the TRPM1 channel to be closed by an unknown mechanism. Opening of TRPM1 channels requires the deactivation of  $G\alpha_o$  (Nawy, 1999, Dhingra et al., 2000, Okawa et al., 2010b), a process that is accelerated by regulator of G protein signaling proteins, RGS7 and RGS11 (Cao et al., 2012). The resulting TRPM1 inward currents were shown to be sensitive to internal calcium ( $Ca_i^{2+}$ ) concentrations in the retinas of dogfish (Shiells and Falk, 1999), tiger salamander (Nawy, 2004, Kaur and Nawy, 2012), and mouse (Berntson et al., 2004a). While the mechanism of modulation of the depolarizing current is unknown, it is not likely to occur through cyclic guanosine monophosphate (cGMP) (Sampath and Rieke, 2004) or  $Ca^{2+}$ -dependent kinases and phosphatases, e.g., calcineurin and CaMKII (Nawy, 2004).

To elucidate the mechanisms underlying rod-to-rod bipolar adaptation and thresholding, we utilized whole-cell patch recordings in dark-adapted slices from rod photoreceptors and rod bipolar cells in C57BL/6J mouse retinas in darkness and during steady-state background light. In rod photoreceptors, we measured adaptation by determining the effect of background intensity on the gain of the dim flash response. We show that changes in rod gain are passed downstream to RBCs and represent a likely feed-forward mechanism for adaptation. Further, we show that background light modulates postsynaptic cascade saturation in dim background intensities, which is reflected in the relief of nonlinearity in a light regime where rod gain is unaffected. We investigated the role of  $Ca^{2+}$  entry during background light exposure. We show that calcium entry during dim background intensities facilitates the reduction of  $R_{max}$ . Collectively, we show that RBC adaptation is both coordinated by and independent of rod adaptation. Thus, RBCs have an intrinsic ability to respond robustly to single-photon absorptions in a minority of the rods, while continuing to signal at brighter intensities that also cause rod adaptation.

### 4.3 Methods

*Animals.* This study was conducted in accordance with the recommendations of the *Guide for the care and use of laboratory animals* of the National Institutes of Health, and the Association for Research in Vision and Ophthalmology Statement for the Use of Animals in Ophthalmic and Vision Research. The animal-use protocol was approved by the University of California, Los Angeles, Animal Research Committee (Protocol no. 14-005). Euthanasia was performed by cervical dislocation. All animals used in this study were between 2 to 6 months of age from approximately equal numbers of both sexes and were reared under a 12 h dark-light cycle. C57BL/6J mice were purchased from The Jackson Laboratory (Bar Harbor, ME) and were not screened for the absence of the Rd8 mutation (Chang et al., 2002).

*Solutions.* Retinal slices were made in HEPES-buffered Ames' medium (Sigma), which contained  $2.38 \text{ g L}^{-1}$  HEPES, and was balanced with  $0.875 \text{ g L}^{-1}$  NaCl to give an osmolarity of  $284 \pm 1 \text{ mOsm}$  at  $\text{pH } 7.35 \pm 0.05$ . Ames-HEPES was kept on ice and continuously bubbled with 100 %  $\text{O}_2$ . Bicarbonate buffered Ames' medium (referred to as buffered Ames' medium henceforth) was made from Ames' medium supplemented with  $1.9 \text{ g L}^{-1}$   $\text{NaHCO}_3$  and equilibrated with 95 %  $\text{O}_2$ /5 %  $\text{CO}_2$  at  $\text{pH } 7.4$ . Internal solution for recording electrodes contained (in mM): 125 K-aspartate, 10 KCl, 10 HEPES, 5 NMG-HEDTA, 0.5  $\text{CaCl}_2$ , 0.5  $\text{MgCl}_2$ , 1 ATP-Mg, 0.2 GTP-Tris, 2.5 NADPH;  $\text{pH}$  was adjusted to  $\sim 7.3$  with NMG-OH and osmolarity was adjusted to  $\sim 280 \text{ mOsm}$ . For experiments investigating effects of calcium buffering on RBC adaptation, a new internal, recording solution was made that, additionally, contained 10 mM 1,2-Bis(2-Aminophenoxy)ethane-N,N,N',N'-tetraacetic acid (BAPTA) (Sigma; A4926; lot# SLCF0254). All other constituents were identical to the normal internal solution.

*Dissection and slice preparation.* Mice were dark-adapted for 12 to 20 h prior to the start of the experiment. All experiments began in the morning. Dissections were performed under infrared illumination ( $\lambda \geq 900 \text{ nm}$ ) with infrared image converters, which were head mounted (ITT Industries) or scope mounted (B.E. Meyers, Redmond, WA). Following eu-

thanasia, eyes from mice were enucleated, the anterior portion of the eye was cut, and the lens and cornea were removed. Eyecups were stored at 32 °C in buffered Ames' medium in a light-tight container machined from Delrin<sup>®</sup> (DuPont, Wilmington, DE). Under an infrared-equipped dissection microscope (Carl Zeiss), eyecups were bisected through the optic nerve head with a #10 scalpel, and the retina was carefully removed from the retinal pigmented epithelium (RPE) with fine forceps. The isolated retinal piece was embedded in a low-temperature gelling Agarose (3%; Sigma-Aldrich) in HEPES-buffered Ames' medium. Cross-sectional retinal slices (200  $\mu\text{m}$  in thickness) were cut in chilled, oxygenated Ames-HEPES with a vibratome (VT-1000S; Leica) and transferred either to a recording chamber, or to the storage container, for use later in the experiment. During recordings, the retinal slice was stabilized with a custom-made, laser-cut, stainless steel (420 grade; polished) anchor, which was adhered to the recording chamber with a small amount of petroleum jelly (Vaseline<sup>®</sup>). The slice was superfused with buffered Ames' medium at  $\sim 4 \text{ mL min}^{-1}$ . The bath temperature was held at  $36 \pm 1 \text{ }^\circ\text{C}$  by a temperature controller with feedback (TC-324B; Warner Instruments, Holliston, MA).

*Physiological recordings from rod photoreceptors and rod bipolar cells.* Recordings from individual cells were made by whole-cell patch-clamp from dark adapted retinal slices as described previously (Arman and Sampath, 2010). Rods were visualized at 60x magnification with an infrared light-emitting diode (LED) source ( $\lambda = 940 \text{ nm}$ ; Cairn Research) attached to the transmitted light path of the physiology microscope (Eclipse FN1; Nikon). Rod somata were identified by morphology and location in the outer nuclear layer (ONL). RBC somata were identified by morphology and location in outermost portion of the inner nuclear layer as well as by characteristic flash responses. Some RBCs were filled with fluorescent dye (100  $\mu\text{M}$ ; Alexa Fluor 750,  $\lambda_{max} = \sim 750 \text{ nm}$ ; ThermoFisher), loaded in the recording pipette. They were subsequently imaged with a Hamamatsu ORCA-flash4.0LT+ (model C11440, Hamamatsu Photonics K.K.).

Filamented borosilicate-glass capillaries (BF120-69-10; Sutter Instruments, Novato, CA) were pulled on the day of the experiment with a P-97 Flaming/Brown micropipette puller

(Sutter Instruments) to a tip resistance in the bath medium of 15 to 19 M $\Omega$  for rods and 13 to 16 M $\Omega$  for RBCs. Cells were voltage-clamped (rods:  $-40$  mV, RBCs:  $-60$  mV or  $+50$  mV) with an Axopatch 200B patch-clamp amplifier (Molecular Devices). Series resistance of the recording pipette was compensated at 75 to 80 % to prevent error in clamping potentials, and pipette capacitance was neutralized prior to “break-in” (Sherman et al., 1999, Sigworth, 1995). The patch seal was assessed after “break-in”, and recordings were terminated if the seal resistance was below  $\sim 1$  G $\Omega$  or the access resistance exceeded  $\sim 200$  M $\Omega$ . All reported values have been corrected for liquid junction potentials (Neher, 1992), which were estimated previously to be  $\sim 10$  mV for our recording solutions (Ingram et al., 2019).

Recordings were low-pass filtered at 5 kHz by the patch-clamp amplifier and digitized at 10 kHz with a 16-bit A/D converter (ITC18/USB18; HEKA Elektronik). The sampling rate was high enough to ensure negligible variability between stimulus and acquisition clock-synchronization from experiment to experiment. Further zero-phase shift digital filtering was performed offline with a 7th order Butterworth filter and the FilterM C-Mex package (Simon, 2011). Typical filtering bandwidths were 0 to 30 Hz, and any deviations from this value for specific experiments are listed in the corresponding text of the figure legends and results section. Data were collected in MATLAB (R2018b; The Math Works, Natick Massachusetts, USA) with the open-source software package, Symphony Data Acquisition System (<https://symphony-das.github.io>). All offline data visualization and analysis was performed with custom scripts and the Iris DVA framework (open-source; <https://github.com/sampath-lab-ucla/IrisDVA>; see also Appendix A) for MATLAB (R2021a-2022a).

*Light stimulation.* Stimuli were delivered with a dual OptoLED light stimulation system (Cairn Research, Faversham, UK) through a custom-built optical pathway that feeds into the transmitted light path of the physiology microscope. The stimulus and background LEDs had peak wavelengths of  $505 \pm 5$  nm and  $405 \pm 5$  nm. Light sources were attenuated by absorptive neutral-density filters (Thorlabs). At the beginning of each experiment, the microscope field-stop aperture was focused at the level of the slice to provide uniform illumination and was reduced to limit the stimulation region to a spot  $\sim 200$   $\mu$ m in diameter.



The intensities of the LEDs were measured with a calibrated photodiode (Graseby Optonics) through a photodiode amplifier (PDA200C; Thorlabs). Light intensities were calibrated as effective photons ( $\lambda$ s) per squared micrometer ( $\gamma \mu\text{m}^{-2}$ ) and adjusted for the absorption spectrum of rhodopsin (Govardovskii et al., 2000, Nymark et al., 2012). Stimulus intensities were then converted to light-activated rhodopsin ( $R^*$ ) by accounting for the effective collecting area of a rod outer segment.

We estimated the effective collecting area of individual rods from the trial-to-trial variability in the responses to a fixed-stimulus. Under the assumption that photon absorption obeys Poisson statistics, the mean number of photoisomerizations produced by the flash can be estimated by dividing the squared mean response by its variance:

$$\bar{\eta} = \frac{\bar{I}^2}{\sigma_I^2}, \quad (4.1)$$

where  $\bar{I}$  is the average response and  $\sigma_I^2$  is the variance produced by the flash (Field and Rieke, 2002b). We calculated  $\bar{\eta}$  from 4 to 6 flash intensities for 15 rods, and the collecting area was determined as the slope of the line relating  $\bar{\eta}$  to the flash intensity. The average and 95 % bias-corrected and *accelerated* ( $BC_a$ ) confidence interval (see *Statistics*) of the collecting area was estimated to be 0.26 (0.14, 0.35)  $\mu\text{m}^2$  (see Fig. 4.1).

*Relationships of responses to stimulus and background intensity.* To calculate the normalized amplitude for the photoreponse to a given stimulus intensity, we correlated each response with a template generated from the average response across all flash intensities. We then took the amplitude relative to a baseline measured in the 200 ms prior to flash delivery (Sampath and Rieke, 2004). The amplitudes were scaled by the maximal response to the brightest flashes. This template-scaling procedure produced more consistent estimates of the more variable dim flash responses compared to measuring peak current deflections. Response amplitudes were then related to flash intensities,  $\Phi$ , with a Hill equation,

$$\frac{R}{R_{Max}} = \frac{1}{1 + \left(\frac{I_{1/2}}{\Phi}\right)^n} \quad (4.2)$$

where  $I_{1/2}$  is the value of the stimulus intensity producing a half-maximal response, and  $n$  is the Hill coefficient.

To determine the effects of background light on maximum response amplitudes, responses to saturating flash intensities were recorded in the presence of a variety of background light intensities. These responses were bracketed by saturating flash responses recorded in darkness. A line was fit with respect to time between the peaks of the flashes in darkness, and the predicted maximal response,  $\hat{R}_{\max}$ , was estimated to be the solution to the fit at the time of the peak measured in the presence of a background light (see Figs. 4.7 and 4.10). To measure the amount of suppression of the maximal response amplitude, the peak of the saturated response during the presentation of background light was divided by the predicted maximal response.  $R_{\max}/\hat{R}_{\max}$  amplitudes were then related to background intensities,  $\Phi_B$ , with an inverse Hill function with parameters for initial offset,  $R_0$ , background intensity of half-maximal attenuation,  $I_{1/2}^B$ , and the Hill exponent,  $n$ .

$$\frac{R_{\max}}{\hat{R}_{\max}} = R_0 - \frac{\Delta R \Phi_B^n}{I_{1/2}^B{}^n + \Phi_B^n}. \quad (4.3)$$

In this equation,  $\Delta R = R_0 - R_s$ , and  $R_s$  represents the settling point of the maximal attenuation.  $\Delta R$  can then be taken as a metric for the maximal suppression of  $R_{\max}$  by background light exposure (Fig. 4.8).

*Calculation of gain.* Rod photoreceptor gain was measured from current responses in whole-cell voltage-clamp ( $-40$  mV) to dim flashes of 505 nm light. Gain was calculated as described previously (Dunn, 2006). Briefly, sections of the record with a response (“hit”) and without a response (“miss”) were correlated with a template derived from averaging all flash trials at a given background intensity. The mean of the hit-trial correlations with the template were given by  $m_{\text{flash}} = fg$ , where  $f$  is the flash strength in  $R^*$  and  $g$  is the gain of the response. Gain was averaged across multiple flash intensities for each background, and gain values were scaled by the gain in darkness such that the gain in darkness was  $1 \text{ pA } R^{*-1}$ .

*Statistics.* All uncertainties were calculated by Monte Carlo simulations (bootstrap) with 10,000 replicates except for time-series data, which instead used 2000 simulations in the interest of reducing computation time. Uncertainty is expressed as means and 95 % confidence intervals. To increase accuracy and mitigate errors that arise from the nonparametric sit-

uation, confidence intervals were estimated by the  $BC_a$  method (Efron, 1987, DiCiccio and Efron, 1996).

In cases where fitting procedures were used, e.g., stimulus-response relationships, fits were performed with a total least squares method, also known as orthogonal regression, according to the Total Least Squares Approach to Modeling Toolbox for MATLAB (Petráš and Bednárová, 2010). Data were binned by logarithmic-spaced intervals, which introduced an uncertainty in the variables. We mitigated these effects by estimating total error during the fitting procedure. The fitting procedure was bootstrapped by resampling from residuals of individual cells, i.e., stimulus-response sets (Freedman, 1981, Efron and Tibshirani, 1986). The data were resampled, binned, and fit for 10,000 repetitions generating sampling distributions of model parameters. Uncertainty regions of the fitting parameters are presented as  $BC_a$  95% confidence intervals. Uncertainty regions of the regression lines are the 95% confidence intervals generated from each bootstrapped fit over an interpolating region according to the variable's domain, and they were displayed as a shaded region surrounding the fit traces. Statistical significance of fitting parameters, where applicable, was determined from the  $BC_a$  95% confidence regions, which corresponds to the  $p < 0.05$  level (Efron and Tibshirani, 1986).

Statistical comparisons between BAPTA and control conditions for  $R_{\max}$  experiments were made by first assessing a one-way, repeated measures ANOVA, by a custom bootstrap approach for unbalanced design in MATLAB. This custom algorithm is equivalent to the standard linear mixed-effects model, except that bootstrap replicates are calculated from the residuals as the fixed-effects estimator (Freedman, 1981). *Post hoc* analysis proceeded if the results of ANOVA indicated a significant effect, i.e.,  $p < 0.05$ . Pairwise testing was performed on all pairs by a custom bootstrap algorithm of Welch's T-test for unequal variances (Welch, 1938, Welch, 1947). To account for multiple testing errors, all p-values were adjusted for false discovery rate (Benjamini and Hochberg, 1995).

## 4.4 Results

### 4.4.1 Determination of the rod collecting area

To understand how light signals are transmitted through the first retinal synapse and processed by RBCs, we first needed to calibrate our apparatus and determine the relationship between our light stimulus and the absorption of photons in rod photoreceptors. Photon densities ( $\gamma \mu\text{m}^{-2}$ ) were measured with a radiometer attached to a photo-amplifier and converted to photoisomerizations ( $R^*$ ) with measured rod collecting areas (Fig. 4.1). We used voltage-clamped recordings from rod photoreceptors and measured the trial-to-trial variability in the responses to a fixed-intensity flash. Under the assumption that photon absorption follows a Poisson process, the mean number of photoisomerizations can be estimated by a scale factor,  $\bar{\eta}$ , relating the averaged, squared response amplitude to the variance of the response (Eqn. 4.1). 10 to 30 fixed-intensity flashes were delivered successively, and the current responses were recorded (Fig. 4.1A-left). This process was repeated for 6 different flash intensities chosen in a random order, for a range of 2 to 4 intensities per cell. Responses were averaged (Fig. 4.1A-right), and  $\bar{\eta}$  was estimated as in Eqn. 4.1. Estimates for  $\bar{\eta}$  are shown in Fig. 4.1B. The collecting area,  $A_{\text{eff}}$ , was estimated as the slope of regression line relating  $\bar{\eta}$  to photon density. The mean collecting area from 15 rods was  $0.26 (0.14, 0.35) \mu\text{m}^2 \gamma^{-1}$ .

### 4.4.2 Photoreceptor gain is dependent on background light levels

Rod photoreceptors can detect single photons (Baylor et al., 1979) and remain sensitive to flashes of light over a range of about 2 log-units of ambient illumination. The hyperpolarized membrane potential of rods in darkness is well positioned to ensure that rod glutamate release rate is highly sensitive to the small, graded potential changes produced by dim flashes. Rod adaptation to background light results in decreased sensitivity with increased background intensity. This phenomenon is common among other sensory adaptation modalities and, in photoreceptors, is characterized by increases in the speed of response decay and decreases in response amplitudes (Fig. 4.2). In the rod bipolar pathway, thousands of rods converge

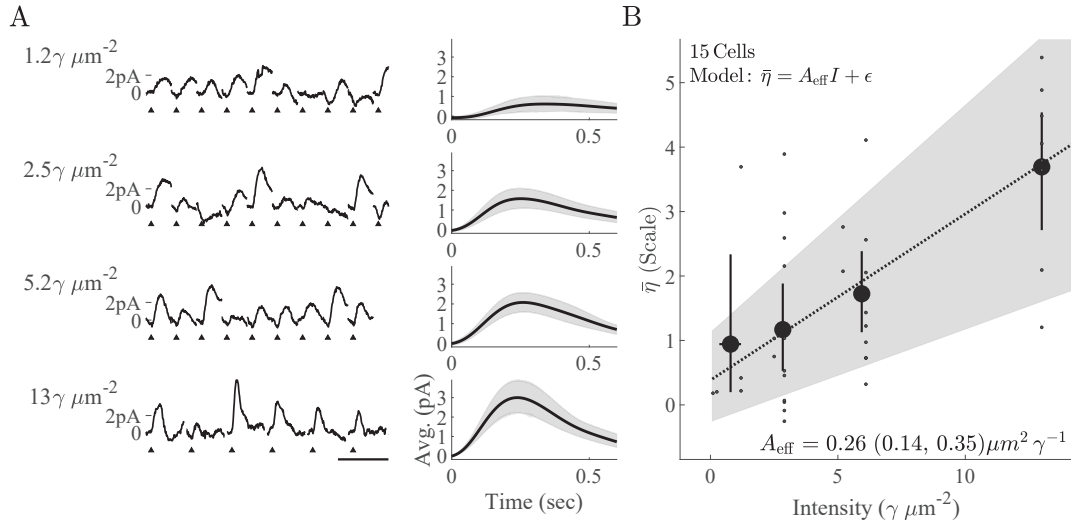


Figure 4.1: *Determination of effective collecting area.* **A.** Representative current responses (*left*;  $V_m = -40$  mV) to 10 ms flashes delivering 1.2, 2.5, 5.2 and  $13 \gamma \mu\text{m}^{-2}$ . Averaged responses (black) from 15 rods are shown on the right with 95% BC<sub>a</sub> confidence regions (gray). *Horizontal scale bar is 2 s for all axes.* **B.** Scale estimates,  $\bar{\eta}$ , as a function of flash intensity,  $I$ . Individual estimates are shown as small markers, mean and 95% BC<sub>a</sub> intervals are depicted by large markers and vertical lines. The effective collecting area,  $A_{\text{eff}}$ , was determined from the slope of the best fitting line (*Dashed line*, 95% BC<sub>a</sub> confidence regions in gray) from the regression of scale onto flash intensity, and was calculated to be  $0.26 (0.14, 0.35) \mu\text{m}^2$ .

onto single AII amacrine cells through RBCs (Tsukamoto et al., 2001). A key feature of the pathway is control over the gain during photon-event transmissions, to avoid saturating downstream neurons (Dunn, 2006).

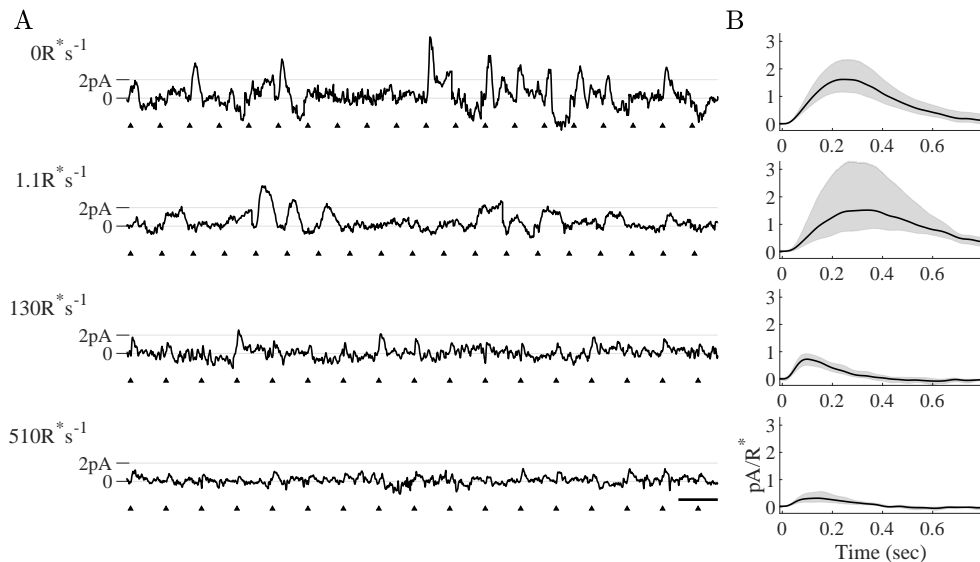


Figure 4.2: *Dim flash responses are sped and reduced by background light.* **A.** Representative current records ( $V_m = -40$  mV) from dark-adapted C57BL/6J rods in darkness ( $0R^* s^{-1}$ ), and background intensities of 1.1, 130 and  $510R^* s^{-1}$ . Flashes of fixed intensity were delivered as indicated by the arrowheads. Scale bar (bottom right of A) indicates 200 ms and applies to all plots in A. **B.** Averaged gain,  $m_{\text{flash}}/f$ , from 2 to 3 flash intensities, corresponding to the background intensities in A.

We measured the gain of rod photoreceptors by recording responses to brief flashes of light that elicited no more than 20% of the maximal response, in darkness and in varied background intensities (Fig. 4.2A). We then averaged the trials of flash responses (“hits”) and calculated the gain from the correlation with a template derived from the average of all trials. Averages were then scaled by the flash intensity (Fig. 4.2B and Methods (§ 4.3)). Gain in each background intensity was scaled by the gain in darkness,  $G/G_{\text{dark}}$ , and was plotted as a function of background intensity in Fig. 4.3.

At dim backgrounds producing fewer than  $2R^* s^{-1}$ , we observed on average a slight increase in gain before gain fell inversely proportional to increases in background intensity.

Previous reports showed that changes in sensitivity as a function of background intensity were well-characterized by the Weber-Fechner relation, which estimates a 'dark light' constant that identifies the background light level required to reduce sensitivity by half. Our measurement of gain is similar to that of measurements of sensitivity (Morshedian and Fain, 2017), and we found a similar result fitting the Weber-Fechner function to gain (Fig. 4.3 smooth trace,  $I_0 = 49.7 (23.2, 134) \text{ R}^* \text{ s}^{-1}$ ). The large variability can probably be attributed to the difficulty of maintaining whole-cell recordings from rods stable for the long periods of time required for these measurements. This profile of gain change is in agreement with previous reports of background dependence of gain in rod photoreceptors (Dunn, 2006) and identifies a component of rod pathway adaptation which may be imparted by rod adaptation alone.

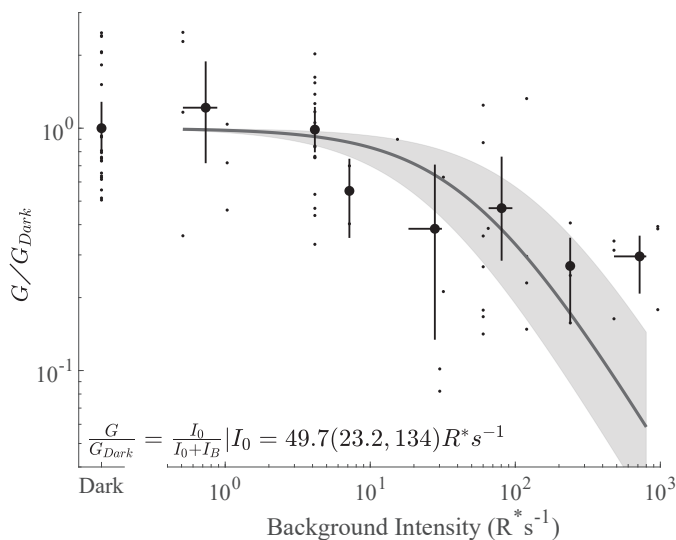


Figure 4.3: *Gain at photoreceptors is reduced by background light.* Dark-scaled gain,  $G/G_{Dark}$ , as a function of background intensity,  $I_B$ . The reduction in gain loosely follows a Weber-Fechner relationship,  $I_0/(I_0 + I_B)$  with a background intensity which decreases gain by half,  $I_0$ , of  $49.7 (23.2, 134) \text{ R}^* \text{ s}^{-1}$ .

### 4.4.3 Background light asynchronously affects rod-bipolar response dynamics

Light responses of mouse RBCs in dark-adapted retinas show a nonlinear dependence on stimulus intensity at the transmission of photon absorptions through the synapse between the rod and RBC (Field and Rieke, 2002b). This nonlinearity is due to the RBC mGluR6 transduction cascade, which operates near saturation in darkness. The nonlinearity produces a threshold-like filtering of rod signals to improve fidelity. The extent of nonlinearity is altered by changes in the extent of mGluR6 cascade saturation imposed by application of APB or LY341495, or by presentation of a weak background light (Sampath and Rieke, 2004). Further, the nonlinearity appears to be preset by the RBC (Okawa et al., 2010a). We sought to extend previous findings and derive parameters for future mathematical modeling of adaptation in higher-order processing of signals through the rod pathway.

To characterize the biophysical nature of RBC adaptation, we measured current responses to brief flashes of light in slice preparations of dark-adapted retinas (Fig. 4.4). We visually identified RBC somata by their location at the boundary of the inner nuclear layer and the outer plexiform layer, by their characteristically large and rapid flash responses, and by filling cells with Alexa Fluor 750 added to the recording solution for morphological verification at the end of the experiment (Fig. 4.4A). Response families to increasing flash intensities were recorded in a series of background intensities, and responses were averaged at each flash intensity. Increases in background light resulted in more rapid and smaller-amplitude responses (Fig. 4.4B). Flash intensity ranges used for each background are listed in Table 4.1. Note that the amplitude of the inward-current deflections corresponded with flash intensity, such that the brightest flashes caused the largest inward current deflections. We observed that the relationship between flash intensity and response amplitude apparently linearized with even the dimmest of background intensities. Furthermore, we saw a distinct reduction in maximal response amplitude, which was accompanied by an apparent acceleration of response decay. It should be noted that, unlike photoreceptors which are best fit with a first-order decay exponential (Chen et al., 2000, *for example*), the decay phase of RBC flash responses is non-uniform across flash intensities and often has an oscillatory component. For



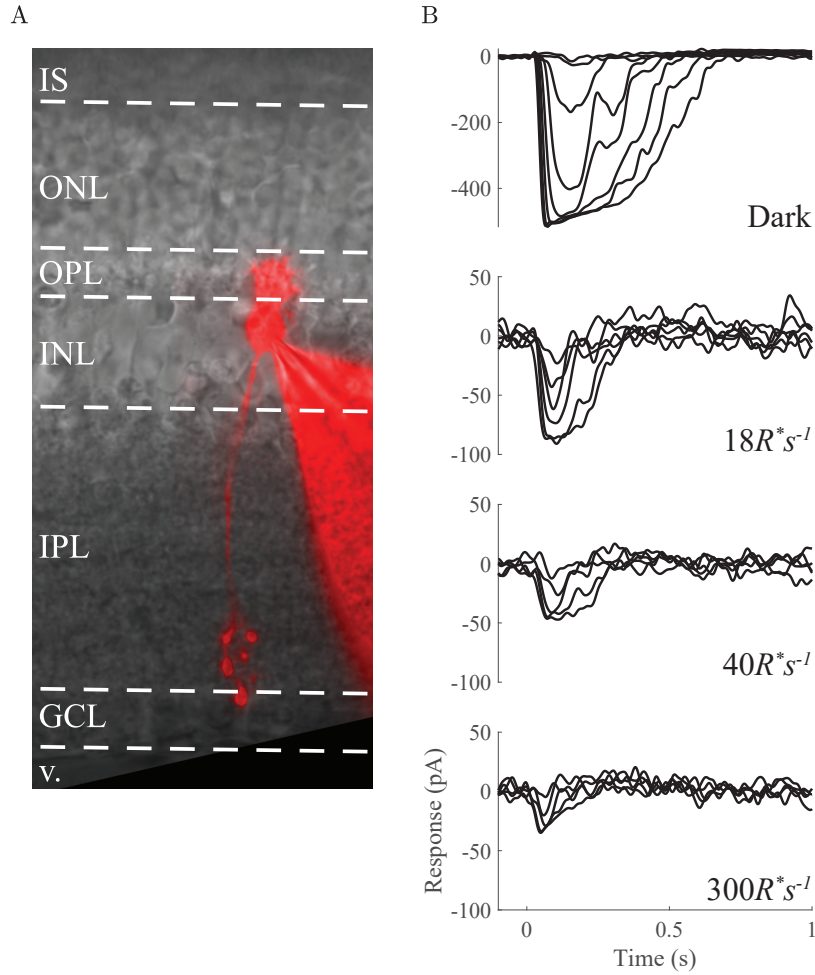


Figure 4.4: *Rod bipolar cell responses in background light.* **A.** Rod bipolar cells (filled with Alexa750 dye, red) were recorded from retinal slices using whole-cell patch configuration in voltage-clamp mode ( $V_m = -60$  mV). **B.** Current responses to brief flashes of light from RBCs (from top to bottom) in darkness ( $R_{max} = -320$  ( $-407$ ,  $-261$ ) pA), and in the following background illuminations:  $18 \text{ R}^* \text{ s}^{-1}$  ( $R_{max} = -81.0$  ( $-118$ ,  $-47.7$ ) pA),  $40 \text{ R}^* \text{ s}^{-1}$  ( $R_{max} = -43.2$  ( $-57.2$ ,  $-30.1$ ) pA), and  $300 \text{ R}^* \text{ s}^{-1}$  ( $R_{max} = -25.4$  ( $-31.1$ ,  $-20.4$ ) pA). Filter bandwidth: 0 to 50 Hz.  $R_{max}$  values are given as mean (95% BC<sub>a</sub> confidence intervals). *Abbreviations:* IS, inner segment; ONL, outer nuclear layer; OPL, outer plexiform layer; INL, inner nuclear layer; IPL, inner plexiform layer; GCL, ganglion cell layer; v., vitreous.

these reasons, we did not attempt to quantify a time-constant of decay. Instead, we focused on the stimulus-response parameters as measures of the effects of background light on RBC flash responses.

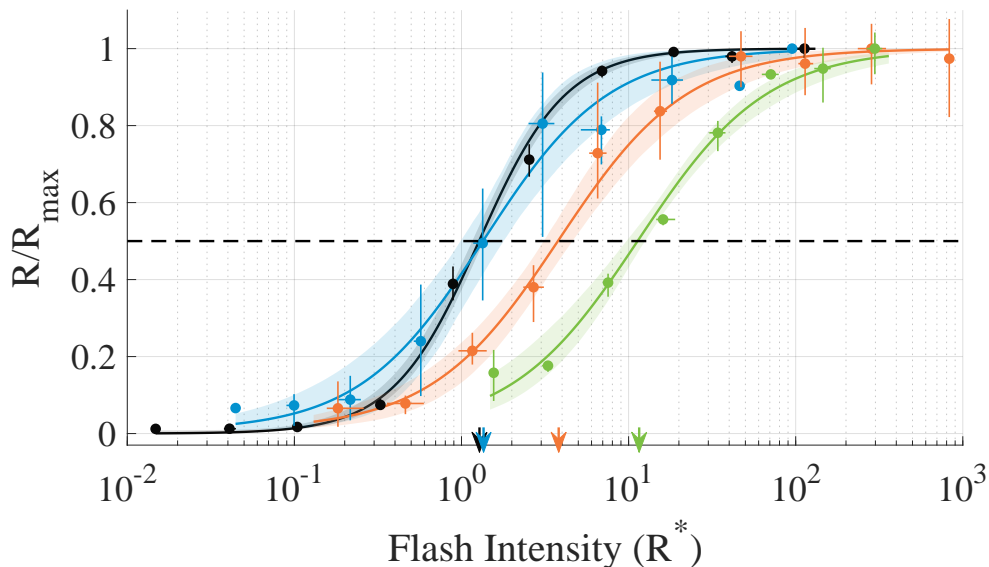


Figure 4.5: *Effects of background light on stimulus-response relationships.* Normalized response amplitudes as a function of flash intensity were fit with a Hill equation (Eqn. 4.2, smooth lines). Background intensities used: darkness (black),  $1.4 \text{ R}^* \text{ s}^{-1}$  (blue),  $51 \text{ R}^* \text{ s}^{-1}$  (orange), and  $600 \text{ R}^* \text{ s}^{-1}$  (green). As background light intensity increased, first, a flattening of the stimulus-response curve was observed (blue), which corresponded to a decrease in the  $n$  parameter from 1.6, in darkness, to  $\sim 1$  by  $10 \text{ R}^* \text{ s}^{-1}$  (see Table 4.1). Then a rightward shift in the  $I_{1/2}$  parameter from 1.27 (1.19, 1.39)  $\text{R}^*$  in darkness (black arrow), to 3.84 (3.16, 4.73)  $\text{R}^*$  in a background light of  $51 \text{ R}^* \text{ s}^{-1}$  (orange arrow), and 11.5 (10.1, 12.8)  $\text{R}^*$  in a  $600 \text{ R}^* \text{ s}^{-1}$  background light (green arrow). *Markers and vertical lines indicate mean and 95 percent  $BC_a$  confidence intervals.*

To characterize the biophysical properties of the RBC flash-response, we fit a 2-parameter Hill equation (Eqn. 4.2) to normalized response amplitudes versus stimulus intensity. Response amplitudes for each cell were calculated from 2 to 5 runs of flash-intensity families that covered the dynamic range of the RBC response (see Table 4.1). Flash intensities were roughly doubled through the flash family protocol. Maximal responses, in darkness and in

background light, were highly variable, falling from  $-320$  ( $-407$ ,  $-261$ ) pA in darkness to  $-18$  ( $-26$ ,  $-11$ ) pA in  $600 \text{ R}^* \text{ s}^{-1}$ . To normalize response amplitudes to the range 0 to 1, amplitudes were scaled by the maximal response amplitude,  $R/R_{\text{max}}$ , on a cell-to-cell basis (Fig. 4.5). We generated stimulus-response curves from fitted parameters (Fig. 4.5 *smooth lines*) and  $\text{BC}_a$  confidence regions (*shaded regions*) and plotted them for a selection of background intensities in Fig. 4.5. In dim backgrounds (producing fewer than  $\sim 2 \text{ R}^* \text{ s}^{-1}$ ; blue curve), we observed a flattening of the stimulus-response curve accompanied with almost no shift in the  $I_{1/2}$  parameter. By a background intensity producing  $51 \text{ R}^* \text{ s}^{-1}$  (orange curve), a level at which rod gain is reduced by half, the stimulus-response curve was right-shifted by a little more than two-fold while not appearing to flatten any further. In the brightest background intensities tested ( $600 \text{ R}^* \text{ s}^{-1}$ , green curve), the stimulus-response curve right-shifted further, reflecting a log-unit decrease in sensitivity. Fitting parameters from all of the backgrounds tested are given in Table 4.1.

The nonlinearity in the RBC stimulus-response curve is quantified by the Hill coefficient,  $n$ . The rod stimulus-response curve is best fit with an exponent of 1 (see Ch. 3) or by a saturating single-exponential function (Chen et al., 2010). For RBCs, the Hill coefficient is much larger in darkness. Estimates from fitting Eqn. 4.2 to the RBC responses were the following:  $n = 1.68$  (1.55, 1.89)  $\text{R}^*$   $I_{1/2} = 1.27$  (1.19, 1.39)  $\text{R}^*$ . Increases in background intensities that were too dim to desensitize rods, i.e., producing fewer than  $\sim 3 \text{ R}^* \text{ s}^{-1}$ , drastically flattened the stimulus-response curve, reducing  $n$  to 1.02 (0.85, 1.3) in  $2.8 \text{ R}^* \text{ s}^{-1}$  ( $p < 0.05$ ). Note that over the same background regime, the dimmest flashes on average elicited a greater fractional response. Further, responses to near-saturating flashes were slightly compressed (compare blue to black plots in Fig. 4.5). For visual comparison,  $n$  parameter fits were plotted against background intensities in Fig. 4.6A. These results show that relief of the nonlinearity occurs at background intensities too dim to elicit changes in rod gain control.

The Hill parameter,  $I_{1/2}$ , is a robust estimate of the RBC flash sensitivity that is independent of the maximal response amplitude (Okawa et al., 2010b). To estimate RBC flash sensitivity, we took the inverse of the  $I_{1/2}$  parameter and plotted the averaged values scaled

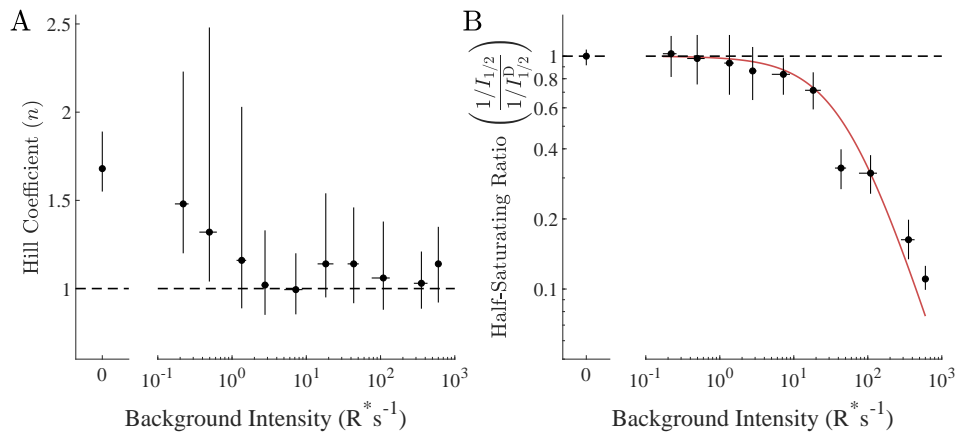


Figure 4.6: *Hill fit parameters for rod bipolar cell response-intensity relationships.* **A.** Hill coefficients as a function of background intensity. Points indicate means and lines indicate  $BC_a$  95 confidence intervals. Dashed line at  $n = 1$  represents complete relief of nonlinearity. **B.** RBC sensitivity,  $1/I_{1/2}$ , scaled by sensitivity in darkness as a function of background intensity. The dashed line in B indicates sensitivity in darkness of  $1/1.68 R^*$ . For comparisons, we show the Weber relation from the reduction in rod photoreceptor gain with  $I_0 = 49.7$  (23.2, 134)  $R^* s^{-1}$  (smooth line in Fig. 4.3). RBC sensitivity appears to have a similar background dependence as that of rod gain. *Data are also summarized in Table ??*

by the value in darkness as a function of background intensity in Fig. 4.6B. RBC sensitivity declined with increases in background intensity in the same regime as rod gain changes. To compare changes in rod bipolar flash sensitivity to gain in rod photoreceptors we overlaid the Weber-Fechner relationship from rod gain experiments (shown in red), with  $I_0 = 49.7$  (23.2, 134)  $\text{R}^* \text{s}^{-1}$ . The decline in RBC flash sensitivity remarkably parallels the changes in rod sensitivity (Chen et al., 2010, Morshedean and Fain, 2017) and rod gain (Fig. 4.3) observed during rod adaptation. These data suggest that rod adaptation has a direct influence on the flash sensitivity of RBCs during rod-bipolar adaptation. This direct influence appears at backgrounds brighter than those that produce the relief in nonlinearity. These observations support the hypothesis that the nonlinearity is post-synaptic in origin (Sampath and Rieke, 2004, Okawa et al., 2010a), and RBC sensitivity may be imparted by rods. Together, our results suggest there is a mechanism of adaptation, independent of rod adaptation that is intrinsic to RBCs.

#### 4.4.4 Background light suppresses the RBC maximal response

In the whole-cell patch configuration, RBC flash responses degrade in quality and amplitude over the time span of a 1 to 2 min following ‘break-in’. The reason for this rundown is unknown; however, we found that by decreasing the size of the recording electrode to resistance values of about  $16 \text{ M}\Omega$ , we could extend the duration of responsiveness by more than a minute. We first analyzed maximal responses from families of graded flash intensities. However, by the second to third family the maximal response was as low as 60% of the first maximal response, even with smaller recording pipettes and abundant nucleoside triphosphates in the recording solution. We characterized the rundown in our slice preparations in preliminary experiments, where we repeatedly delivered saturating flashes in darkness. We found that the maximal response amplitude slowly degrades in a linear trend over time (*data not shown*). In similar experiments, we found that the maximal recovery of the photoreponse peak on backgrounds of either  $50 \text{ R}^* \text{ s}^{-1}$  or  $200 \text{ R}^* \text{ s}^{-1}$  was between 5 to 10 s, followed by a linearly decreasing response amplitude over the course of  $\sim 2$  min, which was not re-

Background (R* s <sup>-1</sup> )	$\Phi$ (R*)	I <sub>1/2</sub> (R*)	$n$
Dark [46]	0.015→120	1.27 (1.19, 1.39)	1.68 (1.55, 1.89)
0.22 [3] (0.17, 0.26)	0.011→21	1.24 (1.04, 1.56)	1.48 (1.2, 2.23)
0.5 [5] (0.36, 0.62)	0.03→71	1.3 (1.03, 1.68)	1.32 (1.04, 2.48)
1.4 [4] (1.2, 1.6)	0.044→95	1.36 (1.03, 1.86)	1.16 (0.888, 2.03)
2.8 [5] (2.5, 3.1)	0.022→84	1.47 (1.16, 1.96)	1.02 (0.851, 1.33)
7.2 [5] (5.1, 8.9)	0.09→94	1.52 (1.29, 1.86)	0.994 (0.854, 1.2)
18 [7] (14, 23)	0.051→220	1.78 (1.49, 2.15)	1.14 (0.95, 1.54)
44 [5] (36, 51)	0.16→830	3.84 (3.19, 4.73)	1.14 (0.917, 1.46)
110 [4] (76, 130)	0.058→420	4.04 (3.38, 4.95)	1.06 (0.88, 1.38)
360 [5] (280, 430)	0.26→1000	7.8 (6.4, 9.46)	1.03 (0.886, 1.21)
600 [3] (600, 600)	1.5→330	11.5 (10.1, 12.8)	1.14 (0.921, 1.35)

Table 4.1: *Stimulus-response properties for RBCs*. Values are reported as means (95% BC<sub>a</sub> confidence interval) where applicable. Hill fit parameters for half-saturating intensities, I<sub>1/2</sub>, and Hill coefficients,  $n$ , were derived from fitting Eqn. 4.2 to normalized response amplitudes elicited from specified stimulus intensity ranges,  $\Phi$ , during the presentation of the corresponding background intensity. Counts are shown in square brackets next to the corresponding background.

covered by turning off the background light. Likewise, recovery during dark adaptation in the period following the cessation of a 10 to 12s background light was observed to reach a maximum in 5 to 10s, followed, again, by linearly decreasing response amplitudes. These observations were similar with those made in dogfish ‘ON’ bipolar cells (Shiells and Falk, 1999) and tiger salamander RBCs (Nawy, 2004), albeit on a faster time course. Other reports suggest that the initial transient peak of the saturated response, termed ‘inactivation’, is recovered rapidly within 2s following background light exposure (Berntson et al., 2004a). From these results, we devised a protocol to study maximal response amplitudes in mouse RBCs that mitigated the effects of rundown (Fig. 4.7 *top*).

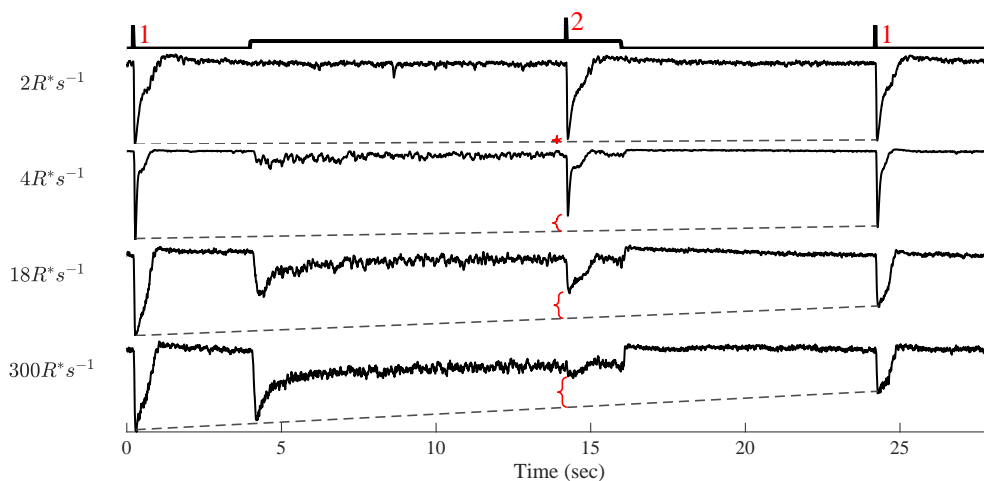


Figure 4.7: *RBC maximal response is attenuated in background light.* Current responses of RBCs were recorded, in voltage clamp ( $V_m = -60\text{mV}$ ), to brief flashes of light that were delivered in during the presentation of a background light (2), bracketed by brief flashes in darkness (1). Stimulus monitor is shown at the top. To account for cellular rundown, a linear trend was computed from the maximal response peaks in darkness (dashed line), and the maximal response amplitudes during background illumination were calculated relative to their expected maximum (red brackets). Intensities of flashes in darkness (1) were 20 to 30  $R^*$ . Flashes delivered during background illumination (2) were 20 to 1000  $R^*$  and were scaled with the background intensity to ensure a saturated response (see Table 4.1 for intensity ranges).

To verify that  $R_{\text{max}}$  amplitude attenuation was due to background light and not cellular

rundown, we required maximal responses in darkness and in background light from the same cell. The experiment was conducted as shown in Fig. 4.7 *top*. A saturating flash was delivered in darkness (intensity 1), and the cell was allowed to recover to baseline. Then, a background light was turned on and held constant for 8 to 10s before a second saturating flash was delivered (intensity 2). The background light was then turned off, and the cell was allowed another 8 to 10s to adapt to darkness. A final saturating flash was then delivered (intensity 1, again) before terminating the experiment. Assuming a linear degradation of the maximal response, we fit a line to the peaks in the bracketing dark responses with respect to time (Fig. 4.7 *dashed lines*). Using the parameters of these linear fits, we calculated the expected maximal response peak at the time of the measured peak of the response in background light (Fig. 4.7 *red brackets*). As the background light level was increased, the maximal response peak was attenuated further from the expected maximum (compare peaks at stimulus 2 to corresponding dashed line). Note that in brighter backgrounds where rod adaptation is occurring, we observed slightly larger differences between the bracketing dark response peaks. This method allowed us to account to some degree for any effects of rod adaptation on the maximal response of RBCs.

To characterize the relationship between background intensity and the amount of attenuation of the maximal response, we took the ratio of the recorded response peaks in background light,  $R_{\max}$ , as a fraction of the predicted maximum,  $\hat{R}_{\max}$ . The fractional maximum responses,  $R_{\max}/\hat{R}_{\max}$ , are plotted in Fig. 4.8. We quantified this relationship by estimating parameters of an inverse Hill function (Eqn. 4.3), which fit remarkably well (Fig. 4.8 *smooth curve*). In the dimmest background intensities we tested, the fractional maximum response never exceeded that of the response in darkness ( $R_0 = 0.92$  (0.90, 0.95)). In a background producing  $2.5 \text{ R}^* \text{ s}^{-1}$ , the response maximum was consistently  $\sim 90\%$  of predicted, corresponding to a response peak of  $-281$  ( $-416$ ,  $-186$ ) pA. In brighter backgrounds, attenuation rapidly increased before tapering off around  $R_{\max}/\hat{R}_{\max} = 0.61$  (0.67, 0.56) ( $\Delta R = 0.31$  (0.25, 0.37)). In the brightest background we tested,  $400 \text{ R}^* \text{ s}^{-1}$ , the attenuation reached below 0.5, which corresponded to a peak amplitude of  $-18.3$  ( $-36.5$ ,



$-11.1)$  pA<sup>1</sup>. The inflection point of the model, i.e., the background level which produced half-maximal attenuation, was  $I_{1/2}^B = 6.0$  (4.2, 7.9)  $R^* s^{-1}$ . Interestingly, this desensitization occurred at a background intensity brighter than the point at which the stimulus-response nonlinearity was completely relieved. Furthermore, desensitization was maximized in backgrounds dimmer than the flash sensitivity drop-off ( $\sim 50 R^* s^{-1}$ ). These results suggest that attenuation of  $R_{\max}$  is neither directed by relief of nonlinearity nor imparted by rod adaptation. Together, we show that RBC adaptation may have more than one distinct molecular mechanism.

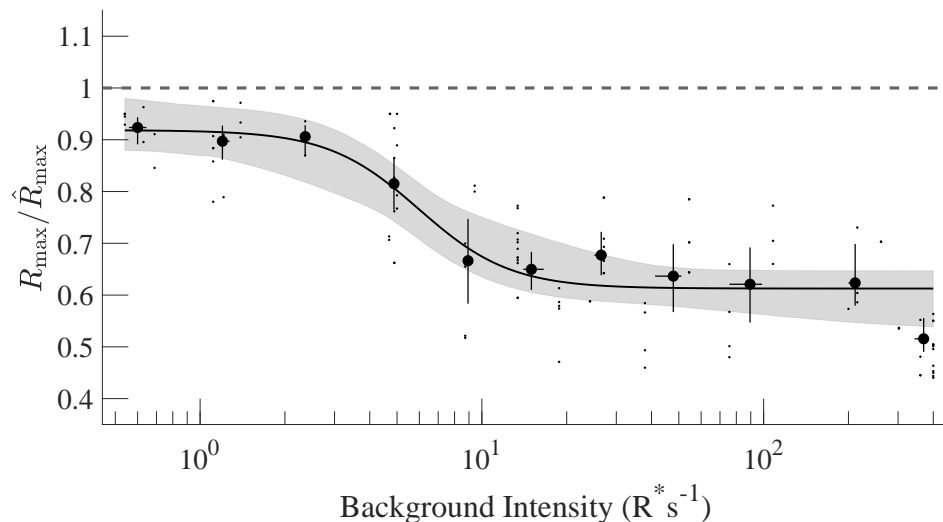


Figure 4.8: *Maximal response amplitudes are attenuated in background light.* Relative change in  $R_{\max}$  from darkness as a function of background intensity. Peak responses,  $R_{\max}$ , from experiments described in Fig. 4.7 were scaled by the predicted maximal response,  $\hat{R}_{\max}$ . Individual cells are shown as small points, means and 95%  $BC_a$  confidence intervals are shown as large points with vertical lines. Data were binned logarithmically with respect to background intensity, and an inverse Hill function was fit to the data (Eqn. 4.3, smooth curve, 95%  $BC_a$  confidence region is shown in gray shaded area). Fitted parameters for RBCs were:  $R_0 = 0.92$  (0.90, 0.95),  $\Delta R = 0.31$  (0.25, 0.37),  $I_{1/2}^B = 6.0$  (4.2, 7.9)  $R^* s^{-1}$  and  $n = 2.7$  (1.3, 3.0).

<sup>1</sup>In backgrounds brighter than this, response peaks of the single flash response were too difficult to distinguish from the noise, unlike in flash families where averaging allows responses to be distinguished.

#### 4.4.5 Calcium entry during light exposure modulates the RBC maximal response

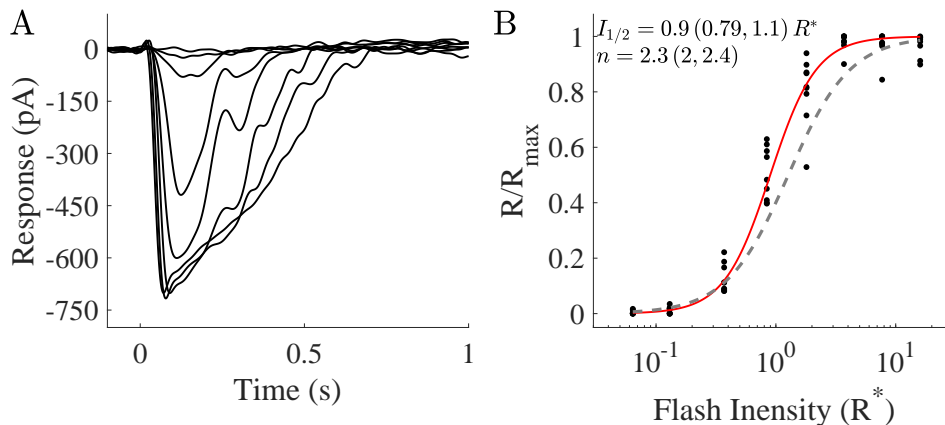


Figure 4.9: *Dialysis of 10 mM BAPTA increases nonlinearity in darkness.* **A.** Representative RBC responses with 10 mM BAPTA loaded in the recording pipette. Current responses, in voltage clamp ( $V_m = -60$  mV), to 10 ms flashes of the following intensities: 0.064, 0.13, 0.37, 0.84, 1.8, 3.7, 7.7 and 16  $R^*$ . **B.** Normalized response amplitudes for 9 cells (black points) fit with Eqn. 4.2 (red curve) compared to the Hill fit from control cells (dashed curve). Hill fit parameters for red curve were:  $I_{1/2} = 0.9 (0.79, 1.1) R^*$  and  $n = 2.3 (1.9, 2.4) R^*$ . Averaged maximal responses ( $R_{max}$ ) in darkness were  $-330 (-480, -230)$  pA. Uncertainties are expressed as means with BC<sub>a</sub> 95% confidence intervals in parentheses.

To study the effects of calcium on RBC adaptation, we loaded the recording pipette with the fast calcium chelator BAPTA (10 mM, Sigma). It was previously shown for mouse RBCs that BAPTA buffering of  $Ca_i^{2+}$  reduced transient peaks of the photoresponse and increased nonlinearity of the stimulus-response curve (Berntson et al., 2004a). We recorded flash response families from RBCs in darkness (Fig. 4.9A) and generated a stimulus-response curve from 9 cells (Fig. 4.9B). Confirming prior reports, we found a slight increase in sensitivity, i.e., a reduction in  $I_{1/2}$  ( $0.9 (0.79, 1.1) R^*$ ,  $p < 0.05$ ), and a strong increase in nonlinearity ( $n = 2.3 (1.9, 2.4) R^*$ ,  $p < 0.05$ ). In contrast to previous reports with application of 10 mM BAPTA, we did not observe a significant difference in averaged maximal responses in darkness ( $-330 (-480, -230)$  pA) compared to control conditions ( $R_{max} = -320 (-407,$

−261) pA). Further, response kinetics did not appear appreciably slower. This is probably due to differences between our recording solution and those used in other reports.

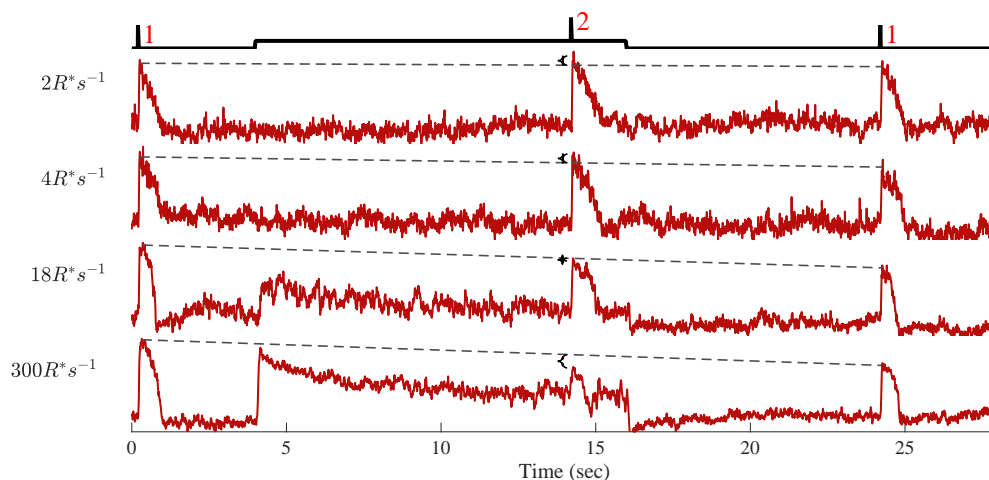


Figure 4.10: *Large positive holding voltage and BAPTA decrease the effect of background illumination on maximal response amplitudes.* Current responses to saturating flashes were recorded, as in Fig. 4.7, with the addition of 10 mM BAPTA to the recording pipette and at a holding potential of  $V_m = +50$  mV. Brief flashes of light were delivered during the presentation of a background light (2), bracketed by brief flashes in darkness (1). Stimulus monitor is shown at the top. Dashed lines indicate the expected rundown for the shown cell as calculated from linear fits to the peaks, with respect to time, of the saturating flash responses in the bracketing dark regions. Black braces at the peaks of the responses in background light indicate the fractional difference between the response peak and the expected peak (dashed line).

RBC responses to prolonged steps of light have a characteristic transient peak followed by a rapid sag toward a plateau, a feature that is nearly abolished by application of BAPTA or holding the cell at a large positive voltage (Berntson et al., 2004a, Nawy, 2004). If calcium entry into the RBC dendrites drives the rapid inactivation of the TRPM1 current, and the TRPM1 channel is directly, or indirectly, affected by local increases in  $Ca_i^{2+}$ , then it is possible that the buffering capacity of BAPTA may be overwhelmed by  $Ca^{2+}$  entry (Legendre et al., 1993) or not rapid enough to prevent action in the micro-domain of the channel. This might explain why paired pulses with BAPTA loaded in the pipette still

showed a reduction in amplitude by about 20% in short-duration paired-pulse experiments (Berntson et al., 2004a).

To eliminate the possibility of this phenomenon, we recorded responses to saturating flashes in darkness and in backgrounds, with the membrane potential clamped to +50 mV and with 10 mM BAPTA in the recording pipette (Fig. 4.10). Using the same protocol and analysis as described earlier (Figs. 4.7 and 4.8), we show that peak responses increasingly exceeded predicted maximums in dim background levels less than  $\sim 10 \text{ R}^* \text{ s}^{-1}$  (see below and Fig. 4.11). Note that current deflections are outward oriented<sup>2</sup> due to the holding potential being near the reversal potential of  $\text{Na}^+$  (Nernst potential of +56 mV for our solutions). In backgrounds brighter than  $\sim 10 \text{ R}^* \text{ s}^{-1}$ , response peaks were increasingly smaller fractions of  $\hat{R}_{\text{max}}$ . Interestingly, we observed that the slope of the predicted maximal peaks became steeper with increasing background intensities, again reflecting adaptation in rods. Response peaks in darkness (before background steps) were 78 (74, 86) pA and decreased to 32 (31, 33) pA in  $\sim 300 \text{ R}^* \text{ s}^{-1}$ . Consistent with previous reports, we found that inclusion of BAPTA and holding at  $V_m = -50 \text{ mV}$  abolished the rapid transient peak at the onset of the background step. However, we found that brighter backgrounds still elicited a slower sag component that reached a plateau of 45 (35, 56)% of the maximal response peak in darkness. In control conditions, the plateau reached 27 (21, 35)% of the maximal response peak in darkness, which was slightly significantly less than with BAPTA at a background intensity producing  $300 \text{ R}^* \text{ s}^{-1}$  ( $p = 0.049$ ).

To compare the effects of  $\text{Ca}^{2+}$  on the suppression of  $R_{\text{max}}$ , we calculated fractional maximum responses in background intensities comparable to those calculated in our previous experiments. The background intensity was related to the fractional suppression of  $R_{\text{max}}$ ,  $R_{\text{max}}/\hat{R}_{\text{max}}$ , by fitting an inverse Hill function to the data. The data and background-suppression relationships were plotted, along with the data from control conditions in Fig. 4.11. Similar to previous reports, we observed that buffering  $\text{Ca}_i^{2+}$  abolished suppression of  $R_{\text{max}}$  at scotopic background intensities (Berntson et al., 2004a, Nawy, 1999). In our exper-

---

<sup>2</sup>The outward current is likely to be predominantly carried by potassium ( $\text{K}^+$ ) efflux.

iments the background levels were below  $\sim 10 \text{ R}^* \text{ s}^{-1}$ . It should be noted that the amplitude of saturated responses in backgrounds did not exceed that of saturated responses recorded in the first dark period of the protocol. That is, response peaks were either slightly less than, or identical in amplitude (compare peak heights in Fig. 4.10, for example). However, in brighter background intensities,  $R_{\text{max}}$  suppression was apparent<sup>3</sup>.

From fits using Eqn. 4.3, we found that in the  $\text{Ca}_i^{2+}$ -buffered condition,  $I_{1/2}^B$  shifted rightward significantly from control conditions ( $I_{1/2}^B = 33 (16, 48) \text{ R}^* \text{ s}^{-1}$ ;  $p < 0.05$ ). Concomitantly, the  $R_0$  parameter was significantly higher in the  $\text{Ca}_i^{2+}$ -buffered condition ( $R_0 = 1.03 (0.98, 0.11)$ ;  $p < 0.05$ ). To confirm this difference, we performed a repeated-measures analysis of variance (ANOVA) on the fractional  $R_{\text{max}}$  suppression measurements over the lowest six background levels and found a significant effect of  $\text{Ca}_i^{2+}$ -buffering ( $p = 0.00015$ ), as well as a significant interaction between background level and  $\text{Ca}_i^{2+}$ -buffering ( $p = 0.0002$ ). Through *post hoc* analysis (see Methods (§ 4.3)), we found that control conditions were significantly reduced at the following background intensities:  $4.8 \text{ R}^* \text{ s}^{-1}$  ( $p = 0.0009$ ),  $9.8 \text{ R}^* \text{ s}^{-1}$  ( $p = 0.0051$ ), and  $18.8 \text{ R}^* \text{ s}^{-1}$  ( $p = 0.0091$ ). Although no significant difference was found at the three dimmest background intensities tested, it should be noted that control conditions were on average less by 0.10 (0.044, 0.16). These results suggest that  $\text{Ca}^{2+}$  entry is primarily responsible for desensitization of the photoresponse at background levels too dim to cause rod adaptation. Furthermore, desensitization of the rod photoresponse during rod adaptation may also directly contribute to RBC maximal response amplitudes at brighter backgrounds.

## 4.5 Discussion

Adaptation is characterized by a speeding of the kinetics and a reduction in the amplitude of light responses with increases in ambient illumination (Fain et al., 2001). Adaptation keeps the retina and the rest of the visual system responsive and capable of transmitting properties

---

<sup>3</sup>At intensities brighter than  $300 \text{ R}^* \text{ s}^{-1}$ , we could not distinguish flash responses from the considerable noise.

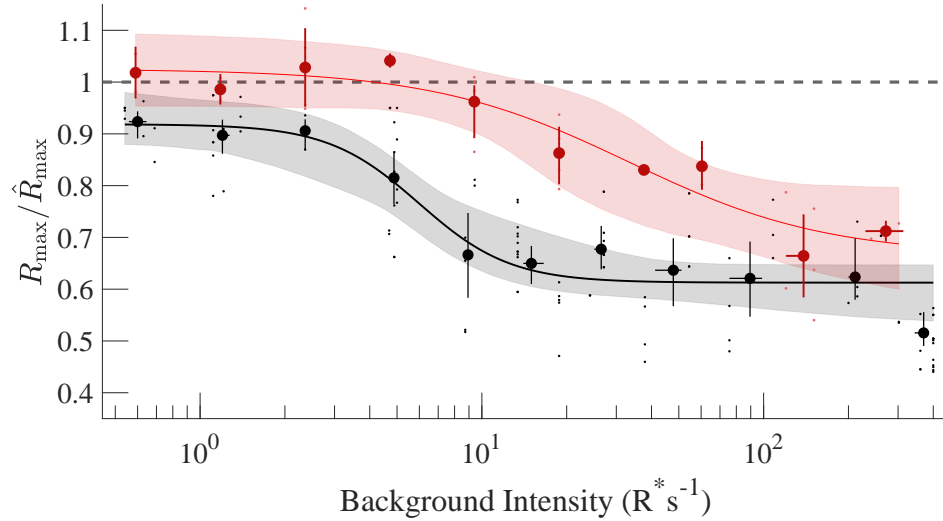


Figure 4.11: *Calcium entry during light exposure modulates the maximal response amplitude.* Relative change in  $R_{\max}$  from darkness as a function of background intensity for control conditions (black;  $V_m = -60$  mV; normal internal) and  $\text{Ca}^{2+}$ -buffered conditions (red;  $V_m = 50$  mV; 10 mM BAPTA internal). Control data are those found in Fig. 4.8. Dim background levels (less than  $\sim 10 \text{ R}^* \text{ s}^{-1}$ ) yielded responses that were sometimes larger than predicted (dashed line) in the  $\text{Ca}^{2+}$ -buffered condition. The relationship of fractional change versus background intensity for the  $\text{Ca}^{2+}$ -buffered condition appeared shifted upward and rightward, with significant changes in two fitted parameters:  $R_0 = 1.03$  (0.98, 0.11) ( $p < 0.05$ ) and  $I_{1/2}^B = 33$  (16, 48)  $\text{R}^* \text{ s}^{-1}$  ( $p < 0.05$ ). Other fitted parameters for the  $\text{Ca}^{2+}$ -buffered condition were  $\Delta R = 0.36$  (0.23, 0.50) and  $n = 1.2$  (0.6, 2.3).

of the visual landscape to downstream neurons. Without adaptation, cells would become saturated and unable to respond to further changes in illumination. The rod pathway is a specialized circuit, capable of converting a few photons into sight by discriminating the absorption of light from cellular noise (Hecht et al., 1941, van der Velden, 1946, Barlow, 1957, Baylor et al., 1979). To achieve this remarkable feat, the pathway must have multiple points of control over responsiveness.

The question as to where these control points are situated has been recently investigated. Previous reports (Dunn, 2006) and our own data (Fig. 4.3) show that rods are able to adjust the gain of the response to a few photons as a function of background illumination. However, gain control in rods and linear pooling of 20 to 100 rods isn't enough to drive the nonlinearity observed in downstream neurons, which experience their own forms of adaptation at background intensities too dim to cause rod photoreceptor adaptation (Rushton, 1965, Sampath and Rieke, 2004, Dunn, 2006). To determine where downstream adaptation begins, we probed the first visual synapse, and our results confirm and expand upon an earlier hypothesis that RBC dendrites are suitable sites of dim light adaptation.

We show that RBC adaptation can be characterized by three parameters of Hill equations: flash sensitivity by the  $I_{1/2}$  parameter, response nonlinearity by the  $n$  parameter, and maximal response amplitude by the  $R_{\max}$  parameter. We have characterized the ranges over which each parameter contributes to adaptation and shown that calcium entry during light exposure imposes a negative feedback on the transduction machinery to set these ranges. We show that RBCs are coordinated with upstream rod photoreceptors, and RBCs have an intrinsic ability to respond robustly to single-photon absorptions in a minority of the rods, while continuing to signal at brighter intensities that also cause rod adaptation.

#### **4.5.1 Feed-forward adaptation**

The synapses between rods and RBCs are tuned to transmit small changes in rod membrane potential to much larger changes in the bipolar-cell membrane potential. Rod synapses accomplish this through implementations of highly sensitive transduction mechanisms, which

both generate and filter noise (Baylor et al., 1979, Rieke and Baylor, 1996, Van Rossum and Smith, 1998, Field and Rieke, 2002a); as well as by tight  $\text{Ca}_i^{2+}$  regulation at the spherule (Morgans et al., 2001, Barnes and Kelly, 2002, Haeseleer et al., 2004), giving essential control over vesicle release. Single-photon absorptions can drive  $\sim 1$  mV changes in membrane potential (Van Rossum and Smith, 1998), enough to elicit a response in downstream bipolar cells. Estimates of the single-photon response in RBCs were up to 10 pA in mouse (Field and Rieke, 2002b, Berntson et al., 2004b). Assuming a  $2 \text{ G}\Omega$  input resistance (Zhou et al., 2006), a shift in the RBC membrane voltage during a single-photon response would be enough to drive L-type  $\text{Ca}^{2+}$  channels at the RBC axon, thus transmitting the signal further downstream.

During prolonged exposure to background light, rod adaptation can be quantified by changes in sensitivity of the single-photon response (Morshedean and Fain, 2017), or by changes in gain of the dim-flash response (Dunn, 2006). Interestingly, rod adaptation follows a Weber contrast function (Aguilar and Stiles, 1954, Morshedean and Fain, 2017), and rods show appreciable adaptation at background levels around  $50 \text{ R}^* \text{ s}^{-1}$  (Fig. 4.2). At this background intensity, we also observed a shift in the  $I_{1/2}$  parameter during RBC adaptation (Fig. 4.6), suggesting that RBC flash sensitivity can be directly controlled by rod adaptation in moderate background illumination. In experiments without calcium feedback, we show that the suppression of  $R_{\text{max}}$  also closely relates to this background intensity, which may represent an upper limit of the intrinsic RBC adaptation mechanism.

In order to maintain responsiveness, the RBC must tune the post-synaptic machinery finely to capture suppression of glutamate release by rods in response to newly arriving photons. If we consider the parameters of the stimulus-response curves in combination with the  $R_{\text{max}}$  effect, the result of adaptation would be to maximize sensitivity to successive photons. In dim backgrounds, this manifests as a  $\text{Ca}^{2+}$ -dependent suppression of  $R_{\text{max}}$ . These changes may also be characterized by a reduction in nonlinearity, which was also observed in dim background intensities (Fig. 4.6). It appears that RBCs have a highly sensitive mechanism to begin adaptation even in extremely dim environments.

In a separate series of experiments not reported in this thesis, I asked whether background



light caused a change in the conductance of the TRPM1 channel. Using nonstationary noise analysis, I estimated the single-channel currents in darkness and in background light and found no differences in single-channel currents at any background level tested. Furthermore, I estimated single channel currents to be similar to previous reports, at 0.4 pA compared to 0.27 pA in (Sampath and Rieke, 2004). Thus, background light leads to a reduction in the number of channels open without affecting the conductance of any one channel.

Interestingly, in the dimmest backgrounds we tested, RBC stimulus-response curves exhibited a flattening, characterized by a decrease in nonlinearity described by the Hill coefficient, while maintaining a stimulus intensity producing a half-maximal response similar to that in darkness. In experiments altering availability of mGluR6 through either activation with receptor agonist, APB, or deactivation with receptor antagonist, LY341495, nonlinearity was characterized by changes to the dim-flash sensitivity (Sampath and Rieke, 2004). In our experiments where BAPTA was included in the recording solution, we observed a stark increase in the nonlinearity of the stimulus-response relationship. Interestingly, this result is similar to the effect of application of mGluR6 agonist, APB, which caused an increased nonlinearity through reduction in dim-flash sensitivity (Sampath and Rieke, 2004). In our case, BAPTA did not reduce amplitudes of dim flashes, but instead led to increased amplitudes at the brighter flash intensities (Figs. 4.9 and 4.5). Consequently, we also observed a leftward shift in the  $I_{1/2}$  parameter, indicating the loading of BAPTA had no appreciable effect on other transduction components. Thus, RBCs remain responsive by a rapid, robust, and  $\text{Ca}^{2+}$ -dependent tuning of the light response.

#### **4.5.2 A role for calcium**

The nonspecific cationic TRPM1 channel is the main channel responsible for the depolarizing currents observed during RBC light responses (Shen et al., 2009, Kaur and Nawy, 2012). TRPM1 is anchored to the post-synaptic membrane through the transmembrane anchoring protein nyctalopin (Pearing et al., 2011) and is apposed to mGluR6, as the result of an extracellular complex containing the anchoring protein ELFN1 (Cao et al., 2015). The

selective wiring of the rod-to-RBC synapse is critically dependent on presynaptic calcium channels (Wang et al., 2017). In several vertebrate species, TRPM1 currents have been shown to be desensitized by background light, a phenomenon that was sensitive to  $\text{Ca}_i^{2+}$  (Kaur and Nawy, 2012, Nawy, 2000, Morgans et al., 2010, Berntson et al., 2004a). We also observed a  $\text{Ca}_i^{2+}$ -dependence of the light response in our  $R_{\text{max}}$  experiments. From our analysis, the  $I_{1/2}^B$  parameter provides an estimate for the background level at which  $R_{\text{max}}$  suppression is half-maximal. Thus,  $I_{1/2}^B$  is functionally relatable to the  $I_0$  parameter of the Weber-Fechner relationship. If  $R_{\text{max}}$  suppression is directly controlled by rod adaptation alone, and  $\text{Ca}^{2+}$  entry during light exposure acts to desensitize TRPM1 channels, then eliminating  $\text{Ca}^{2+}$  entry should shift the  $I_{1/2}^B$  to match the  $I_0$ . However, the shift we observed while holding at a large positive voltage and buffering  $\text{Ca}_i^{2+}$  did not quite reach the level of  $I_0$ . Parameters nevertheless had overlapping confidence intervals, and the shift from control conditions of  $I_{1/2}^B$  was significantly increased ( $p < 0.05$ ). It is possible that the highly uncertain  $\text{Ca}_i^{2+}$  levels exceeded the buffering capacity of our BAPTA-containing recording solution, perhaps as a result of  $\text{Ca}^{2+}$  release from internal stores (Koulen et al., 2005) or some unknown mechanism. This possibility may explain why the  $I_{1/2}^B$  increase during large positive holding potentials and inclusion of BAPTA did not reach the level of rod adaptation more precisely.

In photoreceptors, light closes cGMP channels and leads to a reduction in  $\text{Ca}_i^{2+}$  at the outer segment (Sampath et al., 1999, *for example*). In cones, the transporter NCKX4 is predominantly responsible for rapidly extruding calcium during the light response and resetting the cone  $\text{Ca}^{2+}$  concentration to maintain temporal dynamics. This transporter is also selectively expressed in RBC dendrites (Vinberg et al., 2017), though the role it plays in calcium dynamics of RBCs is unknown. We hypothesize that NCKX4 may be used to rapidly extrude  $\text{Ca}^{2+}$  from the dendrites. Thus,  $\text{Ca}_i^{2+}$  at the RBC dendrites would accumulate in NCKX4<sup>-/-</sup>RBCs, causing a further suppression of  $R_{\text{max}}$ . In preliminary experiments, we used RBC-specific knockouts of NCKX4 and analyzed  $R_{\text{max}}$  suppression. Our preliminary results suggest NCKX4 may play a role in relieving  $R_{\text{max}}$  suppression at dim background intensities (less than  $10 R^* s^{-1}$ ). In other preliminary experiments, data from electroretinogram record-

ings (*from our collaborators at the Kefalov Lab*) suggests that the b-wave was reduced in NCKX4 knockouts as a function of background intensity. In future studies, we will investigate the role of NCKX4 in very dim background intensities, where we might expect the influx of calcium to be small enough not to exceed the exchanger rate.

### 4.5.3 Mechanisms of adaptation

Here, we have investigated mechanisms of rod-to-rod bipolar adaptation in the presence of a background light. We have shown that rod-bipolar adaptation is characterized by parameters of a saturating exponential function. Our results indicate that RBC adaptation is achieved principally by three processes: (1) rapid influx of  $\text{Ca}^{2+}$  during light exposure, which functions to close TRPM1 channels priming them for detection of new photons; (2) RBC dendrites maintaining saturation of the mGluR6 cascade (nonlinearity) to support discrimination of single-photon events conveyed from pooling many noisy rods; and (3) by adaptation conveyed from rod photoreceptors. Our data show that  $\text{Ca}^{2+}$  entry is the primary driver for rapid adaptation over much of the RBC dynamic range. This observation indicates a requirement for the  $\text{Ca}^{2+}$  target to be either the channel itself, or a molecule in very close proximity. Modulation of TRPM1 channels by  $\text{Ca}^{2+}$  should be considered a possibility given that other, structurally homologous, TRPM channels are activated or inhibited directly by  $\text{Ca}^{2+}$  (Zholos et al., 2011, Cohen and Moiseenkova-Bell, 2014). Furthermore, others have suggested that typical  $\text{Ca}^{2+}$  targets are unlikely targets of modulation, including CaMKII, calcineurin (Nawy, 2004), and cGMP modulation (Sampath and Rieke, 2004). Further, our experiments with BAPTA that show  $R_{\max}$  suppression at brighter background levels suggest that the  $\text{Ca}^{2+}$ -binding messenger protein, calmodulin, is not a likely candidate. The  $\text{Ca}^{2+}$  target could be a component of the G protein  $\beta$  and  $\gamma$  subunits, which have unknown actions but may affect TRPM1 activity (Xu et al., 2016).

Our results show that there are at least two forms of adaptation occurring in RBCs: a  $\text{Ca}^{2+}$ -dependent, rapid adaptation resulting in the desensitization of the photoresponse, and adaptation imposed by rod adaptation through reduced changes in glutamate at the synapse.

We also observed an additional component at brighter background intensities occurring as a slow sag and moderate reduction in maximal response amplitude during prolonged ambient light exposure. These mechanisms combine to suppress the number of open channels in the RBC dendrites, priming the cell for further increments in light, albeit desensitized and with accelerated kinetics.

## REFERENCES

- Aguilar, M. and Stiles, W.S. (1954). Saturation of the Rod Mechanism of the Retina at High Levels of Stimulation. *Optica Acta: International Journal of Optics*, 1(1):59–65. 10.1080/713818657.
- Arman, A. Cyrus and Sampath, Alapakkam P. (2010). Patch clamp recordings from mouse retinal neurons in a dark-adapted slice preparation. *Journal of visualized experiments : JoVE*, (43):5–8. 10.3791/2107.
- Barlow, H. B. (1957). Increment thresholds at low intensities considered as signal/noise discriminations. *The Journal of Physiology*, 136(3):469–488. 10.1113/jphysiol.1957.sp005774.
- Barnes, Steven and Kelly, Melanie E. M. (2002). Calcium Channels at the Photoreceptor Synapse. In *Advances in Experimental Medicine and Biology*, volume 514, pp. 465–476. 10.1007/978-1-4615-0121-3\_28.
- Baylor, D. A., Lamb, T. D., and Yau, K. W. (1979). Responses of retinal rods to single photons. *The Journal of physiology*, 288(1):613–34. 10.1113/jphysiol.1979.sp012716.
- Benjamini, Yoav and Hochberg, Yosef (1995). Controlling the False Discovery Rate: A Practical and Powerful Approach to Multiple Testing. *Journal of the Royal Statistical Society: Series B (Methodological)*, 57(1):289–300. 10.1111/j.2517-6161.1995.tb02031.x.
- Berntson, Amy, Smith, Robert G, and Taylor, W Rowland (2004a). Postsynaptic calcium feedback between rods and rod bipolar cells in the mouse retina. *Visual neuroscience*, 21(6):913–24. 10.1017/S095252380421611X.
- Berntson, Amy, Smith, Robert G., and Taylor, W. Rowland (2004b). Transmission of single photon signals through a binary synapse in the mammalian retina. *Visual Neuroscience*, 21(5):693–702. 10.1017/S0952523804215048.
- Cao, Y., Pahlberg, J., Sarria, I., Kamasawa, N., Sampath, A. P., and Martemyanov, K. A. (2012). Regulators of G protein signaling RGS7 and RGS11 determine the onset of the light response in ON bipolar neurons. *Proceedings of the National Academy of Sciences*, 109(20):7905–7910. 10.1073/pnas.1202332109.
- Cao, Yan, Sarria, Ignacio, Fehlhauer, Katherine E., Kamasawa, Naomi, Orlandi, Cesare, James, Kiely N., Hazen, Jennifer L., Gardner, Matthew R., Farzan, Michael, Lee, Amy, Baker, Sheila, Baldwin, Kristin, Sampath, Alapakkam P., and Martemyanov, Kirill A. (2015). Mechanism for Selective Synaptic Wiring of Rod Photoreceptors into the Retinal Circuitry and Its Role in Vision. *Neuron*, 87(6):1248–1260. 10.1016/j.neuron.2015.09.002.

- Chang, B., Hawes, N.L., Hurd, R.E., Davisson, M.T., Nusinowitz, S., and Heckenlively, J.R. (2002). Retinal degeneration mutants in the mouse. *Vision Research*, 42(4):517–525. 10.1016/S0042-6989(01)00146-8.
- Chen, C.-K., Woodruff, Michael L., Chen, F. S., Chen, Desheng, and Fain, Gordon L. (2010). Background Light Produces a Recoverin-Dependent Modulation of Activated-Rhodopsin Lifetime in Mouse Rods. *Journal of Neuroscience*, 30(4):1213–1220. 10.1523/JNEUROSCI.4353-09.2010.
- Chen, Ching-Kang, Burns, Marie E., He, Wei, Wensel, Theodore G., Baylor, Denis A., and Simon, Melvin I. (2000). Slowed recovery of rod photoresponse in mice lacking the GTPase accelerating protein RGS9-1. *Nature*, 403(6769):557–560. 10.1038/35000601.
- Cohen, Matthew R. and Moiseenkova-Bell, Vera Y. (2014). Structure of Thermally Activated TRP Channels. In *Current Topics in Membranes*, volume 74, pp. 181–211. Elsevier. ISBN 9780128001813. 10.1016/B978-0-12-800181-3.00007-5.
- Dhingra, Anuradha, Lyubarsky, Arkady, Jiang, Meisheng, Pugh, Edward N., Birnbaumer, Lutz, Sterling, Peter, and Vardi, Noga (2000). The light response of ON bipolar neurons requires Gao. *Journal of Neuroscience*, 20(24):9053–9058. 10.1523/jneurosci.20-24-09053.2000.
- DiCiccio, Thomas J and Efron, Bradley (1996). Bootstrap Confidence Intervals. *Statistical Science*, 11(3):189–212.
- Dunn, Felice A. (2006). Controlling the Gain of Rod-Mediated Signals in the Mammalian Retina. *Journal of Neuroscience*, 26(15):3959–3970. 10.1523/JNEUROSCI.5148-05.2006.
- Efron, B. and Tibshirani, R. (1986). Bootstrap Methods for Standard Errors, Confidence Intervals, and Other Measures of Statistical Accuracy. *Statistical Science*, 1(1):54–75. 10.1214/ss/1177013815.
- Efron, Bradley (1987). Better Bootstrap Confidence Intervals. *Journal of the American Statistical Association*, 82(397):171–185. 10.1080/01621459.1987.10478410.
- Fain, G. L., Matthews, H. R., Cornwall, M. C., and Koutalos, Y. (2001). Adaptation in vertebrate photoreceptors. *Physiological Reviews*, 81(1):117–151. 10.1152/physrev.2001.81.1.117.
- Field, Greg D. and Rieke, Fred (2002a). Mechanisms Regulating Variability of the Single Photon Responses of Mammalian Rod Photoreceptors. *Neuron*, 35(4):733–747. 10.1016/S0896-6273(02)00822-X.
- Field, Greg D. and Rieke, Fred (2002b). Nonlinear signal transfer from mouse rods to bipolar cells and implications for visual sensitivity. *Neuron*, 34(5):773–785. 10.1016/S0896-6273(02)00700-6.

- Freedman, D. A. (1981). Bootstrapping Regression Models. *The Annals of Statistics*, 9(6). 10.1214/aos/1176345638.
- Govardovskii, V I, Fyhrquist, N, Reuter, T, Kuzmin, D G, and Donner, K (2000). In search of the visual pigment template. *Visual neuroscience*, 17(4):509–28. 10.1017/s0952523800174036.
- Haeseleer, Françoise, Imanishi, Yoshikazu, Maeda, Tadao, Possin, Daniel E., Maeda, Akiko, Lee, Amy, Rieke, Fred, and Palczewski, Krzysztof (2004). Essential role of Ca<sup>2+</sup>-binding protein 4, a Cav1.4 channel regulator, in photoreceptor synaptic function. *Nature Neuroscience*, 7(10):1079–1087. 10.1038/nn1320.
- Hecht, Selig, Shlaer, Simon, and Pirenne, Maurice H. (1941). Energy at the Threshold of Vision. *Science*, 93(2425):585–587. 10.1126/science.93.2425.585.
- Kaur, Tejinder and Nawy, Scott (2012). Characterization of Trpm1 desensitization in ON bipolar cells and its role in downstream signalling. *Journal of Physiology*, 590(1):179–192. 10.1113/jphysiol.2011.218974.
- Koulen, Peter, Wei, Jiao, Madry, Christian, Liu, Jiyuan, and Nixon, Everett (2005). Differentially Distributed IP<sub>3</sub> Receptors and Ca<sup>2+</sup> Signaling in Rod Bipolar Cells. *Investigative Ophthalmology & Visual Science*, 46(1):292. 10.1167/iovs.04-0939.
- Legendre, P., Rosenmund, C., and Westbrook, GL (1993). Inactivation of NMDA channels in cultured hippocampal neurons by intracellular calcium. *The Journal of Neuroscience*, 13(2):674–684. 10.1523/JNEUROSCI.13-02-00674.1993.
- Morgans, Catherine W., Brown, Ronald Lane, and Duvoisin, Robert M. (2010). TRPM1: The endpoint of the mGluR6 signal transduction cascade in retinal ON-bipolar cells. *BioEssays*, 32(7):609–614. 10.1002/bies.200900198.
- Morgans, Catherine W., Gaughwin, Phil, and Maleszka, Ryszard (2001). Expression of the alpha1F calcium channel subunit by photoreceptors in the rat retina. *Molecular vision*, 7(10):202–9.
- Morgans, Catherine W., Zhang, Jianmei, Jeffrey, Brett G., Nelson, Steve M., Burke, Neal S., Duvoisin, Robert M., and Brown, R. Lane (2009). TRPM1 is required for the depolarizing light response in retinal ON-bipolar cells. *Proceedings of the National Academy of Sciences of the United States of America*, 106(45):19174–19178. 10.1073/pnas.0908711106.
- Morshedean, Ala and Fain, Gordon L. (2017). Light adaptation and the evolution of vertebrate photoreceptors. *The Journal of Physiology*, 595(14):4947–4960. 10.1113/JP274211.
- Nawy, Scott (1999). The metabotropic receptor mGluR6 may signal through G(o), but not phosphodiesterase, in retinal bipolar cells. *The Journal of neuroscience : the official journal of the Society for Neuroscience*, 19(8):2938–44.

- Nawy, Scott (2000). Regulation of the On Bipolar Cell mGluR6 Pathway by Ca<sup>2+</sup>. *The Journal of Neuroscience*, 20(12):4471–4479. 10.1523/JNEUROSCI.20-12-04471.2000.
- Nawy, Scott (2004). Desensitization of the mGluR6 transduction current in tiger salamander On bipolar cells. *The Journal of Physiology*, 558(1):137–146. 10.1113/jphysiol.2004.064980.
- Neher, Erwin (1992). Correction for liquid junction potentials in patch clamp experiments. In *Methods in Enzymology*, pp. 123–131. 10.1016/0076-6879(92)07008-C.
- Nymark, S., Frederiksen, R., Woodruff, M. L., Cornwall, M. C., and Fain, G. L. (2012). Bleaching of mouse rods: microspectrophotometry and suction-electrode recording. *The Journal of Physiology*, 590(10):2353–2364. 10.1113/jphysiol.2012.228627.
- Okawa, Haruhisa, Miyagishima, K. Joshua, Arman, A. Cyrus, Hurley, James B., Field, Greg D., and Sampath, Alapakkam P. (2010a). Optimal processing of photoreceptor signals is required to maximize behavioural sensitivity. *The Journal of Physiology*, 588(11):1947–1960. 10.1113/jphysiol.2010.188573.
- Okawa, Haruhisa, Pahlberg, Johan, Rieke, Fred, Birnbaumer, Lutz, and Sampath, Alapakkam P. (2010b). Coordinated control of sensitivity by two splice variants of Gao in retinal ON bipolar cells. *Journal of General Physiology*, 136(4):443–454. 10.1085/jgp.201010477.
- Pearring, Jillian N., Bojang, Pasano, Shen, Yin, Koike, Chieko, Furukawa, Takahisa, Nawy, Scott, and Gregg, Ronald G. (2011). A role for nyctalopin, a small leucine-rich repeat protein, in localizing the TRP melastatin 1 channel to retinal depolarizing bipolar cell dendrites. *Journal of Neuroscience*, 31(27):10060–10066. 10.1523/JNEUROSCI.1014-11.2011.
- Petráš, Ivo and Bednářová, Dagmar (2010). Total least squares approach to modeling: A Matlab toolbox. *Acta Montanistica Slovaca*, 15(2):158–170.
- Rieke, F. and Baylor, D. A. (1996). Molecular origin of continuous dark noise in rod photoreceptors. *Biophysical Journal*, 71(5):2553–2572. 10.1016/S0006-3495(96)79448-1.
- Robson, J.G., Maeda, H., Saszik, S.M., and Frishman, L.J. (2004). In vivo studies of signaling in rod pathways of the mouse using the electroretinogram. *Vision Research*, 44(28):3253–3268. 10.1016/j.visres.2004.09.002.
- Rushton, W A (1965). The Ferrier Lecture, 1962 Visual adaptation. *Proceedings of the Royal Society of London Series B Biological Sciences*, 162(986):20–46. 10.1098/rspb.1965.0024.
- Sampath, Alapakkam P. and Rieke, Fred (2004). Selective Transmission of Single Photon Responses by Saturation at the Rod-to-Rod Bipolar Synapse. *Neuron*, 41(3):431–443. 10.1016/S0896-6273(04)00005-4.



- Sampath, A.P., Matthews, H.R., Cornwall, M.C., Bandarchi, J., and Fain, G.L. (1999). Light-dependent Changes in Outer Segment Free-Ca<sup>2+</sup> Concentration in Salamander Cone Photoreceptors. *Journal of General Physiology*, 113(2):267–277. 10.1085/jgp.113.2.267.
- Shen, Yin, Heimel, J. Alexander, Kamermans, Maarten, Peachey, Neal S., Gregg, Ronald G., and Nawy, Scott (2009). A transient receptor potential-like channel mediates synaptic transmission in rod bipolar cells. *Journal of Neuroscience*, 29(19):6088–6093. 10.1523/JNEUROSCI.0132-09.2009.
- Sherman, Adam J., Shrier, Alvin, and Cooper, Ellis (1999). Series Resistance Compensation for Whole-Cell Patch-Clamp Studies Using a Membrane State Estimator. *Biophysical Journal*, 77(5):2590–2601. 10.1016/S0006-3495(99)77093-1.
- Shiells, R. A. and Falk, G. (1999). A rise in intracellular Ca<sup>2+</sup> underlies light adaptation in dogfish retinal 'on' bipolar cells. *Journal of Physiology*, 514(2):343–350. 10.1111/j.1469-7793.1999.343ae.x.
- Sigworth, Fred J (1995). Electronic Design of the Patch Clamp. In Bert Sakmann and Erwin Neher, eds., *Single-Channel Recording*, chapter 4, pp. 95–127. Springer US, Boston, MA. ISBN 978-1-4419-1230-5. 10.1007/978-1-4419-1229-9\_4.
- Simon, Jan (2011). *FilterM*. MATLAB Central File Exchange. <https://www.mathworks.com/matlabcentral/fileexchange/32261-filterm>.
- Trexler, E Brady, Casti, Alexander R R, and Zhang, Yu (2011). Nonlinearity and noise at the rod-rod bipolar cell synapse. *Visual neuroscience*, 28(1):61–8. 10.1017/S0952523810000301.
- Tsukamoto, Yoshihiko, Morigiwa, Katsuko, Ueda, Mika, and Sterling, Peter (2001). Microcircuits for Night Vision in Mouse Retina. *The Journal of Neuroscience*, 21(21):8616–8623. 10.1523/JNEUROSCI.21-21-08616.2001.
- van der Velden, H.A. (1946). The Number of Quanta Necessary for the Perception of Light of the Human Eye. *Ophthalmologica*, 111(6):321–331. 10.1159/000300352.
- Van Rossum, M. C.W. and Smith, R. G. (1998). Noise removal at the rod synapse of mammalian retina. *Visual Neuroscience*, 15(5):809–821. 10.1017/S0952523898155037.
- Vinberg, Frans, Wang, Tian, De Maria, Alicia, Zhao, Haiqing, Bassnett, Steven, Chen, Jeannie, and Kefalov, Vladimir J. (2017). The Na<sup>+</sup>/Ca<sup>2+</sup>, K<sup>+</sup> exchanger NCKX4 is required for efficient cone-mediated vision. *eLife*, 6:1–23. 10.7554/eLife.24550.
- Wang, Yuchen, Fehlhauer, Katherine E., Sarria, Ignacio, Cao, Yan, Ingram, Norianne T., Guerrero-Given, Debbie, Throesch, Ben, Baldwin, Kristin, Kamasawa, Naomi, Ohtsuka, Toshihisa, Sampath, Alapakkam P., and Martemyanov, Kirill A. (2017). The Auxiliary Calcium Channel Subunit  $\alpha 2\delta 4$  Is Required for Axonal Elaboration, Synaptic Transmission, and Wiring of Rod Photoreceptors. *Neuron*, 93(6):1359–1374.e6. 10.1016/j.neuron.2017.02.021.

- Welch, B. L. (1938). The Significance of the Difference Between Two Means when the Population Variances are Unequal. *Biometrika*, 29(3/4):350. 10.2307/2332010.
- Welch, B. L. (1947). The generalisation of student's problems when several different population variances are involved. *Biometrika*, 34(1-2):28–35. 10.1093/biomet/34.1-2.28.
- Xu, Ying, Orlandi, Cesare, Cao, Yan, Yang, Shengyan, Choi, Chan-Il, Pagadala, Vijayakanth, Birnbaumer, Lutz, Martemyanov, Kirill A., and Vardi, Noga (2016). The TRPM1 channel in ON-bipolar cells is gated by both the  $\alpha$  and the  $\beta\gamma$  subunits of the G-protein Go. *Scientific Reports*, 6(February):20940. 10.1038/srep20940.
- Zholos, Alexander, Johnson, Christopher, Burdyga, Theodor, and Melanaphy, Donal (2011). TRPM Channels in the Vasculature. In *Advances in Experimental Medicine and Biology*, volume 704, pp. 707–729. ISBN 9789400702646. 10.1007/978-94-007-0265-3.37.
- Zhou, Zhen-Yu, Wan, Qun-Fang, Thakur, Pratima, and Heidelberger, Ruth (2006). Capacitance Measurements in the Mouse Rod Bipolar Cell Identify a Pool of Releasable Synaptic Vesicles. *Journal of Neurophysiology*, 96(5):2539–2548. 10.1152/jn.00688.2006.

# APPENDIX A

## Iris: data visualization and analysis

### A.1 Introduction

Iris Data Visualization and Analysis (Iris) is a MATLAB (MathWorks, 2021) application graphical user interface and a framework for visualizing, managing and analyzing physiological data. Electrophysiological data are often large, numerous, and comprise comprehensive metadata which are difficult to maintain and process for analysis. Experimenters often rely on extensive sets of physical and digital notes, complex folder structures and proprietary software to parse raw data for publication. As a result, many intermediate and temporary files get created, which may obfuscate the analytical process. In today's publication environment, sharing analysis code and data have become more common-place and there is an ever-growing necessity for transparency and control over collected data. Iris was created for the purpose of abstracting data-processing mechanisms to simplify and standardize analysis workflow across broad-ranging sources of data. As a benefit, data acquired from different systems and experiments can be grouped together into single, comprehensive files allowing for streamlined and straight-forward analysis, easy sharing, thorough process tracking and reproducibility.

### A.2 Software Interface

Iris is an offline interface between the user and their data that enables access to the data and associated metadata, and provides a framework for data wrangling and analysis. The user interface (UI) is a collection of MATLAB figure windows where the primary UI is presented

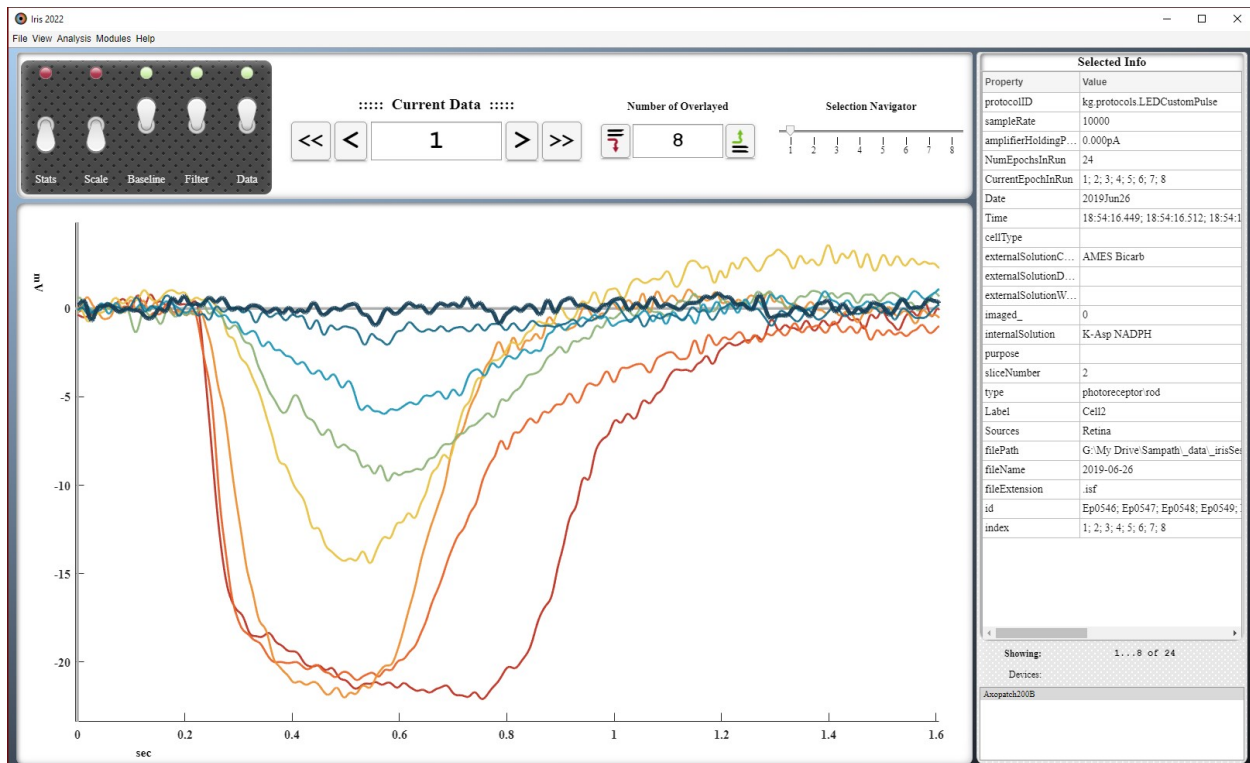


Figure A.1: *Iris* main view. The main UI window with (clockwise from top left) data view toggles, data navigation, overly controls, select display properties for the selected data, data indices indicator, device selector and the data viewer. View toggles, Stats, Scale, Baseline and Filter, alter how data are displayed in the viewer and have corresponding tunable parameters located in the related sections of the Preferences menu. The Data toggle will mark the inclusions status of the currently highlighted data index (see Data Analysis (§ A.4)).

through the Iris primary view window.

### A.2.1 Data Navigation

The Iris main view functions as the graphical interface node to all other operations and views of the loaded data (see Preferences (§ A.3) for detailed description of data toggles). From this UI, the user can visualize and navigate data by index in a similar fashion as array-indexing. The Current Data input field accepts valid MATLAB expressions that result in unsigned integer arrays greater than 0. The buttons surrounding the Current Data input field can be clicked to navigate forwards or backwards through the dataset by small and large jumps (`[>, >>]` & `[<, <<]`, respectively).

To increase or decrease the number of data indices shown, the user can type an integer value greater than 0 into the Overlay input field. The number of overlaid data traces cannot exceed the number of elements in the data array. When more than 1 data is overlaid, the Selection Navigator slider becomes active allowing for easy traversal across the selection. The user may highlight any single index among the selection for the purpose of visual inspection or for toggling the inclusion status via the Data toggle. When an internal selection is made, the data shown for the selected index will have a slightly thicker trace and marker, depending on the Display preference settings.

Users may find navigating large datasets to be easier through the Data Overview (Fig. A.2) interface. The Data Overview UI consists of a file tree (left), a data properties table (right) and an actions drop-down list (below). The file tree displays data IDs, a unique string comprising the datum index from original embedding, organized sequentially from the open file. The data properties table displays all properties and metadata for the current selection. When more than one datum is selected, the data properties table will show only unique values, separated by a semi-colon (`;`).

Navigation through the data indices is possible by clicking on individual datum IDs and multiple selections may be made by holding keyboard modifiers while clicking. Clicking a datum ID then holding down the shift key and selecting another datum will make a

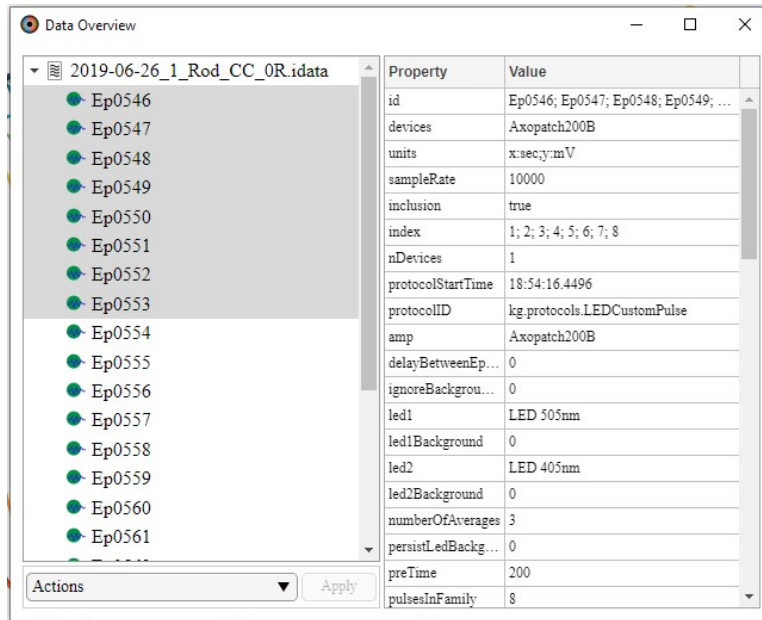
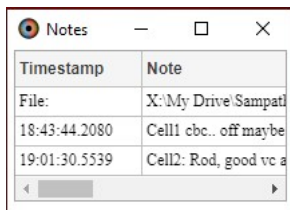


Figure A.2: *Data overview user interface*. A detailed view for all data loaded into Iris. The data tree allows an alternate form of navigating data while loading available metadata for selected data indices directly into the view. Optional processing of the data is available through this advanced data controller. Optionally modify inclusion status, or remove data altogether, of multiple data indices at once by selected the desired action in the drop-down menu and clicking on the “Apply” button.

contiguous selection. Holding down the ctrl key while clicking will add or remove individual data indices to the selection. The Iris main view will automatically update with the changes in selection.

The actions in the Actions drop-down list allow the user to either modify, delete or export the current data selection. The user may set the inclusion status by excluding or including selected data. In some cases, more data may be imported than will be used for analysis and the user may desire to reduce the memory footprint of the current session by deleting the selection or deleting the inverse selection ('unselected'). If the user wishes to extract groups of data for later analysis, the current selection may also be exported to disk either in the IrisData format (\*.idata, see Data Analysis (§ A.4)), the comma-separated values format (\*.csv), or the tab-separated values format (\*.tsv) by using the Export Selected action.

## A.2.2 Metadata Viewers



The screenshot shows a window titled "Notes" with a standard Windows-style title bar (minimize, maximize, close buttons). The window contains a table with two columns: "Timestamp" and "Note". The table has three rows of data. The first row is a header row. The second row shows a file path and a note. The third row shows two timestamps and their corresponding notes. A horizontal scrollbar is visible at the bottom of the table.

Timestamp	Note
File:	X:\My Drive\Sampat
18:43:44.2080	Cell1 cbc.. off maybe
19:01:30.5539	Cell2: Rod, good vc a

Figure A.3: *Notes user interface*. Digital notes stored or loaded with the imported data are viewable through the Iris > View > Notes menu.

Physiological experiments, particularly those conducted in our laboratory, have many configurable pieces unique to a particular experimenter or rig, which must be tracked and documented accordingly. Data acquisition software, whether open-source or proprietary, generate databases of these metadata, information about the specific experiments performed, which can get lost in the data analysis process as early as at the importation step. Iris mitigates this issue by providing a data class which tracks and indexes metadata at the file level and the individual datum level. Most acquisition software available also allows user-created metadata, such as notes (Fig. A.3). Iris offers viewers for these metadata, which

may be accessed through the View menu.

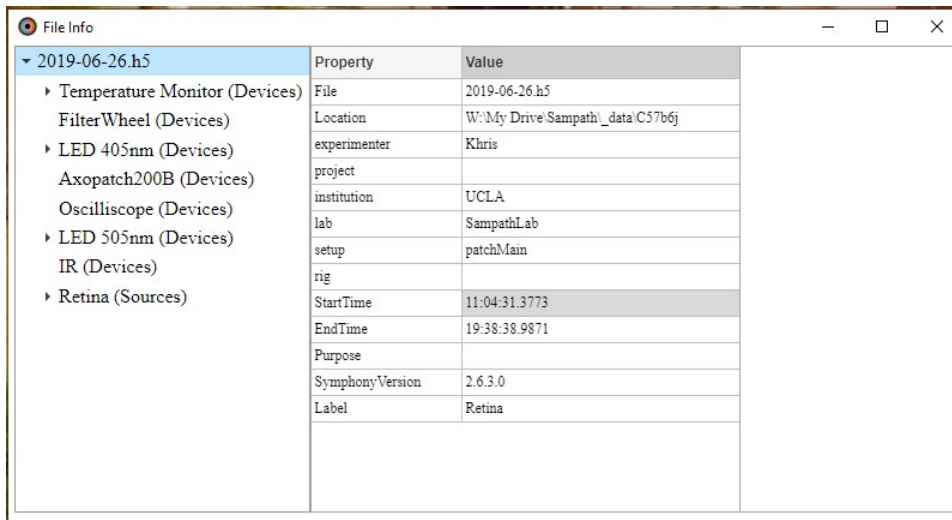


Figure A.4: *File information user interface*. Information from the open files are displayed in the document tree. Details are populated from the metadata structures stored or loaded with the opened data files.

The File Information viewer (Fig. A.4) is a collection of file-level metadata and comprises a tree viewer to traverse high-level configurations. For data collected with Symphony (version 2), this will be populated with device and source configurations (see the Symphony documentation<sup>1</sup> for comprehensive descriptions). For a detailed description of the file metadata structure, see Application Development (§ A.5.4).

The Data properties (Fig. A.5) viewer displays metadata found at the datum level. When multiple data indices are selected, only unique values will be displayed, separated by a semi-colon (;) for each respective datum. The information here is useful for developing custom analyses (see Data Analysis (§ A.4)), and for using the Stats data toggle (see Data (§ A.3.3)).

---

<sup>1</sup><https://cafarm.gitbooks.io/symphony>



Property	Value
id	Ep0546; Ep0547; Ep0548; Ep0549; Ep0550; Ep0551; Ep0552; Ep0553
devices	Axopatch200B
units	x:sec,y:mV
sampleRate	10000
inclusion	true
index	1; 2; 3; 4; 5; 6; 7; 8
nDevices	1
protocolStartTime	18:54:16.4496
protocolID	kg.protocols.LEDCustomPulse
amp	Axopatch200B
delayBetweenEpochs	0
ignoreBackgroundInput	0
led1	LED 505nm
led1Background	0
led2	LED 405nm
led2Background	0
numberOfAverages	3
persistLedBackground	0
preTime	200
pulsesInFamily	8
stimAmplitudes	0.011; 0.026; 0.062; 0.152; 0.368; 0.895; 2.174; 5.283
stimTime	8
tailTime	2292
temp	Temperature Monitor
totalEpochTime	2500
epochStartTime	18:54:16.6994; 18:54:19.1994; 18:54:21.6994; 18:54:24.1994; 18:54:26.6994; 18:54:29.1994
epochDateString	2019Jun26_18:54:16.449; 2019Jun26_18:54:16.512; 2019Jun26_18:54:16.621; 2019Jun26_1
identifier	LEDSinglePulse
displayName	One LED Pulse
lightAmplitude	0.011; 0.026; 0.062; 0.152; 0.368; 0.895; 2.174; 5.283
meanTemperature	35.431; 35.457; 35.466; 35.461; 35.444; 35.436; 35.423
varTemperature	0.00017745; 2.5451e-05; 3.599e-05; 0.00010513; 3.1205e-05; 2.8674e-05; 2.5077e-05; 2.508
unitsTemperature	^(circ)C
amplifierHoldingPotential	0.000pA
NumEpochsInRun	24
CurrentEpochInRun	1; 2; 3; 4; 5; 6; 7; 8

Figure A.5: *Data properties user interface*. Properties are populated from the selected data indices in the Iris primary view. Multiple fields from the data structure are combined into a single table. If multiple indices are selected, unique values for a given property are shown, separated by a semi-colon (;). See Application Development for a complete breakdown of the input data structure.

## A.3 Preferences

Experimental data come in many formats, Iris was designed to be flexible to accommodate simultaneous viewing and processing the data. To achieve this flexibility, Iris is tunable through the preferences window where navigation controls, workspace variables and data processing settings are found. The following sections describe each of the preferences and their impact on the data display and processing. At any point, defaults may be reapplied by selecting the desired section in the preference tree and clicking on the Defaults button (Fig. A.6 *bottom*).

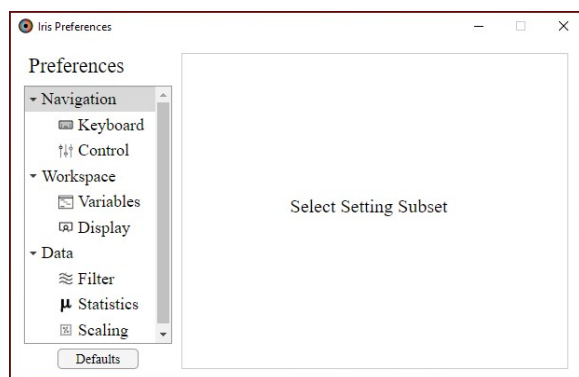


Figure A.6: *Preferences user interface*. Program preferences and interactions may be configured through the `Iris > View > Preferences` menu item.

### A.3.1 Navigation

Navigational preferences contain a detailed list of keyboard commands (also found in Table A.1) and Control settings (Fig. A.7) that modify how the navigation buttons in the Iris main view behave. For ease of navigation, small steps (Data and Overlay) are initiated by using the keyboard arrows and big steps are initiated by holding down the shift key while navigating/overlying with the arrow keys.

---

Command	Action
←, →	Navigate by small datum step
↑, ↓	Change overlay by small datum step
shift + [←, →, ↑, ↓]	Use big step
ctrl/cmd + [←, →]	First, last record
PgUp, PgDn	Navigate within selection
alt + f	Toggle digital filtering
alt + s	Toggle scaling
alt + b	Toggle baseline subtraction
x	Toggle datum inclusion status
ctrl + n	Load new data (close currently open files)
ctrl + o	Load new data from session file (close currently open files)
ctrl + s	Save open data as a session file
ctrl + q	Quit the program
ctrl + i	View open files information
ctrl + t	View digital notes from open files
ctrl + d	Open analysis dialog for selected data
ctrl + p	View selected data properties
ctrl + alt + p	Take screenshot of the iris window

---

Table A.1: *Iris keyboard shortcuts.*

**Control Values**

Data Step Small:	<input style="width: 50px;" type="text" value="1"/>
Data Step Big:	<input style="width: 50px;" type="text" value="10"/>
Overlay Small:	<input style="width: 50px;" type="text" value="1"/>
Overlay Big:	<input style="width: 50px;" type="text" value="5"/>

Figure A.7: *Navigation control preferences.* Adjust step sizes of navigation.

### A.3.2 Workspace

Workspace variables (Fig. A.8) modify the interaction between Iris and the system disk. When saving and exporting data, the user can set a default, safe, location to use as the organizational default root directory by configuring the Output Location field via the corresponding folder button. By default, Iris will attempt to locate the system user’s home directory and create the Iris folder structure as shown in the Workspace variables (Fig. A.8) section. When performing a custom analysis through the Analysis Export (Fig. A.16) window, the default output file name will be a path comprised of the root folder value of the Output Location and the Custom Analysis prefix (Fig. A.8 *bottom*) function.

To adjust the default name, the prefix may be set as an anonymous function to be run at the creation of the Analysis Export window. The prefix must be a valid MATLAB expression which evaluates to a `string` or `char array` type. A preview of the prefix function is viewable below the prefix input field (Fig. A.8).

Display controls (Fig. A.9) modify the look of the axes on the Iris main view. The user may toggle line and marker displays, set thickness and size, respectively. Axial spacing controls are provided for independent axes with the horizontal running axis (X) and vertical

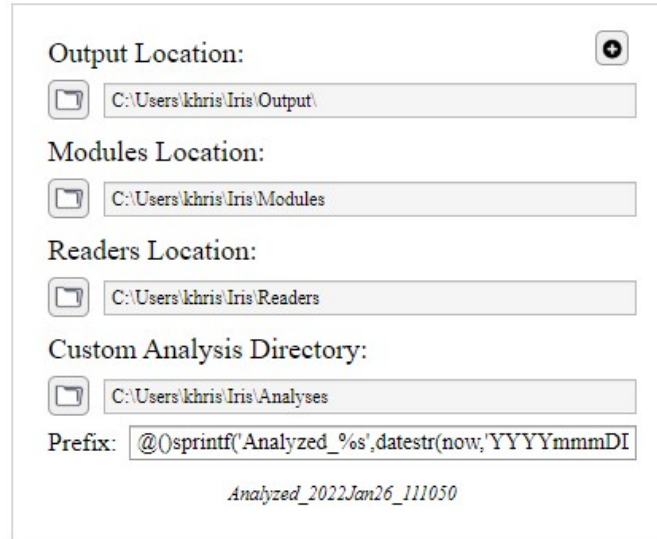


Figure A.8: *Workspace preferences*. Configurable workspace variables. Output location sets the default location for exporting data and analysis results from Iris. Modules, Readers and Analysis directories for user-created extensions. Analysis prefix for automatically generated default values during analysis export.

running axis (Y) allowing linear or logarithmic spacing. Per MATLAB’s convention, data that are negative will not be displayed in logarithmic spacing and a warning will be issued. Should the user wish to display negative data in a logarithmic spacing, we suggest activating the Scale data toggle and setting a custom scaling value (see Data (§ A.3.3)) of  $-1$  for the desired device.

Grid lines along the ordinate, abscissa, or both, may be configured through the Grid drop-down list to improve visualization of data. Iris will always display thick gray lines at the zero-intersects of the axes.

### A.3.3 Data

The following sections describe how data toggles on the Iris main view behave.

Display

Line Display Style: Solid ▼

Line Display Width: 2.0

Marker Display Style: None ▼

Marker Display Size: 8.0

X Axis: Linear ▼    Y Axis: Linear ▼

Grid: None ▼

Figure A.9: *Data display properties*. Configurable settings for displaying data in the Iris main view.

Filter Settings

Butterworth Filter Order: 7 ▼

Low Pass Frequency [Hertz]: 50 ▼

High Pass Frequency [Hertz]: 10 ▼

Filter Type: Lowpass ▼

Figure A.10: *Digital filtering settings*. Configurable options for when the digital filtering switch is thrown in the Iris main view. Filtering is performed using the ButterParam and FilterM (Simon, 2011a, Simon, 2011b).

### A.3.3.1 Data Signal Filtering

Filter settings alter parameters sent to the digital signal processing mechanisms and alter the appearance of the data when the Filter data toggle is activated. Iris utilizes the ButterParam<sup>2</sup> utility (Simon, 2011a) and the zero phase-shift C-MEX<sup>3</sup> implementation of the FiltFiltM tool (Simon, 2011b) to quickly filter the data with a Butterworth digital filter. The parameters for the filter coefficients are tunable through the Order, Pass Frequencies and Type inputs.

### A.3.3.2 Data Aggregation

Statistics

Group By:  Split Devices

None  
CurrentEpochInRun  
DataFile  
Date  
Label

Aggregation Statistic: Mean

Baseline: 1000 pts Offset: 0 pts Fit (Sym)

Show original traces  Baseline zeroing

Figure A.11: *Statistics and data manipulations*. Interface to configurations for when the Stats toggle is thrown on the Iris main view.

The Statistics preferences define the behavior of both Stats and Baseline data toggles on the Iris main view. When activated, the Baseline toggle will attempt to produce a zero-baseline version of the raw data, non-destructively (meaning the underlying raw data is unaltered and just a copy is modified). The baseline method (described further in Custom Analysis (§ A.4.3)) chosen from the drop-down action may be one of Beginning, End, Fit

---

<sup>2</sup>This tool will create and store coefficients on first use making subsequent calls faster.

<sup>3</sup><https://www.mathworks.com/help/matlab/call-mex-files-1.html>

(symmetrical) or Fit (asymmetrical). By default, Iris performs a baseline subtraction by taking the average of the beginning 100 data points from each data trace. Setting an offset value will cause the parser to skip over the number of offset points indicated and then begin the averaging over the next baseline points indicated. Setting the baseline type to End will perform the same action using the end of each data trace as the reference point.

If the Fit method is indicated, the parser will attempt to fit a line either to the beginning and end (Sym) baseline points (with offset) or just the beginning (Asym) baseline points (again with offset). This line will be removed from the whole trace. These “Fit” methods are implemented as a mechanism for dealing with long term drift from datum to datum.

Aggregations may also be performed based on datum-level metadata, simply as a means of verifying combinations of parameter inputs for analyzing data further. One may also employ aggregation statistics as a quick method for exporting a plot of the averaged data to an image using the axes interaction toolbar of the Iris main view axes. To perform aggregation, the user must first select the grouping variables, which may be identified in the data properties (Fig. A.5) interface, from the list, using ctrl or shift to make multiple selections.

When making a selection, we suggest using as few selectors as possible which provide unique values to be grouped upon. If the data to be aggregated is to be averaged based on, for example, stimulus duration, assuming the metadata contains an entry on each datum for the stimulus duration, and the selected indices contain data which fall into a single group of the possible groups formed by assessing the stimulus durations, selecting the stimulus duration property here and then activating the Stats toggle in the Iris main view will cause the aggregates to be drawn instead of the original data. To show the original traces in a light gray color, mark the Show original traces checkbox.

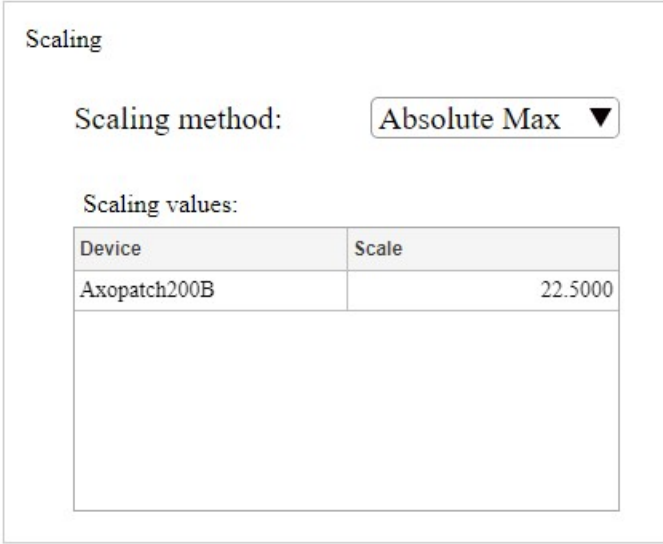
To perform baseline subtraction on the aggregated data (prior to aggregate calculation), deactivate the Baseline data toggle, mark the Baseline zeroing checkbox in the preferences menu, and activate the Stats data toggle. In this way, baseline subtraction will be performed, as described above for the Baseline data toggle, before any aggregation occurs. If



the Baseline data toggle is set to active, and the baseline zeroing checkbox is unchecked, baseline subtraction may occur after aggregation and produce undesired results.

It is important to note that the Stats data toggle, and thus data aggregation, are implemented as a means of data quality control. In some cases, an experiment may encounter some unforeseen artifact or noise that causes some number of data indices to be defunct. Iris provides these visualization tools to prevent performing full analyses and then returning to the original data to truncate or inspect anomalies.

### A.3.3.3 Data Scaling



Scaling

Scaling method: Absolute Max ▼

Scaling values:

Device	Scale
Axopatch200B	22.5000

Figure A.12: *Scaling preferences*. Adjust scaling visualization when the scale toggle is thrown in the Iris primary view.

The Scale data toggle on the Iris main view allows the user to multiply the data for a given device by some scalar scaling factor. The value for this scaling factor can be entered in the Scale preferences manually (Custom) or automatically from the Scaling Method drop-down list. Available automatic methods are one of Absolute Max, Max, and Min<sup>4</sup>.

---

<sup>4</sup>Although shown in the list, the option Select is not currently available.

## A.4 Data Analysis

A key goal of Iris is to make parsing and managing recorded data simple, straightforward and accessible. To achieve this, Iris provides utilities to perform a complete analysis, to extract data as Iris’s custom `IrisData` format to work with outside of the Iris interface, to build custom modules for working with data directly as an extension of the Iris interface, or to export data in standard formats for use outside of the Iris framework altogether. Iris was designed with an import-view-process-export strategy in mind to allow for a clean, generalized pipeline for data analysis.

### A.4.1 Importing Data

Iris is loosely based on a layered architecture to help separate operational logic from data presentation and provide a relatively agnostic approach to managing data. The Iris core framework is comprised of custom MATLAB data class definitions for tracking and handling imported data. Iris was first designed to work with data collected through the open-source Symphony Data Acquisition System (Cafaro et al., 2019) for MATLAB and thus is packaged with file readers for Symphony (versions 1 and 2) HDF5 files. Data can be loaded into Iris using the File menu in the Iris main view. Data files selected through the import mechanism are parsed with a corresponding reader function.

Users may wish to import data not already supported by Iris and thus must create a custom reader. A reader is a function file that accepts a scalar file path input and returns a scalar struct with the following mandatory fields: `Data`, `Meta`, `Notes` (Fig. A.13). Each field must contain a cell array with contents as shown in Fig. A.13 *fields*. The Data struct attributes (Fig. A.13B) are described in detail below and in Fig. A.14.

The Notes cell array must contain an arbitrary height by two cells wide cell array, e.g., for an empty Notes array, it must contain an element with the value: `{0x2 cell}`. For non-empty Notes cells, the expected (though not obligatory) layout is that of timestamp in the first column and note text in the second column (see Fig. A.3). For each open data file,

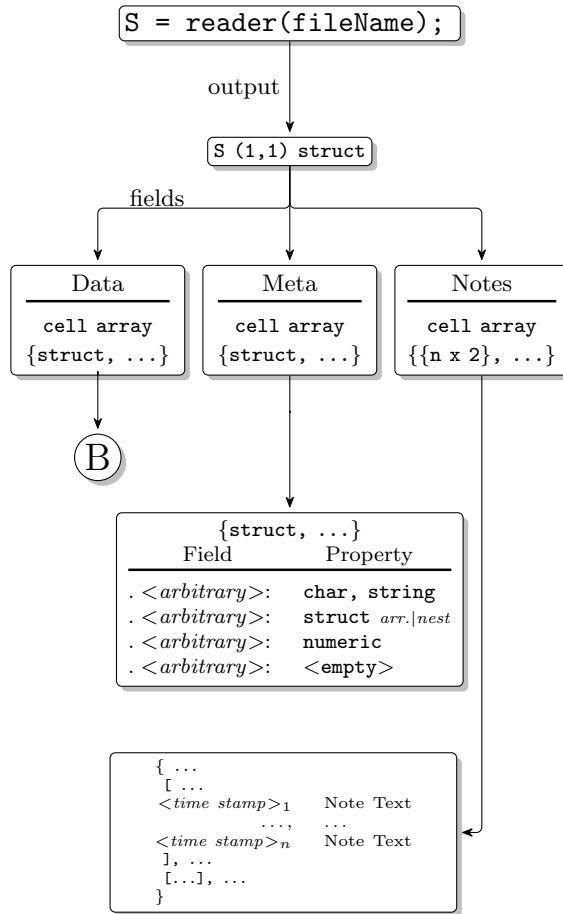


Figure A.13: File reader I/O.

Ⓑ

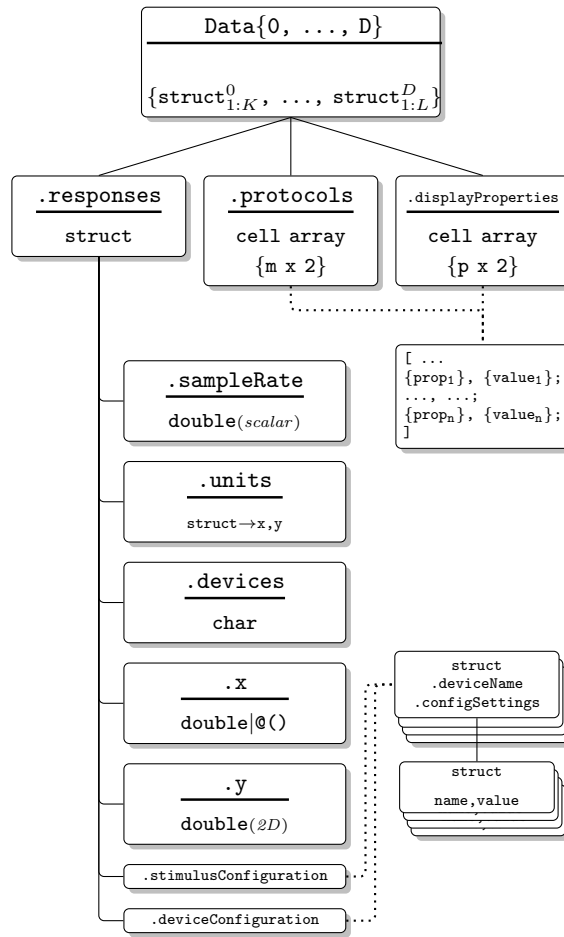


Figure A.14: *Data structure.*

Iris will automatically prepend a row at the start of the associated notes with the file path information.

The Meta field must contain a cell array of scalar structs. Though the root struct must be scalar, any nested structs may be struct arrays and nested struct arrays. Meta fields may be any arbitrary names and may contain any values (as depicted in Fig. A.13). To browse the open file’s Meta fields, Iris provides the File Info viewer where Meta fields containing structs are expanded in the tree list and all other values are coerced to strings for the properties table (see Fig. A.4).

The Data field is the most stringent of the reader output values with specific requirements that are outlined in Fig. A.14. For each cell element in the Data field, a struct

```

>> S = reader(fileName)
struct with fields:

    Notes: {{24x2 cell}}
    Meta: {{1x1 cell}}
    Data: {[150x1 struct]}
>> S.Data{1}(1)
struct with fields:

    protocols: {30x2 cell}
    displayProperties: {21x2 cell}
    responses: [1x1 struct]
>> S.Data{1}(1).responses
struct with fields:

    sampleRate: {[10000],[10000]}
    units: {[1x1 struct],[1x1 struct]}
    devices: {'Axopatch200B','LED505nm'}
    x: {@()((1:20000)-1)'./10000.0,@()((1:20000)-1)'./10000.0}
    y: {[20000x1 double],[20000x1 double]}
    stimulusConfiguration: [1x1 struct]
    deviceConfiguration: [1x5 struct]

```

Figure A.15: *Datum response structure.*

array (one struct element for each datum) is expected with the following 3 field names: `responses`, `protocols`, and `displayProperties`. While required fields, `protocols` and `displayProperties` may be `{0x2}` though an empty entry limits Iris functionality, particularly actions performed through data toggles. Unique property-value pairs in the cell arrays for `protocols` and `displayProperties` fields is shown in the Data Properties viewer (Fig. A.5) and in the Data Overview viewer (Fig. A.2). Thus, properties listed in the `displayProperties` field may be a subset of the properties also listed in the `protocols` field or they may be unique properties. The properties listed in the `displayProperties` field will be shown in the Selected Info table of the Iris main view (see Fig. A.1).

The `responses` field must be a struct containing fields for `sampleRate`, `units`, `devices`, `x`, `y`, `stimulusConfiguration`, and `deviceConfiguration`. Each field must contain a cell array in which each element represents data for a single device, except for configuration fields which may be empty (`[]`) or struct arrays. An example output from a reader function is shown in Fig. A.15. Configuration structs may be nested struct arrays with the general layout shown in the connected (dotted) nodes in Fig. A.14. The configuration struct contains the `deviceName` (`char`) and a `configSettings` struct array for each configuration property

for the device. Each element in the configuration struct array describes configuration settings for a single device. The `configSettings` struct array contain fields, `name`, `value`, for each configuration setting.

### A.4.2 Exporting Data

Iris provides a few mechanisms by which the user may extract data from a larger dataset. Data indices to be exported can be selected and using `Export...` from the Analysis menu. The user will be prompted to make the decision to export the current selection or the whole session and then prompted to select a location. When selecting a location, the user may choose a file type of `*.idata` (detailed in the next section), `*.csv` or `*.tsv`. Choosing the delimited files will only export the `x` and `y` data from the chosen data domain. If the data toggles for Baseline and Filter are active, the user will also be prompted to apply those transformations to the exported data.

### A.4.3 Custom Analysis

Iris was created as a means to manage the metadata and physiological data from an experiment in a convenient, organized fashion. Because Iris operates as a gateway to the data, it does not itself contain any mechanism by which we can automatically perform any analysis. Iris provides a data class (`@IrisData`) for managing the data and metadata of a selection. `IrisData` objects may exported (see the previous section) for storage and later analysis, or they may be used directly in custom analyses, which are managed via the Analysis Export (Fig. A.16) UI. A custom analysis function is simply a matlab function (`*.m`) file with a special header which allows Iris to determine default values (optional).

#### A.4.3.1 Custom Analysis Functions

To create an analysis function, the user may simply create an empty `*.m` file and save it in the User's `Iris\Analyses` folder, or use the convenient interface, found in the Analysis

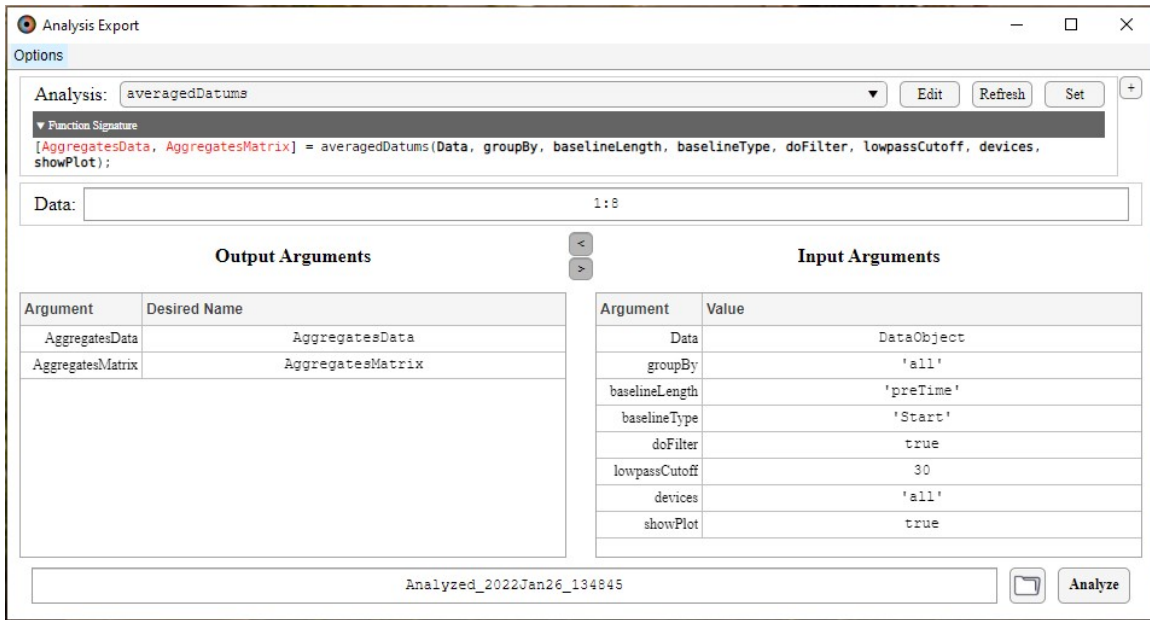


Figure A.16: *The Analysis Export user interface. Custom analysis function interface for user-defined and shared analyses.*

menu (Analyze > New Analysis Fig. A.17). Simply enter the names of the output and input arguments and click create, Iris will create the file in the appropriate folder and open the file in the MATLAB editor.

The analysis function works as would a normal MATLAB function with an added syntactical scope only parsed by Iris, and thus the function may be called directly from the command line or a script should the user decide to do so. Upon selecting the analysis function from the drop-down in the Analysis Export UI (Fig. A.16), the function header is parsed for input argument names and their defaults as denoted by the `:=` operator (an operator that has no meaning elsewhere in MATLAB) within a comment block (Fig. A.18). The output arguments for the function will be stored as named in the Desired Name column of the Analysis Export prompt in the `.mat` file configured in the edit field at the bottom of the prompt. Importantly, the output file will also contain the function call information in a variable named `Call`. This is useful for returning to analyzed data and determining values used in the input arguments.

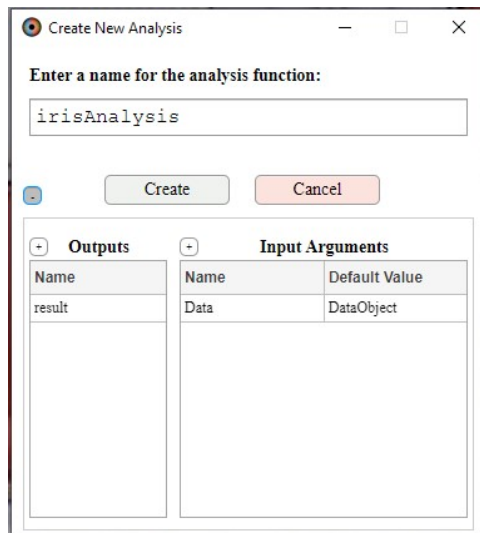


Figure A.17: *New analysis interface*. Iris provides a simple interface to produce a new analysis function for use with the Analysis Export interface. Analysis functions are required to have at least 1 input, for the data object sent from Iris to the function, and 1 output, for the storage of any results.

```

1  function [output1,output2] = analysisTemplate(Data,input1,input2)
2  % --- SET YOUR DEFAULTS BELOW --- %
3  %{
4  DEFAULTS
5  input1:=(1:10)
6  input2=["a","string","array"]
7  %}
8
9  % Begin Analysis
10
11 % ...
12
13 end % end of analysis

```

Figure A.18: *Custom analysis header*. Default argument values may be specified in a comment block.



Much of the underlying functionality of Iris relies on the logic and utility of custom algorithms. These custom utilities are available to the user, their use and investigation is encouraged. For a short list of available utilities, accessible through the `utilities.*` package (see `doc utilities` and Table A.2) while Iris is on the MATLAB path.

#### A.4.3.2 The IrisData Object

The first input argument of an analysis function must contain the incoming data object from Iris. This object is a custom class defined in the `IrisData.m` class file. While developing analyses, one should make sure that Iris is on the MATLAB path, either by installing the CLI and importing Iris libraries or by running Iris in your MATLAB session. The `IrisData` object has a number of useful methods for accessing and working with data. All of the methods can be viewed by using the `doc IrisData` command in the MATLAB command window, a list of Properties is show in Table A.3.

An `IrisData` object is a value type class, which means that the class cannot modify itself and so all methods which make calculations with the data, or attempt to modify the data will produce a new instance of the class. One should avoid overwriting variables, even though it is often tempting to recycle variable names, e.g., do `newData = Data.Filter()`; and instead of `Data = Data.Filter()`;. Because a new instance is created each time a method<sup>5</sup> is called, methods may be chained together to reduce creating intermediate variables. For example, one can apply a digital low-pass filter to the data and perform baseline corrections by chaining the `.Filter()` and `.Baseline()` methods together, i.e., `CleanData = Data.Filter().Baseline()`;. Methods capable of chaining are as follows: `.Baseline()`, `.Aggregate()`, `.Filter()`, and `.Scale()`. These methods operate identically to how the data toggle switches operate in the Iris main view (see Data (§ A.3.3)).

The `IrisData` class also contains a number of static methods which are replicates of the Iris utilities, which are included for portability. Other methods exist to aid in quick

---

<sup>5</sup>Not all methods may be chained.

Function	Description
<code>A2PigmentTemplateFactory</code>	Returns A2 template function for a provided <code>lambdaMax(s)</code> .
<code>AbsMax</code>	Get the absolute max, corrected by the original sign
<code>camelizer</code>	Convert string to camel-case
<code>centerFigPos</code>	Create a position vector for centering figures on screen
<code>collapseUnique</code>	Collapse repeated cell entries as determined by <code>columnAnchor</code> .
<code>createIrisFigure</code>	Creates a figure with iris theming
<code>determineDepth</code>	Determines nested structure depth
<code>determineGroups</code>	Create a grouping vector from cell array input.
<code>domain</code>	Min,max array for each input argument provided
<code>fastKeepField</code>	Removes field from input struct that are not in supplied field names
<code>fastrmField</code>	Removes supplied field names from input struct
<code>findParamCell</code>	Finds (regex) matching Name-Value pairs of nx2 cell array by supplied Name
<code>flattenStructs</code>	Flattens a struct array into scalar struct with array fields
<code>getColorShades</code>	Get a color array nshades x (rgb) x ncolors
<code>getNearestDataPoint</code>	Locate the nearest (x,y) point in data vector to supplied coordinate
<code>getNearestRange</code>	Return N points from values that are closest to a target
<code>isWithinRange</code>	Validates if a value is within a given range [inclusive by default]
<code>listfields</code>	Recursively list nested struct field names
<code>predictLocalLinear</code>	Perform piecewise linear interpolation
<code>r_isFielda</code>	Recursively search a struct for a field name
<code>rep</code>	Repeat array or array elements
<code>resaper</code>	Reshape input vector into matrix with optional overlap and padding
<code>search_recurse</code>	Finds a full path to a given filename.
<code>uniqueContents</code>	Validate cell contents for multiple cells.
<code>unknownCell2Str</code>	Convert a cell's contents to a string (char array)
<code>ValidStrings</code>	A modified version of matlab's <code>validstring</code>

Table A.2: *Iris utility functions*. A detailed view of each utility function may be found by running `doc utilities` at the MATLAB command prompt (while Iris is on the MATLAB path).

processing of contained data, such as the `.plot()`, which simply creates a new figure and plots the contained data. The plot method may be called in function or method form, i.e., `plot(Data,parameters)`; or `Data.plot(parameters)`, where `parameters` are name-value arguments common to MATLAB's `line()` function.

IrisData methods follow a standard name-value input argument pattern and contain the common argument, `'devices'`, which allows the user to perform the requested method on a subset of available devices.

#### A.4.3.3 Accessing Metadata

It is often useful to know information about how each datum was recorded and use that information to make decisions about how to proceed with an analysis. For example, assume we would like to average the traces into groups which correspond to the stimulus intensity of an experiment. During acquisition of these data, the only parameter that changed from datum to datum was the voltage delivered to the light-emitting diode (LED) stimulus. This property is stored with each datum and we can access it in a number of ways. The most convenient method is to use the specifications table for the data, which can be accessed through the IrisData object's `Specs` property like this: `Data.Specs.Table`. This approach will convert any values from the original properties cell array into a string for display in the MATLAB table class. To retrieve the original form of the metadata, use: `Data.Specs.Datums`, which will return a `nx2` cell array for each datum.

#### A.4.3.4 Example Analysis Function

Iris has abstracted much of the tedious data-wrangling so that the user may get to an analysis result more concisely and with fewer lines of code. In Fig. A.19, we show how a grouped averaging could be obtained in just a few lines of code. We provide a function with control over how the data are grouped, whether the baseline subtraction should occur (and how it should proceed, see The IrisData Object (§ A.4.3.2)).

---

<b>AvailableDevices</b>	A list of the available devices from all data.
<b>Data</b>	A struct array containing the collected data.
<b>DeviceMap</b>	A map object with keys which correspond to available devices.
<b>FileHistory</b>	A string array of file names associated with this data file.
<b>Files</b>	A string vector containing the names of the most recent files
<b>InclusionList</b>	The list of inclusions as set during object construction.
<b>IndexMap</b>	A map object with keys which correspond to original index numbers.
<b>MaxDeviceCount</b>	The maximum counted devices for all data.
<b>Membership</b>	A map containing the file name and associated data and notes
<b>Meta</b>	A 'struct' object, holds the metainformation about the files from
<b>Notes</b>	An Nx2 cell array of the pattern timestamp,note.
<b>Specs</b>	A struct hold table and datum properties. Used in groupBy commands.
<b>UserData</b>	A struct containing any extra parameters supplied at construction.
<b>nDatums</b>	The number of available data.

---

Table A.3: *IrisData* properties.

```

1  function [Averages] = averageData(Data,groupBy,baselineRegion,doPlot)
2  %{
3  DEFAULTS
4  groupBy:="lightAmplitude"
5  baselineRegion:="none"
6  doPlot:=true
7  %}
8
9  % Begin Analysis
10 Averages = Data.Aggregate( ...
11     'groupby', groupBy, ...
12     'baselineregion',baselineRegion ...
13 );
14 if doPlot
15     fig = figure;
16     ax = axes(fig);
17     plot(Averages,'Axes',ax,'lineparameters',{'linewidth',1});
18 end
19
20 end

```

Figure A.19: *Custom analysis example*. Custom analysis functions may produce plots and export (through output arguments) results easily.

#### A.4.4 Custom Modules

Iris provides a simple mechanism by which an IrisData object can be sent to a third party application created as either a class definition (`@moduleName`) or through the MATLAB AppDesigner (`*.mlapp`). The only requirement is that the resulting object contain a public method, `.setData()` which accepts an IrisData class object. The module file should be stored in the Iris Custom Modules directory (see Workspace (§ A.3.2)).

### A.5 Quick Start

Iris DVA is a user-interface tool designed to facilitate offline analysis of physiological data. Iris functions as a window into your data, a wrangler of metadata and a pathway to reproducible analyses and results. Iris is extensible and provides an avenue for scientists to quickly analyze data with their own custom MATLAB functions or through custom user interfaces. Because Iris uses a cache approach, original data files remain unchanged.

#### A.5.1 Requirements

Iris was developed to be compatible with Windows, Mac and Linux operating systems though all development was in a Windows 64-bit environment. The minimum system requirements are the same as the requirements to run MATLAB in your environment. The recommended system is Windows 10 pro 64-bit workstation with 12+ Gb of RAM. This recommendation comes from the expectation that raw data are often large. The recommended MATLAB version is 2021b, 64-bit though Iris is compatible with 2018b+ releases. If using a version 2019b or earlier, there will be some loss of functionality.

## A.5.2 Installation

Download the latest `mlappinstall` from the releases page of the GitHub repository<sup>6</sup> and install using the MATLAB app installer (from the toolstrip or by `matlab.apputil.install` at the MATLAB command line). Once Iris is installed, the application can be launched from the MATLAB applications toolbar.

From within Iris, the command line interface may be installed `Help > Install Helpers`. The CLI is a MATLAB command toolkit that enables interaction with Iris and utilities within from the MATLAB command window. Installing the CLI enables access the `IrisDVA` abstract class, with methods listed in Table A.4.

---

Method	Input Arguments	Description
<code>.start</code>	<code>[dataFile, []]</code>	Run Iris, optionally load data
<code>.update</code>	<code>mlappinstall</code> file	Update Iris with supplied <code>mlappinstall</code> file
<code>.import</code>		Load Iris libraries into MATLAB session path
<code>.detach</code>		Remove Iris libraries from MATLAB session path
<code>.installedVersion</code>		Check Iris installed version
<code>.isRunning</code>		Check if an instance of Iris is running
<code>.isMounted</code>		Check if Iris on the MATLAB session path

---

Table A.4: *Iris command line interface.*

## A.5.3 Known Issues

Iris utilizes MATLAB's web-based uifigures for the user interface. As this is still relatively new and under active development by The MathWorks Inc., some bugs and under-optimized features may cause interference with the usability of Iris. Most of the issues (described below) are resolved by the MATLAB 2021b release, nevertheless, we describe the issues for

---

<sup>6</sup><https://github.com/sampath-lab-ucla/IrisDVA/releases/latest>

the sake of transparency.

*Web-UI.* Because Iris development started in 2016 (2016b release) and the functionality of `uifigure` was severely lacking in comparison to today's `uifigure`, we employed a number of hacks to get a semblance of usefulness for the application. Some of those UI hacks are no longer needed but don't impact functionality and so haven't been migrated out. Thus, you may encounter some UI elements that don't display as intended and startup times may be slow.

*Coalescer recursion.* Starting in MATLAB 2020a, this appears to have become a non-issue. The short description for this issue is that MATLAB will occasionally call a `drawnow` function, which may lead to a infinite recursion in the `flushCoalescer` method of the internal `FigureController` class. The complete issue is described well on the MATLAB answers<sup>7</sup> page. As of the MATLAB 2020b release, the infinite recursion seems to be gone, but there is an occasional lag following actions which result in a call to `drawnow`. As of the MATLAB 2021a release, there is no detectable issue.

*Performance.* Iris was originally written to view, manage and analyze data acquired using Symphony DAS which utilizes the hdf5 format. A main goal was to prevent needing Symphony installed on the analysis machines, primarily because Symphony was written for a Windows environment and we had a lot of Mac users in the lab. For this reason, I opted for taking a page-cache approach of caching data directly in volatile memory. I never got around to optimizing the hdf5 reading method (for either Symphony 1 or Symphony 2 files), so it may take some time to load a single experiment. In my experience, the typical Symphony 2 file from an experiment is 100-200Mb on disk. This results in a  $\approx 3$  minute load time on our Intel i7 pc and  $< 30$  seconds on our Intel Xeon E5 workstation. In 2020b, MATLAB modified the parsing algorithms for mat-files that has caused a significant hit to reading/writing performance (in our hands). For future optimization, MATLAB release notes for 2021b introduce new low-level hdf5 methods that will make optimizing this process easier.

---

<sup>7</sup><https://www.mathworks.com/matlabcentral/answers/467671>

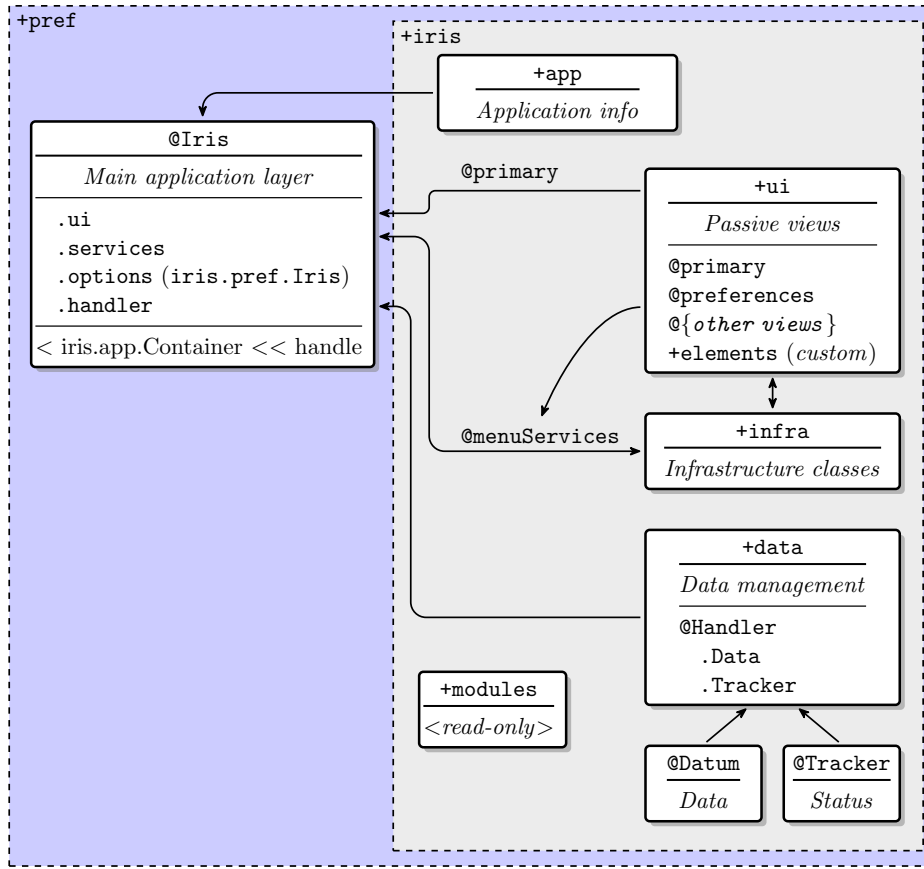


Figure A.20: Application layout.

#### A.5.4 Application Development

Iris was designed based, loosely, on the concept of layered architecture to keep isolated components easily modifiable and segregate core structures from user interfaces (Fig. A.20). The application is hosted through a main `@iris` class and sits on top of a preferences (`+pref`) layer. For simplicity in documenting developmental progress and for creating a single repository for all application text, application information is encapsulated in a separate set of classes (`iris.app.*`).

The internal architecture is divided into three layers: data, services, and presentation. The data layer is comprised of a tracker and handler which manage imported data and contain logic for file and index tracking during interaction. The services layer manages communication between the presentation layer and the main application class. The presentation layer



comprises passive views for each of the user interface elements. Views may be constructed of either the traditional MATLAB figure environments or the new web-based (`uifigure`) environments using the appropriate container class. Each view may optionally contain a preference class (`iris.pref.<view name>`) to manage any persistent and default values for ui elements. The Iris main view is presented through the `@primary` (`iris.ui.primary`) UI class, which directly reports to the main application layer, unlike all other UI classes.

## REFERENCES

Cafaro, Mark, Midgley, Frank, Neward, Ted, and Wark, Barry (2019). *Symphony Data Acquisition System*. <http://symphony-das.github.io>.

MathWorks (2021). *MATLAB 2021b (9.11)*. The MathWorks Inc., Natick, Massachusetts. <https://www.mathworks.com/>.

Simon, Jan (2011a). *ButterParam*. MATLAB Central File Exchange. <https://www.mathworks.com/matlabcentral/fileexchange/30247-butterparam>.

Simon, Jan (2011b). *FilterM*. MATLAB Central File Exchange. <https://www.mathworks.com/matlabcentral/fileexchange/32261-filterm>.